Mechanical Modelling of Blade Forming and Drainage of Flocculated Suspensions

by

Claes Holmqvist

March 2005 Doctoral Thesis from Royal Institute of Technology Department of Mechanics SE-100 44 Stockholm, Sweden Akademisk avhandling som med tillstånd av Kungliga Tekniska Högskolan i Stockholm framlägges till offentlig granskning för avläggande av teknologie doktorsexamen fredagen den 11:e mars 2005 kl 14.00 i Kollegiesalen, Administrationsbyggnaden, Kungliga Tekniska Högskolan, Valhallavägen 79, Stockholm. ©Claes Holmqvist 2005 Edita AB, Stockholm 2005

Mechanical Modelling of Blade Forming and Drainage of Flocculated Suspensions

Claes Holmqvist 2005

Department of Mechanics, Royal Institute of Technology SE-100 44 Stockholm, Sweden.

Abstract

A method has been developed for flexible modelling of multi-component twinwire blade formers. Features such as suction devices, loadable blades, curved blades, and partial contact between the blades and the forming fabrics are easily incorporated. New results include a series of calculations demonstrating the non-trivial interaction between the pressure pulses when the blades are positioned successively closer together, the effects of suction on the pressure pulse generated by a blade applied to the opposing wire, and how blades of modest curvature do not necessarily stay in contact with the fabric along their full width and the implications of this on the pressure gradients in the machine direction.

The behaviour of the fibre mats as they experience the first of the blade pulses (after having been formed over a roll) is then considered in detail. Typically, the thickness of the mats decreases during the pulse, which reduces the rate of deposition of new fibres onto the webs. The amount of fibres in the sheets therefore changes marginally. Nevertheless, the resistance to drainage presented by the fibre network is seen to increase significantly due to the low permeability in highly compressed layers of the mat. As a result of the pressure gradients in the machine direction, the shear stresses in the plane of the fibre sheets can attain several hundred Pascal next to the forming fabrics.

Further, a model for sheared consolidation of flocculated suspensions is presented that extends the concept of a concentration dependent yield stress, previously employed in studies of uniaxial consolidation, to comprise flocculated phase shear strength. Rate-dependent viscous stresses are also incorporated. The theory is applied to the problem of combined compression and shearing of a strongly flocculated suspension contained between two plates, one being fixed and acting as a perfectly permeable filter, the other movable and acting as a piston by which the load is applied. Qualitatively, the evolution of the volume fraction of solids exhibits the same behaviour as during uniaxial consolidation without shear. Applying shear is however predicted to increase the rate of the drainage process, due to a reduced load bearing capacity of the flocculated phase, and correspondingly higher pore pressures.

Descriptors: blade forming, pressure distribution, interaction, suction, drainage, filtration, sheared consolidation, shear strength, plastic deformation, flocculated suspension, soil mechanics, two-fluid model, mixture model

Preface

This thesis deals with models for the process referred to as 'blade-forming', that is employed in papermachines to drain the fibre suspension and build up the paper sheet. It is also concerned with the behaviour of flocculated fibre suspensions (of which the fibre webs in the paper machine is an example) during filtration. The research was conducted within the framework of FaxénLaboratoriet, a centre of excellence located at the Royal Institute of Technology in Stockholm, Sweden.

The thesis is divided into two parts. In the first of these, an introduction is given to the science of papermaking. A summary of the research conducted by the thesis author and his co-workers is also given, with the objective to clarify its context. The second part consists of five appended scientific papers. When necessary, these have been reset in the format of the thesis.

Stockholm, March 2005 Claes Holmqvist

Appended papers:

- **Paper 1.** Holmqvist, C., Dahlkild, A. & Norman, B., 2005 A flexible approach for modelling flow in multi-component blade formers. Submitted to *Nordic Pulp & Paper Research Journal*
- **Paper 2.** Shugai, G., Holmqvist, C. & Vynnycky, M., 2002 Analysis of a model for twin-wire forming. In *Proceedings of the 12th ECMI Conference*, Jurmala, Latvia
- Paper 3. Holmqvist, C., Dahlkild, A., 2005 Fibre mat behaviour in twin-wire formers. To be submitted
- Paper 4. Holmqvist, C., Dahlkild, A., 2005 Consolidation of sheared, strongly flocculated suspensions. To be submitted
- Paper 5. Holmqvist, C., Dahlkild, A., 2005 Influence of viscous stresses on the sheared consolidation of flocculated suspensions. To be submitted

Division of work between authors

- Paper 1: Claes Holmqvist (CH) performed the theoretical analysis, and developed the numerical algorithm, under the supervision of Anders Dahlkild (AD). Bo Norman provided valuable knowledge about the physics of the blade forming process. The manuscript was prepared by CH.
- Paper 2: CH formulated the problem, and contributed with some observations regarding the behaviour of the numerical solution of the dependent variables. The analytical work was undertaken by Galina Shugai and Michael Vynnycky (MV). The manuscript was prepared by MV.
- Paper 3: The work was conducted by CH, under the guidance of AD. The manuscript was prepared by CH.
- Paper 4: AD provided the original idea to incorporate critical state plasticity theory into a model for sheared flocculated suspensions, and performed the initial derivation of the governing equations. CH carried out the remaining details of the modelling work and solved the equations numerically. The manuscript was prepared by CH.
- Paper 5: The work was conducted by CH, under the guidance of AD. The manuscript was prepared by CH.

Contents

Preface	iv
Part 1. Overview and summary	ix
Chapter 1. Papermaking and forming	1
1.1. Outline of the process from tree to product	1
1.2. The forming section	
1.3. Twin-wire forming	4
Chapter 2. Modelling of multi-component blad	le formers 10
2.1. Research on blade forming and suction shoes	10
2.2. Interaction effects	13
Chapter 3. Drainage of flocculated suspensions	s 22
3.1. Previous modelling work	22
3.2. Constitutive relations	25
3.3. Fibre mat behaviour during pressure pulses	29
3.4. Sheared consolidation of flocculated suspension	as 34
Chapter 4. Concluding remarks	43
Acknowledgments	45
Bibliography	46
Part 2. Papers	51
Paper 1. A flexible approach for modelling flow multi-component blade formers	in 55
Paper 2. Analysis of a model for twin-wire form	ing 79
Paper 3. Fibre mat behaviour in twin-wire form	iers 87

Paper 4. Consolidation of sheared, strongly flocculated suspensions	123
Paper 5. Influence of viscous stresses on the sheared	149

CONTENTS vii

Part 1 Overview and summary

CHAPTER 1

Papermaking and forming

This thesis is concerned with mechanical models for the forming of paper. It is a fair guess that most readers will have at least some knowledge of mechanics in general, since it is one of the fundamental, and classical, engineering sciences. For this reason, it is also easy to find good introductions to the topic. A reader who is not acquainted with the manufacturing of paper will, however, find it harder to come across a presentation of the science of papermaking. To set the stage for the presentation of the work that has been undertaken, I therefore think it is appropriate to dedicate the first chapter of the thesis to an introduction to the modern paper manufacturing process. As will become evident, the drainage process referred to as 'blade forming' is given a more lengthy presentation, since it has been the main focus area of the conducted research.

1.1. Outline of the process from tree to product

There is no precise definition of paper. However, common to all products referred to by that name is that they are nested structures of slender particles, fibres, that are held together without the requirement of other components than the fibres themselves. In most cases these have a biological origin, but synthetic fibres are sometimes used as well.

After first having been developed in China in the 2nd century AD, paper-making has evolved to the interdisciplinary high technology process it is today. The large majority of paper products are wood based, and their production can be divided into three significantly different parts, each of which corresponds to an increased degree of refinement of the raw material:

- Forestry.
- Pulp production.
- Paper production.

During the pulp production, the fibres in the wood are freed through either mechanical or chemical treatment. If this is not carried out on site, they are delivered to the paper mill either as a concentrated suspension, or in the form of dry sheets. At the mill, the pulp is transformed into a dilute suspension and is then processed. Although the techniques employed to produce different paper qualities (called grades) is more or less the same, the characteristics of the final products differ a lot in terms of mechanical and other properties. The dry

1

mass per unit area, i.e. the 'grammage', of board is e.g. about $200-400 \text{ g/m}^2$, whereas that of tissue is only $14-25 \text{ g/m}^2$. The different stages of the paper production are in order:

- Stock preparation.
 - Dissolving the pulp, Refining, Adding additives, Screening.
- Forming.
 - Dilution, Deaeration, Ejection onto the forming fabrics, Dewatering.
- Wet pressing.
- Drying.
- Possibly calandering and/or coating.
- Rolling.

The step referred to as 'forming', will now be discussed in further detail.

1.2. The forming section

The internal structure of the fibre network constituting the paper is to a dominating extent determined in the forming zone of the paper machine. An example of a modern design of this section is illustrated in figure 1.1. In the remaining parts of the process only the structure in the thickness direction (referred to as the 'z-direction', or 'ZD') can be influenced. Consequently, the forming zone has a critical influence on many, but not all, of the important properties of the final product. These include the grammage distribution, called formation, and the strength of the paper. As a result, it is of paramount importance to a papermaker to understand the forming part of the process. This need is the underlying motivation for conducting the research presented in this thesis.

The fibre mass concentration of the thick stock entering the forming section is 3–4%. It is then diluted with water that has been drained at positions further downstream in the forming process, called 'white water', to a concentration of 0.1–1% depending on which grade is being produced. This diluted suspension passes several cleaning/screening devices that remove contaminants before it is fed into a nozzle in the part of the machine referred to as the 'headbox'. The nozzle ejects the suspension upon permeable fabric(s), where the dewatering will take place. The forming fabrics are by papermakers also referred to as 'wires'. In the thesis, the two terms are used interchangeably.

The headbox plays an important role in the forming process. A schematic illustration of its design is given in figure 1.2. The downstream end is a narrow slit, typically about 10 mm high and 10 m wide. It is important to have an uniform flow across the exit, and the upstream part of the headbox is therefore usually a tapered header, the purpose of which is to create an uniform pressure across the machine width (the 'cross direction', or 'CD'). Whatever non-uniformities remain after the tapered header are further reduced by the stepwise enlargement of the flow channels between the header and the nozzle. This part of the headbox is referred to as the 'tube bank'. Finally, the

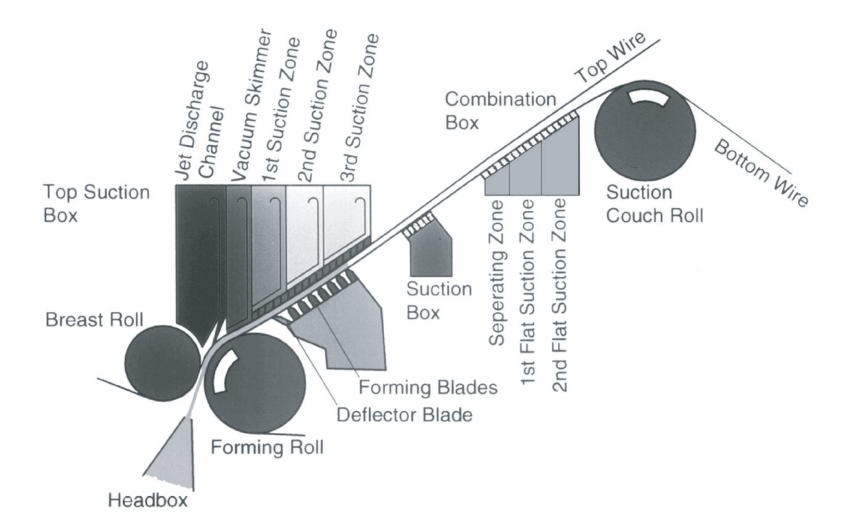


FIGURE 1.1. Illustration of a roll-blade twin wire forming section (the Duoformer CFD forming unit by Voith).

suspension is accelerated to the required speed in the nozzle. Although the concentration is usually low in the headbox, the fibres still have a tendency to form clusters, called flocs, which will result in bad formation in the paper sheet (i.e. uneven grammage distribution). The elongating flow in the nozzle has a positive effect on the dispersion of the fibres, and helps to minimise this problem. In addition, the acceleration dampens the relative turbulence levels in the flow, which is necessary to obtain a jet of good quality, and velocity non-uniformities in the CD are further reduced. However, a disadvantage of the headbox is that the extensional flow causes anisotropy in the fibre orientation. The fibres are aligned in the direction of flow (the 'machine direction', or 'MD'), which for some products has a negative effect on product quality. Experimental studies of the flow in the headbox include the works by Chuang (1982), Shands (1991) and Parsheh (2001). Among the numerical treatments, one can mention those by Farrington (1991), Bandhakavi & Aidun (1999) and Parsheh (2001).

The jet from the headbox impinges at a narrow angle on a forming fabric moving at a speed of up to 30 m/s, depending on the capacity of the machine and the grade that is being produced. As instabilities in the jet might impair the homogeneity of the paper sheet (cf. the study on the hydrodynamics of the liquid jet by Söderberg 1999), the distance travelled by the jet is kept to a minimum, normally 10–20 cm. Often, a speed difference is intentionally maintained between the jet and the fabric in order to favourably influence the structure and properties of the sheet. When the jet hits the fabric, the drainage starts. The water passes through the wire, while the fibres are left on the surface, resulting in the build up of a fibre mat. In the rest of the

4 1. Papermaking and forming

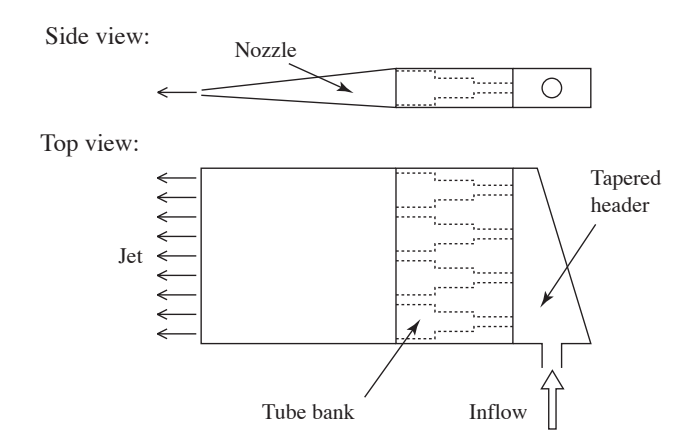


FIGURE 1.2. A schematic illustration of a headbox and its different parts: The tapered header, the tube bank and the nozzle.

forming section, through the action of different dewatering devices (presented in the following paragraphs), the drainage of the suspension continues till a fibre network with an average concentration of about 4 % occupies the region between the wires. Thereafter, a thickening process takes place during which the concentration rises till a sheet of about 20 % fibre mass concentration has been formed. After this the sheet is passed on to the press section.

The easiest way to achieve drainage is to move the wire horizontally and let the pressure head, created by gravity, force the water in the suspension through the fibre mat and the wire. An increased pressure difference across the wire can be obtained by applying suction to the bottom side of the fabric. This method, called Fourdrinier forming, was the one first used to produce paper in a continuous process, and is still widely used, often in combination with other techniques. The machine speeds obtainable in this way are however limited by the instability of the free surface of the suspension residing on top of the wire. To overcome this problem, twin-wire forming was introduced in the 1950's and is now the predominant choice when new machines are built. Overviews of the history of forming and different machine designs have been given by Norman (1989) and Malashenko & Karlsson (2000).

1.3. Twin-wire forming

The basic principle of twin-wire forming is that both sides of the suspension are in contact with a wire at all times. This was not a new idea when practical designs first appeared. However, early attempts had not been successful due to the lack of insight that one must always (at any given position along the MD) allow at least one of the wires to automatically adjust its lateral position as a function of the current operating conditions. Drainage is achieved by deflecting

the path of the fabrics, which are pre-stressed to a tension of about 5–10 kN per metre width, thus creating a positive pressure difference between the region enclosed by the wires and the surroundings. Compared to Fourdrinier forming, twin-wire forming yields considerably higher dewatering rates. This is due to the fibre mats building up on both of the wires simultaneously. In addition, the flow resistance presented by the mat and wire on either side is significantly less than that presented by a single wire and mat after the same amount of total drainage. Another advantage is that carefully performed twin-wire forming gives a paper whose two sides have a more equal structure than does Fourdrinier forming.

1.3.1. Roll forming

During roll forming, the drainage pressure is achieved by wrapping the fabrics over a cylindrical roll, as seen in figure 1.1. In early twin-wire formers, this was the only means employed to achieve drainage. By using a roll with permeable surface, two-sided dewatering can be obtained. Roll forming is a quite gentle method in the sense that the pressure gradients in the MD are not as severe as when blades are applied to the fabrics (cf. section 1.3.2). Further, the amplitude of the dewatering pressure is somewhat lower, of the order 10 kPa, than during blade forming. This yields a good retention of the fibres, the fibre fragments (referred to as 'fine material') and the additives in the suspension, which at higher pressure levels to a larger extent would follow the water through the wires. However, as pressure gradients play an important role in breaking up fibre flocs, their absence yields flocculation and a final paper with bad formation. For studies of the pressure distributions and the drainage rates during roll forming, the reader is referred to the works by Martinez (1998), Zahrai et al. (1998), Dalpke et al. (2004) and Holm (2005).

1.3.2. Blade forming

An alternative technique to achieve drainage is blade dewatering. The wires then follow an overall straight path, from which they are locally deflected by ceramic blades that are applied across the CD. The principle of blade application is illustrated in figure 1.3.c. In the figure, two wires pass a series of three blades of which two are applied to the top fabric and one to the bottom fabric. The deflection of the wires causes a pressure to be built up in the region between them. The underlying mechanism is readily explained: Assume first that the fabrics, and the suspension contained by them, move linearly past the blades, on the verge of touching them but without actually doing so (figure 1.3.a). The pressure in the suspension will then be the same as outside of the wires. If – hypothetically – the bottom blade could be used to push the lower wire upwards without affecting the upper wire, a situation like the one in figure 1.3.b would occur (one could in this subfigure e.g. imagine the upper wire as a permeable stiff wall). It is evident that the available cross section for the flow of suspension has shrunk at the position of the middle blade. In order to adapt

to this situation, the suspension must either pass through the wires, so that less of it has to pass the middle blade, or it must push the upper fabric outwards to create a larger cross section. In reality, both of these things happen simultaneously as illustrated in figure 1.3.c. The contraction experienced by the flow results in a local increase of the pressure which, at the same time, forces liquid through the fibre mats and the wires and displaces the opposing wire. The fabrics, of course, resist displacement due to their tension. An interesting question is why the suspension velocity does not increase at the blade, which would also allow it to pass the narrow section. The answer is by no means trivial. We give a tentative explanation by noting that if the wires are initially parallel (as is the case if the pressure in the gap between the fabrics equals the ambient pressure), the lower wire must at some point curve towards the upper fabric. Since the fabrics are under tension, this implies that the pressure in the gap at that position is higher than outside the fabrics. Consequently, the velocity at that position is lower than far upstream of the blades, which means that a deceleration takes place as opposed to the proposed acceleration.

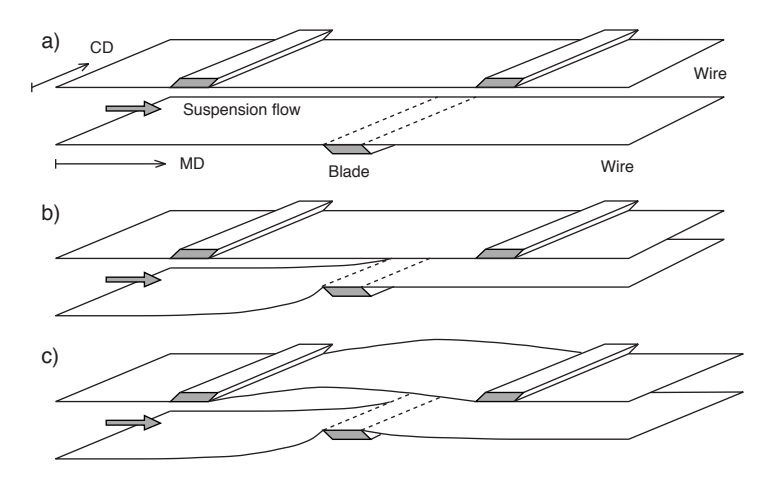


FIGURE 1.3. The principle of blade dewatering. Note that the proportions are not correctly reproduced. MD – Machine Direction, CD – Cross Direction. The different figures a–c are explained in section 1.3.2.

If expelled water adheres to the outer surface of the wires, it will remain till it is removed by centrifugal effects, or it is deflected away by the next blade or some other slicing device. This redirection, which is called 'doctoring', results in a pressure build-up close to the tip of the blade. It will influence the pressure difference across the wire and hence also the local drainage.

Figure 1.3 focuses on the situation in the region around the middle blade. Naturally, the positions of the fabrics at the different blades are not independent of each other. Moving the middle blade upwards will create restrictions on the flow at the upstream and the downstream blades as well, and, due to the same mechanism as explained above, regions of locally high pressure will be generated at these blades. However, the corresponding wire curvatures have not been properly illustrated in the figure. Further, it is stressed that, unlike in the figure, blade dewatering is a slender problem. The distance between the wires is typically in the range 1–10 mm while the distance between the blades is an order of magnitude larger. The extension of the blades in the MD is normally 10–50 mm. All of this should also be put in relation to the width of the machine in the CD, which on a large production unit can be up to 10 m.

When a volume of suspension travels past a series of blades, it will repeatedly be exposed to regions of high pressure resulting in dewatering. From the point of view of the suspension volume, these regions will be experienced as pulses in time, although they are a result of translation in the MD. This has led to the use of the term 'pressure pulse' for the region of increased pressure in connection with a blade. The pressure pulses are of a quite different nature than the dewatering pressure achieved during roll forming. Measurements by e.g. Zhao & Kerekes (1995) and Zahrai et al. (1997) have shown that the magnitude of these pulses can be as high as 25 kPa or more, hence of significantly larger magnitude than what has been reported for roll forming (although, during ordinary operational conditions, the amplitudes of the pulses are not necessarily of such high values). Because of this, pure blade forming results in poor retention, since fibres, fine material and additives then have a high tendency to pass through the fibre mat and the wire until the former has grown sufficiently thick. In addition, the pressure pulses are generally quite localised, and will therefore yield large pressure gradients in the MD. It is believed that this causes disruption of fibre flocs in the suspension, and that it explains the good formation of the final paper sheet that can be obtained by using blades for dewatering (Nordström 1995). The underlying mechanism is not yet properly understood. One theory is that the elongational flow resulting from the pressure gradients in the downstream region of a blade will stretch the flocs and possibly tear them apart. The study by Bergström (2003) indicates that the rupture of flocs in the forming section is due to a shearing mechanism. As a result of the drainage flow, flocs get pinned to the fibre mat, after which they are exposed to the velocity difference in the MD between the undrained suspension and the mat residing on the fabric. If the relative velocity is of sufficient magnitude, the floc can be torn apart. The behaviour of flocs experiencing pressure pulses has also recently been studied by Åkesson (2004).

In order to achieve a process with high retention in the forming section, and an even grammage distribution in the final sheet, it is now common to combine roll forming with blade forming (cf. e.g. figure 1.1). The idea is that fibre mats should be built up on the wires during the roll forming in order to generate sufficiently thick webs to prevent low retention in the subsequent blade section. Only partial dewatering should take place over the roll though, as the purpose of the following blade section is to break up fibre flocs in the

remaining suspension. This would not be possible if the drainage has gone too far.

Since the blades are not permeable, one might suspect that asymmetrical drainage through the two fabrics has a detrimental effect on the quality of the final paper. This is true to a certain extent, but if the blades are applied alternately to the two wires, as in figure 1.3, a sheet with acceptable two-sidedness is obtained.

According to Norman (1989) twin-wire blade formers were first developed by Beloit and Black Clawson at the end of the 1960's. At that time it was not understood that the blades generated pressure pulses. In the Beloit Bel Baie design the blades were not arranged in a straight configuration as is often done today, but instead mounted so that they described a circular arc with the tips lying on the circumference. The arc had a radius an order of magnitude larger than that of a conventional forming roll. Indeed, the wires were wrapped over the blades in order to mimic roll forming with a very large roll. The good formation that was achieved was attributed to a dewatering pressure that was thought to be of low amplitude and long duration, hence rather the opposite of what is actually the case. Norman (1979) was the first to give a reasonably accurate description of the physics of pulsating blade forming.

In the early designs incorporating deflection of the wires by blades, these were mounted in fixed positions. Whenever blades were applied to both wires, or blades were positioned on one side and other dewatering devices on the opposite side, the process got very sensitive to changes in the operating conditions. To understand this, one can e.g. look at the blade/counterblade arrangement illustrated in figure 1.3. It is evident that no drainage pressure is generated in the situation described by figure 1.3.a, where the blades are not acting on the wires. However, if the operating conditions were changed so that the distance between the incoming wires increased, while the blades remained in their positions, the blades would impose an obstruction to the flow and pressure pulses would be generated as in figure 1.3.c. To reduce the sensitivity, adjustable blades should be used, as suggested by Norman (1979). Baumann (1989) described a forming section with fixed blades applied to one of the wires, and flexible blades applied to the other side. These were pneumatically pushed against the wire, and hence the forces by which the blades were applied could be controlled. This has become standard practice.

1.3.3. Suction shoes

Drainage can also be achieved by lowering the pressure outside one of the wires as compared to the pressure on the opposite side (usually the atmospheric pressure). This is the design principle of the 'suction shoes' sometimes employed in the forming zone. By creating a low pressure inside the shoe, water is sucked out through the adjacent fibre mat and wire. To increase the control of the process, the shoe is usually divided into several compartments ('boxes'), with the possibility to set different pressures in each one of them. An illustration

of this is seen in figure 1.1. The upstream and downstream edges of the boxes can generate pressure pulses in the same way as blades do.

CHAPTER 2

Modelling of multi-component blade formers

In this chapter, a review is made of previous research on blade forming, after which the study reported in Paper 1 is discussed. Both Paper 1 and Paper 2 treat the modelling of multi-component forming sections. The latter is concerned with the asymptotic behaviour (far upstream and downstream of the blade section) of essentially the same equations that are solved in Paper 1. It provides insight into nature of the mathematical description, but will not receive any attention in the introductory survey given in the present chapter.

The main concern has been the pressure distributions in the forming section. Being able to determine the variation of the drainage pressure along the MD is vital, if predictions are later to be made regarding issues like dewatering rates and structural changes in the fibre sheets.

2.1. Research on blade forming and suction shoes

2.1.1. Establishing the pressure pulses

Although pressure pulses were predicted by Norman (1979), it was not until the work by Sims (1985) that experimental evidence (for a Beloit Bel Baie blade former) was published. A trailing pressure transducer was inserted through the headbox into the region between the wires, where an increased pressure was detected at each blade. The same technique was also used by Brauns (1986). The amplitudes of the pulses were found to increase when the wire speed or the tension in the wire opposing the blades was increased. Amplitudes of up to 7.5 kPa were detected for some operating conditions. Brauns' work is also interesting because it investigates the effect of applying suction in between the blades. Yet another experimental study using a trailing pressure probe is the one by Bando et al. (1994). This technique is one of few available to measure the pressure during blade forming due to the difficulty in accessing the region between the wires. It has a drawback in that the position of the probe in the ZD can be neither controlled nor determined. It is also unclear to what extent the presence of the probe influences the flow of suspension, and thus the measured pressure, at narrow gap sizes.

Another technique consists of drilling pressure taps (i.e. 'holes') through the blades, to which a measurement device is connected. For obvious reasons, the pressure distribution can then only be obtained in the region covered by the surface of the blade. Such studies have been undertaken by Zhao & Kerekes (1995) and Zahrai *et al.* (1997), and it was found that the pressure pulses can be of as large magnitudes as 25 kPa.

2.1.2. Analytical results

Zhao & Kerekes (1995) performed the first rigorous theoretical analysis of blade dewatering. A quasi one-dimensional model was developed for an isolated blade of infinitesimal extension in the MD. The wires extend an infinite distance in the upstream and downstream directions, and approach and leave the blade parallel at prescribed angles. The problem was treated like that of an inviscid fluid translating between thin, perfectly flexible, moving walls of constant permeability. No effects of fibre web build-up on the drainage resistance (due to deposition of fibres onto the wires) were included. An important condition for the validity of the model is that the characteristic length scale in the MD is much larger than the distance between the wires. The equations were linearised and solved analytically, yielding pressure pulses located upstream of the blade. It was noted that certain parameter combinations yield oscillatory solutions in this region. Downstream of the blade, the analysis gave zero pressure difference across the fabrics and, consequently, straight wires. A comparison with experimental data showed good agreement.

Moch (1995) constructed a one-dimensional model for the flow around a single thin blade, including a variable permeability of the wires in order to simulate the effect of fibre mat build-up. The pressure pulses were found to become of larger amplitude and to extend for a shorter distance in the upstream direction than when no fibres were deposited (as would be the case if the suspension was replaced by pure water). Zhao & Kerekes (1996) performed a study of the influence of suspension concentration on the pressure pulses by using the model developed earlier (Zhao & Kerekes 1995), inserting different values for the constant drainage resistance. They also concluded that increased resistance gave pulses of larger magnitude. An attempt was made to relate the calculated integrated velocity difference between the suspension and the wires with experimental measurements of the formation, and a weak correlation was reported.

Zahrai & Bark (1995) presented a two-dimensional analysis of the application of a thin blade. The combined wire/fibre mat structure was considered to be inertialess and of negligible thickness, with constant permeability. The suspension was modelled as an inviscid fluid. A regular perturbation analysis, using the angle of deflection of the wires as the perturbation parameter, resulted in a linear analytical solution. Upstream of the blade, they found only small gradients in the ZD, and the solution agreed well with the one-dimensional analysis by Zhao & Kerekes (1995). The main difference was that the one-dimensional model predicted a slightly higher pressure amplitude. However, downstream of the blade, the two-dimensional analysis yielded quite large gradients in the ZD. Notably, there was a region close to the blade in the ZD, that extended a short distance downstream of the point of application, where the

pressure was lower than outside of the wires. This is due to the acceleration of the flow around the corner formed by the wire when the thin blade is applied to it. In their study, Zahrai & Bark (1995) made no assumption about the magnitude of the ratio between the length scales in the MD and the ZD. As a consequence, they were able to include the bending stiffness of the wires in their analysis. It was found that it had no influence outside a very small region close to the (thin) blade. A more accurate criterion for the appearance of oscillations in the dependent variables than that derived by Zhao & Kerekes (1995) was given as well. Among the first two dimensional models of blade dewatering should also be mentioned the study by Nigam & Bark (1997), where potential flow theory was used to study blade dewatering with a single flat or cylindrically curved blade. Linear analytical results were obtained through a perturbation analysis.

2.1.3. Numerical results

Zahrai & Bark (1996) and Zahrai et al. (1997) developed a numerical method for solving the non-linear equations describing the two-dimensional flow over a blade of arbitrary shape. It was applied to a flat and to a triangular blade, and the results were compared with experimental data obtained using blades with pressure taps. Good and reasonable agreement was found for the triangular and the flat blade, respectively. During the numerical simulations, the drainage resistance was assumed to be constant.

Green & Kerekes (1996) numerically solved a one-dimensional non-linear model for a single thin blade incorporating a variable permeability for the wire/fibre mat. The same conclusions were drawn regarding the influence of fibre mat build up as those made by Moch (1995). In the model, the wire/fibre mat was attributed a constant mass per unit area, and it could be concluded that the influence of fabric-inertia on the calculated variables was small. The influence of wall shear stress was accounted for in a rudimentary way. By testing viscosity values of different magnitudes, it was concluded that this parameter had a negligible influence on the pressures calculated with their model. An indication of the effects of doctoring of drained water was found by prescribing a pressure distribution on the outside of the wire in contact with the blade. It was concluded that, as a result, the amplitude of the pressure pulse increased. Green et al. (1997) developed the model to deal with a blade of finite extension in the MD. Like Zahrai & Bark (1996) and Zahrai et al. (1997) they observed that, unless the blade is of short length, it produces two pressure pulses – one that is associated with wrap of the wires around the front edge and one with wrap around the back edge. The model was also used to study the effect of blade wear (Green & Roshanzamir 1997).

Roshanzamir et al. (1998) performed viscous two-dimensional simulations with a blade of finite extension in the MD. The wire/fibre mat was given a finite but constant thickness, and a constant flow resistance. This was the first treatment including viscosity in a rigorous way, albeit under the assumption

that the suspension behaves like a Newtonian fluid. Hence, an estimate of the shear in the suspension was obtained. The viscosity level did however not influence the calculated pressures. Roshanzamir $et\ al.\ (1999)$ extended the model to include effects of doctoring of water drained upstream of the blade. Although the pressure building up on the outside of the wire due to the deflection of the approaching water was limited to a very short distance upstream of the blade, it was found that it can significantly affect the amplitude of the pressure pulse in between the wires, thus confirming what was indicated by Green & Kerekes (1996). More or less the same study can also be found in the reference Roshanzamir $et\ al.\ (2001)$. The effect, on a blade pulse, of adding an inertial term to the permeability law for the drainage fabric was investigated by Roshanzamir $et\ al.\ (2000b)$. It was concluded that the influence on the pressure distribution was small, as compared to applying a purely viscous drainage law that results in the same amount of expelled water.

Green (1999, 2000) presented a one-dimensional model where suction was applied in between two thin blades. Roshanzamir et al. (2000a) presented a viscous 2D simulation of the same problem. Downstream of the first (upstream) blade, the pressure in the gap between the fabrics was found to rapidly decrease to a level half way between the pressure on the suction side and the pressure outside the opposing wire. This corresponded to the pressure in the gap being 3–5 kPa lower than the ambient pressure, which in the simulations resulted in an increased bending of the outer wire over the blades, and consequently pressure pulses of larger amplitude than if no suction was applied. It is, however, unlikely that such a pressure difference over the wire opposing the suction device could occur in a real forming section.

Although no time-dependent analyses of blade forming have been carried out, such studies have been undertaken for roll forming by Turnbull *et al.* (1997) and Chen *et al.* (1998).

2.2. Interaction effects

Previous work has given us insight into the physics of different devices employed in blade forming. However, the focus has been on single components, e.g. a single blade. As is obvious from figure 1.1, a blade forming section does not consist of a single component. Instead, several blades are applied in series, and often to both of the wires and in combination with one-sided suction. The question naturally arises as to what extent the different devices interact with each other. Previously, no models have been developed that clarify how the configuration of the devices influences the process. Hence, the design of forming sections, trouble-shooting, or tuning of the controllable parameters after changes in the process, necessarily involves extensive use of trial and error techniques. Especially when developing new designs, it would be advantageous if theoretical analysis could replace some experimental work, at least in the early stages. Since it is prohibitively expensive to disrupt the production in a

mill, one must today resort to using pilot paper machines for trials. Although less expensive, this is by no means a cheap solution.

2.2.1. A module based model of a forming section

In Paper 1, a model is presented by which blade forming sections of quite arbitrary configurations can be studied (for a more lengthy treatment, see also Holmqvist 2002), in particular with respect to the drainage pressure distribution. The ambition during its development was to obtain a numerical tool that is flexible enough to permit major alterations of the geometry, and a rather free choice of operation parameters. This was achieved by defining fundamental building blocks, 'modules', from which the desired forming section is constructed. Each such module represents a segment of the machine, consisting of either two free fabrics (and, naturally, the suspension mixture contained between them), or one free fabric and a blade, as illustrated in figure 2.1. Suction boxes are accounted for by specifying a low pressure on the back side of the wire to which the device is applied, thus increasing the effective drainage pressure. The modules are solved independently and matched to each other iteratively. By keeping the interface between the modules simple, considerable flexibility is achieved.

To obtain a tractable description of the process, certain simplifications had to be made. It is assumed that the fibre mats residing on the wires are separated by a region of suspension of high mobility, referred to as the 'free suspension', or sometimes the 'bulk' of the suspension. The free suspension is supposed to behave like an inviscid fluid, which is justified according to the scaling analysis in Paper 3. Confer also the study by Roshanzamir et al. (1998), in which Newtonian viscous stresses are found to have a small effect on the blade pulses. It is reasonable to assume that blade forming is a slender problem, in the sense that the characteristic distances, over which the dependent variables change, are much longer in the MD than in the ZD. An analysis akin to the shallow water wave theory (cf. e.g. Acheson 1990) then reveals that the pressure and velocity of the suspension are only dependent on the position along the MD.

Each combination of fabric and fibre mat (henceforth in this chapter referred to as simply the 'fabric', or 'wire') is treated like a single entity, perfectly flexible and of negligible mass and thickness. It follows that when the term 'suspension' is employed in the remainder of this chapter, we are always referring to the free suspension. The classical Euler-Bernoulli beam theory is employed to model the tensioned fabrics, the flow through which is assumed governed by the purely viscous Darcy's law. A drainage resistance that increases linearly with the accumulated quantity of water expelled at upstream stations accounts in a rudimentary way for the build up of fibre mats on the wires. Where applicable, i.e. unless it yields unphysical solutions, the fabrics are assumed to follow the surfaces of the blades. The drainage flow is set to zero at wire-blade contacts.

The resulting governing equations are similar to those employed by e.g. Green & Kerekes (1996) and Green & Roshanzamir (1997) to model a single blade applied to a pair of fabrics. Since the sole independent variable is the position along the MD, the computational effort to solve each module is small. It is further reduced by partly integrating the system analytically prior to the numerical treatment.

To solve a module, a certain amount of information must be available. For example, in the case of a module consisting of two free wires, that information includes the position in the ZD of the fabrics at the inlet and outlet of the module, the drainage resistances at the upstream end, and the pressure and velocity of the suspension at the downstream end. Normally, only part of the necessary information is available for each module. This is the origin of the need to match the modules iteratively to each other. The unknown parameters are guessed, and the solutions for the different modules are updated repeatedly till they fit together in a physically correct manner. The quality of the solution after each iteration is quantitatively measured by 'matching criteria', or 'matching functions', which express the requirement that certain dependent variables are continuous across module boundaries (i.e. the position of the wires, the velocity of the suspension, the pressure, and the drainage resistances), as well as other conditions which must be fulfilled. A blade that is to be applied with a certain force results in a condition on the slopes of the fabric at the blade edges (stemming from a force balance in the ZD for the blade). If curved blades are employed, it is not certain, and not required, that the blades remain in contact with the wire along its full width in the MD. This is handled by introducing the position in the MD of the interfaces between the modules as unknowns, which are then determined by requiring that the fabric is tangential to the blade at the point of contact. The matching functions are defined in such a way that perfect compliance corresponds to a zero returned value. The problem of determining the unknown parameters and, in the process, the solution of the governing equations in the forming section, hence turns into the problem of finding a root.

2.2.2. Three blades and a suction box

The procedure outlined in paragraph 2.2.1 is applied in Paper 1 to study a small blade forming section consisting of three blades and a suction box, as illustrated in figure 2.1. The suction device is located between the blades furthest upstream and downstream (it covers the region $x_{u2} \leq x \leq x_{d1}$), facing the middle blade. The velocity of the fabrics is U, and the density and effective viscosity of the suspension are denoted ρ and μ_c , respectively. Both wires are tensioned to T, and the initial resistance to drainage is R_0 . If desired, these last two parameters can be set different for each fabric. Far upstream, the wire separation is h_0 . The blades are of width D, and the spacing between them, defined as the distance between the trailing edge of one blade and the leading edge of the next blade downstream (which is applied to the opposite fabric), is

 δ_b . The (constant) concentrations in the free suspension, and in the mat, are ϕ_s and ϕ_m , respectively, and the permeability of the webs/wires is assumed to be of constant value k. The middle blade is applied by a force Q per unit width of the machine. Since the blades are not necessarily flat, we let the functions $f_u(x)$, $g_m(x)$ and $f_d(x)$ (which refer to the upstream, middle and downstream blade, respectively) trace out the surfaces of the blades in the ZD. x is the position in the MD. Note that $g_m(x)$ is only known up to a constant, which is determined from the force by which the blade is applied. The position of the fabric in contact with the fixed blades is denoted f(x), whereas the position of the opposite fabric is g(x). The drainage pressure, and the suspension velocity in the machine direction, are p(x) and u(x), respectively.

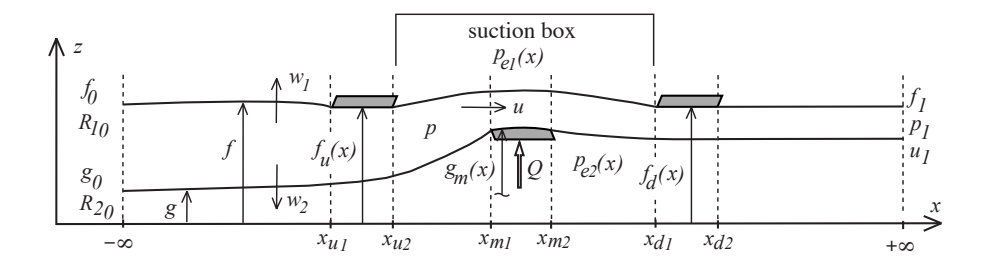


FIGURE 2.1. Schematic view across a blade forming section consisting of three blades. The dashed lines indicate module boundaries. The two 'upper' blades are fixed, whereas the 'middle' blade is adjustable in the ZD and is applied with a prescribed force Q. The suspension flows from left to right between the wires. The external pressures $p_{e1}(x)$ and $p_{e2}(x)$ can be set to arbitrary values, hence permitting devices for one-sided suction to be simulated, e.g. the box in the figure. f_0 , g_0 and f_1 denote known fabric positions upstream and downstream of the blade section. p_1 and u_1 are the pressure and velocity at the outlet of the considered domain. w_1 , w_2 represent drainage flow, and R_{10} , R_{20} are the initial drainage resistances of the wires. Note that the relation between the dimensions in the x- and z-directions is not properly illustrated. Confer the text for additional explanations of the notation.

2.2.3. Applying a suction pressure

In figure 2.2, the effect on the pressure distribution of applying one-sided suction is demonstrated. We first consider the case without suction, i.e. $p_v = 0$. Due to the close spacing of the blades, the generated pulses have partly merged. Also, to achieve a wrap of the fabrics over the trailing edge of the third blade, and thus mimic the effects of a fourth (loadable) blade, the third blade is given a different position in the ZD than the outlet of the considered domain (cf.

the caption of fig. 2.1 and 2.2). When the suction is applied, the pulses at the middle blade are reduced. This is natural. In chapter 1, it was concluded that the pressure pulses are a result of the need for the flow to adapt to the reduced gap size when a blade is applied. Due to the suction, the drainage through the fabric opposite the middle blade is enhanced. The large pressure drop across the wire/mat also pulls that fabric into the suction box, which increases the cross section available to the flow. As a result of these two factors combined, the constriction created by the blade is less severe than without suction, which explains the reduced amplitude of the pulse.

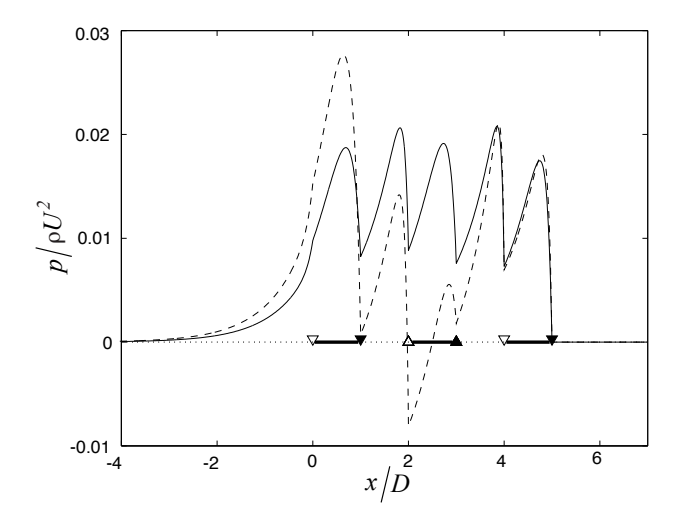


FIGURE 2.2. The effect on the pressure distribution of one-sided suction of magnitude p_v in the forming section in fig. 2.1. (—) $p_v=0$, (- - -) $p_v/(\rho U^2)=-0.016$. $Th_0/(\rho U^2D^2)=0.18$, $\beta\phi_s/\phi_m=0.103$ where $\beta=\mu h_0^2/(\rho UDk)$, Q/T=0.036. $\delta_b/D=1$. $f_0/h_0=f_1/h_0=1$, $g_0=0$, $p_1=0$, $u_1/U=1$, $R_0h_0/(\rho UD)=0.194$. $f_u(x)/h_0=1$, $f_d(x)/h_0=0.78$ and $g_m(x)=constant$, i.e. flat blades. The triangles indicate the positions of blade edges. The upstream and downstream end of the considered domain is located at, respectively, x/D=-14.1 and 7.14.

Note also that the amplitude of the first pulse in figure 2.2 is significantly increased when suction is applied, an effect resulting from a larger wrap of the fabrics over the upstream blade. To a much smaller degree, the same occurs at the downstream blade. An important feature of the suction profile in figure 2.2 is that the region in which the pressure is lower than the atmospheric pressure, i.e. where p(x) < 0, is located above the middle blade. This prevents backflow through the wire opposite the suction box, of either previously drained water or air. The model is not capable of correctly handling such 'reversed

drainage' (although a solution is obtained), a deficit it shares with all previously developed models for blade sections and suction boxes. Since situations of this kind can easily be envisaged, it can probably be regarded as the most serious weakness of the model. If the middle blade had not been applied during the suction, a pressure p(x) < 0 (i.e. lower than in the surroundings) would have been predicted by the simulations in a large part of the region between the upper blades. The fabric not in contact with the suction box would, due to the higher ambient pressure, be 'pushed' towards the suction box. In a real situation, there is no mechanism to maintain such a reversed pressure difference between the surroundings and the suspension, and it is likely that the pressure in the gap is never significantly lower than outside of the fabrics. Neither water nor air flowing through the forming fabric from the outside would, through drag forces, be able to give the fabric a curvature comparable to that of the wire in contact with the suction box. Note that the latter is curved as a result of a pressure drop generated almost exclusively over the fibre mat. This pressure drop can be large due to the relatively low permeability of the mat. On the other hand, during 'reversed drainage', the fibre mat cannot transmit large forces to the fabric, and the forming fabric itself is designed to present little resistance to liquid flow. Surface tension menisci in the pores between the strands in the wire are also unlikely to be strong enough to prevent backflow, and thus sustain a pressure difference of the required magnitude. These issues are further discussed by Holmqvist (2002), as well as some ideas regarding ways to improve the model to better handle situations where there are tendencies to backflow.

2.2.4. Spacing between the blades

A good example of non-trivial interaction between pressure pulses is given in figure 2.3, which contains the pressure distributions obtained in four simulations where the blades are positioned successively closer together. No suction is applied. Here, we have $f_0/h_0 = f_u(x)/h_0 = f_d(x)/h_0 = f_1/h_0 = 1$. Hence, the fabrics are not wrapped over the trailing edge of the third blade, which explains the absence of a pressure pulse at that position. In figure 2.3.c and 2.3.d, the pulses due to the upstream blade and the leading edge of the middle blade are merging more and more. What is most interesting, however, is how the pulses at the trailing edge of the middle blade and the leading egde of the third blade are reduced when δ_b decreases, almost to the point of disappearing for the smallest δ_b . These results cannot be deduced from studies of a single blade applied to a pair of fabrics.

2.2.5. Blade curvature and pressure gradients

Although non-flat blades are normally not deliberately employed, curvature can arise from wear of the blade surface. Such blades have previously been studied by Green & Roshanzamir (1997). The pressure distributions in figure 2.4 correspond to blades with different (constant) radii of curvature, ϱ . The

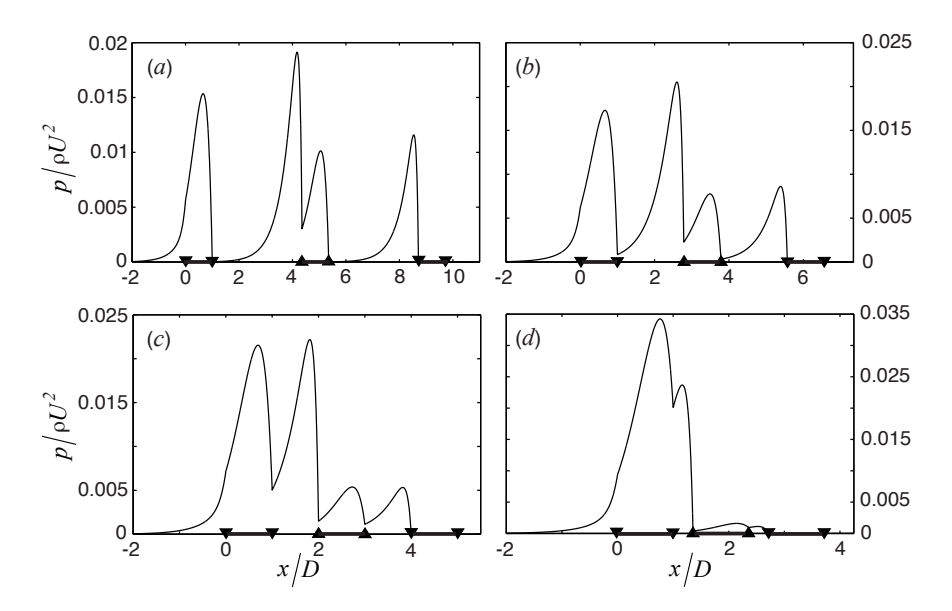


FIGURE 2.3. The influence of the blade spacing on the pressure pulses. No suction. (a): $\delta_b/D = 3.4$. (b): $\delta_b/D = 1.8$. (c): $\delta_b/D = 1$. (d): $\delta_b/D = 0.36$. $Th_0/(\rho U^2 D^2) = 0.114$, $\beta\phi_s/\phi_m = 0.103$ where $\beta = \mu h_0^2/(\rho UDk)$, Q/T = 0.043. $f_0/h_0 = f_1/h_0 = 1$, $g_0 = 0$, $p_1 = 0$, $u_1/U = 1$, $R_0h_0/(\rho UD) = 0.194$. $f_u(x)/h_0 = f_d(x)/h_0 = 1$. Note the different scales in the different subfigures.

circular blades are symmetric with respect to the 'top' of the blades. In the ZD, the two upper blades are positioned so that their tops (this word is employed even though the curved blade surfaces are pointing downwards) are at the same level as the positions f_0 and f_1 , cf. figure 2.1. Like before, the position of the middle blade is determined as a part of the solution.

The curvatures of the blades are small, in the sense that the top of the blades only protrudes a small distance Δb with respect to the base of the blades (see fig. 2.5). Roughly, we have that $\Delta b/h_0 = D^2/(8h_0\varrho)$. If e.g. h_0 , D and ϱ are taken to be 2 mm, 14 mm and 0.6 m, respectively (yielding $\varrho/D = 42.9$ like in the case of the dotted curve in fig. 2.4), we find that the surface of the blade merely protrudes a distance equivalent to 2 % of the far upstream gap size. Nevertheless, there is still an influence on the pressure distributions, as revealed in figure 2.4. The amplitudes of the pulses are modestly affected. The most important influence of the blade curvature is presumably observed on the pressure gradients in the MD. It is recalled from chapter 1 that these are believed to play an important role to the break-up of fibre flocs, which is essentially the reason why blades are employed in the drainage process. An important part of Paper 3 in this thesis is the insights it provides regarding

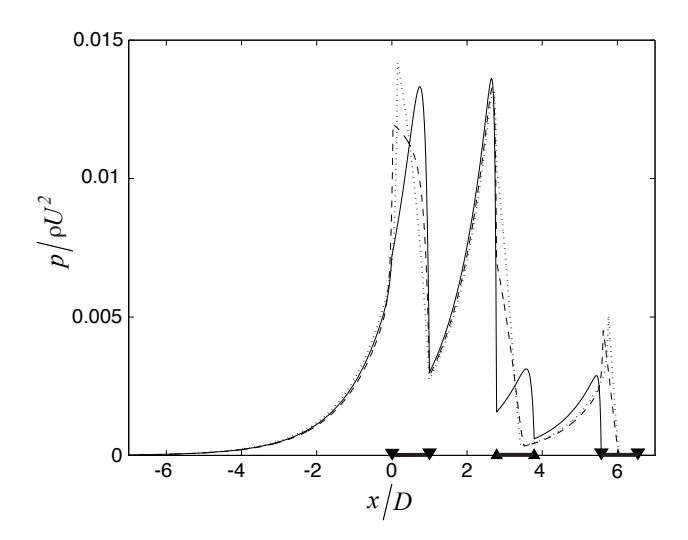


FIGURE 2.4. The influence of blade curvature on the pressure pulses. No suction. Circular blades with radius of curvature ϱ . (—): Flat blades. (- - -): $\varrho/D = 71.4$. (···): $\varrho/D = 42.9$. $Th_0/(\rho U^2 D^2) = 0.147$, $\beta \phi_s/\phi_m = 0.103$ where $\beta = \mu h_0^2/(\rho U D k)$, Q/T = 0.033. $\delta_b/D = 1.8$. $f_0/h_0 = f_1/h_0 = 1$, $g_0 = 0$, $g_1 = 0$, $g_1/U = 1$, $g_0/(\rho U D) = 0.114$. Confer the text for the details regarding the blade positions in the ZD.

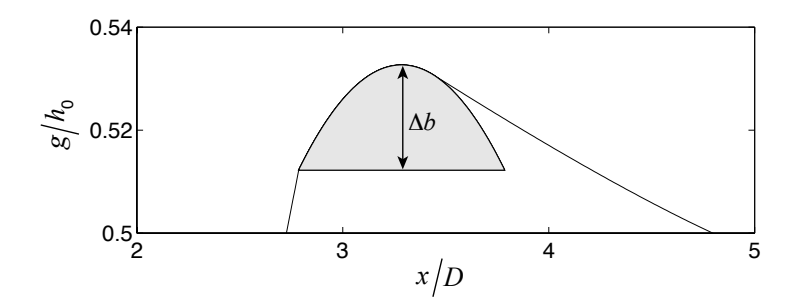


FIGURE 2.5. The path of the lower wire, g(x), as it wraps the middle circular blade (of curvature $\varrho/D=42.9$) in the simulation corresponding to the dotted curve in figure 2.4. Note that only partial contact between the blade and the wire is obtained on the downstream side of the blade.

the role played by the pressure gradients in the MD in the generation of shear stresses in the fibre webs residing on the fabrics. The pressure gradients for the cases in figure 2.4 are plotted in figure 7 of Paper 1. The observed tendency is that curved blades reduce the gradients associated with the downstream part

of the pressure pulses, but sometimes enhance gradients during the build-up of the drainage pressure (see below). Once the connection between the pressure distribution in the blade forming section and the formation in the final sheet is better understood, blade curvature could perhaps be a means to obtain the most advantageous forming conditions.

The pressure gradients were not commented upon by Green & Roshanzamir (1997). Another effect revealed by the simulations of curved blades, and which has not been previously reported, is the fact that the fabrics are not necessarily in contact with the entire surface of the blades. Figure 2.5 illustrates the situation in the region around the middle blade for the case $\varrho=42.9$ in figure 2.4. Actually, none of the curved blades in the simulations in that figure are in complete contact with the fabrics. Partial contact on the upstream side of some blades explains the above mentioned effects on the gradients in the MD upstream of the maximum pulse pressure. In such situations, where the fabric makes contact with the blade downstream of the leading edge, high pressures are built up over a short distance in order to deflect the fabric so that it makes contact with the blade tangential to its surface. Evidence of partial wire-blade contacts is seen in figure 2.4 where the slopes of the pressure curves change discontinuously at positions other than at blade edges.

It should be mentioned that no effects related to the wedge-shaped space between the fabric and the blade surface, that is present at partial contact, have been taken into account. It is possible that water drained at upstream stations, adhering to the external surface of the fabrics, can be forced back in through the fabrics as a result of such gaps on the upstream side of the blades. Both when $\varrho = 71.4$ and 42.9, partial contacts are observed on the upstream side of the blades applied to the upper fabric.

CHAPTER 3

Drainage of flocculated suspensions

Using the model presented in the previous chapter, it is possible to predict the pressure distributions in a variety of forming sections operating under different conditions. Although of simple nature, the model has been found to yield pressures that are in fair agreement with more advanced studies of single blades, as well as experimental measurements (cf. Paper 1 and Holmqvist 2002). However, it is currently not possible to fully benefit from our knowledge of the pressure distributions, since so little is known about the details of the coupling between these and their effects on fibre flocs and the fibre mats. Since the fibre mats will become the final paper sheet, establishing such relationships is extremely important. In Paper 3, 4 and 5, a tentative is made to deal with this issue. Paper 3 treats the behaviour of a fibre mat subjected to a blade pressure pulse, whereas in Paper 4 and 5, a model is presented for the consolidation of a flocculated suspension subjected to both normal loads and shear loads. This chapter of the thesis is devoted to a review of these three papers. It is worth noting that not only would realistic descriptions of the fibre mats allow us to learn more from existing predictions of the drainage pressure under various operational conditions. By combining the new models with previously developed models for the forming process, e.g. in the form of more accurate boundary conditions, they could in their turn improve the calculations of the pressure distributions and the drainage rates.

3.1. Previous modelling work

In studies trying to predict the pressure distributions during forming, the resistance to drainage presented by the fabrics and the fibre webs they support, is commonly either considered to be constant (e.g. Zhao & Kerekes 1995; Zahrai & Bark 1995; Zahrai et al. 1997; Roshanzamir et al. 1998) or is assumed to increase at a rate proportional to the (superficial) drainage velocity, which is also referred to as the drainage flux (e.g. Green & Kerekes 1996; Roshanzamir et al. 2000a). The first of these two alternatives is clearly simplistic. The second one rests on the assumptions that the drainage resistance is proportional to the amount of fibres in the mat, and that the increase of the quantity of fibres is determined solely by the drainage flux and the concentration in the free suspension above the mat. Although somewhat more elaborate, it has nevertheless been put forward in an ad hoc manner, without considering the reactions of the

fibre network constituting the web when it is subjected to the drainage flow, and how this in turn influences the macroscopic dewatering resistance.

The fibre sheet can be envisaged as a permeable and deformable solid structure, saturated with a liquid. The reaction to applied loads of such porous media is a problem relevant to many applications. Traditionally, the behaviour of such systems has been considered in situations where the load is applied uniaxially. The first treatments are found in the field of soil mechanics (cf. the classical textbook by Terzaghi 1943). Later, Shirato et al. (1970) and Adorján (1975) developed theories for the settling (i.e. sedimentation) of flocculated suspensions. Note that the term 'flocculation' in general is employed to indicate the presence of an interconnected network of particles, that through mechanical contacts can transmit forces over distances considerably longer than the size of the particles. Conceptually, one then deals with (large) regions of networked material, rather than individual flocs as is sometimes the case in papermaking. However, the fibre webs residing on the fabrics fall within the definition of a 'flocculated suspension', in the sense intended by most researchers outside the paper industry. In their work, Shirato et al. and Adorján attributed a concentration dependent strength to the network. When the loads transmitted to the flocculated structure exceeds that strength, collapse of the network occurs, under the expulsion of water, until the solid structure through hardening is again capable of carrying the applied load. The internal friction between the phases is accounted for by Darcy's law.

Both Shirato et al. and Adorján assume that the network stress always equals the yield limit, which is not evident a priori. A less restrictive assumption is made by Buscall & White (1987) in their treatment of sedimentation of flocculated suspensions. In order to describe the collapse process, the network is equipped with a concentration dependent dynamic compressibility. constitutive function governs the rate at which the flocculated structure is compressed. However, under the assumption that the work performed on the suspension during the collapse is (mainly) dissipated in the pore liquid, and not through breaking and/or reformation of the inter-particle bonds, a scaling analysis reveals that the stresses in the network never significantly exceed the yield-limit (Buscall & White 1987; Landman et al. 1988). The supposition regarding the dissipation mechanism amounts to the statement that the collapse rate of the network is determined by the need to displace the water from in between the particles, rather than by the need to displace the particles relative each other. Howells et al. (1990) also employ the same concept to model settling in suspensions, whereas Landman et al. (1991), Landman & Russel (1993) and Landman et al. (1995) use it in the context of pressure filtration.

Within the field of papermaking, models of the same nature have been developed for the forming of the webs on the wires. An exhaustive review of the early works is made by Meyer (1971). These treatments differ from those of e.g. Shirato *et al.* and Adorján, only in that other constitutive relations are used in order to account for the particular characteristics of pulp suspensions.

However, it was not until the fairly recent study by Martinez (1998), that a solution which accounts for the effects of mat compressibility was actually calculated in the context of the forming process in paper machines. In that work, the analysis by Landman $et\ al.$ (1991) is adapted to roll forming, and the drainage rates are calculated from measured pressure distributions. Reasonable agreement is found with experimental data, the predictions were reportedly in error of about 10 %. Martinez' modelling assumptions result in an ordinary differential equation for the concentration across the fibre mat. Boxer $et\ al.$ (2000) suggest that only a drainage pressure distribution that is constant in the MD is consistent with the model, and provide an analytical solution of the equations based on this supposition.

In an analysis similar to that by Martinez (1998), Zahrai et al. (1998) derive an expression for the evolution of the thickness of the fibre mats along the MD in a roll former. Assuming a constant drainage pressure, it is shown that the governing equations permit a similarity solution for the concentration in the mats. Although the solution is not calculated, the analysis reveals that the mat thickness is proportional to the square root of the distance travelled in the MD. This information was then employed to account for the drainage resistance of the mats in simulations of the drainage pressure during roll forming, using a model previously developed by Zahrai et al. (1997) for studies of blade forming. The unknown proportionality constant in the expression for the thickness of the mats was determined by calibrating the drainage rates to the data by Martinez (1998) (a similar value for this constant was also deduced from the uniaxial filtration data by Mantar et al. 1995). The predicted evolution of the drainage pressure along the MD was in good agreement with the pressure pulses employed by Martinez in his calculation of the corresponding drainage rates.

Recently, Lobosco (2004) has presented a model for the drainage of a fibre mat filling the available space between two forming fabrics, and the resulting description is analogous to the problem of uniaxial piston driven consolidation. The suspension is subjected to a series of pressure pulses, and large gradients in the fibre concentration are observed in the ZD close to the wires. The constitutive relation employed by Lobosco, connecting the local stress in the fibre network to the local volume concentration of fibres, is interesting, since it accounts for the hysteresis effects during loading and unloading of the flocculated structure that have been observed in experiments (cf. e.g. Vomhoff & Schmidt 1997).

Normally, the inter-particle forces are assumed to be independent of the rate at which the flocculated suspension is deformed. An exception is the work on consolidation by Gustavsson (2003), aimed at sludge dewatering. She supposes that the inter-particle forces manifest themselves both as a rate-independent 'particle pressure', and viscous shear stresses. The latter are

¹Like the liquid phase pressure, this stress is isotropic.

modelled after a Newtonian pattern, by attributing an effective viscosity, dependent on the concentration and the shear-rate, to the particle phase. Another characteristic of Gustavsson's model worth pointing out is that it is not limited to uniaxial situations.

It should also be mentioned that the consolidation models for liquid-particle suspensions in general (although not always explicitly stated) comprise Terzaghi's effective stress principle (cf. e.g. Terzaghi 1943). It implies that, at equilibrium, an external load applied to the flocculated suspension is balanced by the sum of the interstitial pore pressure and the superficial average particle stress. Its validity requires point-like contacts between the particles, and between the particles and surrounding surfaces. This requirement is not necessarily fulfilled in the case of pulp suspensions (Kataja et al. 1995).

3.2. Constitutive relations

Naturally, the applicability of the developed models for flocculated suspensions requires certain constitutive relations to be determined for the system under consideration. As examples, one can note that the strength of the flocculated network must be related to some measure(s) defining the internal structure, and that the forces resulting from relative motion between the liquid and the solid phase must be related to the magnitude of the relative velocity and the structure of the network. In the studies reported in this thesis, as in previous investigations into filtration of flocculated suspensions, the network structure is only taken into account through the volume concentration of the solid phase, which clearly does not contain any information about directional dependencies. This independence is obviously inherited by all quantities defined as functions of the concentration, and the corresponding models are isotropic.

3.2.1. Internal friction forces and permeability

The relative motion between the liquid and the solid constituents in the suspension gives rise to the resistance to flow through the flocculated structure that is observed at the macroscopic level. The modelling of these forces is normally phenomenological, and based on the average velocities of the phases. In many cases it is sufficient to assume that the inter-phase forces are proportional to the relative velocity between the constituents (referred to as Darcy's law), if the proportionality factor is in turn taken to depend on the network structure. Normally, it is supposed that the factor is set by the 'permeability' of the flocculated network (which is often taken to be a function of the volume fraction of solids) and the viscosity of the liquid. The resulting model is acceptable when the inter-phase forces are of purely viscous (frictional) nature. Occasionally, also the inertia of the flow through the porous structure must be taken into account. A popular way to achieve this is to add a term proportional to the square of the relative velocity to Darcy's law, and the total inter-phase forces are then hence considered to be the sum of the viscous and the inertial contributions. This approximation is referred to as Forchheimer's relation. In this

thesis, only the viscous part of the inter-phase forces is accounted for. In the experimental study by Wildfong $et\ al.\ (2000\ a)$, it is concluded that for dewatering velocities of the same magnitudes as those encountered in commercial papermachines, inertial effects make a significant contribution to the resistance to drainage presented by the forming fabrics. However, no inertial effects are conclusively seen to influence the solid-liquid forces inside the fibre sheets, and it is these fibre webs that have been the concern of the work on drainage reported in the thesis. It is worth noticing, that when a fibre mat and a wire are considered as an ensemble, the main contribution to the dewatering resistance presented by the two components is made by the fibre sheet. Further, there is also an effect of fibres blocking the pores in the surface of the wire, and due to this the total drainage resistance is larger than the sum of the resistances presented by the fibre web and the forming fabric considered separately.

Due to its inseparable relation to the viscous resistance, the permeability of porous materials has received a lot of attention. Frequently, power law relationships have been employed to correlate experimental measurements of the permeability to the volume fraction of solids, e.g. $k(\phi)/\mu_c \sim a\phi^b$, where $k(\phi)$, μ_c , ϕ , a and b are, respectively, the permeability, the dynamic viscosity of the liquid, the volume fraction of solids, and two fitting constants. Theoretical models have also been developed, and many of the classical ones are still in use (cf. e.g. Scheidegger 1957; Dullien 1992). In order to derive theoretical expressions for the permeability, one can imagine the flow in the material to occur either in a system of closed conduits, or around solid particles forming a spatial array. In the simplest approach of the former kind, the interconnectivity of the conduits is neglected. As a consequence, the resulting 'capillaric' permeability models are inherently one-dimensional. Nevertheless, they are in widespread use in engineering applications, especially the Kozeny-Carman model (cf. Dullien 1992, p. 254), which has been successfully applied to granular materials.

Characteristic of most granular media, such as e.g. sand, is that the individual particles in many cases are essentially incompressible, and that the corresponding porous structures have void fractions (or, alternatively, volume fractions of solids) in a quite narrow range. Fibrous porous beds, on the other hand, can form at significantly lower volume fractions of solids, and are in general highly compressible². Caution should therefore be exercised when applying a traditional permeability model to a fibrous medium. A survey of experimental and theoretical works regarding the permeability of fibrous materials is undertaken by Jackson & James (1986). Ingmanson et al. (1959) present a modification of the Kozeny-Carman theory that is applicable to fibrous mats subjected to drainage, when the fibres are randomly oriented in the plane normal to the liquid flow. It accounts for the large variations of the

²It can be argued that the permeability concept is only relevant at sufficiently elevated concentrations, and therefore, especially when flocculated colloidal suspensions are considered, researchers sometimes instead prefer to talk about a concentration dependent 'hindered settling factor' (see e.g. Landman *et al.* 1988), which accounts for the hydrodynamic drag. In practice, though, there is no difference.

volume fraction of particles across the thickness of the mat, which results from the different loads felt by different parts of the fibre network. At low concentrations, a simplified version of the permeability expression can be employed, that is essentially a power-law of the same appearance as discussed previously in this section, namely $k(\phi) = 1/(3.5\phi^{1.5}S_0^2)$, where S_0 is the specific surface of the fibres. For fibres of known shape, this parameter can be calculated directly, whereas for wood fibres it must be determined experimentally (under wet conditions due to the swelling of the fibres when they are immersed in water). Ingmanson et al. (1959) give the value $3.08 \cdot 10^5$ m⁻¹ for an unbeaten bleached sulphite wood pulp, from which fibre fragments and other 'fines' had been removed. The small particles are however important to the specific surface and the drainage resistance of industrial pulps, as has been observed in studies by Mantar et al. (1995), Wildfong et al. (2000a), Wildfong et al. (2000b) and Paradis et al. (2003). Values for the specific surface encountered in the literature typically lie in the range $10^5 - 10^6$ m⁻¹.

Koponen et al. (1998) calculate the permeability of fibre mats whose structure closely resembles those of paper sheets, by means of numerical simulations. These are performed from 'first principles', and there are no adjustable parameters. Among the findings, it is seen that the modified Kozeny-Carman theory by Ingmanson et al. yields permeabilities that are in good agreement with the numerically obtained values, especially for volume fractions of solid less than 0.1. In the study by Aaltosalmi et al. (2004), permeabilities determined by the same numerical technique are compared to experimental values, and it is found that the calculations accurately predict permeabilities in the direction perpendicular to the fibre sheets, whereas experimental uncertainties prevents conclusions for the in-plane direction.

3.2.2. Network strength

A number of experimental studies have been devoted to the investigation of different properties of flocculated colloidal suspensions. Of particular concern to the work reported in this thesis, is that finite yield-stresses are observed during both normal compression and shearing of the suspension. Such results are reported by Buscall et al. (1986) for polystyrene latex dispersions, by Buscall et al. (1987) in situations where the particles consist of polystyrene latex, attapulgite clay and bentonite, and by Channell & Zukoski (1997) for aggregated alumina suspensions. Power-law expressions have been found to give reasonable fits to the experimental measurements. In the case of the alumina suspensions, the power-law exponent is found to be almost the same for the yield-limit in shear and in uniaxial compression. Normally, the yield-stress is significantly lower in shear than in compression. As pointed out by Buscall & White (1987), this is natural, since in shear a much larger fraction of the inter-particle bonds are in a state of tension than during compaction, where the majority of the bonds are in a state of compression.

In addition to the yield-stress of the flocculated structure, the above referenced studies also consider other properties of the suspension, such as e.g. elastic shear and bulk moduli. Recent developments of the techniques to measure yield-stress and permeability for flocculated suspensions as a function of concentration are presented by, among others, Landman *et al.* (1999), Usher *et al.* (2001) and Yeow & Leong (2001).

Although providing insights into the behaviour of flocculated suspensions in general, there are certainly qualitative differences between colloidal systems and flocculated fibre suspensions. The length of the wood fibres used to produce paper is typically at least two orders of magnitude larger than the size of the particles in the colloidal suspensions mentioned above, and the diameter of the fibres is one order of magnitude larger. The same can be said about many industrially relevant synthetic fibres when compared to colloidal particles. Partly due to the geometrical differences, the nature of the inter-particle forces is different. Kerekes et al. (1985) defines four different mechanisms that generate forces acting at the particle contact points in a fibre suspension; colloidal effects, mechanical surface linking, elastic fibre bending, and surface tension. Presumably, forces due to surface linking and elastic bending are the most important to the strength of a fibre network. They are normally not present in colloidal suspensions, at least not to the same extent as when the flocculated structure consists of fibres. During papermaking, the effects of surface linking are often enhanced due to the shredding and permanent deformations of the fibres that sometimes occur during the preparation of the pulp.

For flocculated fibre suspensions, power laws have almost exclusively been used to correlate empirical data of the strength (yield-limit) in uniaxial compression to the concentration of fibres. Typically, steady-state experiments are performed and an expression of the form $\sigma_y(\phi) = m\phi^n$ is adopted, where σ_y denotes the uniaxial yield limit and m and n are fitting constants. Nordén & Kauppinen (1994) provide the values $m = 5.0 \cdot 10^5$ Pa and n=2.6, whereas Ingmanson et al. (1959) give $m = 2.0 \cdot 10^5$ Pa and n=2.7. Naturally, the values depend on the considered pulp. During repeated loading and unloading of fibre webs, the network strength exhibits hysteresis. However, as shown by Vomhoff & Schmidt (1997), both the loading and the unloading behaviour is consistent with power law behaviour.

Similarly, measurements of the yield limit in shear is commonly fitted to a function of the form $\tau_y = r\phi^s$, where τ_y , r and s are, respectively, the shear yield stress, and two fitting parameters, the values of which depend on the suspension under consideration. Experimental studies of τ_y have been undertaken for pulp suspensions by Gullichsen & Härkönen (1981), Bennington et al. (1990), Swerin et al. (1992) and Wikström & Rasmuson (1998). To give an idea of the network strength, we mention that Bennington et al. found r and s for different pulps to lie in the ranges $10^5 - 10^6$ Pa and 2.72 - 3.56, respectively. A theoretical model for the yield strength was also presented, based on the assumption that the resistance to deformation of the network is a result of friction forces between

elastically deformed fibres. According to the model, the yield strength should be proportional to ϕ^3 . This is consistent with the experimental data, but the predicted dependence of the yield limit on the aspect ratio of the fibres, and their elastic modulus, do not agree with the observations. From this, Bennington *et al.* conclude that other mechanisms than fibre bending are also relevant to the yield strength. Another model for the network strength, that allows for a continuous fibre length distribution, is presented by Andersson *et al.* (1999). Fibre suspensions containing substantial amounts of gas, in addition to the liquid and the solid phase, have been considered by Bennington *et al.* (1995). Again, power-laws of the type $\tau_y = r\phi^s$ were seen to well describe the data. Since the volume fraction of wet pulp fibres is difficult to measure, expressions based on the mass fraction of fibres are suggested by both Bennington *et al.* (1990) and Bennington *et al.* (1995). A review of older studies is made by Kerekes *et al.* (1985).

3.3. Fibre mat behaviour during pressure pulses

Paper 3 considers the behaviour of the fibre mats in a twin-wire roll-blade former, as they experience the pressure pulse generated by the first of the blades. The forming section is illustrated in figure 3.1, and the resemblance to figure 1.1 is evident. The fibre sheets residing on the fabrics are assumed separated by a region of freely moving suspension. A scaling analysis reveals that this separating layer of 'free suspension' (also referred to as the 'bulk' of the suspension) can be treated as an inviscid fluid. Since we are primarily interested in the fibre mats, the role of the free suspension is merely to provide boundary conditions on the pressure and the velocity in the MD, at the free suspension side of the sheets. For this purpose, the solution by Zhao & Kerekes (1995) for these quantities is adopted. All interaction between the fibre mats and the bulk of the suspension is hence disregarded.

3.3.1. Compression transversal to the fabrics

Like in the treatment by Martinez (1998) of drainage during roll forming, a description of the compression behaviour in the direction transversal to the web is obtained by adapting the analysis by Landman et al. (1991) to the situation at hand. The influence of the shear-strength of the fibre network on the compaction process is neglected, and the inter-fibre forces are supposed to present themselves merely as an isotropic stress, the 'particle pressure'. In essence, a uniaxial description of the drainage process is obtained, and with respect to deformations perpendicular to the fabrics, the fibre sheets are modelled as a plastic-rigid material exhibiting a concentration dependent yield stress. When the yield limit is exceeded, the fibre network is compressed, resulting in an increased number of fibre-fibre contacts, and a stronger network. This strain-hardening proceeds till the network is again capable of balancing the load.

By taking care to avoid relaxation of the loads transmitted to the fibre webs, we can assure that the fibre structure is always yielding, or on the verge

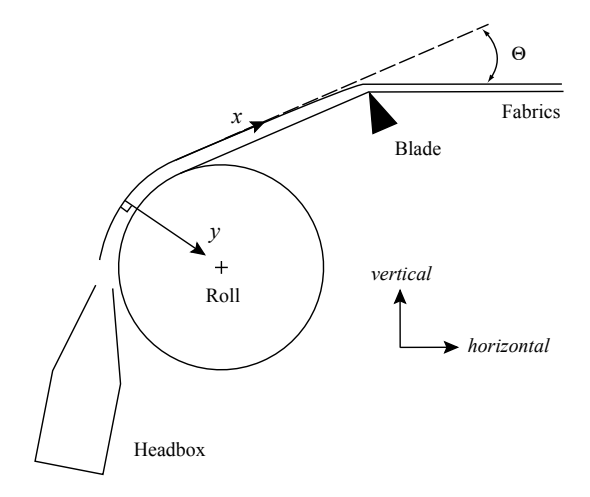


FIGURE 3.1. The roll-blade twin-wire former treated in Paper 3. Compare this figure to the 'real' forming section depicted in fig. 1.1.

of doing so, and consequently the yield limit function provides a direct relation between the stresses in the network and the volume fraction of fibres. This is crucial to the undertaken analysis. However, as a consequence, the drainage pressure cannot be allowed to decrease. Highly compacted parts of the mats would then be of such strength that locally the network behaves like a stiff structure. By contemplating the forming section in 3.1, one realises that normally the drainage pressure would decrease after the roll before it increases again as the blade is approached. In order not to violate the modelling assumptions, it is therefore necessary to assume that the blade is located sufficiently close to the roll that the drainage pressures generated by the two components merge into a single pressure distribution, monotonically increasing in the MD. No consideration is given to the possibility of interaction between the blade and the roll. Instead, the roll is assumed to generate a pressure of constant amplitude given a priori (a simplistic assumption, as shown by Holm 2005). The blade pulse is calculated using the theory by Zhao & Kerekes (1995), but only the part of the pulse where the magnitude of the pressure exceeds the roll pressure is used. At upstream positions, the drainage pressure is set by the roll. This also determines the location of the blade in the MD.

The resistance to drainage presented by the wires is neglected. As a result of the constant roll pressure, the variation of the concentration across the thickness of the fibre mats formed by the roll is then self-similar (Zahrai et al. 1998). In Paper 3 it is found that the similarity solution is closely approximated by the solution to a related asymptotic drainage problem, which can be solved analytically. Since the attention of the study is on the region of the blade pulse, such asymptotic webs are assumed to reside on the wires at the

position where the blade pulse first dominates over the roll pressure. Further, since it is desirable that the region where the blade pulse dominates is of as long reach as possible, the roll pressure was set to a fairly low value. At the onset of the blade pulse, the fibre mats are hence probably less dense than they would have been during normal operational conditions.

The evolution along the MD of the concentration across the mats were calculated for different sets of parameters, and examples are given in figure 5 of Paper 3. On the free suspension side of the mats, the concentration equals the gel value, at which an interconnected network first starts to form. Further towards the wire, increasingly more load is transmitted to the particle network through friction between the liquid and the fibres, and the maximum concentration is hence found on the fabric side of the web. The variation between the two extreme values is quite gradual, and there does not seem to be tendencies to 'clogging', in which case a thin cake of high concentration and low permeability forms at the fabric and acts as a lid, preventing efficient drainage. However, the pressure in the bulk of the suspension is normally influenced by the resistance to drainage presented by the fibre network, and if this coupling is accounted for, the conclusion might be different.

3.3.2. Drainage resistance

Figure 3.2 presents the evolution along the MD of the drainage resistance and the amount of fibres in the webs for two cases corresponding to pressure pulses that differ significantly in terms of both reach and magnitude. In the caption of the figure, references are made to the parts in Paper 3 where the details concerning the simulations are presented.

In the right subfigure, it is seen that the fibre contents of the webs only increase modestly during the pulses. This is readily explained by the compressibility of the sheets. As a result of the drainage flow through the fibre networks, the mats are compacted. By consequence, the suspension side surfaces of the webs move towards the fabrics, leading to small velocity differences between the mat surfaces and the drainage flow, and thus also to low fibre deposition rates. Nevertheless, according to the left diagram in figure 3.2, the dewatering resistance of the webs, defined as the ratio between the drainage pressure and the drainage flux, increases to a much larger degree during the pressure pulses. The explanation is the low permeability arising when parts of the networks become highly compacted. Clearly, the increase of the dewatering resistance along the MD is not adequately accounted for by assuming that it is proportional to the quantity of fibres in the web. Neither is this amount directly controlled by the drainage flow. The influence of structural changes in the fibre mats on the resistance need to be taken into account. It should also be pointed out that the model in Paper 3 neglects all effects stemming from fibre fragments and other small particles plugging the pores in the fibre network. In the experimental study of sheet forming by Wildfong et al. (2000b), the pore plugging by fine

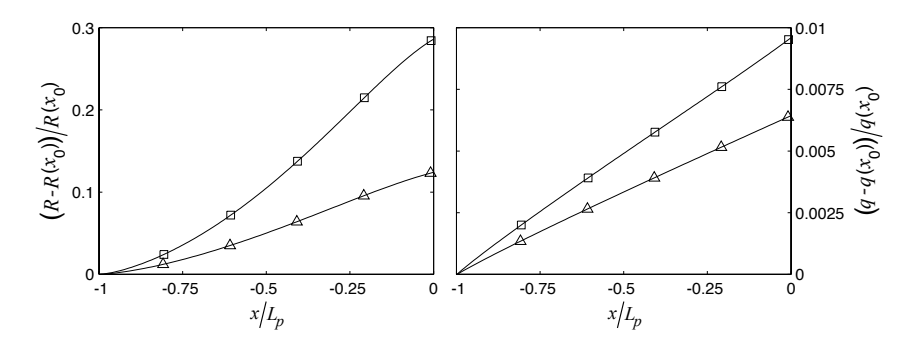


FIGURE 3.2. Left subfigure: The increase of the drainage resistance, R(x), normalised with the initial value $R(x_0)$. Right subfigure: The increase of the quantity of fibres in the mat, q(x), scaled with $q(x_0)$. x_0 is the position in the MD where the blade pulse first dominates over the roll pressure, and the simulations start. The position in the MD, x, is scaled with the length of the pressure pulse, L_p . x=0 is the position where the pulse attains maximum amplitude. \triangle : simulation A. \square : simulation C. The pressure pulse is of longer reach and higher amplitude in case C than in case A. Cf. tables 1 and 2 in Paper 3 for parameter values, and fig. 4 in the same paper for the pressure pulses.

material in commercial pulps is observed to contribute more to the drainage resistance than the reduced permeability caused by the compression.

3.3.3. Shear stresses

The fibre networks constituting the mats are exposed to shear stresses in the plane of the sheet for two reasons. Firstly, the free suspension that is convected towards the fabrics during the drainage needs to be accelerated to the local velocities in the mat. Secondly, the pressure gradients in the MD act equally on both the free suspension and the mat mixture, and shear stresses in the webs prevent the mat suspension from being displaced relative the fabric to the same extent as the bulk of the suspension.

Due to the neglect of the (rate-independent) shear-strength of the fibre networks, the deformations in the plane of the webs resulting from the shear loads are in Paper 3 governed by rate-dependent 'viscous' stresses in the fibre sheets. Little is known about the viscous deformation behaviour of fibre mats under the conditions encountered in twin-wire forming sections. In Paper 3, a power law based on the empirical expression by Bennington & Kerekes (1996) is used for the apparent viscosity of the suspension mixture as a function of the fraction of fibres. Despite the fluid-like character of the mat mixture when the shear strength of the network is disregarded, it was found that the larger

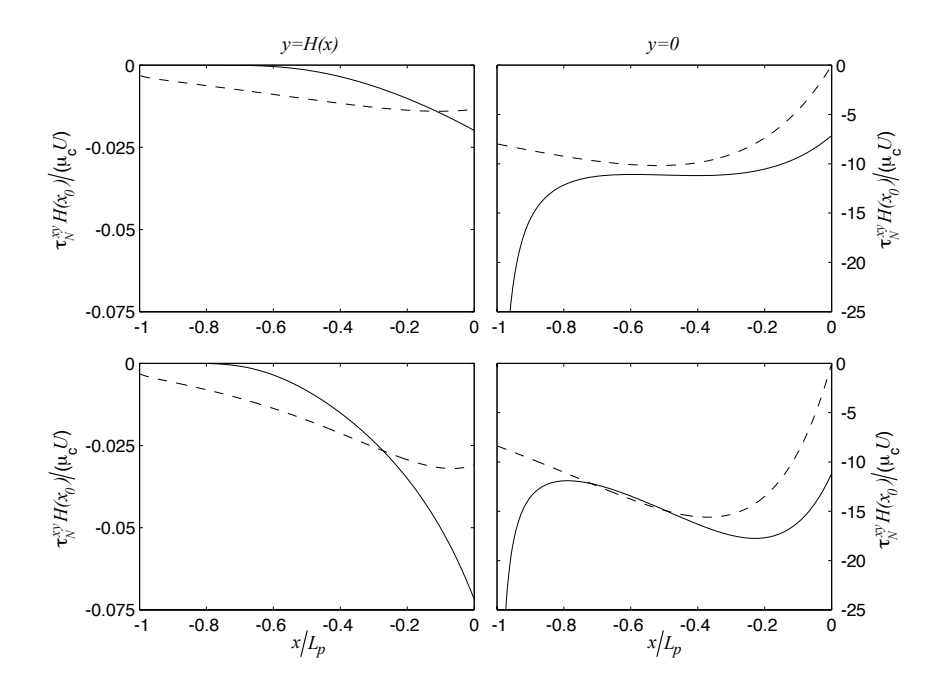


FIGURE 3.3. The shear stress τ_N^{xy} in the plane of the mat next to the free suspension (y=H(x)), and next to the fabric (y=0), for the same cases as are presented in fig. 3.2. Top subfigures: Case A. Bottom subfigures: Case C. μ_c , U and $H(x_0)$ are, respectively, the viscosity of the liquid phase, the wire speed and the thickness of the sheets at the onset of the pressure pulse. The stress scale $\mu_c U/H(x_0)$ equals 30 Pa. The position x in the MD is scaled by the length of the pulse, L_p . The solid lines are estimates based on the velocity profile in the mat. The dashed lines are estimates based on the assumption that the entire mat perfectly follows the wire during the passage over the blade. Cf. Paper 3 for details.

parts of the fibre sheets (in the thickness direction) essentially follow the wires during the passage over the blade, rather than take on the velocity of the bulk of the suspension. As long as this general tendency remains true, predictions of the shear stresses, particularly at the levels in the ZD close to the fabrics, remain insensitive to the constitutive model for the stresses in the web.

Figure 3.3 provides estimates of the shear stresses in the plane of the sheets for the same cases that are presented in figure 3.2. The solid lines are based on the profiles in the ZD of the mixture velocity component parallel to the wires. The dashed lines are based on the assumption that the entire mats perfectly follow the wires during the passage over the blade. The reader is referred to Paper 3 for the details regarding the simulations. Due to reasons also explained

in that paper, the solid curves should be looked upon with caution far upstream of the blade (i.e. at low values of x/L_p). Where the dashed and the solid lines approach each other, and downstream of that region, the estimates represented by the solid curves should be reasonable. The pressure scale $\mu_c U/H(x_0)$ is 30 Pa, where μ_c , U and $H(x_0)$ are, respectively, the viscosity of the liquid phase, the wire speed and the thickness of the sheets at the onset of the pressure pulse. Consequently, the maximum shear stress at the free suspension side of the mats is -0.59 Pa and -2.2 Pa in simulation A and C, respectively. At the fabric side of the mats, the maximum values (neglecting the upstream part) are several hundred times larger, -0.34 kPa and -0.54 kPa in simulation A and C, respectively.

Of the two mechanisms causing these shear stresses, the one related to the pressure gradients in the MD is by far the most important. Had it not been present, the same shear stresses would have been predicted at the fabric surfaces as those given by the dashed curves for the suspension side of the mats. It is recalled that only the region upstream of the position corresponding to the peak of the blade pulse is treated. The gradients in the region downstream of that position are significantly larger than in the considered domain, and it is thus possible that the mats are subjected to even larger stresses (of opposite sign) in that region.

Even if the predictions of the shear stresses are insensitive to the choice of constitutive model, the magnitude of the displacements is not. Due to the impact of sheet deformations on the characteristics of the final product, and given the large shear stresses caused by the pressure gradients in the blade forming section, models need to be developed that accurately incorporates the shear strength of the fibre network.

3.4. Sheared consolidation of flocculated suspensions

Paper 4 and Paper 5 in this thesis present a model for the drainage of flocculated suspensions in which the previously neglected shear-strength of the particle network is included. Although the thesis is concerned with papermaking, the provisional nature of many aspects of the model makes it general, and the basic ideas should be applicable to many liquid—solid systems exhibiting finite resistance to shear deformations. Essentially, it is a generalisation of the yield-stress models previously employed in uniaxial descriptions of consolidation.

3.4.1. Outline of a constitutive model

In traditional studies of consolidation, it is supposed that the load transmitted to the suspension is oriented in a single direction during the whole process. As a result, it suffices to express the stresses in the particle network with one scalar measure, the particle 'pressure' p_d . In a more general situation, this is not adequate. It is reasonable to expect that if a shear load and a normal

³In a real situation, the network stress counteracting the external load will be composed of contributions from both the isotropic particle pressure, and deviatoric stresses. However, in

load is simultaneously applied to a suspension (as is the case in e.g. fig. 3.5), the course of events will be different than if merely a normal load is employed. The shear stress should result in additional strains on the inter-particle bonds, and decrease the capacity of the network to resist the normal load. In order to account for such effects, we introduce a scalar measure q_d of the shear stresses (i.e. the 'deviatoric' stresses), the precise definition⁴ of which is given in Paper 4. Here, as an explanation and a motivation, we content ourselves by saying that for a purely elastic material⁵, p_d would determine the stored elastic energy due to volumetric deformations, whereas q_d would determine the elastic energy stemming from isochoric shape changes. By means of a function $F(p_d, q_d, \phi)$, we then introduce a criterion that determines when the network is loaded to such an extent that it yields. If the stresses generated in the flocculated structure are such that $F(p_d, q_d, \phi) < 0$, the network can resist the transmitted loads without deforming. On the other hand, if $F(p_d, q_d, \phi) = 0$, the network will deform permanently (or 'plastically'). The relation $F(p_d, q_d, \phi) = 0$ defines a 'yield-surface' in the (p_d, q_d) -plane that replaces the one-dimensional yield criterion $f(p_d, \phi) = 0$ employed in the uniaxial studies. The dependence of the yield criterion on the volume fraction of solids, ϕ , assures that the strength of the flocculated structure is set by the concentration of particles. It is also important to realise that each material point in the network is equipped with its one yield-surface. Since ϕ often depends on the spatial position, so does the yield limit. In Paper 4 and 5, a yield-surface is employed that was originally proposed by Roscoe & Burland (1968) in the field of soil mechanics. It is illustrated in figure 3.4.

Under no circumstances is it possible that $F(p_d, q_d, \phi) > 0$. If the loads are such that the flocculated structure is compressed, the local concentration of fibres will increase, and also the number of inter-particle bonds. The magnitude of the inter-particle forces may also change as a result of the compression. Presumably they grow stronger due to e.g. higher normal forces at the contact points between the particles. The net effect is that the network grows stronger. In the constitutive model, this strain-hardening means that the size of the yieldsurface increases in such a way that $F(p_d, q_d, \phi) = 0$ is fulfilled throughout the deformation process. In other words, the stress state, measured by (p_d, q_d) , remains on the yield-surface when the network is deformed. To facilitate the analysis, it is in Paper 4 and 5 assumed that the criterion $F(p_d, q_d, \phi) = 0$ is always satisfied. Hence, it is not necessary to deal with stress states located inside the yield-surface. However, the prize that must be paid is that the loads transmitted to the flocculated structure needs to be of such magnitude that the material is always yielding, or on the verge of doing so. For the model problem considered in Paper 4 and 5, this is not a severe restriction.

uniaxial experiments, it is impossible to distinguish between the two contributions, and they may therefore equally well be lumped together in the particle pressure.

⁴Essentially, q_d is the von Mises effective stress, well known from classical plasticity theory. ⁵The reader should note that our model does not comprise elastic behaviour.

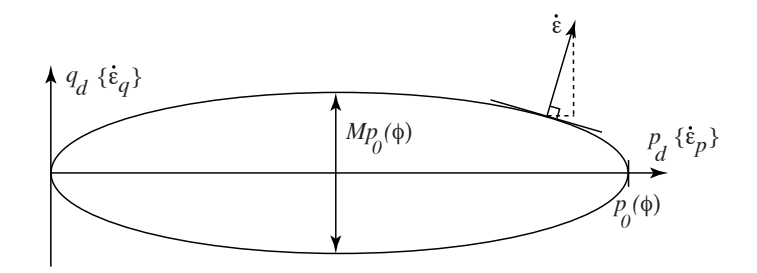


FIGURE 3.4. The yield-surface employed in Paper 4 and 5. p_d is the isotropic particle pressure, q_d the scalar measure of the deviatoric inter-particle stresses. The surface is an ellipse, centred at $(p_0(\phi)/2,0)$, and with a major and minor axis of length $p_0(\phi)$, and $Mp_0(\phi)$, respectively. Note how the size of the yield-surface depends on the volume fraction of the solid phase, ϕ . The shape factor M is constant. The axes can also be associated with the volumetric deformation rate $\dot{\varepsilon}_p$, and the shear rate $\dot{\varepsilon}_q$. $\dot{\varepsilon} = (\dot{\varepsilon}_p, \dot{\varepsilon}_q)$ denotes a general deformation rate. Compression corresponds to $\dot{\varepsilon}_p > 0$.

By way of the yield criterion $F(p_d, q_d, \phi) = 0$, we have defined which stress states result in deformations of the flocculated structure. However, we must also specify the direction of the deformations. The word 'direction' is here employed in a wide sense, since what is actually required is that the relative size of the different strain-rate components is determined⁶. In Paper 4 and 5, an associated flow rule is adopted. We shall here refrain from discussing in detail what this means. However, it is instructive to relate the consequences of the assumption to the yield-surface in figure 3.4. According to the associated flow rule, the p_d -direction in that figure also represents volumetric deformation rates $\dot{\varepsilon}_p$ (compression corresponds to $\dot{\varepsilon}_p > 0$). In the same way, the q_d -axis represents the shear rate measure⁷ $\dot{\varepsilon}_q$. A general deformation rate, represented by the vector $\dot{\varepsilon} = (\dot{\varepsilon}_p, \dot{\varepsilon}_q)$, contains both types of deformations. When yielding occurs, the adopted flow rule implies that the deformation rates are such that the vector $\dot{\varepsilon}$ is directed along the outward pointing normal to the yield-surface at the position (p_d, q_d) .

Having said this, some general conclusions can be drawn by considering figure 3.4. In the presence of a finite 'shear load' q_d , the resistance of the solid structure to an isotropic load p_d is smaller than when $q_d = 0$. In the latter case, deformations occur when $p_d = p_0(\phi)$, and we hence identify the function

⁶The absolute magnitude of the strain-rates cannot be obtained without considering the inter-play between different mechanisms as expressed by the momentum balances for the liquid and the solid phase.

⁷The rate of strain at some point in a material is defined by the rate of strain tensor, which have six independent components. The deformation rates $\dot{\varepsilon}_p$ and $\dot{\varepsilon}_q$ are scalar measures of the combined effects of the strain-rates, just like p_d and q_d are measures of the stress state.

 $p_0(\phi)$ as the isotropic load yield limit. If $p_d < p_0(\phi)/2$, and q_d is augmented progressively till the network starts to deform, an expansion will take place (i.e. $\dot{\varepsilon}_p < 0$). According to the reasoning earlier in this section of the thesis, the volume fraction of particles will then decrease and the solid structure becomes weaker. This behaviour might be realistic for some systems, such as saturated granular materials. Whether it is also a reasonable scenario in the case of flocculated fibre suspensions is not considered here. In this thesis, we are only concerned with non-expanding cases, i.e. $p_d \geq p_0(\phi)/2$. Shear deformations without volumetric deformation can only take place when $p_d = p_0(\phi)/2$. This condition is referred to as the 'critical state'. It is clear from figure 3.4 that the associated flow rule then does not provide any information regarding the magnitude of the shear rates. When $\dot{\varepsilon}_p = 0$, any value of $\dot{\varepsilon}_q$ results in a deformation rate vector $\dot{\varepsilon} = (\dot{\varepsilon}_p, \dot{\varepsilon}_q)$ normal to the yield-surface.

This situation of undetermined shear rates at the critical stress state is explicable. Under ordinary conditions (corresponding to compression of the network) the loads transmitted to the particle structure are balanced through the strain-hardening mechanism. However, at the critical state, due to the vanishing volumetric deformations, this mechanism is not active. If the model is not to fail in such situations, some other type of stresses than the interparticle forces hitherto discussed must be present. According to e.g. the study referenced in the next paragraph, it is reasonable to suppose that these stresses are of viscous (rate-dependent) nature.

It is here appropriate to make a comment on the experimental study of flocculated alumina suspensions by Channell & Zukoski (1997). They measured the shear load required to maintain a certain strain rate in a situation of continuous shear. As discussed in Paper 4 and 5, in such situations all parts of a flocculated network obeying the constitutive model outlined above will eventually reach the critical state. If the assumed viscous stresses that then control the shear deformations are small compared to the rate-independent shear stress measure $q_d = Mp_0(\phi)/2$, an experimentalist might conclude that the shear load which have to be applied to the suspension in order to obtain the desired shear rate, is independent of that shear rate. This is indeed what Channell & Zukoski observed for low shear rates (less than about 1 s⁻¹) at concentrations above the volume fraction at which an interconnected network first starts to form. At higher shear rates, however, the required load increased rapidly, clearly indicating the presence of rate-dependent stresses.

In Paper 4, rate-independent inter-particle stresses of the kind discussed in this section are included in the momentum balance for the particle phase in a two-fluid description of a flocculated suspension. All inertial effects are neglected. To avoid indeterminate shear rates at critical stress states, the model is in Paper 5 extended to incorporate also viscous stresses. These are attributed to the solid phase, and are modelled after a Newtonian pattern.

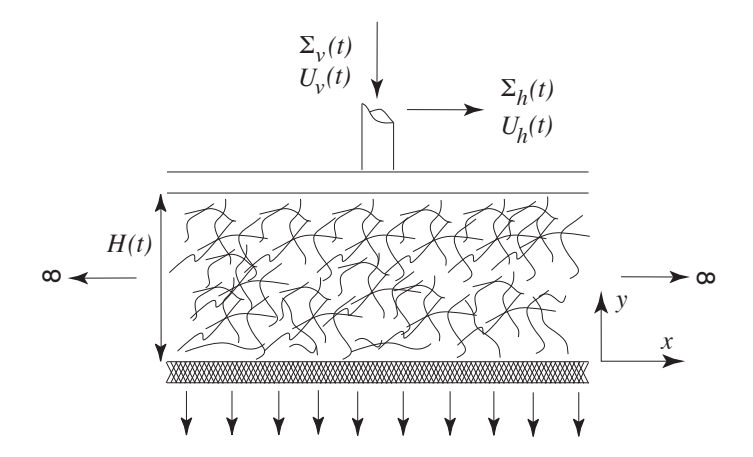


FIGURE 3.5. The drainage problem considered in Paper 4 and 5. A flocculated suspension is trapped between two infinite flat plates, one which is impermeable to both phases (the 'piston'), and one which is permeable to the liquid phase only (the 'filter'). The piston is employed to apply a vertical and horizontal time dependent load to the suspension ($\Sigma_v(t)$ and $\Sigma_h(t)$, respectively), either directly or by specifying the corresponding velocity components $U_v(t)$ and $U_h(t)$. The gap size is denoted H(t).

3.4.2. Sheared piston driven consolidation

The theory for the shear strength of flocculated mixtures is in Paper 4 and 5 applied to the sheared consolidation problem depicted in figure 3.5. A flocculated suspension is trapped between two parallel flat plates of infinite extension. The upper plate, referred to as the 'piston', is movable and impermeable to both phases. The lower plate is fixed and functions as a filter that is impermeable only to the particle phase, and perfectly permeable to the liquid phase. All effects from particles blocking the pore openings on the filter surface are neglected. The velocities of both phases are assumed to obey no slip conditions at the plates. The vertical and horizontal load by which the piston is applied to the suspension is denoted $\Sigma_v(t)$ and $\Sigma_h(t)$, respectively. The corresponding velocity components of the piston are $U_v(t)$ and $U_h(t)$, respectively. The deformations are restricted to the xy-plane of figure 3.5.

It is apparent that the model problem is a somewhat generalised version of the much studied case of uniaxial pressure filtration. Due to this, the role played by the deviatoric rate-independent stresses resulting from inter-particle forces is elucidated, and comparisons with previous studies are straightforward. It is found that the evolution of the concentration in the gap between the piston and the filter qualitatively follows the same advection—diffusion type of behaviour

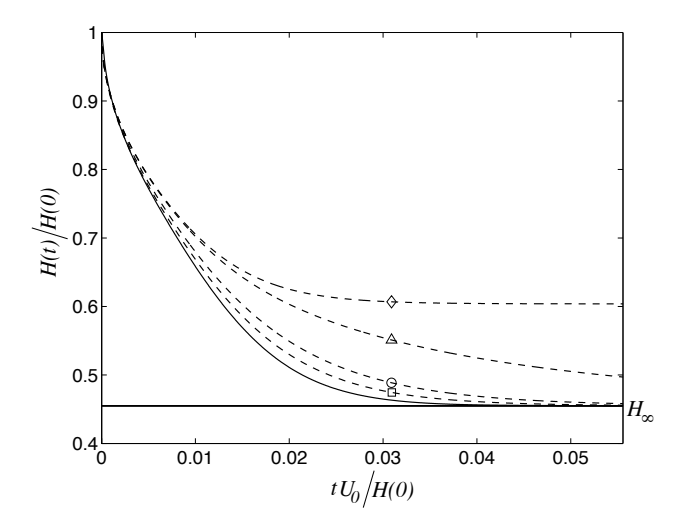


FIGURE 3.6. The evolution of the gap H(t) as a function of time. $\Sigma_v(t)$ and $U_h(t)$ are constant. $U_0 = \Sigma_v/\left(S_0^2\mu_cH(0)\right)$. M=0.287. $p_0(\phi)=\sigma_0\phi^n$, where n=2.5 and $\sigma_0/\Sigma_v=500$. Dashed lines: Purely plastic calculations. \diamond : $U_h=0$. \triangle : $U_h/U_0=32.4$. \circ : $U_h/U_0=162$. \square : $U_h/U_0=324$. Solid line: Visco-plastic calculation, $U_h/U_0=3240$, $\Lambda=5.6\cdot 10^{-3}$, where $\Lambda=(\mu_c/\mu_d)/\left(S_0H(0)\right)^2$. The horizontal line $H=H_\infty$ corresponds to the asymptotic gap size. Cf. Paper 5 for the details.

that is observed in uniaxial studies. Nevertheless, there are quantitative differences between the sheared compression and its uniaxial counterpart. Applying a shear-load in addition to the transversal load is predicted to increase the rate of the compression. Due to the higher strains on the inter-particle bonds when a shear load is applied, the capacity of the network to resist the transversal load decreases. As a result, more of the external load is transmitted to the pore liquid than in the corresponding uniaxial case. The higher pore pressure makes the expulsion of liquid more efficient.

The evolution of the gap size H(t) between the plates as a function of time is given for several different simulations in figure 3.6. In the ones referred to as 'purely plastic', only the rate-independent inter-particle stresses are included. In the 'visco-plastic' case, also rate-dependent stresses are incorporated in the description of the particle phase. These viscous stresses are of Newtonian type, and a constant apparent dynamic viscosity μ_d has been attributed to the solid phase. The vertical piston load $\Sigma_v(t)$ and the horizontal piston velocity $U_h(t)$ are held constant. The evolution of the horizontal load $\Sigma_h(t)$ is given in figure 3.7 for the different cases. The results in figures 3.6 and 3.7 are presented in scaled forms. The velocity scale U_0 is $\Sigma_v/(S_0^2\mu_cH(0))$, where μ_c and S_0

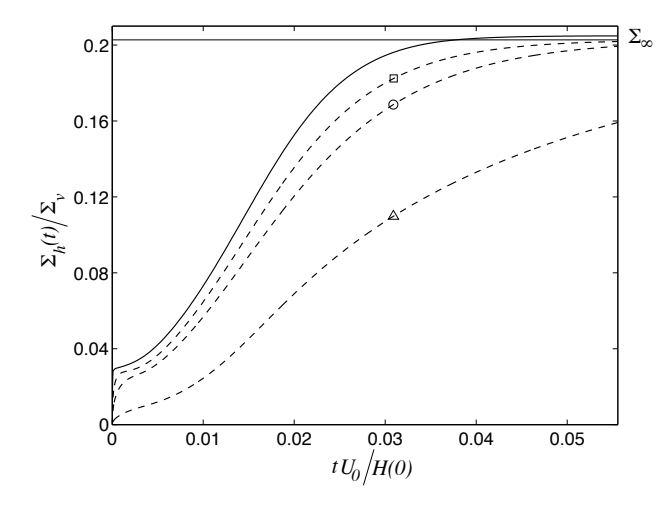


FIGURE 3.7. Comparison of the shear loads $\Sigma_h(t)$ for the same cases as in fig. 3.6. Cf. the caption of that figure for an explanation of the different line-types. For the case corresponding to $U_h=0$, we have $\Sigma_h\equiv 0$. The horizontal line $\Sigma_h=\Sigma_\infty$ corresponds to the asymptotic load in the purely plastic simulations.

are the dynamic viscosity of the liquid phase and the specific surface of the particles, respectively. In Paper 4 it is found that this is a suitable scale for the vertical velocity components after sufficiently long time. It is not really adequate for the horizontal components, which explains the large values of the horizontal velocities. The magnitude of the viscous stresses compared to the rate-independent stresses is expressed by the parameter Λ , which is defined in the caption of figure 3.6. As a reference, figure 3.6 also contains the evolution of the gap size H(t) in a situation of uniaxial consolidation with the same vertical load Σ_v . For the details regarding the simulations, the reader is referred to Paper 5.

In figure 3.6 it is seen how the rate of the consolidation process is increased when the piston is given higher horizontal velocities U_h . This trend is seen both in the purely plastic and the visco-plastic simulations. Larger velocities U_h correspond to higher shear loads, as can be deduced from fig. 3.7. Eventually, the drainage of liquid ceases, and the volumetric deformations vanish, i.e. $\dot{\varepsilon}_p = 0$. However, the shearing motion of the piston continues, and all parts of the network are therefore at critical state. When the dewatering ceases, the load Σ_v is at all levels balanced solely by the rate-independent stresses in the particle network⁸. This, together with the information that the solid phase is at critical state, permits us to conclude that the concentration is homogeneous

⁸In the absence of vertical deformations, there are no viscous normal stresses, wherefore this is true also for the visco-plastic model.

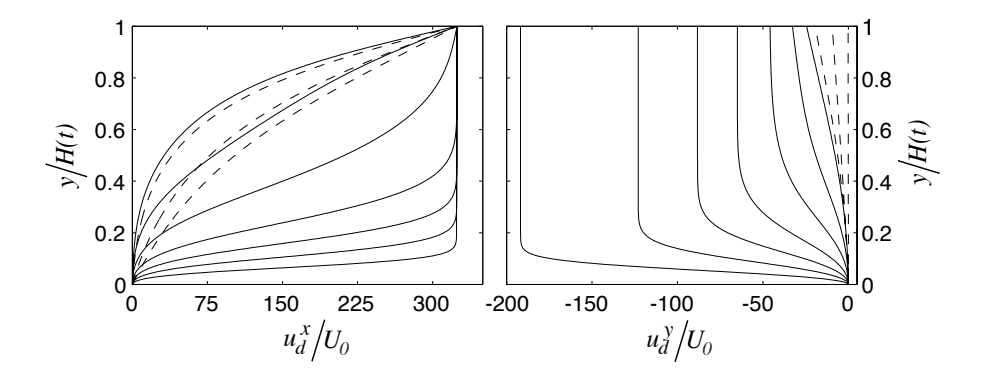


FIGURE 3.8. Velocity profiles for the solid phase in the gap between the plates at the instances $tU_0/H(0)/10^{-3} = 0.075$, 0.15, 0.3, 0.6, 1.2, 2.4, 4.8, 9.6, 19.2, 50. The co-ordinate y is the vertical position. The piston and the filter are located at y = H(t) and y = 0, respectively. Left subfigure: horizontal velocity component $u_d^x(y,t)$. For the solid curves, time increases with distance from the abscissa, whereas the opposite is true for the dashed curves (which correspond to the last three times). Right subfigure: vertical velocity component $u_d^y(y,t)$. Time increases from left to right. Both subfigures: The vertical load Σ_v is constant and the horizontal piston velocity $U_h/U_0 = 324$. The simulation corresponds to the case \square in fig. 3.6 and 3.7.

in the region between the plates. Further, since Σ_v is the same in all simulations, so is the asymptotic concentration and also the asymptotic gap size $H(t \to \infty) = H_{\infty}$, as seen in figure 3.6. For the uniaxial case, the asymptotic plate separation is larger (and the concentration of particles is lower) than for the sheared cases, since the flocculated structure then does not have to balance the shear load in addition to the transversal load Σ_v .

In the case of the purely plastic model, the applied horizontal shear load is necessarily balanced by the rate-independent stresses alone. As the asymptotic concentration is given by the vertical load Σ_v , which is the same in all situations, the fact that the network is at critical state then leads us to conclude that the asymptotic shear stress $\Sigma_{\infty} = \Sigma_h(t \to \infty)$ is the same regardless of the value of U_h . Consequently, the asymptotic piston load $(\Sigma_v, \Sigma_\infty)$ does not determine the shear rates in the gap between the plates. The conclusion must be that the shear rate profile is dependent on the load-history when the purely plastic model is employed. Incorporating even small viscous stresses eliminates this artefact, and one then finds that the piston load Σ_∞ uniquely defines the plate velocity U_h , and vice versa (given a certain vertical load Σ_v).

Figure 3.8 contains the horizontal and vertical velocity profiles for the solid phase in the purely plastic simulation for which $U_h/U_0=324$. Note that the time interval between two consecutive profiles increases as time proceeds. Initially, there are no velocity gradients in the region next to the piston. The upper part of the network thus translates like a stiff cake. Close to the filter, however, the deformation rates are high. With time, the deformations spread to the entire region between the plates. Progressively, the compression ceases and the horizontal velocity approaches an asymptotic profile. In the purely plastic simulations, due to the dependence of the asymptotic shear rate on the load history, we can only speculate about the exact form of the limit profile. As soon as viscous stresses are present, however, the situation is different. An apparent viscosity dependent on the volume fraction of solids then always results in a linear asymptotic velocity profile.

3.4.3. The model problem vs. a real forming section

The model illustrated in figure 3.5 is in several respects not representable of the conditions encountered in the forming section of a papermachine. First of all, as is concluded in Paper 3, gradients in the MD are certainly not negligible. However, the modelling assumptions made in Papers 4 and 5 remove all such effects. Secondly, the piston does not have any real counterpart in a twinwire forming section. In a uniaxial study, we could argue that the piston represents a surface at which the relative velocity between the fibres and the liquid vanish, and that such a surface (in an ideal situation) is found at the symmetry plane between the two forming fabrics. Nevertheless, the ambition is to study filtration in the presence of shear loads. The analogy between the piston driven filtration and the twin-wire forming section then fails since the symmetry plane implies vanishing shear stresses, which is clearly not the case at the piston.

In an appendix to Paper 5, the constitutive theory developed for the sheared consolidation is employed to derive an asymptotic solution for the concentration in a mat of flocculated suspension, that is on one side bounded by clear fluid and on the other by a permeable solid surface, subjected to a combination of drainage flow and cross flow of pure liquid. This alternative consolidation problem resembles the filtration process at the early stages of the forming of a paper sheet.

CHAPTER 4

Concluding remarks

A tool has been developed for predicting the pressure distributions in multicomponent twin-wire blade forming sections. It has been employed to study the effects on the pressure distribution from the interaction between the pulses generated by different blades, and between blades and devices for one-sided suction.

However, a lot of work remains before it is possible to quantitatively link the pressure distributions to the effects on the final paper sheet. In the thesis, some steps have been taken in that direction. It should be noted, that in the presented models it is tacitly assumed that it is meaningful to describe the fibre phase as a continuum. Due to the small thickness of the fibre sheets in the forming section, the appropriateness of this approach should be contemplated when considering the results. It is nevertheless motivated by the relative ease by which continuum models can be developed.

The study of the behaviour of a fibre mat as it experiences a blade pressure pulse illustrates how the knowledge of the pressure distributions could be employed to analyse the effects on the fibre webs of the drainage process in the forming section. In that particular study, there is no interaction between the calculation of the drainage pressure and the reactions of the fibre mat, but it could easily be envisaged.

It was found that the fibre mats are subjected to significant shear stresses as a result of the pressure gradients in the machine direction. This observation emphasizes the need to develop models for the drainage process that accurately incorporate the shear strength of the fibre network. Unless such become available, the relative displacements during the forming process of fibres (or flocs) in the plane of the sheet will not be possible to analyse theoretically. A tentative model of that kind has been developed, by merging a plasticity theory for the quasi-static yielding of soil with a two-fluid model for the flocculated suspension. It will need further improvements before it can be considered to describe a flocculated fibre network with any degree of accuracy. However, it is hopefully possible to continue to draw upon the theories developed in the field of solid mechanics in order to model effects arising from e.g. structural anisotropy.

For the time being, the most serious obstacle to further development of the model is that too little is known, even qualitatively, about the behaviour of

44 4. CONCLUDING REMARKS

fibre networks under conditions like the ones prevailing in the forming section of papermachines. Naturally, this makes it difficult to decide in which way the modelling work should proceed, not to mention the determination of values for various parameters in the model. The latter problem will become even more pronounced if the model grows in complexity. A possible extension of the theoretical work, which could yield interesting results already within the existing framework, is to account for the presence of fine material in the fibre suspension. It would both be valuable to predict how the fine material is distributed across the thickness of the sheet, and to consider its influence on the drainage flow through the webs.

Acknowledgments

On the day of my doctoral dissertation, I will present the work reported in this thesis alone. However, this does not reflect the circumstances under which it has come about. Several people have contributed to the thesis, either directly or by giving me the support that I needed. I am much indebted to my supervisor Docent Anders Dahlkild. He was actually the first person ever who attempted to teach me about fluid mechanics, a long time ago, and he has not stopped since. Without his guidance, this thesis would have looked very different, and not to the better. I would also like to express my gratitude to Professor Bo Norman. He has continuously shared his vast knowledge of papermaking, which has greatly helped to maintain the focus of the work on the issues of practical relevance. My thanks also go to Professor Fritz Bark, for accepting me as a Ph.D. student within the FaxénLaboratoriet, and for always having a very positive attitude towards my project, as well as in general.

During my years at the Department of Mechanics, I have had the great fortune to meet many nice and interesting people, with a wide variety of backgrounds. Although these persons may not in all cases have had a direct influence on my work, I would like to acknowledge how essential they have been to make the Department the stimulating place of work that I find it is, and not the least for having become my friends.

The financial support for this project has been provided by the Swedish Agency for Innovation Systems (VINNOVA), and the industrial partners within the FaxénLaboratoriet.

The words that I am writing in this acknowledgement are the very last that remain to complete my doctoral thesis. There is one person who more than anyone else has had to make sacrifices in order for me to arrive at this point. Caroline, for this, and everything else, je t'aime.

Bibliography

- AALTOSALMI, U., KATAJA, M., KOPONEN, A., TIMONEN, J., GOEL, A., LEE, G. & RAMASWAMY, S. 2004 Numerical analysis of fluid flow through fibrous porous materials. *Journal of Pulp and Paper Science* **30** (9), 251–255.
- Acheson, D. 1990 Elementary Fluid Dynamics. Oxford University Press.
- Adorján, L. A. 1975 A theory of sediment compression. In 11th International Mineral Processing Congress, pp. 297–318. Cagliari.
- AKESSON, K. 2004 Floc behaviour in a twin-wire blade pressure pulse. Licentiate thesis, Royal Institute of Technology (KTH), Stockholm.
- Andersson, S. R., Ringnér, J. & Rasmuson, A. 1999 The network strength of non-flocculated fibre suspensions. *Nordic Pulp and Paper Research Journal* **14** (1), 61–70
- Bandhakavi, V. & Aidun, C. 1999 Analysis of turbulent flow in the converging zone of a headbox. In *TAPPI Engineering Conference*, pp. 1135–1154.
- BANDO, T., IWATA, H. & NAGANO, A. 1994 Drainage mechanism on a twin-wire former. part 1: Factors affecting on the drainage phenomena. *Japan Tappi* 48 (7), 1493–1498.
- Baumann, W.-D. 1989 Duoformer-D a new approach to top wire forming. In *TAPPI Twin Wire Seminar*, pp. 115–120.
- Bennington, C. P. J., Azevedo, G., John, D. A., Birt, S. M. & Wolgast, B. H. 1995 The yield stress of medium- and high-consistency mechanical pulp fibre suspensions at high gas contents. *Journal of Pulp and Paper Science* **21** (4), 111–118.
- Bennington, C. P. J. & Kerekes, R. J. 1996 Power requirements for pulp suspension fluidization. *Tappi Journal* **79** (2), 253–258.
- Bennington, C. P. J., Kerekes, R. J. & Grace, J. R. 1990 The yield stress of fibre suspensions. *Canadian Journal of Chemical Engineering* **68**, 748–757.
- Bergström, R. 2003 Fibre flocculation during twin-wire roll forming. Licentiate thesis, Royal Institute of Technology (KTH), Stockholm.
- BOXER, T., DODSON, C. T. J. & SAMPSON, W. W. 2000 Analytic solution to the martinez dewatering equations for roll gap formers. *Journal of Pulp and Paper Science* **26** (11), 391–394.
- Brauns, R. 1986 Wet end developments. In CPPA Technical Section Annual Meeting, vol. A, pp. 275–282.

- Buscall, R., McGowan, I. J., Mills, P. D. A., Stewart, R. F., Sutton, D., White, L. R. & Yates, G. E. 1987 The rheology of strongly-flocculated suspensions. *J. Non-Newtonian Fluid Mech.* **24**, 183–203.
- BUSCALL, R., MILLS, P. D. A. & YATES, G. E. 1986 Viscoelastic properties of strongly flocculated polystyrene latex dispersions. *Colloids and Surfaces* 18, 341– 358.
- BUSCALL, R. & WHITE, L. R. 1987 The consolidation of concentrated suspensions, part 1—the theory of sedimentation. J. Chem. Soc., Faraday Trans. 1 83, 873– 891.
- CHANNELL, G. M. & ZUKOSKI, C. F. 1997 Shear and compressive rheology of aggregated alumina suspensions. AIChE Journal 43 (7), 1700–1708.
- Chen, E., Schultz, W. & Perkins, N. 1998 A two-dimensional viscous model of a wet paper forming process. In *TAPPI Engineering Conference*, pp. 53–61.
- CHUANG, S. 1982 Microturbulence generation in a papermachine headbox. In TAPPI Engineering Conference, pp. 205–213.
- Dalpke, B., Kerekes, R. J. & Green, S. I. 2004 Modelling jet impingement and the initial drainage zone in roll forming. *Journal of Pulp and Paper Science* **30** (3), 65–70.
- Dullien, F. A. L. 1992 Porous Media: Fluid Transport and Pore Structure, 2nd edn. San Diego: Academic Press Inc.
- FARRINGTON, T. A. 1991 A numerical investigation of three tissue machine headboxes. In AIChE Proceedings, Forest Products Symposium, pp. 177–188.
- GREEN, S. 2000 Modeling suction shoes in twin-wire blade forming: Results. *Journal of Pulp and Paper Science* **26** (2), 53–58.
- Green, S. & Kerekes, R. 1996 Numerical analysis of pressure pulses induced by blades in gap formers. In *TAPPI Engineering Conference*, pp. 185–192.
- Green, S. & Roshanzamir, A. 1997 The effect of blade wear on twin wire blade forming. In *TAPPI Engineering & Papermakers Conference*, pp. 889–896.
- Green, S., Zhao, R. & Kerekes, R. 1997 Pressure distribution between forming fabrics in blade gap formers: Blades of finite width and fabrics of finite stiffness. In 83rd Annual Meeting, Technical Section CPPA, pp. 89–95.
- Green, S. I. 1999 Modeling suction shoes in twin-wire blade forming: Theory. *TAPPI Journal* 82 (9), 136–142.
- Gullichsen, J. & Härkönen, E. 1981 Medium consistency technology, I. fundamental data. *TAPPI Journal* **64** (6), 69–72.
- Gustavsson, K. 2003 Mathematical and numerical modeling of 1-d and 2-d consolidation. PhD thesis, Royal Institute of Technology (KTH), Stockholm.
- HOLM, R. 2005 Fluid mechanics of fibre suspensions related to papermaking. PhD thesis, Royal Institute of Technology (KTH), Stockholm.
- HOLMQVIST, C. 2002 Modelling of the pressure distributions in twin-wire blade formers. Licentiate thesis, Royal Institute of Technology (KTH), Stockholm.
- Howells, I., Landman, K. A., Panjkov, A., Sirakoff, C. & White, L. R. 1990 Time-dependent batch settling of flocculated suspensions. *Appl. Math. Modelling* 14, 77–86.
- INGMANSON, W. L., ANDREWS, B. D. & JOHNSON, R. C. 1959 Internal pressure distributions in compressible mats under fluid stress. Tappi J. 42 (10), 840–849.

- Jackson, G. W. & James, D. F. 1986 The permeability of fibrous porous media. Canadian Journal of Chemical Enngineering 64, 364–374.
- KATAJA, M., KIRMANEN, J. & TIMONEN, J. 1995 Hydrostatic and structural pressure in compressed paper webs and press felts. Nordic Pulp and Paper Research Journal 10 (3), 162–166.
- Kerekes, R. J., Soszynski, R. M. & Tam Doo, P. A. 1985 The flocculation of pulp fibres. In *Papermaking Raw Materials. Transactions of the Eight Fundamental Research Symposium*, pp. 265–310. London: Mechanical Engineering Publications, Ltd.
- KOPONEN, A., KANDHAI, D., HELLÉN, E., ALAVA, M., HOEKSTRA, A. & KATAJA, M. NISKANEN, K. 1998 Permeability of three-dimensional random fiber webs. *Physical Review Letters* **80** (4), 716–719.
- LANDMAN, K. A. & RUSSEL, W. B. 1993 Filtration at large pressures for strongly flocculated suspensions. *Phys. Fluids A* 5 (3), 550–560.
- LANDMAN, K. A., SIRAKOFF, C. & WHITE, L. R. 1991 Dewatering of flocculated suspensions by pressure filtration. *Phys. Fluids A* **3** (6), 1495–1509.
- LANDMAN, K. A., STANKOVICH, J. M. & WHITE, L. R. 1999 Measurement of the filtration diffusivity $D(\phi)$ of a flocculated suspension. AIChE J. **45** (9), 1875–1882.
- LANDMAN, K. A., WHITE, L. R. & BUSCALL, R. 1988 The continuous-flow gravity thickener: Steady state behaviour. AIChE J. 34 (2), 239–252.
- LANDMAN, K. A., WHITE, L. R. & EBERL, M. 1995 Pressure filtration of flocculated suspensions. *AIChE Journal* **41** (7), 1687–1700.
- Lobosco, V. 2004 On the modelling of mechanical dewatering in papermaking. PhD thesis, Royal Institute of Technology (KTH), Stockholm.
- Malashenko, A. & Karlsson, M. 2000 Twin wire forming an overview. In 86th Annual Meeting, PAPTAC, pp. 189–201.
- Mantar, E., Co, A. & Genco, J. 1995 Drainage characteristics of pulp slurries under dynamic conditions. *Journal of Pulp and Paper Science* **21** (2), 44–50.
- MARTINEZ, D. M. 1998 Characterizing the dewatering rate in roll gap formers. *Journal of Pulp and Paper Science* **24** (1), 7–13.
- MEYER, H. 1971 Hydrodynamics of the sheet-forming process. *TAPPI Journal* **54** (9), 1426–1450.
- Moch, N. 1995 On variable permeability during the dewatering process in paper machines. Master's thesis, Royal Institute of Technology (KTH), Stockholm.
- NIGAM, M. & BARK, F. 1997 An analytical method to calculate the flow past a blade in twin-wire formers. *Tech. Rep.*. Department of Mechanics, Royal Institute of Technology (KTH), Stockholm.
- Nordén, H. V. & Kauppinen, P. 1994 Cake filtration with application to dewatering of pulp. Nordic Pulp and Paper Research Journal (4), 208–213.
- Nordström, B. 1995 Effects of headbox design and dewatering conditions on twinwire forming of TMP. PhD thesis, Royal Institute of Technology (KTH), Stockholm.
- Norman, B. 1979 Principles of twin-wire forming. Svensk Papperstidning 82 (11), 330–336.

- NORMAN, B. 1989 Overview of the physics of forming. In Fundamentals of Papermaking, Transactions of the Ninth Fundamental Research Symposium, , vol. 3, pp. 73–149.
- PARADIS, M. A., GENCO, J. M., BOUSFIELD, D. W., HASSLER, J. C. & WILDFONG, V. 2003 Measurement of drainage under conditions of known shear rate. *Journal* of Pulp and Paper Science 29 (12), 395–400.
- Parsheh, M. 2001 Flow in contractions with application to headboxes. PhD thesis, Royal Institute of Technology (KTH), Stockholm.
- ROSCOE, K. H. & BURLAND, J. B. 1968 On the generalised stress-strain behaviour of 'wet' clay. In *Engineering Plasticity* (ed. J. Heyman & F. A. Leckie), pp. 535–609. Cambridge: Cambridge University Press.
- ROSHANZAMIR, A., GREEN, S. & KEREKES, R. 1998 Two-dimensional simulation of pressure pulses in blade gap formers. *Journal of Pulp and Paper Science* **24** (11), 364–368.
- ROSHANZAMIR, A., GREEN, S. & KEREKES, R. 2000a Two-dimensional simulation of suction shoes in gap formers. *Journal of Pulp and Paper Science* **26** (4), 158–162.
- ROSHANZAMIR, A., GREEN, S. & KREKES, R. 2000b The effect of non-darcy's law drainage on the hydrodynamics of blade gap formers. In *TAPPI Papermakers Conference and Trade Fair*, pp. 701–708.
- ROSHANZAMIR, A., KEREKES, R., GREEN, S. & OLLIVIER-GOOCH, C. 1999 Hydrodynamic pressure generated by doctoring in blade gap formers. In *TAPPI Engineering/Process and Product Quality Conference & Trade Fair*, pp. 1181–1189.
- ROSHANZAMIR, A., OLLIVIER-GOOCH, C., KEREKES, R. J. & GREEN, S. I. 2001 Hydrodynamic pressure generated by doctoring in blade gap formers. *TAPPI Journal* 84 (7).
- Scheideger, A. E. 1957 The Physics of Flow Through Porous Media. University of Toronto Press.
- Shands, J. 1991 Mechanics of stock jump at jet impingement. *Journal of Pulp and Paper Science* 17 (3), 92–99.
- SHIRATO, M., KATO, H., KOBAYASHI, K. & SAKAZAKI, H. 1970 Analysis of settling of thick slurries due to consolidation. *J. Chem. Engng Japan* 3, 98–104.
- SIMS, D. 1985 Twin wire forming developments. In *TAPPI Twin Wire Seminar*, pp. 43–51.
- SÖDERBERG, D. 1999 Hydrodynamics of plane liquid jets aimed at applications in paper manufacturing. PhD thesis, Royal Institute of Technology (KTH), Stockholm.
- SWERIN, A., POWELL, R. L. & ODBERG, L. 1992 Linear and nonlinear dynamic viscoelasticity of pulp fiber suspensions. Nordic Pulp and Paper Research Journal (3), 126–132.
- Terzaghi, K. 1943 Theoretical Soil Mechanics. New York: John Wiley & Sons.
- Turnbull, P. F., Perkins, N. C., Schultz, W. W. & Beuther, P. D. 1997 One-dimensional dynamic model of a paper forming process. *TAPPI Journal* **80** (1), 245–253.
- USHER, S. P., DE KRETSER, R. G. & SCALES, P. J. 2001 Validation of a new filtration technique for dewaterability characterization. *AIChE Journal* 47 (7), 1561–1570.

- Vomhoff, H. & Schmidt, A. 1997 The steady-state compressibility of saturated fibres at low pressures. *Nordic Pulp and Paper Research Journal* 12 (4), 267–269.
- WIKSTRÖM, T. & RASMUSON, A. 1998 Yield stress of pulp suspensions, the influence of fibre properties and processing conditions. Nordic Pulp and Paper Research Journal 13 (3), 243–250.
- WILDFONG, V., GENCO, J., SHANDS, J. & BOUSFIELD, D. 2000a Filtration mechanics of sheet forming. part I: Apparatus for determination of constant-pressure filtration resistance. *Journal of Pulp and Paper Science* 26 (7), 250–254.
- Wildfong, V., Genco, J., Shands, J. & Bousfield, D. 2000b Filtration mechanics of sheet forming. part II: Influence of fine material and compression. *Journal of Pulp and Paper Science* **26** (8), 280–283.
- YEOW, Y. L. & LEONG, Y. K. 2001 Compressive yield stress from multiple-speed centrifuge measurements. *AIChE Journal* 47 (12), 2798–2806.
- ZAHRAI, S. & BARK, F. 1995 On the fluid mechanics of twin wire blade forming in paper machines. *Nordic Pulp and Paper Research Journal* **10** (4), 245–252.
- Zahrai, S. & Bark, F. 1996 Analytical and numerical approaches to solve the model equations for the flow of pulp in blade forming process. *AIChE Symposium Series* **92** (311), 68–73.
- ZAHRAI, S., BARK, F. & NORMAN, B. 1997 An analysis of blade dewatering in a twin-wire paper machine. *Journal of Pulp and Paper Science* 23 (9), 452–459.
- Zahrai, S., Martinez, M. D. & Dahlkild, A. A. 1998 Estimating the thickness of the web during twin-wire forming. *Journal of Pulp and Paper Science* **24** (2), 67–72.
- Zhao, R. & Kerekes, R. 1995 Pressure distribution between forming fabrics in blade gap formers: Thin blades. *Journal of Pulp and Paper Science* **21** (3), 97–103.
- Zhao, R. & Kerekes, R. 1996 The effect of consistency on pressure pulses in blade gap formers. Paperi Ja Puu Paper and Timber 78 (1–2), 36–38.

Part 2

Papers

1

Paper 1

A flexible approach for modelling flow in multi-component blade formers

By Claes Holmqvist¹, Anders Dahlkild¹ and Bo Norman²

¹Department of Mechanics, KTH, SE-100 44 Stockholm, Sweden ²Department of Fibre and Polymer Technology, KTH, SE-100 44 Stockholm, Sweden

Submitted to Nordic Pulp & Paper Research Journal

The internal structure of the fibre network constituting a paper is to a dominating extent determined in the forming zone of the paper machine. In this article we present a method for modelling the pressure distributions in blade forming sections, which is commonly considered to be a key quantity of the process. The ambition is to obtain a tool by which the interaction between the different components of blade sections can be studied. It is achieved by defining modules out of which arbitrary sections can be constructed. The modules are solved independently and matched to each other iteratively. Keeping the interface between the modules simple provides great flexibility in the modelling. By virtue of a slenderness assumption, the equations governing each module can be reduced to one-dimensional form, hence limiting the computational work and permitting systems of many components to be studied. Dimensionless numbers defining the problem are identified, and the magnitude of the nonlinear effects are estimated. Simulations are presented that illustrate the potential of the method.

1. Introduction

In the forming section of paper machines, a dilute suspension of fibres and water is ejected into the gap between two moving tensioned permeable fabrics that bound and guide the suspension. In a blade former, drainage through the fabrics, which are usually referred to as wires, is achieved by applying ceramic blades to the fabrics across the width of the machine; see Figure 1. The local deflection of the wires implies a constriction for the flow of suspension. The result is a local increase in the suspension pressure, which attempts to increase the distance between the wires and simultaneously yields drainage of the water through the fabrics, hence allowing the suspension to pass the obstacle. During the dewatering, fibres are deposited on the wires in a sedimentation like process. As drainage continues, the thickness of the fibre mats will increase until eventually they occupy the entire region between the fabrics. Further drainage is then best described as a thickening process. Apart from resulting in necessary dewatering of the pulp, which is often enhanced by artificially

reducing the atmospheric pressure outside one of the fabrics (i.e. applying one-sided suction), it is generally accepted that the processes in this part of the machine has a significant influence on the distribution of the fibres in the fibre mats, and consequently on the quality of the final product. This motivates the development of models of blade formers.

Previous works. The local nature of the pressure generated when a blade is applied to a pair of fabrics was predicted by Norman (1979), and first experimentally verified by Sims (1985). More detailed pressure measurements have been performed by Zahrai et al. (1997) and Zhao & Kerekes (1995). In the latter study, Zhao & Kerekes also presented a one-dimensional linear analytical analysis of the pressure generated by a thin blade applied to a pair of fabrics. It was followed by two-dimensional linear analytical analyses by Zahrai & Bark (1995) for a thin blade, and by Nigam & Bark (1997) for a flat or a cylindrically curved blade. Non-linear two-dimensional numerical simulations were performed by Zahrai & Bark (1996) and Zahrai et al. (1997). Under the assumption that the fibre suspension can be described as a Newtonian fluid, Roshanzamir et al. (1998) and Roshanzamir et al. (1999) undertook the first calculations where viscosity was incorporated in a rigorous way. Investigations of the effects from reducing the ambient pressure outside one of the wires in between two thin blades have been performed by Green (2000), Green (1999), and by Roshanzamir et al. (2000a).

Motivation. The work previously undertaken has focused on single devices, e.g. a single blade, and do not provide any information about the interaction between the different components. Hence, based on them little can be said about how important parameters varies throughout real forming sections. Our ambition is therefore to present a model that permits us to study the effects on the pressure distribution of the interaction between the different blades and the devices for applying one-sided suction. The model should be flexible enough to allow major alterations of the geometry, and a rather free choice of operation parameters. Such a model can also be employed for the design, trouble-shooting and tuning of full scale blade sections.

Outline. In §2 we formulate a one-dimensional description of the process. The system of ordinary differential equations is partly integrated in §3, and a solution algorithm is presented. It is based on the concept of modules out of which arbitrary forming sections can be constructed, and which are solved independently and then matched. Simulations that illustrate the potential of the model are presented in §4, together with a comparison with previously published results for a single blade. Numerical issues such as grid independence and convergence rate are commented upon. Conclusions are formulated in §5.

2. The Governing Equations

The geometry of our problem is such that the ratio between the dimensions in the spanwise direction, y, and characteristic lengths in the streamwise direction, x, is at least of the order 100. Thus we can readily assume that it suffices to

perform the analysis in the xz-plane of Figure 1. A stationary formulation of the problem will be presented.

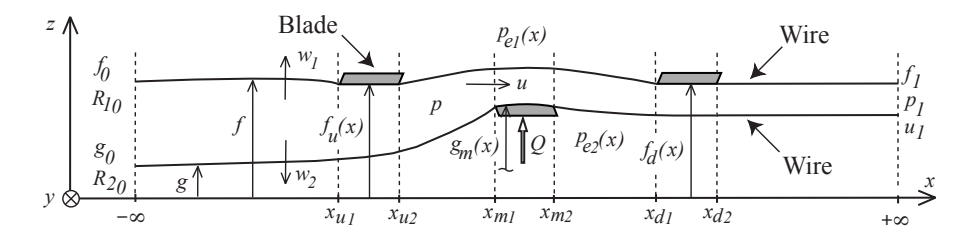


FIGURE 1. Schematic view across a blade forming section consisting of three blades. The suspension flows from left to right between the wires. The external atmospheric pressure can be set to arbitrary values, hence permitting devices for one-sided suction to be simulated. Note that the relation between the dimensions in the x- and z-directions are not correct. Confer the text for the notation.

It is assumed that the region between the wires exhibits a sandwich structure, where the fibre webs residing on the fabrics are separated by a region of suspension of low concentration. This is likely to be a reasonable description in the upstream part of the domain. Further downstream the fibre mats completely fill the distance between the fabrics, a situation which will not be treated in the present study.

In what follows, the subscript i takes the values 1 and 2, which refers to the upper and the lower fabric, respectively.

2.1. The flow through the fabrics and fibre mats

We shall consider each wire, and the fibre mat it supports, to be a single continuous medium, and refer to the ensemble of the two components as either the *fabric* or the *wire*, unless otherwise specified. Any influence of blockage effects at the interface between the fabrics and the fibre webs will thus be neglected.

Roshanzamir et al. (2000b) found that inertial effects have little influence on the drainage flow through the wires. Darcy's law will therefore be used to describe the drainage. We shall assume that the fabrics are thin and that they have a constant (finite) permeability k_{ζ} in the direction ζ , which is perpendicular to the surface and directed away from the suspension. The permeability in the plane of the wires is considered to be negligible. Assuming further that the pressure varies linearly between the value p_{wi} at the suspension side of the fibre web, and p_{ei} on the outer side of the wire, and denoting the combined thickness of the fibre mat and the wire l_i , the (superficial) drainage velocity,

 w_i , is given by the relation

$$w_i = \frac{1}{R_i}(p_{wi} - p_{ei}) \quad i = 1, 2.$$
 (1)

Here, a drainage resistance $R_i = \mu l_i/k_\zeta$ has been introduced, where μ is the dynamic viscosity of the liquid phase. As l_i increases due to fibre deposition, R_i will increase as well. Let ξ be the direction locally tangential to the fabric surface, positive in the direction of the suspension flow. Conservation of fibres yields

$$\frac{\mathrm{d}R_i}{\mathrm{d}\xi} = \frac{1}{U} \frac{\mu}{k_\zeta} \frac{\alpha_s}{\alpha_p} \frac{p_{wi} - p_{ei}}{R_i} \quad i = 1, 2,$$
(2)

where we have assumed that all of the fibres in the suspension are added to the fibre web during drainage. U is the constant speed of the fabrics, and α_p and α_s are the constant volume concentrations of fibres in the mats and the suspension, respectively. Let D and d denote characteristic lengths of the problem in the x- and z-directions, respectively. The distance between the wires is typically an order of magnitude smaller than the length of the blades and the spacing between the blades. A reasonable assumption is therefore that the ratio $\lambda = d/D$ is small, which can be verified a posteriori. Provided that $\lambda^2 \ll 1$, the derivative with respect to ξ in (2) can be replaced with a derivative with respect to x.

As soon as a volume of liquid has been drained from the region between the wires it is considered to have left the system permanently, and will not receive further attention.

2.2. The momentum of the wires and the fibre mats

Consider the upper wire in Figure 1. Its position in the z-direction is denoted f. Making use of our previous assumption $\lambda^2 \ll 1$, and if the fabric behaves according to the classical Euler-Bernoulli beam theory, a force balance yields

$$mU^{2}\frac{\mathrm{d}^{2}f}{\mathrm{d}x^{2}} = p_{w1} - p_{e1} + T_{1}\frac{\mathrm{d}^{2}f}{\mathrm{d}x^{2}} - B\frac{\mathrm{d}^{4}f}{\mathrm{d}x^{4}},$$
(3)

where the constant parameters T_1 , B and m are the axial wire tension per unit width, the bending stiffness per unit width, and the mass per unit area in the xy-plane, respectively. They are of the order 10 kN/m, 10^{-2} Nm and 1 kg/m^2 , respectively. Clearly, as U is of the order 10 m/s, mU^2 is negligible in comparison with T_1 , and we can consider the fabric to be inertialess. In addition, as was noted by Zahrai & Bark (1995), we see that the effects of bending stiffness are only important if we consider length scales in the x-direction of the order $\sqrt{B/T_1}$ (approximately 1 mm) or smaller. As d is of the order 1 mm, and we in §2.3 make simplifications based on the assumption that the relevant length scale D is such that $\lambda \ll 1$, we would not be able to correctly resolve the effects of bending stiffness even if the corresponding term in (3) was included. It will

hence be ignored and the following equation used for the upper fabric,

$$p_{w1} - p_{e1} + T_1 \frac{\mathrm{d}^2 f}{\mathrm{d}x^2} = 0.$$
 (4)

It expresses a balance between the pressure drop across the fabric and the wire tension, related through the wire curvature. An analogous equation holds for the lower wire in Figure 1, whose position in the z-direction is denoted g. The only difference with respect to (4) is that the pressure terms are of opposite sign. Further, as D should be in the range 0.05–0.1 m, we expect from (4) that the pressures generated by the blades are of the order 1 kPa.

2.3. The free suspension

Roshanzamir et al. (1998) came to the conclusion that even quite large values of Newtonian viscosity (compared to water) had little influence on the calculated drainage pressure generated by a blade. Consequently, it is here assumed that the suspension between the fibre mats behaves like an inviscid fluid governed by Euler's equations. Provided that $\lambda \ll 1$ it is found, in analogy with the shallow water wave theory (cf. e.g. Acheson 1990), that the gradients in the z-direction of the pressure and the x-component of the suspension velocity are negligible. These quantities are denoted p and u, respectively. The momentum equation is thus reduced to

$$u\frac{\mathrm{d}u}{\mathrm{d}x} + \frac{1}{\rho}\frac{\mathrm{d}p}{\mathrm{d}x} = 0\,, (5)$$

where ρ is the bulk density of the suspension. We can now substitute p for p_{wi} in (1)–(4) as we know that the former variable is independent of z.

Integrating the 2-D continuity equation in the z-direction across the gap between the wires we obtain

$$\frac{\mathrm{d}}{\mathrm{d}x}\Big(u(f-g)\Big) = -(w_1 + w_2). \tag{6}$$

2.4. The presence of blades

The equations in $\S 2.1-2.3$ refer to parts of the domain where no blades are applied to the fabrics. A fabric in contact with a blade is assumed to follow the blade surface. Its position in such a region is hence known if the blade is fix, or known up to some constant if the blade is applied with a prescribed force (see $\S 3$). The equilibrium equation for the corresponding wire, i.e. (4) or its analogous counterpart for the lower fabric, is then not enforced. Assuming that no drainage takes place across the wire in contact with the blade, p_{ei} equals p along the blade, which is inserted in the remaining equations.

¹It is well known that the fibre suspensions dealt with in paper manufacturing has a very complicated rheology. However, as is observed by e.g. Zahrai & Bark (1996), good agreement between experiments and models is found for the pressure assuming that the suspension is an inviscid fluid.

2.5. Dimensionless variables

The variables are now scaled in order to obtain dimensionless quantities to be used henceforth. These will be denoted exactly as their dimensional counterparts. The pressures p and p_{ei} are scaled by ρU^2 , the suspension velocity u by U, the drainage bulk velocities w_i by λU , the drainage resistances R_i by $\rho U/\lambda$, the wire positions f and g by d, and, finally, x by D. Throughout the rest of this study no references will be made to the dimensional variables. (5) turns into

$$u\frac{\mathrm{d}u}{\mathrm{d}x} + \frac{\mathrm{d}p}{\mathrm{d}x} = 0\,, (7)$$

whereas (4) and its counterpart for the lower wire become respectively

$$p - p_{e1} + \varepsilon_1 \frac{\mathrm{d}^2 f}{\mathrm{d}x^2} = 0, \qquad (8)$$

$$p - p_{e2} - \varepsilon_2 \frac{\mathrm{d}^2 g}{\mathrm{d}x^2} = 0. \tag{9}$$

The ε_i are parameters related to the tensions T_i in the fabrics, and can be expressed in terms of the slenderness ratio λ and dimensionless groups We_i related to each wire, analogous to Weber numbers,

$$\varepsilon_i = \frac{T_i d}{\rho U^2 D^2} = \frac{\lambda}{W e_i} \quad i = 1, 2.$$
 (10)

The evolution of the drainage resistances (2) is now given by

$$\frac{\mathrm{d}R_i}{\mathrm{d}x} = \kappa w_i \quad \text{where} \quad \kappa = \frac{\alpha_s}{\alpha_p} \frac{\mu}{\rho U D} \frac{d^2}{k_{\zeta}} \quad \text{and} \quad i = 1, 2.$$
 (11)

 κ can be divided into two components, the ratio α_s/α_p , and the remaining part, denoted β . The first of these controls the growth rate of the fibre mats when fibres are deposited. β is a dimensionless intrinsic resistance to flow through the fabric/fibre mat, as opposed to the R_i that are integrated (total) resistances. (1) and (6) have the same appearances in dimensionless form.

Necessary conditions to solve the system consisting of (1), (6) and (7)–(11) are given in §3.

3. Solution Algorithm

3.1. A module based algorithm

Any blade section can be divided into regions containing either two free wires, or a free wire and a blade, as indicated by the dashed lines in Figure 1. Consider each such region to be an individual module that can be solved independently of the other modules provided that the necessary conditions on the dependent variables are available. As no other kind of modules than the ones indicated in Figure 1 will be necessary, if a straightforward and robust algorithm for linking the modules to each other were at hand, it would be easy to solve arbitrary blade sections. In §3 we shall present one way of doing this. It should also be noted that the division indicated by the dashed lines in Figure 1 is very

natural, since different sets of equations are used when both of the wires are free, and when a blade is in contact with one of the fabrics (see $\S 2$).

Let us consider an assembly of n modules M^i that together constitute a model of a certain blade section (see Figure 2). The superscript i shall be used to refer to the ith module. Out of the boundary conditions necessary

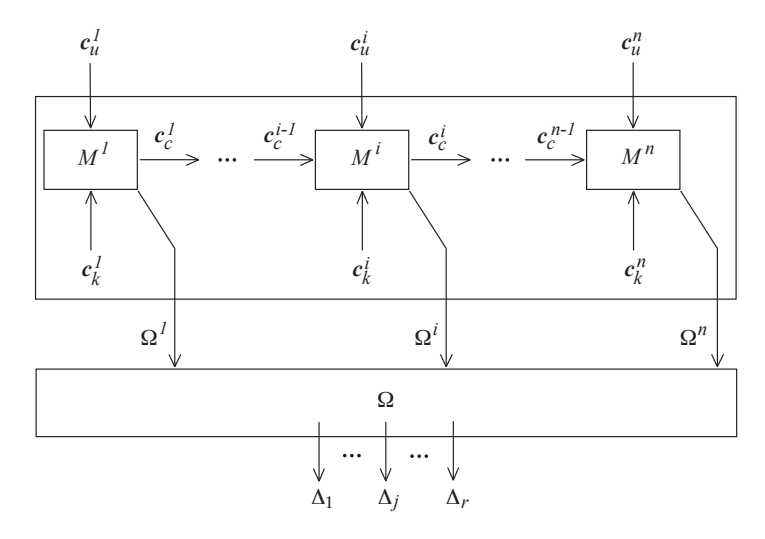


FIGURE 2. An assembly of modules M^i , i=1...n. The known and guessed parameters (c_k^i and c_u^i , respectively) result in partial solutions Ω^i that give a solution $\Omega = \sum_i \Omega^i$ for the complete domain. Ω is then used to calculate quantitative values Δ_j of how well the solutions from the different modules complies with the matching criteria.

to solve the governing equations for the module M^i , certain are known and are grouped together in the vector \mathbf{c}_k^i . Others, denoted by \mathbf{c}_u^i , are not known a priori, and must be determined in the solution process. Apart from the evolution of the dependent variables throughout the module, symbolically given by Ω^i , the module also delivers a vector of parameters \mathbf{c}_c^i , based on Ω^i , that are used as boundary conditions for the neighbouring module M^{i+1} . Denote \mathbf{c}_u the vector containing all unknown parameters, and whose components are given by the composition of the different \mathbf{c}_u^i . Let us guess \mathbf{c}_u and thereafter calculate the evolution Ω of the variables throughout the model. If the guessed \mathbf{c}_u is not correct, the Ω^i will not fit with each other in a physically correct manner across the module boundaries. The real solution must fulfil matching criteria Δ_j , $j=1\ldots r$, that ensures a correct fit between the modules (r equals the number of components in \mathbf{c}_u , which is also the total number of unknown boundary conditions in all modules).

The solution procedure for the modules (see §3.2) defines a continuous function Z such that $c_u \xrightarrow{Z} \Delta$, where Δ is the vector whose components are the Δ_j . Provided that the Δ_j are defined such that compliance with criterion j corresponds to $\Delta_i = 0$, obtaining the physically correct solution Ω means finding the root to Z. In the present study this has been done by using either the Gauss-Newton method (Dennis 1977) or the Levenberg-Marquardt method (Levenberg 1944; Marquardt 1963; Moré 1978), combined with a safeguarded mixed quadratic and cubic polynomial interpolation and extrapolation line-search method, to minimise $S_{\Delta} = |\Delta|^2$. Both of the methods perform satisfactory. In each iteration, the Gauss-Newton method minimises a local quadratic approximation of S_{Δ} , in which the contributions from the second derivatives to the Hessian of S_{Δ} are neglected. The more robust Levenberg-Marquardt method is a blend of the steepest descent method and the Gauss-Newton method. The former is used far from the minimum, but as the extremum is approached, the Levenberg-Marquardt method turns into the latter in a continuous fashion.

3.2. Solving the modules

Consider first the i^{th} module, which is assumed to contain two free fabrics. It is consequently described by the system consisting of (1) and (6)–(11). From (7) we immediately get that

$$p = C_1 - \frac{u^2}{2} \,, \tag{12}$$

where from now on C_l (l = 1,...) will denote constants of integration. Apart from (8) and (9), the governing equations are valid at the module boundaries (see §3.3). C_1 is hence the same constant throughout the whole model domain². Constants of integration which appear in equations derived from (8) or (9), and which may hence take different values in different modules, are distinguished by a module superscript, C_l^i .

Define a variable $k = (\varepsilon_1 f + \varepsilon_2 g)/(\varepsilon_1 + \varepsilon_2)$. Apparently, if $\varepsilon_1 = \varepsilon_2$, k is the position of the centreline between the two fabrics. Let \tilde{x} be a local co-ordinate system with the origin at the inlet to the module. Subtracting (9) from (8) and integrating yields

$$k = \int_0^{\tilde{x}} \int_0^{\tilde{x}'} F^i(\tilde{x}'') \, d\tilde{x}'' \, d\tilde{x}' + C_2^i \tilde{x} + C_3^i \quad \text{where}$$

$$F^i(\tilde{x}) = \frac{p_{e1}^i(\tilde{x}) - p_{e2}^i(\tilde{x})}{\varepsilon_1 + \varepsilon_2} \, .$$

$$(13)$$

Note that if $p_{e1}^i = p_{e2}^i$, k changes linearly through the module. Let h = f - g denote the distance between the wires. Combining (6) and (11), and then

 $^{^{2}}$ Equation (7) would not have been valid at a module boundary if, for some reason, a point force were acting on the suspension at that position.

integrating, it is found that

$$uh = -\frac{R_1 + R_2}{\kappa} + C_4. (14)$$

Adding (8) and (9) provides us with an equation for h. Eliminating p in this equation with (12) we obtain a relation for h and u,

$$\frac{\mathrm{d}^2 h}{\mathrm{d}x^2} + \frac{\varepsilon_1 + \varepsilon_2}{\varepsilon_1 \varepsilon_2} \left(C_1 - \frac{u^2}{2} \right) - \frac{p_{e1}^i}{\varepsilon_1} - \frac{p_{e2}^i}{\varepsilon_2} = 0.$$
 (15)

The equation for h together with (1) and (11) can also be turned into an equation for R_1 ,

$$\frac{R_1^2}{2} + \kappa \frac{\varepsilon_1 \varepsilon_2}{\varepsilon_1 + \varepsilon_2} \frac{\mathrm{d}h}{\mathrm{d}x} = -\kappa \frac{\varepsilon_1}{\varepsilon_1 + \varepsilon_2} G^i(\tilde{x}) + C_5^i \quad \text{where}$$

$$G^i(\tilde{x}) = \int_0^{\tilde{x}} \left(p_{e1}^i(\tilde{x}') - p_{e2}^i(\tilde{x}') \right) \mathrm{d}\tilde{x}' .$$
(16)

An analogous equation holds for R_2 . Now, if (16) and its counterpart for R_2 is combined with (14), we obtain a second relation involving h and u,

$$\kappa^{2}(C_{4} - uh)^{2} \left(\kappa^{2}(C_{4} - uh)^{2} + 8\kappa \frac{\varepsilon_{1}\varepsilon_{2}}{\varepsilon_{1} + \varepsilon_{2}} h_{x} + 4\left(\kappa \frac{\varepsilon_{1} - \varepsilon_{2}}{\varepsilon_{1} + \varepsilon_{2}} G^{i}(\tilde{x}) - C_{5}^{i} - C_{6}^{i}\right)\right) + 4\left(\kappa G^{i}(\tilde{x}) + C_{5}^{i} - C_{6}^{i}\right)^{2} = 0.$$
 (17)

Note that (15) and (17) can easily be combined into a single equation for h. We shall refrain from this as the highest derivative in the resulting equation would then not appear linearly, as is the case in the system (15), (17).

The conditions specified to determine the module solution are indicated in Table 1. The position of the outlet is denoted \tilde{x}^i_{out} . The entries in the table denote the values of the variables at the respective position. Other combinations

	Position (\tilde{x})		
	0	\tilde{x}_{out}^i	
f	f_{in}^i	f_{out}^i	
g	g_{in}^i	g_{out}^i	
R1	R_{1in}^i	_	
R2	R_{2in}^i	_	
u	_	u_{out}^i	
p		p_{out}^i	

Table 1. Boundary conditions specified for a module containing two free wires. $\tilde{x}=0$ and $\tilde{x}=\tilde{x}^i_{out}$ correspond to the inlet and the outlet, respectively. (—) indicates that no condition is specified at that position.

than the one presented in the table are possible. To reduce the size of c_u when modules are combined, it would be preferable to specify the conditions on the four last variables in the table at the same \tilde{x} -position, e.g. $\tilde{x}=0$. However, if the module extends towards infinity in the upstream direction, regardless of what is specified at \tilde{x}_{out}^i , p always tends asymptotically to the pressure of the surrounding atmosphere $(p_a=0)$ in the upstream direction. This is seen both in numerical computations and in the analytical first order solution obtained from a regular perturbation analysis in the parameter γ , defined by $h_{in}^i = (1-\gamma)h_{out}^i$. Consequently, specifying the physically correct condition p=0 at the upstream end of an infinitely long module does not introduce any information into the problem. Moving the condition to \tilde{x}_{out}^i yields a well-posed problem. Having done this, it turned out that the root to Z was found faster if the conditions on R_i (i=1,2) were given at $\tilde{x}=0$.

Modules where one of the fabrics is in contact with a blade are treated in a similar fashion (the details can be found in the presentation by Holmqvist (2002)), and the governing equations are reduced to two expressions linking h and u, corresponding to (15) and (17). The blade is assumed fix during the derivation. Loadable blades are discussed in §3.3. The boundary conditions used are a straightforward choice of those given in Table 1.

The integration constants C_1 , C_2^i and C_3^i are determined analytically from the boundary conditions. The remaining three must be determined in the numerical solution process³. Central finite difference approximations of (15) and (17) are introduced at the interior mesh points of a uniform grid. Skewed discretisations of (17) are used at the edge nodes. At the inlet node, algebraic equations approximating (16), and its counterpart for R_2 , are also formulated. All approximations are second order accurate (including those needed in §3.3–3.4), and are explicitly given by Holmqvist (2002). The algebraic equation system thus obtained is sparse, and since it is straightforward to construct the Jacobian explicitly, we solve the system by the damped Newton's method. The linear equation system appearing at each iteration is solved through LU-factorisation with partial pivoting, by a method that takes into account the sparse structure of the coefficient matrix. Prior to the factorisation, the columns of the system matrix are permuted through minimum degree ordering, in order to yield sparser factors (Gilbert et al. 1992).

3.3. The matching criteria

The dependent variables f, g, p, u and the drainage resistances R_i , are all necessarily continuous across module boundaries. To see why this is so, we could e.g. look at (12). If there is a discontinuity in p, there will be one in u as well. f and g are continuous for obvious reasons, which is hence also true for h. As we are dealing with an incompressible fluid, we realise that

³Note that it would be sufficient to determine C_1 and C_4 in only one of the modules. As the modules are intended to be solved independently of each other, it is however done in all modules.

the discontinuity in u would require a finite drainage over an infinitesimal distance in the x-direction, in other words infinite drainage velocities w_i , which is physically unreasonable. Hence, u, p and R_i (i = 1, 2) must be continuous.

Consider the boundary between a module containing two free wires, and a module containing a blade. We assume without loss of generality that the blade is applied to the lower fabric, and that the interface between the modules is located at x_b . (8) is valid at this point, and integrating it across x_b demonstrates that the derivative of the position of a free fabric is continuous across module boundaries. (9) is however not valid at x_b . The edge of the blade acts as a point force Q_b on the fabric, a possibility that was not included in the derivation of the equation. In the following form, though, it can be applied at x_b ,

$$p - p_{e2} - \varepsilon_2 \frac{\mathrm{d}^2 g}{\mathrm{d}x^2} - Q_b \delta(x_b) = 0.$$
 (18)

Above, $\delta(x)$ is Dirac's function. Integrating the equation across x_b , we find that there is a discontinuity in the slope of the wire,

$$\frac{\mathrm{d}g}{\mathrm{d}x}(x_b^+) - \frac{\mathrm{d}g}{\mathrm{d}x}(x_b^-) = -\frac{Q_b}{\varepsilon_2},\tag{19}$$

where the superscripts '-' and '+' here and elsewhere denote the upstream and downstream side, respectively. The discontinuity is a result of our neglect of the bending stiffness of the fabrics.

Any of the requirements of continuity are candidates for the criteria Δ_j . However, some of them are immediately fulfilled by passing information from one module to the next via the vectors \mathbf{c}_c^i during the solution process. The magnitude of the discontinuities are straightforward quantitative measures of the degree of compliance of the criteria.

Introducing matching criteria also enables the modelling of more exotic features such as loadable blades. We exemplify this by considering the middle blade in Figure 1, which is applied to the fabric with a force Q per unit width in the y-direction (scaled by T_2). The position of the blade in the z-direction is determined by formulating a Δ_j enforcing the equilibrium equation

$$\frac{\mathrm{d}g}{\mathrm{d}x}(x_{m1}^{-}) - \frac{\mathrm{d}g}{\mathrm{d}x}(x_{m2}^{+}) - \frac{Q}{\lambda} = 0.$$
 (20)

 x_{m_1} and x_{m_2} are the positions of the upstream and downstream edges of the blade, respectively.

When non-flat blades are applied, the fabrics do not necessarily remain in contact with the blade along the full length, which was one of the assumptions made in §2. Sometimes this results in erroneous solutions. In a correct solution the fabrics are either wrapped over the edges, or leave/make contact with the blades tangentially. This follows from the observation that a point force on a wire must necessarily be directed towards the suspension. When an unphysical blade—wire contact occurs, the point where the fabric first (or last) is in contact with the blade is introduced as an unknown parameter in c_u . It is then determined by introducing a matching criterion requiring that, at that

point, the slope of the wire and the blade surface must be equal. From the viewpoint of the model, the blade is cut off so that the contact with the fabric naturally occurs over the full length. In reality, the neglected part of the blade might have some influence on the process, e.g. by giving rise to an increase in the effective drainage resistance in the vicinity of the contact point, due to the limited space available between the fabric and the blade.

As, normally, only the position of one of the fabrics is given at the down-stream end of the blade section, a condition have to be formulated to determine the other (unknown) wire location. The condition $p = p_{e1} = p_{e2} = 0$ at that end translates into dh(x)/dx = 0.

3.4. Composite modules

Each new module enlarge c_u , which in turn augments the demands on the algorithm responsible for finding the roots of Z. This is a potential limitation on the size of the blade sections that can be modelled. It is, however, possible to construct larger modules than the fundamental ones discussed above, and thus reduce the total number of modules that have to be used in a given situation. We note that a module containing a blade always have neighbouring modules containing two free fabrics. Without loss of flexibility we can define *composite modules* consisting of two fundamental modules — an upstream one with two free wires, M_i^{i+1} , and a downstream one containing a fabric and a blade, M_i^i

The boundary conditions that have to be specified at the outlet of the upstream module, and at the inlet of the downstream one, now become internal unknowns in the composite module and equations have to be formulated for them. The purpose of specifying p_{out}^{i+1} is normally to provide information so that C_1 can be determined in M_w^{i+1} . As this constant have the same value in both of the modules, p_{out}^{i+1} needs hence not be included among the 'new' unknowns. Continuity of the dependent variables provides trivial equations linking the values of the variables at the outlet of M_w^{i+1} and the inlet of M_b^i . Consequently we can limit our discussion to the equations needed to replace the conditions on the position and the drainage resistance of the free fabric at the inlet of M_b^i . Note that the blade is assumed fix, and the position of the contacting wire is hence given by a known function. Furthermore, the drainage resistance of the wire in contact with the blade is constant. Hence the conditions related to the free fabric are the only ones needed. The requirement for continuity of the slope of the free wire, together with the relation between the fabric position (i.e. f or g), h and k, can be turned into an equation for the unknown fabric position at the inlet of M_h^i . An algebraic equation for the drainage resistance of the free wire at the inlet of M_b^i is obtained by discretising (16), or its analogous counterpart, at the outlet of M_w^{i+1} and then employing the continuity of the R_i (i = 1, 2). See Holmqvist (2002) for the details.

Of course, if deemed necessary, composite modules consisting of more than two fundamental modules can be constructed in the same manner as described above.

4. Numerical Simulations

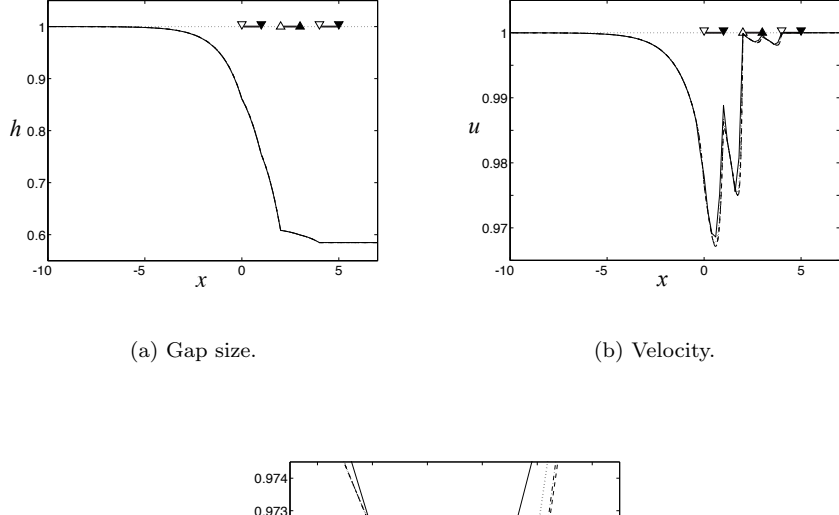
The approach presented in $\S2-3$ will now be employed to study the blade section in Figure 1. It contains three blades. A device for one-sided suction is assumed located between the two upper blades. Our model of the section is composed of three composite modules of the kind introduced in §3.4 followed by a module containing two free fabrics. The location of the blades are defined by the coordinates of their leading and trailing edges, denoted $x_{u1,2}$, $x_{m1,2}$ and $x_{d1,2}$ in Figure 1, together with the corresponding functions $f_u(x)$, $g_m(x)$ and $f_d(x)$ for their contact surfaces. The middle blade is applied to the fabric by the constant force Q, and the function $g_m(x)$ is hence only known up to a constant that is determined as described in §3.3. The fabrics extend far in the upstream and downstream directions. The information that is needed to determine the integration constants is also indicated in Figure 1, and includes the positions of the fabrics at the inlet, f_0 and g_0 , the initial drainage resistances of the fabrics, R_{10} and R_{20} , the position of the upper wire at the outlet, f_1 , and the pressure and the velocity at the outlet, p_1 and u_1 , respectively. Far downstream we always have p=0 and u=1. Unless otherwise specified, $p_{e_1}(x)=p_{e_2}(x)=0$. A comparison with results obtained by Zahrai et al. (1997) involving only a single blade will also be made.

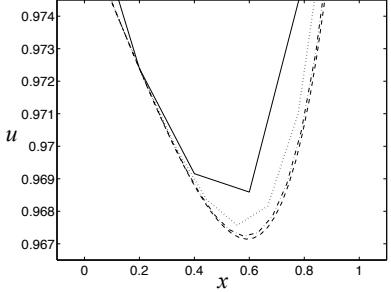
The lengthscales D and d will now be defined as the length of the blades (they are assumed to all be of the same size) and the far upstream distance between the fabrics, respectively. The spacing between the blades will be denoted δ_b , and is constant in the presented calculations. It is defined as the distance between the trailing edge of one blade and the leading edge of the next blade downstream (applied to the opposite fabric).

When applicable, the symbols ∇ and \triangle indicate the positions of the edges of blades applied to the upper and lower fabric, respectively. A filled triangle indicates that the corresponding edge is located at the interface between two modules. The blades are also indicated by solid horizontal lines between the edge symbols.

4.1. Verification

Numerical experiments were performed to verify a correct implementation of the algorithm. It was seen that the convergence rate was quadratic, in accordance with the discretisation, and that grid independence could be achieved on relatively coarse grids. An example is seen in Figure 3, where it is evident that grid independence has been achieved for a node spacing of $\Delta x = 0.025$. It happens earlier for h than for u, which is to be expected since h is an integrated quantity (the integral of the w_i), and as such rather insensitive. All the curves fall on top of each other in Figure 5.3(a). The number of nodes used to resolve a blade is a good indication of the coarseness of the grid, as the drainage pressure generated by a blade when it deflects the fabrics extend a comparable distance. The remaining results that will be presented were calculated with $\Delta x \leq 0.01$.





(c) Velocity, close-up.

FIGURE 3. Confirmation of grid independence. In all the figures: (—) $\Delta x = 0.2$, (···) $\Delta x = 0.1$, (-··) $\Delta x = 0.05$, (-··) $\Delta x = 0.025$. $We_1 = We_2 = 0.57$, $\lambda = 0.2$, $\kappa = 0.144$, Q = 0.041. $f_0 = f_1 = 1$, $g_0 = 0$, $p_1 = 0$, $u_1 = 1$, $R_{10} = R_{20} = 0.272$. $\delta_b = 1$. $f_u(x) = f_d(x) = 1$ and $g_m(x) = constant$, i.e. flat blades. Four modules with boundaries at x = -20, 1, 3, 5, 10.

Zahrai et al. (1997) performed a two-dimensional simulation of a single flat blade applied to a pair of fabrics that approach and leave parallelly at prescribed angles far upstream and downstream. The pressure distribution next to the wire in contact with the blade is reproduced in Figure 4, together with the corresponding results obtained by the presented method using two modules — one composite module and a downstream module containing two free wires. As it was found by Zahrai et al. (1997) that the pressure gradients in the z-direction are very small (supporting the conclusion in $\S 2.3$) it is justifiable to compare

the two results. Considering that our model is one-dimensional, the agreement

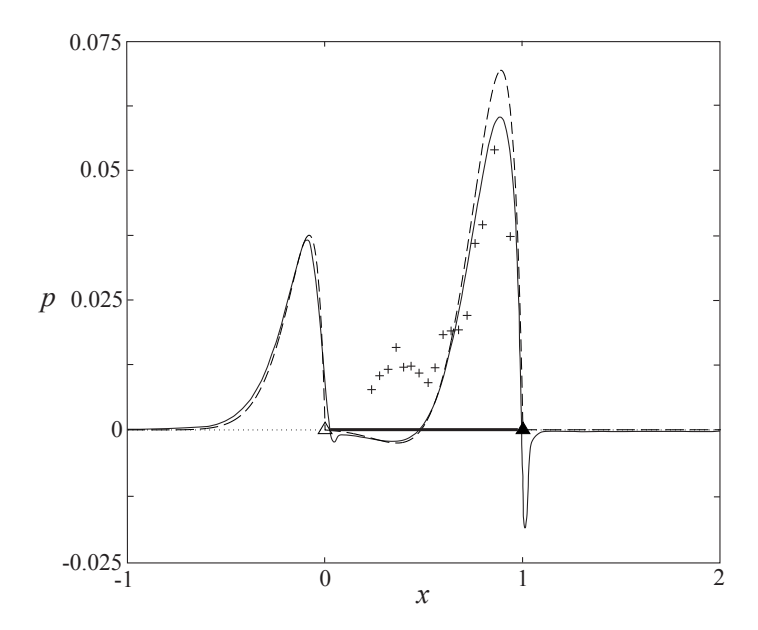


FIGURE 4. Application of a single flat blade located between x=0 and x=1. (- - -) present method using one composite module and one module containing two free fabrics (boundaries at x=-4, 1, 2). (—) 2D simulation by Zahrai et al. (1997). $We_1=We_2=4$, $\lambda=0.06$, $\kappa=0$. Far upstream: $R_1=R_2=0.093$, $\mathrm{d}f/\mathrm{d}x=\mathrm{d}g/\mathrm{d}x=0.583$. Far downstream: p=0, u=1, $\mathrm{d}f/\mathrm{d}x=\mathrm{d}g/\mathrm{d}x=-1.17$. (+) indicate experimental measurements by Zahrai et al. (1997).

is reasonably good. The one-dimensional method slightly overestimates the pressure pulses, which is in agreement with the findings by Zahrai & Bark (1995), who undertake a comparison between linear one-dimensional and two-dimensional investigations of a single thin blade. The negative peaks in the two-dimensional simulation are due to a strong acceleration of the suspension around the sharp corners presented by the blade edges. It is not possible to capture this with a one-dimensional model. The other regions of negative pressure are due to damped stationary capillary waves forming on the fabrics if the scaled drainage resistances exceed a value determined by the We_i and λ (Zahrai & Bark 1995). These waves yield oscillations in the pressure.

4.2. Results

Figure 5 is an example of interaction between components, and illustrates the effect of applying one-sided suction on the drainage pressure generated by the

blades. In a paper machine, more than three blades are normally used. To achieve a wrap of the fabrics over the trailing edge of the third blade, and hence simulate the effects of a second loadable blade, we specified $f_d(x) = 0.78$. The external pressure functions are identically zero, except in between the upper blades, where we have $p_{e1} = p_v$. The other parameters defining the simulation are given in the caption of Figure 5. Note in the figure how the pressure pulses

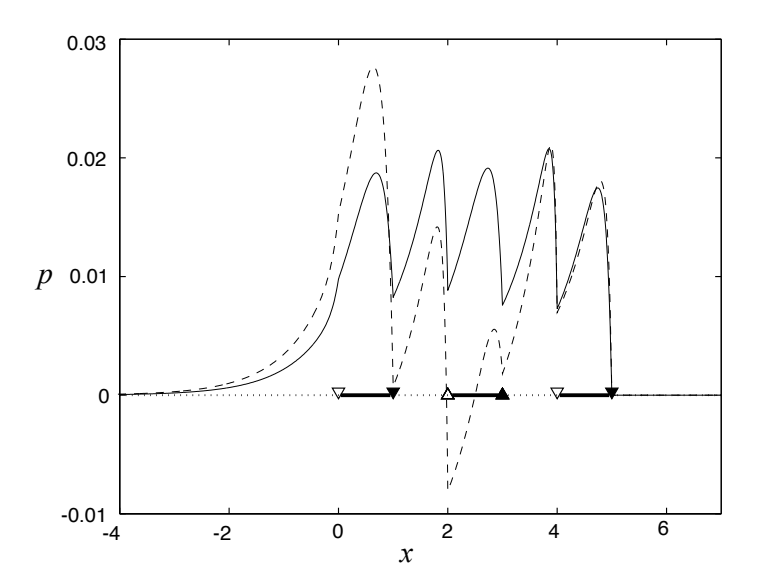


FIGURE 5. The effect on the pressure distribution of one-sided suction. (—) $p_v = 0$, (- - -) $p_v = -0.016$. $We_1 = We_2 = 0.795$, $\lambda = 0.143$, $\kappa = 0.103$, Q = 0.036. $f_0 = f_1 = 1$, $g_0 = 0$, $p_1 = 0$, $u_1 = 1$, $R_{10} = R_{20} = 0.194$. $\delta_b = 1$. $f_u(x) = 1$, $f_d(x) = 0.78$ and $g_m(x) = constant$, i.e. flat blades. Four modules with boundaries at x = -14.4, 1, 3, 5, 7.14.

are not independent, but merge with each other. The most interesting feature is however that the pressure pulses generated by the blade facing the suction box are significantly reduced as a consequence of the suction. When suction is applied, the drainage through the upper fabric increases and it is pulled towards the suction side. As a consequence, the flow does not experience such a severe constriction from the opposed blade, and the pressures pulses become of less amplitude.

At the upstream blade in figure 5, the contributions to the pressure from the two blade edges have merged to a single pulse. It is amplified when suction is applied, as a larger wrap over the trailing edge is then achieved. Due to the vertical position of the downstream blade, the relative change of the wrap at that blade is much smaller, and the corresponding change in the pressure is hardly visible.

The pressure ditributions in figure 6 correspond to blades with different (constant) radii of curvature, ϱ , scaled by D. The circular blades are symmetric with respect to an axis normal to the blade surface at the midpoint of the blades, which is hence an extremum of the function defining the blade surface. The vertical position of these extrema is 1 for the two upper blades, which is also the position of the corresponding flat blades. Although the curvature of the blades are small (the surfaces of the blades protrude a distance $1/(8\lambda\varrho) + O(\lambda^{-1}\varrho^{-3})$ expressed as a fraction of d), there is clearly an influence on the pressure. Note that, in the case of flat blades, there is no increase in p downstream of the leading edge of the last blade. Zhao & Kerekes (1995) found that a linear solution to the one-dimensional problem yields p=0 downstream of a deflection of the fabrics. This result carries over to the nonlinear case, which is seen if that solution is sought as an infinite series of subsequent linearisations. As there are no further deflections of the fabrics downstream of the leading edge of the third flat blade, p=0 in that region. The simulations reveal that none of the curved blades are in contact with the fabrics along their full length. The downstream half of the last blade is never in contact with the fabric, which is natural since the outlet of the model domain is at the same vertical position as the lowest point of the third blade. As for the middle blade, 46% and 31%of the downstream half is in contact with the wire when ρ is 71.4 and 42.9, respectively. The upstream halves of the first and the last blades are not in complete contact with the fabrics either. Evidence of the partial contact is seen in figure 6 where the slope of the pressure curves change discontinuously at positions other than at blade edges.

The sigificance of blade curvature is probably most strongly related to the effects on the pressure gradients, as these are believed to influence the distribution of fibres in the webs. The gradients are plotted in figure 7 for the different radii of curvature in figure 6. It is seen that the negative peaks, which correspond to strong accelerating forces and elongational flow, are much reduced when curved blades are employed. At the same time, large positive peaks appear at the front of the first and the third blade, implying strong decelerating forces. They are a result of incomplete contact between the upstream part of the blade and the fabric. A pressure of large magnitude is built up along a short distance, which deflects the wire so that it makes contact with the blade surface tangentially.

In order to investigate the magnitude of nonlinear effects, a first order solution was also obtained for the geometry in Figure 1 by performing a regular perturbation analysis in the parameter Q. Again a modular approach was used. Although the modules could in principle be matched analytically, thus yielding a fully analytical solution, the same iterative procedure as in the nonlinear case was performed for practical reasons. In Figure 8 we compare the linear and the nonlinear method by considering the magnitude of the pressure in front of the

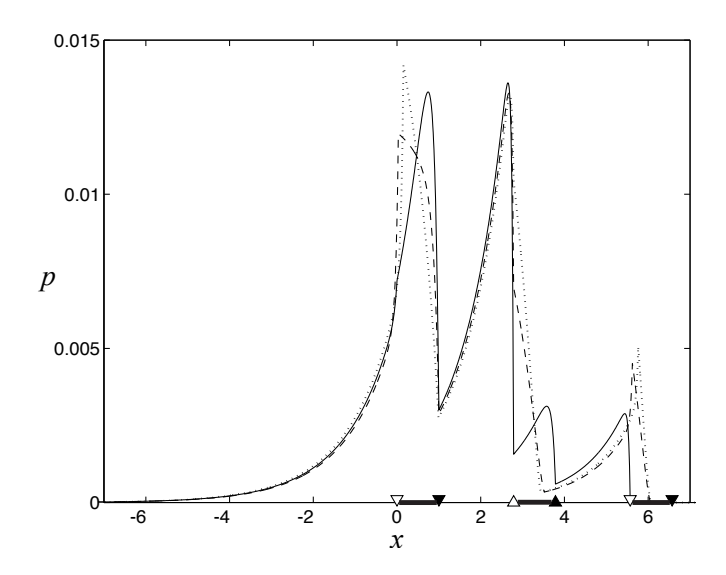


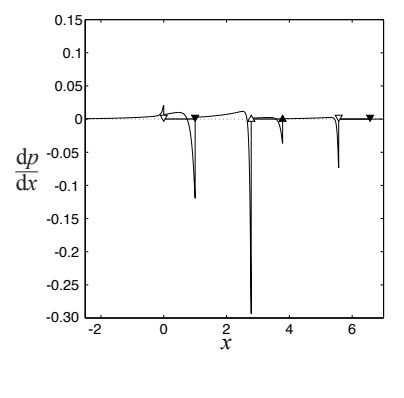
FIGURE 6. Pressure distributions for blades of different curvature. (—) Flat blades, (---) $\varrho = 71.4$, (···) $\varrho = 42.9$. $We_1 = We_2 = 0.972$, $\lambda = 0.143$, $\kappa = 0.103$, Q = 0.033. $f_0 = f_1 = 1$, $g_0 = 0$, $p_1 = 0$, $u_1 = 1$, $R_{10} = R_{20} = 0.114$. $\delta_b = 1.79$. The details of the blade vertical positions are found in §4.2. Four modules with boundaries at x = -14.3, 1, 3.79, 6.58, 20.88.

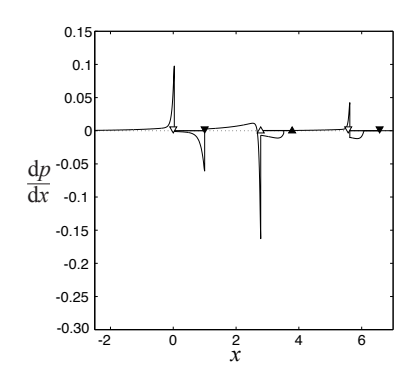
blade furthest upstream. The highest values of Q approach industrially relevant blade forces, and we see that nonlinear effects are significant if qualitative results are sought.

5. Conclusions

The division of the domain into fundamental 'building blocks', referred to as *modules*, have proved to be an effective strategy in the development of models for blade sections. By making the links between the modules as simple as possible, alterations of the geometry are easily undertaken. It was also found that features such as loadable blades and partial blade–fabric contact could be easily implemented as a consequence of the very straightforward connection of the modules.

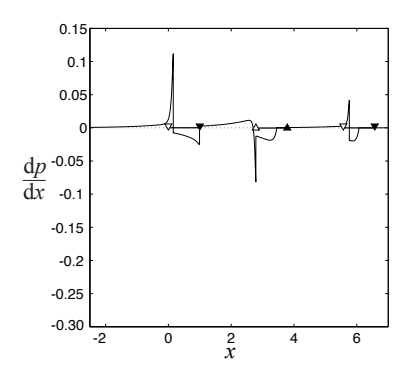
By virtue of a slenderness assumption, the governing equations could be reduced to a one-dimensional system dependent upon the distance along the direction of flow. Three relevant dimensionless parameters were identified, namely λ/We_i where λ is a slenderness ratio and the We_i (i=1,2) are analogous to Weber numbers for each fabric, and $(\alpha_s/\alpha_p)\beta$ where the ratio between the volume concentrations determines the rate of the fibre mat growth due to





(a) Flat blades.

(b) Circular blades, $\varrho = 71.4$.



(c) Circular blades, $\varrho = 42.9$.

FIGURE 7. The influence on the pressure gradients of blade curvature. Four modules. The parameters and module boundaries are the same as in the caption of figure 6.

deposition and β is an intrinsic resistace to flow through the fabrics and the webs.

A comparison with more elaborate (but less flexible) experimental and numerical investigations of a single blade, indicate that the output is sufficiently accurate to yield insight into the pressure distributions in multi-component blade sections. It was also noted that the discrepancy between the output from a linear version of the model and the nonlinear results is sufficiently large to motivate a nonlinear treatment.

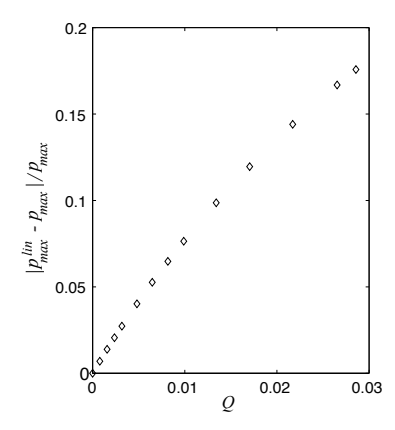


FIGURE 8. Magnitude of nonlinear effects. p_{max}^{lin} and p_{max} denote the amplitudes of the pressure peak in front of the first blade in a linear and a nonlinear calculation, respectively. $We_1 = We_2 = 1.25$, $\lambda = 0.143$, $\kappa = 0.343$. $f_0 = f_1 = 1$, $g_0 = 0$, $p_1 = 0$, $u_1 = 1$, $R_{10} = R_{20} = 0.114$. $\delta_b = 1.79$. $f_u(x) = f_d(x) = 1$ and $g_m(x) = constant$, i.e. flat blades. Four modules with boundaries at x = -14.3, 1, 3.79, 6.58, 10.15.

The numerical simulations presented in the paper show the influence of blade curvature on the pressure distributions. Notably, we saw that blades of modest curvature do not necessarily stay in contact with the fabric along their full length, and that this has implications on the pressure gradients. Further, it was seen how applying one-sided suction reduces the magnitude of the pressure pulses generated by the blade facing the suction device.

We conclude by observing that for the first time a method is now available for studying the interaction between the components in blade forming sections. In addition, the relative simplicity of the employed method give reason to believe that it could become a valuable tool when dealing with full scale blade sections.

6. Acknowledgements

Financial support was provided by the Swedish Agency for Innovation Systems (VINNOVA) and the industrial partners in the FaxénLaboratory.

References

Acheson, D. 1990 Elementary Fluid Dynamics. Oxford University Press.

- Dennis, J. E. 1977 Nonlinear least-squares. In The State of the Art in Numerical Analysis: Proceedings of the 2nd Conference on the State of the Art in Numerical Analysis Held at the University of York, April 12th-15th, 1976, Organized by the Institute of Mathematics and Its Applications (ed. D. A. H. Jacobs), pp. 269-312. London: Academic Press.
- GILBERT, J. R., MOLER, C. & SCHREIBER, R. 1992 Sparse matrices in MATLAB: Design and implementation. SIAM Journal on Matrix Analysis and Applications 13 (1), 333–356.
- Green, S. 2000 Modeling suction shoes in twin-wire blade forming: Results. *Journal of Pulp and Paper Science* **26** (2), 53–58.
- GREEN, S. I. 1999 Modeling suction shoes in twin-wire blade forming: Theory. TAPPI Journal 82 (9), 136–142.
- Holmqvist, C. 2002 Modelling of the pressure distributions in twin-wire blade formers. Licentiate thesis, Royal Institute of Technology (KTH), Stockholm.
- LEVENBERG, K. 1944 A method for the solution of certain problems in least squares. Quart. Appl. Math. 2, 164–168.
- MARQUARDT, D. 1963 An algorithm for least-squares estimation of nonlinear parameters. SIAM Journal on Applied Mathematics 11, 431–441.
- Moré, J. J. 1978 The Levenberg-Marquardt algorithm: Implementation and theory. In Numerical Analysis: Proceedings of the Biennial Conference held at Dundee, June 28–July 1, 1977 (ed. G. A. Watson), Lecture Notes in Mathematics, vol. 630, pp. 104–116. Berlin: Springer Verlag.
- NIGAM, M. & BARK, F. 1997 An analytical method to calculate the flow past a blade in twin-wire formers. *Tech. Rep.*. Department of Mechanics, Royal Institute of Technology (KTH), Stockholm.
- Norman, B. 1979 Principles of twin-wire forming. Svensk Papperstidning 82 (11), 330–336.
- ROSHANZAMIR, A., GREEN, S. & KEREKES, R. 2000a Two-dimensional simulation of suction shoes in gap formers. *Journal of Pulp and Paper Science* **26** (4), 158–162.
- ROSHANZAMIR, A., GREEN, S. & KREKES, R. 2000b The effect of non-darcy's law drainage on the hydrodynamics of blade gap formers. In *TAPPI Papermakers Conference and Trade Fair*, pp. 701–708.
- Roshanzamir, A., Green, S. I. & Kerekes, R. J. 1998 Two-dimensional simulation of pressure pulses in blade gap formers. *Journal of Pulp and Paper Science* **24** (11), 364–368.
- ROSHANZAMIR, A., KEREKES, R., GREEN, S. & OLLIVIER-GOOCH, C. 1999 Hydrodynamic pressure generated by doctoring in blade gap formers. In *TAPPI Engineering/Process and Product Quality Conference & Trade Fair*, pp. 1181–1189.
- SIMS, D. 1985 Twin wire forming developments. In *TAPPI Twin Wire Seminar*, pp. 43–51.
- Zahrai, S. & Bark, F. 1995 On the fluid mechanics of twin wire blade forming in paper machines. *Nordic Pulp and Paper Research Journal* **10** (4), 245–252.
- Zahrai, S. & Bark, F. 1996 Analytical and numerical approaches to solve the model equations for the flow of pulp in blade forming process. *AIChE Symposium Series* **92** (311), 68–73.

Zahrai, S., Bark, F. & Norman, B. 1997 An analysis of blade dewatering in a twin-wire paper machine. *Journal of Pulp and Paper Science* 23 (9), 452–459.
 Zhao, R. & Kerekes, R. 1995 Pressure distribution between forming fabrics in blade

gap formers: Thin blades. Journal of Pulp and Paper Science 21 (3), 97–103.

Paper 2

2

Analysis of a model for twin-wire forming

By Galina Shugai, Claes Holmqvist and Michael Vynnycky

FaxénLaboratoriet, Royal Institute of Technology, 100 44 Stockholm, Sweden

Published in Proceedings of the 12th ECMI Conference

A model for the dewatering of pulp suspension in the twin-blade forming papermaking process is formulated and analysed. The slenderness of the geometry permits reduction to a one-dimensional problem, which can be rewritten in the form of a highly non-linear second-order ODE. Analysis of its asymptotic structure up- and downstream indicates a strategy for computing solutions numerically. Subsequent results indicate that at industrially realistic suction pressures, the pressure within the pulp suspension will be lower than the surrounding ambient pressure, suggesting model breakdown as air is entrained.

1. Introduction

Twin-wire blade forming is a papermaking process in which a fibre-water suspension is forced into a gap between two moving permeable wires (fabrics) under tension (see Fig. 1). The fabrics are passed through a series of blades which deflect the fabrics locally, thereby inducing pressure pulses that result in the dewatering of the suspension, as well as the build-up of a fibre mat on the fabrics. Dewatering is favoured by a large pressure gradient across each wire and fibre mat, directed into the region between the fabrics, and attempts are often made to lower the ambient pressure on the outer side of a fabric by applying a so-called suction shoe between the blades; typically, however, more dewatering occurs at the suction side of the sheet, creating non-uniformities in the cross-section of the finished product.

In recent years, several papers (e.g. Zahrai 1997; Roshanzamir et al. 1998; Green 2000; Roshanzamir et al. 2000) have dealt theoretically with various aspects of the twin-forming process. In this paper, we concentrate on the mathematical aspects of those models, as well as the possibility that, under certain operating conditions, the pressure outside one of the wires is higher than that between the wires. Consequently, air exterior to the wire can be sucked into the suspension, causing a void to form inside the fibre mat. For this study, we consider the simplest geometrical configuration, namely the 3-blade system shown in Fig. 1.

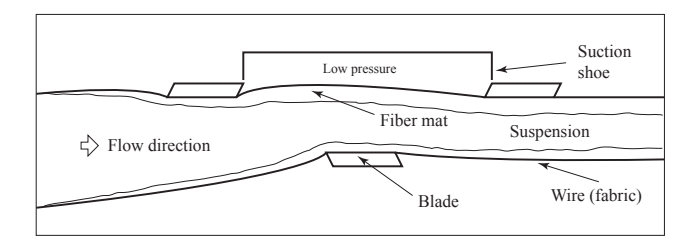


Figure 1. Schematic of blade-dewatering

2. Modelling assumptions and equations

The assumptions used in the present paper are similar to those in earlier studies e.g. Zahrai (1997) and Green (2000). A steady state 2D model is considered, with the fabrics being modelled as elastic membranes that are initially stretched at constant tensions, T_f and T_g , and which both move with constant speed from left to right. The thickness of each fabric is assumed to be negligible, and the flow though the fabrics is described by Darcy's law; in addition, the location of each fabric is a priori unknown and must be found as part of the solution. Far upstream of the blades, the fabric velocities are assumed to be equal to that of the suspension, which itself is taken to be a Newtonian fluid with constant viscosity. The problem is formulated in terms of point forces that act on the fabric only at the blade edges, and the pressure at the suction shoe, which occupies the interval between the first and third blade (see Figure 1).

Typically (see Table 1 further down), the gap between the fabrics is much smaller than the length scale along along the fabric. Using this assumption, the full 2D model equations, consisting of mass and momentum conservation for the pulp, as well as force balances for each of the fabrics, can be simplified to a system of ordinary differential equations for the dimensionless quantities P, U, R_f, R_g, f and g (respectively, the pressure, the horizontal velocity, the drainage resistances of the upper and lower mats (laws for which have been obtained previously, Green 2000) and the positions of the upper and lower wires) as a function of the coordinate in the horizontal direction, X. These are

$$P' + UU' = 0, (1)$$

$$(U(f-g))' = -\left(\frac{1}{R_f} + \frac{1}{R_g}\right)P + \frac{P_s m(X)}{R_f},$$
 (2)

$$R_g' = \kappa \left(\frac{P}{R_g}\right),\tag{3}$$

$$R_f' = \kappa \left(\frac{P - P_s m(X)}{R_f} \right), \tag{4}$$

$$0 = P - P_s m(X) + \varepsilon_f f'' - Q_{-1} \delta(X+1) - Q_1 \delta(X-1), \quad (5)$$

$$0 = P - \varepsilon_g g'' - Q_0 \delta(X), \qquad (6)$$

U_0	fabric velocity	$25 \mathrm{ms}^{-1}$
ho	pulp density	$10^3 \; {\rm kgm}^{-3}$
L	distance between blades	$0.025 \mathrm{\ m}$
h_0	initial distance between wires	$0.002 \mathrm{\ m}$
Q_{-L}, Q_g, Q_L	force per unit width at blades	$300\mathrm{Nm}^{-1}$
$R_{f0}^{\dim}, R_{q0}^{\dim}$	initial drainage resistance	$3.4\times10^4\mathrm{Nsm}^{-3}$
p_{atm}	atmospheric pressure	10^5 Pa
p_s	suction pressure	10^4 Pa
K	(see below)	$9 \times 10^6 \mathrm{Pam}^{-2} \mathrm{s}$

Table 1. Physical quantities used in the model

where m(X) = H(X+1) - H(X-1), H(X) is the Heaviside function and δ is the Dirac delta function. Equations (1)-(6) are subject to the boundary conditions

$$U(-\infty) = 1, R_g(-\infty) = R_{g0}, R_f(-\infty) = R_{f0}, f(-\infty) - g(-\infty) = 1.$$
 (7)

Note that there are no explicit boundary conditions as $X \to \infty$, although we would expect on physical grounds that all variables should be finite there. Formally, these equations constitute the leading order inviscid core flow, which is coupled to a free boundary problem for the location of the fabrics; the details of the viscous boundary layer on each fabric can be worked out afterwards if necessary, although this is beyond the scope here.

The dimensionless parameters in equations (1)-(7) above are: P_s , κ , ε_f , ε_g , Q_{-1} , Q_0 , Q_1 , R_{f0} , R_{g0} . These are related to the physical quantities U_0 , ρ , L, h_0 , Q_{-L} , Q_g , Q_L , R_{f0}^{dim} , R_{g0}^{dim} , T_f , T_g , p_s , K (for their physical meaning and numerical values, see Table 1) by

$$\begin{split} \varepsilon_f &= \frac{T_f h_0}{\rho U_0^2 L^2}, \ \varepsilon_g = \frac{T_g h_0}{\rho U_0^2 L^2}, \ Q_{-1} = \frac{Q_{-L}}{\rho U_0^2}, \ Q_0 = \frac{Q_g}{\rho U_0^2}, \ Q_1 = \frac{Q_L}{\rho U_0^2}, \\ P_s &= \frac{p_s - p_{atm}}{\rho U_0^2}, \ \kappa = \frac{K h_0^2}{\rho U_0 L}, \ R_{f0} = \frac{R_{f0}^{\dim} h_0}{\rho U_0 L}, \ R_{g0} = \frac{R_{g0}^{\dim} h_0}{\rho U_0 L}. \end{split}$$

Note here that K is a constant that depends on headbox consistency, fibre furnish and the ability of the forming fabric to retain fines (see Green 2000). Typical values for the dimensionless parameters are then

$$\varepsilon_f, \varepsilon_g \sim 0.04; \ Q_{-1}, Q_0, Q_1 \sim 0.02; \ P_s \sim -0.016; \ \kappa \sim 0.06; \ R_{f0}, R_{g0} \sim 0.1.$$

3. Analysis

The above system of equations can be reduced to just a second-order system of ODES for R_g and the distance between the two fabrics, h := f - g. For the

case when $\varepsilon_f = \varepsilon_g \equiv \varepsilon$, we have

$$2\frac{R_g R_g'}{\kappa} + \left\{ \frac{1 - \frac{\left(R_{f0}^2 + R_g^2 - R_{g0}^2 - 2\kappa P_s[(X+1)H(X+1) - (X-1)H(X-1)]\right)^{\frac{1}{2}}}{\kappa} - \frac{R_g - R_{g0}}{\kappa}}{h} \right\}^2 = 1, (8)$$

$$\varepsilon h' + \frac{R_g^2 - R_{g0}^2}{\kappa} - Q_{-1}H(X+1) - Q_1H(X+1) - Q_0H(X)$$
$$-P_s\left[(X+1)H(X+1) - (X-1)H(X-1) \right] = 0, \tag{9}$$

subject to $h(-\infty) = 1$, $R_g(-\infty) = R_{g0}$. Once these are solved, the remaining dependent variables can be obtained as

$$R_f = \left\{ R_g^2 + R_{f0}^2 - R_{g0}^2 + 2\kappa P_s \left[(X+1) H (X+1) - (X-1) H (X-1) \right] \right\}^{\frac{1}{2}},$$

$$U = \frac{1}{h} \left\{ 1 - \frac{R_f - R_{f0}}{\kappa} - \frac{R_g - R_{g0}}{\kappa} \right\}, P = \frac{1}{2} \left(1 - U^2 \right).$$

One might be tempted at this point to proceed to a numerical solution of the initial value problem for $-\infty < X < \infty$ given by (8) and (9). First, however, it is prudent to examine the asymptotic behaviour of h in these equations as $X \to \pm \infty$. As $X \to -\infty$, we have that $h \sim 1 + \hat{h}$, where

$$\hat{h} \sim \exp\left(\left\{\frac{1}{2}\left[\frac{1}{R_{g0}} + \frac{1}{R_{f0}}\right] \pm \sqrt{\frac{1}{4}\left[\frac{1}{R_{g0}} + \frac{1}{R_{f0}}\right]^2 - \frac{2}{\varepsilon}}\right\}X\right)$$
 (10)

If $\left[\frac{1}{R_{g0}} + \frac{1}{R_{f0}}\right]^2 > \frac{8}{\varepsilon}$, both exponents are positive and the solution decays. If $\left[\frac{1}{R_{g0}} + \frac{1}{R_{f0}}\right]^2 < \frac{8}{\varepsilon}$, we have oscillating decay. As $X \to +\infty$, we have $h \sim h_{\infty} + \hat{h}$, where

$$\hat{h} \sim \exp\left(\left\{\frac{1}{2}\left[\frac{1}{R_{g\infty}} + \frac{1}{R_{f\infty}}\right] \pm \sqrt{\frac{1}{4}\left[\frac{1}{R_{g\infty}} + \frac{1}{R_{f\infty}}\right]^2 - \frac{2h_{\infty}}{\varepsilon}}\right\} X\right)$$
(11)

with

$$R_{g\infty} = \sqrt{R_{g0}^2 + \kappa (Q_{-1} + Q_1 + Q_0 + 2P_s)}, h_{\infty} = 1 - \frac{R_{g\infty} - R_{g0}}{\kappa} - \frac{R_{f\infty} - R_{f0}}{\kappa},$$

and $R_{f\infty} = \sqrt{R_{f0} + \kappa (Q_{-1} + Q_1 + Q_0 - 2P_s)}$. Thus, the real parts of both exponents are positive, suggesting that the only consistent asymptotic structure as $X \to \infty$ can be $h \equiv h_{\infty}$.

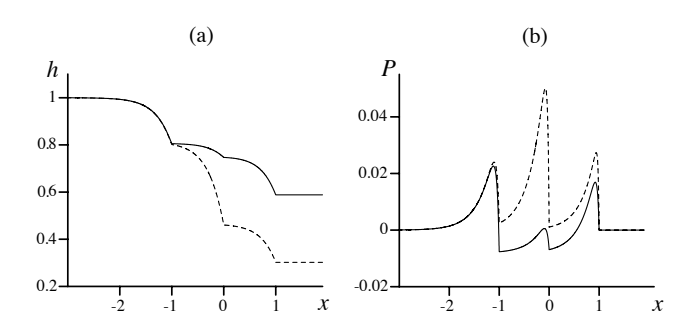


FIGURE 2. (a) Distance between the wires, h; (b) Dimensionless pressure, P

4. Numerics, results and discussion

A consequence of these findings, which we found with our own numerical experimentations, is that a conventional attempt to solve (8) and (9) as an initial value problem starting at $X=-\infty$ will fail because of the two exponential modes as $X\to +\infty$. The correct approach is to use the analysis above to solve an initial value problem starting at X=1 and to integrate backwards towards $X=-\infty$, since the presence of the two decaying modes as $X\to -\infty$ will ensure that the conditions $h(-\infty)=1$, $R_g(-\infty)=R_{g0}$ will automatically be satisfied. As for appropriate "initial" conditions at X=1, it is clear from (8) and (9) that we require $R_g(1)=R_g(\infty)$, $R'_g(1)=0$.

Two sets of results are shown in Figure 2; in both cases, the broken line indicates results when no suction pressure is applied $(P_s = 0)$, whilst the unbroken line is for when a value typically used in industry is applied $(P_s = -0.016)$. Figure 2(a) gives the h profiles, and indicates how the depth of fluid decreases as dewatering proceeds. Figure 2(b) shows the pressure distributions. In both cases, the pressure pulses associated with dewatering are evident, but for the case where $P_s = -0.016$, it becomes apparent that the pressure between the wires is actually less than the ambient atmospheric pressure, implying the entrainment of air. This constitutes model breakdown for such high suction pressures, and it is clear that a more sophisticated dewatering model will be required to account for this regime.

References

Green, S. 2000 Modeling suction shoes in twin-wire blade forming: Results. *Journal of Pulp and Paper Science* **26** (2), 53–58.

ROSHANZAMIR, A., GREEN, S. & KEREKES, R. 2000 Two-dimensional simulation of suction shoes in gap formers. *Journal of Pulp and Paper Science* **26** (4), 158–162.

- ROSHANZAMIR, A., GREEN, S. I. & KEREKES, R. J. 1998 Two-dimensional simulation of pressure pulses in blade gap formers. *Journal of Pulp and Paper Science* **24** (11), 364–368.
- Zahrai, S. 1997 On the fluid mechanics of twin-wire formers. PhD thesis, Royal Institute of Technology (KTH), Stockholm.

Paper 3

3

Fibre mat behaviour in twin-wire formers

By Claes Holmqvist and Anders Dahlkild

Department of Mechanics, KTH, SE-100 44 Stockholm, Sweden

To be submitted

A model is presented for the behaviour of the fibre mats as they experience the first pressure pulse in a blade forming section, after having been formed over a roll. The compressibility of the webs is seen to significantly reduce the velocity difference between the mat surfaces and the suspension flow towards the fabrics, and thus also the rate of deposition of new fibres onto the mats. Typically, the thickness of the mats is reduced during the blade pulse, despite the deposition. Although the fibre content of the webs increases only modestly, the drainage resistance is found to increase significantly during the passage over the blade, due to the reduced permeability in the highly compacted regions of the mats. The shear stress parallel to the fabrics varies several orders of magnitude across the thickness of the fibre networks. Assuming that the whole of the mats essentially retain the speed of the fabrics, the shear stress during a pulse representative of normal operational conditions reaches a magnitude of about 1 Pa at the free suspension sides of the fibre mats, and several hundred times that value at the fabric surfaces. This emphasizes the need to develop models that accurately incorporates network shear strength in order to quantitatively predict the deformations in the plane of the sheets.

1. Introduction

In the forming section of a twin-wire paper machine, an increased pressure is generated between the fabrics. This pressure induces a drainage of suspension through the fabrics. Fibres are deposited on the wires, and webs are formed that are initially separated by a region of suspension of low concentration and relatively high mobility. As the drainage process continues, the fibre mats will eventually occupy the entire region between the wires and the separating layer will disappear, causing the nature of the dewatering process to change from filtration to what might be referred to as thickening.

Several models have been developed to predict the pressure distribution in the forming section. Roll forming have e.g. been studied by Zahrai et al. (1998), and Dalpke et al. (2004). Zhao & Kerekes (1995) and Zahrai & Bark (1995) perform linear analytical studies of the application of a thin blade to a pair of fabrics. Nonlinear numerical studies are undertaken by, among others, Zahrai et al. (1997) and Roshanzamir et al. (2000). The effects on the pressure

distribution of the interaction between different components in the forming section are investigated by Holmqvist (2002). Common to these works, with exception for the study by Zahrai et al. (1998), is that little attention is paid to the presence of the fibre webs on the fabrics. The combined drainage resistance of the wire and the fibre mat is either assumed constant, or is assumed to increase at a rate proportional to the drainage flux. The latter alternative implies the supposition that the resistance to drainage is proportional to the quantity of fibres in the web, and that this amount in turn is proportional to the (superficial) drainage velocity. Nevertheless, good agreement is found between the calculated pressures and experimental measurements (see e.g. Zhao & Kerekes 1995; Zahrai et al. 1997). It should be noted, however, that these comparisons only involve single components, such as a single blade, and that the accumulated discrepancy could perhaps become large if a complete forming section was modelled. In order to improve the models of the forming section, it is desirable to include the effects of the fibre networks present between the fabrics in a more rigorous way. The motivation for this is not only that it will improve the predictions of the pressure and the drainage rates. As the fibre webs in the forming section will eventually become the final paper sheet, understanding how they are effected by the forming process is of paramount importance.

Models have been developed for uniaxial pressure filtration of flocculated suspensions, such as the works by Landman et al. (1991) and Landman & Russel (1993). These account for the resistance to deformation exhibited by the interconnected network of solid particles immersed in the suspending fluid, and for the effects of reduced permeability of the network as it is compacted. Martinez (1998) adapts the analysis by Landman et al. (1991) to predict the drainage rate during roll forming. Zahrai et al. (1998) employ the same concepts to derive an expression for the fibre mat thickness during roll forming, which is then used in a calculation of the pressure distribution¹. Reasonable agreement is found with experimental results. In a recent study by Lobosco (2004), a uniaxial model is presented for the dewatering of a fibre suspension network filling the gap between two forming fabrics (a situation analogous to piston-driven pressure filtration). The suspension is subjected to a time-varying load representing pressure pulses, and large concentration gradients are observed in the fibre web.

The ambition in the present article is to study the behaviour of one of the fibre mats in a twin-wire former when it is subjected to a pressure pulse induced by a blade. Like Martinez before us, we shall follow Landman *et al.* (1991) in the derivation of an equation for the deformation of the fibre web in the direction perpendicular to the fabric. No strain-rate dependent stresses are included in this direction, and the fibre network is modelled as a plastic material. In the

¹Neither Martinez nor Zahrai *et al.* present the solution for the fibre-concentration in the mat, although Martinez does calculate it.

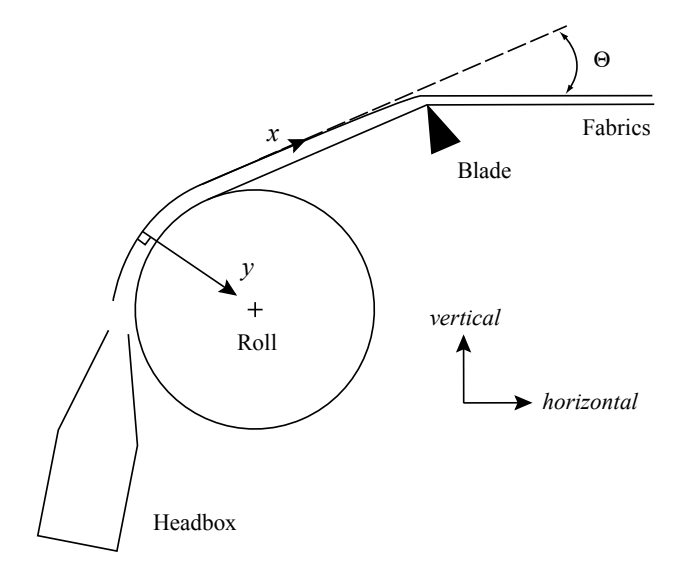


FIGURE 1. Schematic illustration of the modelled forming section. Note that the proportions are not correct.

direction parallel to the wire, the modelling assumptions result in deformationrates controlled by the viscous properties of the suspension mixture. From the numerical solution of the governing equations, we are able to draw conclusions about the influence of structural changes in the network on the resistance to drainage presented by the web. We are also able to estimate the magnitude of the shear stresses experienced by the mat as a result of the pressure pulse and the drainage flow.

2. Formulation

Consider a small twin-wire forming section, consisting of a roll followed by a single thin blade, as is illustrated in figure 1. The treatment is based on the assumption that the fibre sheets forming on the wires are separated by a layer of freely moving suspension, see figure 2. Our fibre suspension has two incompressible constituents, a particle (fibre) phase and a liquid (water) phase. It is tacitly assumed that it is meaningful to model both phases as continua.

The extent of the fibre mats is defined by stating that in the bulk of the suspension, the volume concentration of fibres, denoted ϕ , is so low that forces cannot be transmitted over longer distances by particle contacts, whereas in the mat this is possible. Note that this does not exclude the presence of fibre flocs in the free suspension. It merely says that the flocs are not to such a large degree in contact with one another that it severely hinders their ability to move relative each other. The limiting concentration is called the 'gel point', and is denoted ϕ_g . When $\phi > \phi_g$, a network of interconnected particles is present that makes a finite resistance to deformation. At any position in the network,

the stress state can be divided into an isotropic component, denoted p_d , and a deviatoric part. Even though the deviatoric stresses are not necessarily of insignificant magnitude, we shall choose to neglect them in the present paper, and only retain the 'particle pressure' p_d . Since a single scalar quantity then measures the load intensity, the constitutive model of the fibre network can be made very simple. Let us define a yield function f, that represents the strength of the material, and assume that it is only dependent on the local concentration of fibres. The following power law is adopted,

$$f(\phi) = m(\phi - \phi_q)^n \,, \tag{1}$$

where m and n are empirical constants. Notice that the network makes no resistance to deformation when $\phi = \phi_g$. Similar looking expressions have been introduced by other authors, see e.g. Martinez (1998) and Zahrai et al. (1998). Whenever $p_d < f(\phi)$, the network locally behaves like a stiff body, whereas if $p_d > f(\phi)$, the network collapses till the concentration has increased enough to yield a structure strong enough to balance the applied load. Following Buscall & White (1987), we assume the collapse to be sufficiently rapid for us to set $p_d = f(\phi)$ all through the collapse process. This is likely to be a good description if the collapse is rate-determined by the expulsion of water from in between the fibres, rather than the necessity to displace fibres in relation to each other.

The suspension in between the mats is taken to be of homogeneous concentration $\phi_0 < \phi_g$. In the mats the concentration is a function of position $\phi(y,t) \ge \phi_g$.

The problem is assumed two-dimensional and stationary in a spatially fixed natural co-ordinate system (x,y), where x is the distance travelled along the machine direction, and y is the direction normal to one of the fabrics. It is supposed that the gap between the wires is sufficiently small compared to the radius of curvature of the fabrics that the problem can be considered plane, i.e. the (x,y)-system can be treated as an ordinary Cartesian system. If λ is the ratio between the characteristic length scales parallel and transversal to the fabrics, this is equivalent to stating that $\lambda^2 \ll 1$. In what follows, we shall only study the fibre mat residing on the fabric whose suspension side by definition is located at y=0. The free suspension side of the fibre mat is found at y=H(x). This side will sometimes be referred to as the 'upper' side of the web, since it corresponds to a larger y-value.

Let u_d and u_c denote the mass-averaged interstitial velocities of the two phases², where, here and henceforth, the subscripts d and c will be used to distinguish between the dispersed fibre phase, and the continuous liquid phase, respectively. The densities of the constituents are denoted ρ_d and ρ_c . The following quantities are also defined,

$$\boldsymbol{j}_d = \phi \boldsymbol{u}_d \,, \tag{2}$$

 $^{^2}$ As the constituents are incompressible, these velocities equal the corresponding volume averaged quantities.

$$\mathbf{j}_c = (1 - \phi)\mathbf{u}_c, \tag{3}$$

$$\mathbf{j} = \mathbf{j}_d + \mathbf{j}_c \,, \tag{4}$$

91

$$\boldsymbol{u}_r = \boldsymbol{u}_d - \boldsymbol{u}_c \,, \tag{5}$$

$$\rho_s = \phi \rho_d + (1 - \phi)\rho_c \,, \tag{6}$$

$$\boldsymbol{u}_s = \frac{\rho_d \phi \boldsymbol{u}_d + (1 - \phi)\rho_c \boldsymbol{u}_c}{\rho_s}, \qquad (7)$$

where j_d and j_c are the fibre and liquid volume flux densities (i.e. the superficial velocities), j is the mixture (or suspension) volume flux density, u_r is the relative velocity between the phases, and ρ_s and u_s are the mixture density and velocity, respectively. The suspension is governed by the following equations, (see e.g. Ungarish 1993, p. 22),

$$\nabla \cdot \boldsymbol{j} = 0, \tag{8}$$

$$\nabla \cdot \boldsymbol{j_d} = 0, \tag{9}$$

$$\rho_s \boldsymbol{u}_s \cdot \nabla \boldsymbol{u}_s = -\nabla p_c - \nabla p_d + \nabla \cdot \boldsymbol{\tau}_N - \nabla \cdot \left(\phi (1 - \phi) \frac{\rho_c \rho_d}{\rho_s} \boldsymbol{u}_r \boldsymbol{u}_r \right). \tag{10}$$

The equations (8) and (9) enforces volume continuity of the mixture and the dispersed phase, respectively. Equation (10) is the momentum balance for the suspension, where p_c is the liquid pressure. Strain-rate dependent stresses are accounted for by τ_N . These will be modelled after a Newtonian pattern, and we therefore equip the suspension with an effective kinematic viscosity function

$$\nu_s(\phi) = \nu_c \left(1 + a\phi^b \right) \,. \tag{11}$$

Here, ν_c is the kinematic viscosity of the liquid phase, and a and b are empirical constants. Power law expressions for the viscosity of fibre suspensions have previously been introduced by, among others, Bennington & Kerekes (1996). The last term on the right hand side of (10) is an inertial 'diffusion stress'. To close the system we adopt the following constitutive relation for u_r ,

$$\boldsymbol{u}_r = -\frac{k(\phi)}{\mu_c} \nabla p_d \,, \tag{12}$$

where $k(\phi)$ is a permeability function, and μ_c is the dynamic viscosity of the liquid phase. Relation (12) can be derived from a two-fluid model of the suspension, in which inertia of the relative motion is neglected and the coupling between the two phases is modelled by Darcy's law. We introduce it here as a postulate, and note that the fibres and the liquid are assumed to follow each other perfectly unless this is prevented by inter-particle forces.

The formulation of equations governing the pressure build-up in the free suspension and the positions of the wires is not considered here. Our concern is only the regions closest to the fabrics (see figure 2), i.e. the regions which may be regarded as concentration and velocity boundary layers surrounding the free suspension (note that the concentration boundary layers are simply the mats). As boundary conditions at the wires, we adopt a no slip condition for the suspension flow parallel to the fabrics, and a no penetration condition for

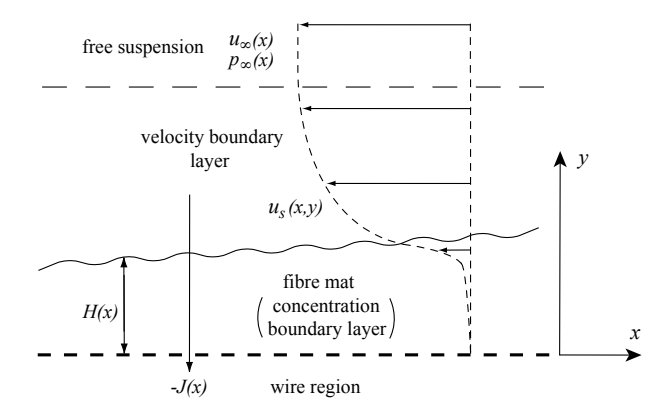


FIGURE 2. Different regions: the wire, the fibre mat, the velocity boundary layer (including the mat), and the free suspension. A schematic illustration of the horizontal velocity profile in the suspension relative the fabric is given. When drawn as in the figure, u_s is negative, which is the case when the liquid pressure $p_c > 0$. The fibre mat thickness is H(x), and the total drainage flux is J(x) (positive in the direction of increasing y-values).

the fibre velocity perpendicular to the wires. The retention is hence assumed to be perfect. Further, the liquid pressure is taken to be zero at the position of the wires. There is thus no pressure drop across the fabrics themselves, and 'blockage effects' from fibres filling the pore openings on the fabric surface are neglected. In the outer part of the boundary layers, the variables must adapt to the conditions of the free suspension. At last, inlet conditions for the boundary layers are found by considering a preformed fibre mat from an earlier stage of the forming section. Here, we assume a fibre mat emanating from a roll dewatering stage. The velocity of the suspension in the mat is supposed to equal the velocity of the free suspension at the start of the blade pressure pulse.

3. Analysis

3.1. Estimation of magnitudes

Given the value of ρ_d in table 2, it is seen from (6) that the relative difference $(\rho_s(\phi) - \rho_c)/\rho_c$ is less than 5% when $\phi < 0.25$, which is approximately the range of concentrations encountered in this study. We shall thus henceforth set $\rho_s(\phi) = \rho_c$ in all regions.

In figure 1, a pressure pulse is generated by wrapping the fabrics over the blade by a small angle θ , thus creating a constriction to which the flow must adapt. A close-up of the region around the blade is seen in figure 3. The pressure build-up is an effect of the combined finite resistance to drainage of

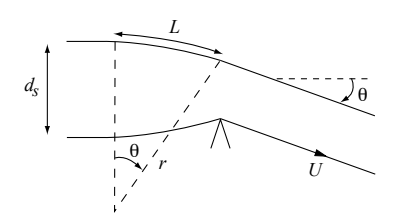


FIGURE 3. Schematic close-up of the deflection in the blade region. d_s : initial gap size, θ : wrap angle, r: radius of curvature of the fabric, L: measure of the reach of the pulse, U: machine speed.

the wires and the adhering webs, denoted R. To achieve a (superficial) drainage velocity w_0 , a pressure p_0 is needed, and

$$p_0 \sim Rw_0 \,, \tag{13}$$

where from now on we suppose that $p_c = 0$ corresponds to the surrounding atmospheric pressure. Let L denote the length in the machine direction over which the pulse acts, and the fabrics curve. Clearly, $L \sim \theta r$, where r is the radius of curvature of the fabrics. Further, the reduction of the gap size is at the blade seen to be of magnitude $\Delta h \sim \theta L$. If the liquid pass more or less unhindered through the fabric, $Lw_0 \sim \Delta hU$, providing

$$w_0 \sim \theta U$$
. (14)

Inserting the relation for w_0 into the expression (13) yields,

$$p_0 \sim \theta U R$$
. (15)

The pressure is also directly related to the curvature and the wire tension, $p_0 \sim T/r \sim T\theta/L$, and the reach of the pulse is hence

$$L \sim \frac{T}{UR} \,, \tag{16}$$

which yields the reduction of the gap size

$$\Delta h \sim \frac{\theta T}{UR}$$
. (17)

The rate of change of momentum perpendicular to the upstream path of the fabrics (neglecting drainage) is $\rho_c d_s U^2 \theta$, where d_s denotes the distance between the fabrics upstream of the pulse. The pressure gradient deflecting the suspension gives therefore rise to a pressure difference across the gap between the fabrics that is roughly $\rho_c U^2 \theta d_s / L$, which is normally significantly less than the pressure p_0 given by (15) (cf. tables 1 and 2 for typical parameter values). The pressure can therefore be considered as roughly constant in the suspension between the fabrics/webs, and both wires have approximately the same curvature.

The rate of change of horizontal momentum, as the suspension is slowed down by the increasing pressure, provides the magnitude of the relative velocity in the x-direction between the suspension and the fabrics during the pressure pulse,

$$u_0 \sim \frac{p_0}{\rho_c U} \sim \frac{\theta R}{\rho_c} \sim \frac{R}{\rho_c U} w_0 \,.$$
 (18)

Now, let v_0 denote the magnitude of the velocity in the direction perpendicular to the fabrics. Note that this velocity does not necessarily equal the drainage velocity. Continuity requires that $u_0/L \sim v_0/d_s$. Together with (16) and (18), this implies

$$v_0 \sim \Lambda w_0 \sim \Lambda \theta U$$
 where $\Lambda = \frac{2R^2 d_s}{\rho_c T}$. (19)

From (15) it is clear that a small resistance R has a damping effect on the pulse. Actually, Zhao & Kerekes (1995) show that $\Lambda \leq 1$ is required for the damping to be sufficiently strong to avoid oscillating solutions³. Above, we assumed the liquid to pass easily through the wires, and consequently Λ to be small. However, the solution by Zhao & Kerekes indicates that (15), and by consequence the rest of the analysis, holds for $\Lambda \lesssim 1$. Typically, $\Lambda \sim 1$ (cf. tables 1 and 2). Further, the pulse can be regarded as a damped capillary wave, and the effects of the blade are thus only seen upstream of the blade. Downstream, $p_c = 0$, and the fabrics run in parallel. It follows that (17) provides an indication of the total reduction of the gap size due to the pulse.

We conclude by commenting that it is straightforward to show that $1/\theta$ is actually analogous to a Weber number, expressing the ratio between the flux of momentum between the fabrics, and the pressure due to the wire-tension and curvature, acting over a distance L.

3.2. Equations for the free suspension

In the free suspension occupying the region between the webs there are, by definition, no inter-particle stresses, and hence $u_r = 0$. Decompose the mixture velocity in this region according to

$$\mathbf{u}_s = (U + u_\infty)\mathbf{e}_x + v_\infty\mathbf{e}_y. \tag{20}$$

In Appendix A it is demonstrated that, in the x-direction, the momentum balance in the bulk of the suspension turns into

$$U\frac{\mathrm{d}u_{\infty}}{\mathrm{d}x} = -\frac{1}{\rho_c}\frac{\mathrm{d}p_{\infty}}{\mathrm{d}x}.$$
 (21)

The bulk flow is hence inviscid, but adjacent to the mats, there are velocity boundary layers of thickness L/\sqrt{Re} , the Reynolds number being defined as

$$Re = \frac{LU}{\nu_0} \,, \tag{22}$$

where $\nu_0 = \nu_s(\phi_0)$. From the point of view of the boundary layers, the pressure pulse $p_{\infty}(x)$, and thereby $u_{\infty}(x)$, may be regarded as prescribed functions,

 $^{^{3}}$ In the analysis, R is constant.

whereas the magnitude of v_{∞} immediately outside of the velocity boundary layer will follow as part of the analysis of the layers.

3.3. Equations for the boundary layers

Conservation of the suspension mixture as a whole is expressed by (8). In the boundary layer, we shall suppose that it simplifies to (see appendix B.1)

$$\frac{\partial j^y}{\partial u} = 0, (23)$$

since the velocity component along the wire deviates only weakly from the constant speed U of the fabrics. The validity of (23) is somewhat tenuous, since it depends on the fibre mat being much thinner than the gap between the wires (alternatively $\Lambda \ll 1$), but it will be accepted in the present study as it greatly facilitates the treatment.

Based on the estimates in section 3.1, conservation of the dispersed phase, equation (9), yields the governing equation for the compaction of the fibre mats (see appendix B.2)

$$U\frac{\partial \phi}{\partial x} + j^y \frac{\partial \phi}{\partial y} = \frac{\partial}{\partial y} \left(\phi (1 - \phi) \frac{k(\phi)}{\mu_c} \frac{\partial p_d}{\partial y} \right) , \qquad (24)$$

where according to (23), the mixture flux perpendicular to the fabrics is only a function of the position in the machine direction, i.e.

$$j^y = J(x). (25)$$

The terms on the left hand side of (24) represents, in turn, convection of fibres in the x-direction, due to the motion of the fabrics, and convection towards the wire as fibres are entrained by the mixture flux in that direction. On the right hand side, there is a diffusive term, corresponding to the relative transport of fibres due to gradients in the inter-particle pressure. We shall suppose that this pressure always equals the yield pressure of the network,

$$p_d = f(\phi) \,, \tag{26}$$

which according to the discussion in section 2 is reasonable only if there is no position in the fibre network where the load is relaxed. The consequences of relation (26) are further discussed in section 4.

Now define a 'diffusivity function',

$$D(\phi) = \phi(1 - \phi) \frac{k(\phi)}{\mu_c} f'(\phi), \qquad (27)$$

so that (24) can be written

$$U\frac{\partial\phi}{\partial x} + J(x)\frac{\partial\phi}{\partial y} = \frac{\partial}{\partial y}\left(D(\phi)\frac{\partial\phi}{\partial y}\right). \tag{28}$$

The permeability $k(\phi)$ is assumed given by the modified form of the Kozeny-Carman equation that is introduced for low concentration fibre mats by Ingmanson *et al.* (1959),

$$k(\phi) = \frac{1}{3.5S_0^2 \phi^{1.5}},\tag{29}$$

in which S_0 is the specific surface of the fibres.

Introduce the mixture velocity components u_s and v_s relative the fabrics such that

$$\mathbf{u}_s = (U + u_s)\mathbf{e}_x + v_s\mathbf{e}_y. \tag{30}$$

They are of sizes u_0 and w_0 , respectively, and, according to (14) and (18), thus much smaller than U.

The momentum balance (10) is in appendix B.3 shown to reduce to the following in the y-direction,

$$0 = \frac{\partial p_c}{\partial y} + \frac{\partial p_d}{\partial y} \,. \tag{31}$$

Inertial and strain-rate dependent effects are hence negligible, and there is a balance between liquid pressure and inter-particle forces. Equation (31) is a manifestation of Terzaghi's effective stress principle (Terzaghi 1943), which, in order to be valid, requires the particle-particle and particle-surface contacts to be point-like (Kataja et al. 1995).

Parallel to the fabrics, both inertia and strain-rate dependent forces take part in the balance. In appendix B.3 it is seen that, in the velocity boundary layer, the significant terms of (10) in that direction are

$$U\frac{\partial u_s}{\partial x} + v_s \frac{\partial u_s}{\partial y} = -\frac{1}{\rho_c} \frac{\partial p_c}{\partial x} - \frac{1}{\rho_c} \frac{\partial p_d}{\partial x} + \frac{\partial}{\partial y} \left(\nu_s(\phi) \frac{\partial u_s}{\partial y} \right). \tag{32}$$

3.4. Connecting the regions

The mixture flux density is related to the mass-averaged suspension velocity through

$$\mathbf{j} = \mathbf{u}_s - \phi(1 - \phi) \frac{\rho_d - \rho_c}{\rho_s} \mathbf{u}_r.$$
 (33)

Since in the free suspension $u_r = 0$, we there have $v_s = j^y$. This is not strictly true in the fibre mat, but we adopt this approximation which holds if the relative density difference between the phases is neglected, and thus $v_s = J(x)$ in the boundary layers. Integration of (31) yields

$$p_c + p_d = p_{\infty}(x). (34)$$

Further, introduce the measure $\Delta u_s(x, y)$, expressing the velocity deficit (parallel to the fabrics) with respect to the bulk velocity in the suspension velocity boundary layer,

$$[\boldsymbol{u}_s \cdot \boldsymbol{e}_x]_{\text{bl}} = U + u_s = U + u_{\infty}(x) + \Delta u_s.$$
 (35)

Thus, if $\Delta u_s = 0$, the velocity component parallel to the fabrics equals the velocity in the free suspension, whereas if $\Delta u_s = -u_\infty(x)$, the velocity equals

that of the fabrics. Now, by using (34) in (32), and then inserting (35), we obtain the equation

$$U\frac{\partial \Delta u_s}{\partial x} + J(x)\frac{\partial \Delta u_s}{\partial y} = \frac{\partial}{\partial y} \left(\nu_s(\phi) \frac{\partial \Delta u_s}{\partial y} \right) , \qquad (36)$$

where (21) have been used to eliminate the pressure gradient.

At this point, two similar equations are available for the compaction normal to the fabrics and the displacements parallel to the fabrics, i.e. (28) and (36). We shall now determine expressions for the flux J(x) and the mat height H(x). By using the definitions (2)–(5), and the postulate (12), the fibre phase velocity perpendicular to the fabrics can be expressed as

$$v_d = J(x) - (1 - \phi) \frac{k(\phi)}{\mu_c} \frac{\partial p_d}{\partial y}.$$
 (37)

Since all fibres are retained by the wires, $v_d = 0$ at y = 0. Using (26) and (27), the mixture flux is thus seen to be given by

$$J(x) = \left[\frac{D(\phi)}{\phi} \frac{\partial \phi}{\partial y}\right]_{y=0}.$$
 (38)

The volume of fibres per unit area in the cross machine direction of the forming section is

$$q(x) = \int_0^{H(x)} \phi \, \mathrm{d}y. \tag{39}$$

By considering a control volume around a segment of the fibre mat it is easy to derive an expression for the rate of change of q due to transport of fibres from the free suspension into the fibre mat,

$$U\frac{\mathrm{d}q}{\mathrm{d}x} = -\phi_0 \left(J(x) - U\frac{\mathrm{d}H}{\mathrm{d}x} \right). \tag{40}$$

Note that the build-up of fibres in the mat is affected by the evolution of the mat thickness along the machine direction. It is the difference between the drainage flux and the rate of displacement of the top of the mat that determines the amount of deposited fibres. A relation similar to (38), linking dH/dx to the concentration gradient at y = H(x), can be obtained by differentiating (39), evaluating the integral in the resulting expression with the help of (28), and then combining the obtained expression with (40). We prefer, however, to obtain the fibre mat thickness from the integral equation obtained by direct integration of (40),

$$H(x) = H(x_0) + \frac{1}{\phi_0} \int_{H(x_0)}^{H(x)} \phi \, dy + \frac{1}{U} \int_{x_0}^x J \, dx', \qquad (41)$$

which is solved simultaneously with the differential equations. The position $x = x_0$ is the upstream end of the solution domain, where a finite fibre mat is already present. It should be observed that the dependence upon x in the differential equations (28) and (36) only enters as a result of the convection

along the fabrics with speed U. The problem is thus parabolic, and 'initial conditions' must be specified at $x = x_0$.

3.5. Initial and boundary conditions

We shall now formulate the explicit boundary and initial conditions necessary to solve the governing equations. Since $p_c = 0$ at the fabrics, relation (34) provides the following boundary condition

$$\phi = \phi_w(x) = f^{-1}(p_\infty(x))$$
 at $y = 0$. (42)

At y = H(x), the liquid pressure is $p_{\infty}(x)$. By considering the balance (34) we conclude that the top of the network never carries any load. Hence,

$$\phi = \phi_q \quad \text{at} \quad y = H(x).$$
(43)

This remains true regardless of the strength of the drainage flux J(x), as long as there is a region of suspension of concentration ϕ_0 lower than the gel concentration outside of the mat. The only possible way to transmit load to the fibre mat is through inter-phase drag. The transferred load is hence monotonously increasing as the fabric is approached, starting from zero at the top of the mat.

For the velocity Δu_s , we have the conditions

$$\Delta u_s = -u_{\infty}(x) \quad \text{at} \quad y = 0, \tag{44}$$

$$\Delta u_s \to 0 \quad \text{as} \quad y \to \infty \,.$$
 (45)

In addition, at y = H(x), continuous shear stress and velocity must be ensured. Hence, as the concentration is discontinuous across y = H(x), and consequently also the effective dynamic viscosity $\nu_s(\phi)/\rho_c$, there will be a discontinuity in the velocity gradient at that position.

An initial concentration profile $\phi(x_0,y)$ is needed at the start of the pressure pulse. For this purpose, let us assume that the drainage pressure is constant in the roll section, and consider what kind of fibre mats are built up as the fabrics pass that part of the machine. It is found by Zahrai et al. (1998), that $H(x) \sim \sqrt{x}$ during constant pressure roll forming of a suspension of constant concentration (through perfectly permeable fabrics). Further, the authors show that the fibre concentration profiles are self-similar, $\phi(y/H(x))$, although the similarity solution itself is not given. Even if it is a straightforward task to obtain the similarity solution for the roll forming part numerically, we choose a different approach enabling an analytical solution.

In a special situation, there exists an asymptotic solution to equation (28) as $x \to \infty$. Suppose that we let a suspension of concentration $\phi_0 < \phi_g$ be filtered by a constant pressure p_{∞} . Assume further that the mixture only contains a certain amount of fibres per unit length of the wire, and that when these have all been deposited, only clear liquid flows through the mat. Asymptotically, the web will cease to compact, and the state would appear steady when travelling with the fabrics (i.e. there is no dependence on the position

x). Since then $v_d = 0$ in the mat, we obtain a separable differential equation for $\phi(y)$ by inserting (26) into (37). Integrating it in the y-direction reveals,

$$-yJ = \int_{\phi_m}^{\phi(y)} \frac{D(\phi)}{\phi} d\phi, \qquad (46)$$

where J is now constant. Evaluating (46) at y = H, and combining the result with the same relation, we find an equation for the asymptotic concentration profile as a function of y/H,

$$\frac{y}{H} \int_{\phi_w}^{\phi_g} \frac{D(\phi)}{\phi} d\phi = \int_{\phi_w}^{\phi(y/H)} \frac{D(\phi)}{\phi} d\phi.$$
 (47)

As $D(\phi)$ is known, we can for every choice of y/H calculate $\phi(y/H)$. The drainage pressure influences the shape of the profile through ϕ_w . The constant mat thickness H is determined by the amount of fibres contained in the web. Alternatively, H can be chosen at will, and the necessary amount of fibres needed to achieve that thickness can be calculated. Again using (37), this time after having replaced the particle pressure by the liquid pressure via expression (31), the asymptotic flux through the mat follows from an integration across the mat,

$$J = -p_{\infty} / \int_0^H \frac{\mu_c}{(1 - \phi)k(\phi)} dy.$$
 (48)

Note that, for a given drainage pressure, the concentration profiles for different H are of the same shape when plotted versus y/H. This is analogous to the similarity solution for the constant pressure roll forming case discussed above, where the profiles at different positions x are of the same shape when plotted versus y/H(x). The total amount of fibres per unit length for the asymptotic case of thickness H would then correspond to the amount of fibres accumulated up to a certain position x in the roll forming case in a mat of the same thickness. To investigate this analysis closer, (28) was solved for constant drainage pressures p_{∞} , using a thin incipient fibre mat as initial condition. It was clearly seen that the solutions became self-similar downstream. Further, it was noted that the shape of the similarity solution was very close to the asymptotic profile. Therefore, due to the simplicity of the analytical solution (47), asymptotic profiles of suitable thickness $H(x_0)$ was used as initial condition $\phi(x_0, y)$.

The initial condition for the velocity is simply $\Delta u_s(x_0, y) = 0$.

4. Results

4.1. About the simulations

As pointed out in section 2, we are not concerned with the details of the pressure build-up in the free suspension. Instead, the analytical solution presented by Zhao & Kerekes (1995) for the drainage pressure generated by a pair of fabrics deflected over a blade will be used to obtain $p_{\infty}(x)$ and $u_{\infty}(x)$. The theory assumes the blade to be thin, i.e. without extension in the machine direction,

and a constant drainage resistance R. We have used the resistance of the initial mat at $x = x_0$, which equals the integral in (48) evaluated for the initial concentration distribution. Obviously, the resistance is expected to increase in the machine direction, as the fabrics pass over the blade, and equations (15) and (16) indicate that the effect will be a pressure pulse of larger magnitude, but of shorter reach. This is in accordance with results in the literature (see e.g. Green & Kerekes 1998). Since for our purposes we only need a qualitatively correct solution for the free suspension, we disregard the influence of factors not accounted for in the analytical solution.

When the constitutive relation (26) was introduced, it was observed that its validity requires the loads in the network not to relax at any position. From the condition that the liquid pressure is zero at the wire surface, and equation (34), follows that a relaxation will occur at the fabric if $p_{\infty}(x)$ is not monotonically increasing in the machine direction. If $p_{\infty}(x)$ decreases, a stiff region appears next to the wire, in which the inter-particle stresses cannot be found directly from the concentration. In order not to violate the load restriction, we shall neglect the initial part of the blade pulses obtained from the theory by Zhao & Kerekes, and assume that the pulse immediately starts at the pressure which was used to generate the initial fibre mat, i.e. $p_{\infty}(x_0) = p_{roll}$. The roll pressure will deliberately be chosen small, in order to make a large part of the following pulse active. We must also neglect the part of the pulse downstream of its maximum value.

Table 1 contains sets of parameter values (named A–F) used to calculate the presented results, as well as the symbols that distinguish between the different cases in the result plots. In addition, the parameters in table 2 are unchanged between the simulations. The values of m and n are the same as those chosen by Zahrai et al. (1998). Also according to these authors, typical values of S_0 lie in the range $10^5 - 10^6$ m⁻¹. We have decided upon certain values and from them calculated $l = 1/S_0$. The initial drainage resistances $R(x_0)$ are also found in table 1. For reference, Zhao & Kerekes (1995) estimate that a TMP fibre mat of basis weight 10 g/m² correspond to a drainage resistance of about 20 kNs/m³⁴. The parameters a and b are chosen so that fair consistency is obtained with the approximate relation for the dynamic viscosity of pulp suspensions given by Bennington & Kerekes (1996). The experiments conducted to determine the viscosity were performed under conditions quite different from those encountered in a blade forming section. We also note that the concentrations ϕ_0 and ϕ_g in table 2 are slightly outside the validity range $0.02 \lesssim \phi \lesssim 0.25$ provided by Bennington & Kerekes for the viscosity expression. Their findings nevertheless yield an indication of the magnitude of the effective viscosity. The density of wet fibres varies considerably, since the water retention capacity of the fibres is highly dependent on how they have

⁴Presumably, the resistance of the fabric is included in this value, whereas in table 1 it is not.

		A	В	$^{\mathrm{C}}$	D	\mathbf{E}	F
\overline{U}	[m/s]	18	18	18	18	18	10
T	[kN/m]	10	10	10	10	10	6
d_s	[mm]	2	2	2	2	2	5
$H(x_0)$	[mm]	0.6	0.6	0.6	0.6	0.6	1.2
θ	[rad]	0.015	0.02	0.025	0.017	0.02	0.044
$S_0/10^5$	$[m^{-1}]$	7.7	7.7	7.7	11	4.4	7.7
l	$[\mu \mathrm{m}]$	1.3	1.3	1.3	0.95	2.2	1.3
$R(x_0)$	$[kNs/m^3]$	42	42	42	79	14	85
Symbol			0		\Diamond	◁	+

TABLE 1. Parameter sets used in the simulations. In addition, table 2 contains input parameters that are the same in all simulations.

m	500 kPa	a	$2.8 \cdot 10^{5}$	μ_c	$10^{-3} \mathrm{Pas}$
n	2.5	b	3.1	ν_c	$10^{-6} \text{ m}^2/\text{s}$
	0.01	$ ho_c$	10^3 kg/m^3 $1.2 \cdot 10^3 \text{ kg/m}^3$	p_{roll}	4.3 kPa
	0.005	$ ho_d$	$1.2 \cdot 10^3 \text{ kg/m}^3$		

TABLE 2. Parameter values that are not changed between the different simulations.

been treated. The actual value is bound by ρ_c and the density of dry cellulose $(1.5 \cdot 10^3 \text{ kg/m}^3)$, and we therefore arbitrarily set $\rho_d = 1.2 \cdot 10^3 \text{ kg/m}^3$.

Appendix C contains an outline of the numerical solution procedure.

4.2. The concentration boundary layer

The pressure pulses corresponding to the simulations A-F are collected in figure 4. Both the magnitude and the reach of the pulses varies considerably, depending on the employed set of parameters. Note e.g. the influence of the specific surface: Simulation D and E are performed with similar parameter values (the wrap angles differ slightly), except that for case D (symbol \diamond) S_0 is $1.1 \cdot 10^6 \text{ m}^{-1}$, whereas for case E it is $4.4 \cdot 10^5 \text{ m}^{-1}$ (symbol \triangleleft). These choices are both within the range of magnitudes of the values cited in the literature for the specific surface, the former yielding lower permeabilities, the latter higher. In figure 4, the corresponding pressure distributions are of very different amplitude, and the upstream reach of the pulse in simulation D is twice that of simulation E.

During the compaction, the distribution of fibres in the mat changes. Figure 5 contains concentration profiles at different positions along the machine direction for the simulations C and F in table 1 (left and right subfigure, resp.). The co-ordinate x have been normalised with the length L_p of the

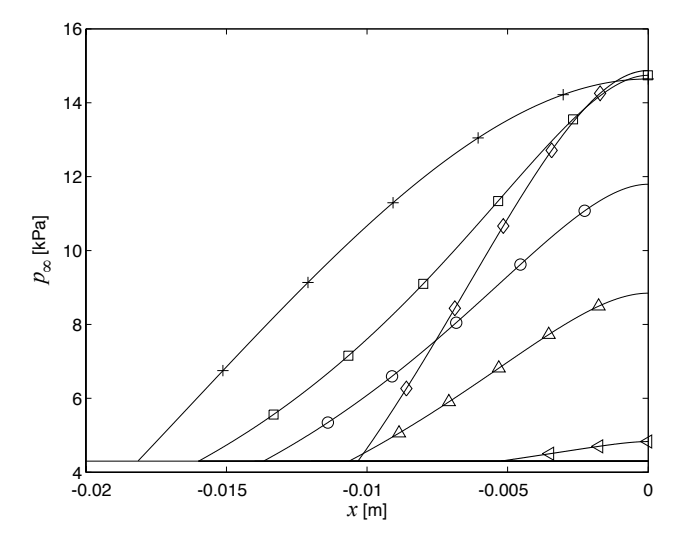


FIGURE 4. The pressure distributions corresponding to the parameter sets in table 1: A (\triangle), B (\circ), C (\square), D (\diamond), E (\triangleleft) and F (+). Maximum pressure is reached at x=0. The horizontal line indicates the magnitude of the roll pressure, $p_{roll}=4.3$ kPa. The solution by Zhao & Kerekes (1995): $p_{\infty}(x)=\theta R(x_0)U\left[exp\left(2(x-x_b)c_2/L\right)-exp\left(2(x-x_b)c_1/L\right)\right]/\sqrt{1-\Lambda}$, where $c_{1,2}=(1\pm\sqrt{1-\Lambda})/\Lambda$ and x_b is the position of the blade.

simulated part of the pulse, so that $x/L_p = -1$ corresponds to the position where $p_{\infty}(x_0) = p_{roll}$, and $x/L_p = 0$ to the position where $p_{\infty}(x)$ attains its maximum value. The initial asymptotic profiles are given as dashed lines. As seen in figure 4, the pressure pulses for case C and F are of the same amplitude and comparable reach. The initial fibre mat is twice as thick in simulation F as compared to C. In both situations, the mat is more compacted closer to the wire (at y=0). This is a consequence of the load transferred to the network increasing in the direction towards the fabric (cf. section 3.5). At the upper surface of the web, the network is unloaded and $\phi = \phi_q$. On the other hand, the concentration at the fabric surface ϕ_w is directly given by the drainage pressure through (42). It is noteworthy that the span of concentrations in the mats increases significantly in both simulations as a result of the pressure pulse. Although qualitatively very similar, there are small quantitative differences between the cases C and F. It is seen that thickness of the fibre mat is more reduced by the pulse (in relative terms) in simulation C than in F. Further, the concentration profiles in simulation F present a somewhat more marked change of slope at about $y/H(x_0) = 0.3 - 0.4$. In certain dewatering applications, 'clogging' can reduce the efficiency. A high degree of compaction

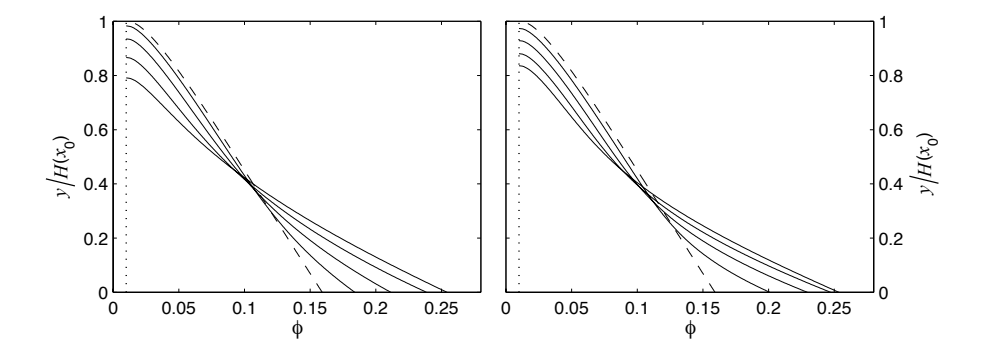


FIGURE 5. Concentration profiles at $x/L_p =$ -1, -0.75, -0.5, -0.25 and 0, for simulations C (left subfigure) and F (right subfigure), corresponding to comparable pressure pulses. $H(x_0)$ for case F is twice the value of case C. Cf. table 1 for parameter values. Stations closer to the blade correspond to larger values of ϕ at y=0. The dashed lines are the initial asymptotic solutions. The vertical dotted lines indicate the gel concentration ϕ_q .

of the particle network then occurs at the outlet, and a thin cake of high concentration and low permeability forms that acts as a lid, preventing efficient drainage of the uncompressed 'inner' regions of the suspension, where the network is almost unloaded. The ϕ -profiles in figure 5 are representative of all the considered cases. Thus, 'clogging' does not appear to be an issue with the present model, notwithstanding the possibility of this occurring if the increase in R(x) is accounted for in the pressure pulse.

The drainage flux J(x) (i.e. the superficial drainage velocity), as well as the rate of displacement of the to top of the fibre mat UdH/dx, are presented for the simulations A and C in the left half of figure 6. The values have been scaled with the speed of the fabrics. The cases A and C differ with respect to the wrap angle θ , which is 0.015 rad in the former calculation, and 0.025 rad in the latter. In figure 4 it is seen that the pressure pulse thus acts over a longer distance, and is of larger amplitude, in case C as compared to A. The consequence is a drainage flux, and a rate of change of the mat thickness, that is of higher magnitude in C than in A. At the upstream end, dH/dx is positive for both cases. Hence, the fibre mat gets thicker in the machine direction due to fibre deposition. Almost immediately, however, the drainage flux grows strong enough to outweigh the effect of the deposition. The drag between the liquid and the fibre network causes sufficient compression of the web for the thickness to decrease, and for dH/dx to become negative. According to (40), the rate of fibre deposition onto the web is proportional to the distance between the solid and the dashed curves in figure 6, and is thus roughly equal in A and C, and almost constant throughout the pulses.

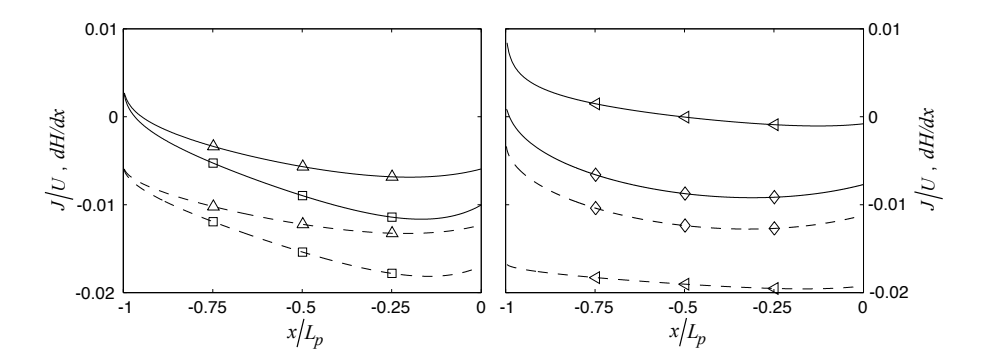


FIGURE 6. The drainage mixture flux J(x) (dashed curves), and the displacement rate of the top of the fibre mat UdH/dx (solid curves), normalised with the wire speed U. The position x is scaled with the length of the pressure pulse, L_p . Left subfigure: Case A (\triangle) and C (\square). Right subfigure: Case D (\diamond) and E (\lhd). Cf. table 1 for parameter values.

The increase of the amount of fibres in the mat, relative to the quantity at the start of the pulse, is plotted for A and C in figure 8. One should note that the quantity of fibres in the mat increases only about 1% and 0.7% during the pulse, for case A and C, respectively. These values should be compared to the evolution of H(x), which is presented in figure 7. Case A yields a final web that is about 92% of the initial height. The corresponding ratio is 79% for case C. The major effect of the drainage is hence to compress the mat, rather than to increase the web thickness by adding fibres. From the left graph in figure 6, it can be be concluded that the maximum value of the deposition rate would have been about 2 and 3 times higher in simulations A and C, respectively, had the mat had a constant thickness during the pulse. It is possible that the observed behaviour would not be so pronounced at subsequent blades, downstream of the first one, since the fibre network is there more compacted, and thus stronger, already at the onset of the pulse. Forming the initial mat using a higher roll pressure might also reduce the observed behaviour, for the same reason.

The right half of figure 6 contains plots of J(x) and UdH/dx for the simulations D and E. These are conducted with similar wrap angles, but with values for the specific surface of the fibres that differs significantly. Case D corresponds to a mat of low permeability. The peak pressure is of the same magnitude as in simulation C (see figure 4), whereas, due to the high resistance, the drainage flux is only of the same magnitude as observed for case A in the left half of figure 6. From the plot of J(x) and UdH/dx, it can also be concluded that the rate of fibre deposition is low. Since, in addition, the reach of the pressure pulse is fairly short, the quantity of fibres in the mat only increases about 0.35% during the pass over the blade. Figure 7 contains

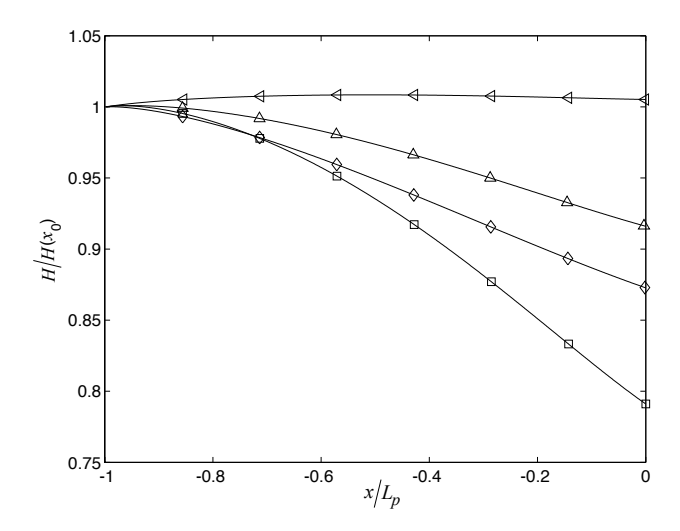


FIGURE 7. The evolution of the fibre mat thickness H(x), normalised with the initial thickness $H(x_0)$, in the simulations A (\triangle) , C (\Box) , D (\diamond) and E (\triangleleft) . The position x is scaled with the length of the pressure pulse, L_p . Cf. table 1 for parameter values.

the corresponding evolution of H(x). On the other hand, simulation E is performed with a value for the specific surface such that the resistance to drainage is low (considering mat thickness and concentration distribution). Although the pressure is now of small magnitude, figure 6 reveals that the drainage flux is slightly larger than for case C. Due to the small interface drag, and the high deposition rate, the mat thickness changes fairly slowly in the machine direction, growing during the first half of the pulse, and decreasing during the second half. H(x) for this case is plotted in figure 7. Neverthelss, due to the very short pulse length, the relative increase of the amount of fibres in the mat is a modest 1% for calculation E.

In addition to the evolution of the amount of fibres in the web, figure 8 shows the increase of the drainage resistance R(x), relative to the value $R(x_0)$ of the initial fibre mat, for the simulations A and C. It is interesting to see that although the amount of fibres in the mats changes by less than a percent, the total change of the drainage resistance is approximately 13% and 29% for case A and C, respectively. This increase is thus not due to the fibres added to the mat, but to the reduced permeability of the compacted web, especially in the highly compacted regions close to the fabric (cf. fig. 5). We note that, in an experimental study of the filtration resistance of a fibre sheet formed under constant drainage pressure, Wildfong et al. (2000) find that the resistance R(x),

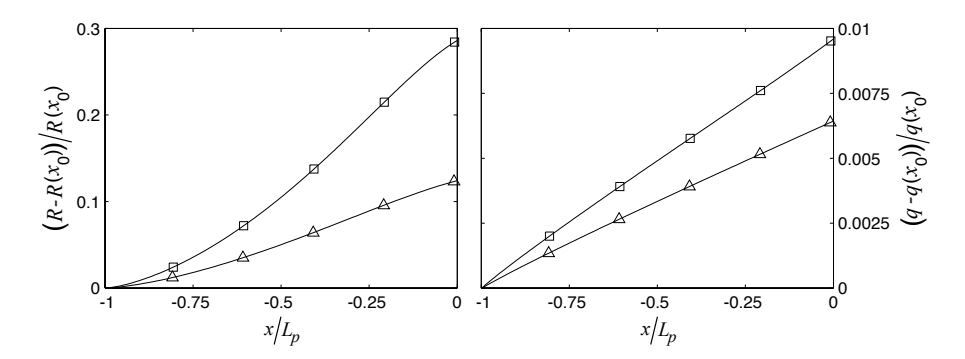


FIGURE 8. Left subfigure: The increase of the drainage resistance, R(x), normalised with the initial value $R(x_0)$. Right subfigure: The increase of the quantity of fibres in the mat, q(x), scaled with $q(x_0)$. \triangle : simulation A. \square : simulation C. The position x is scaled with the length of the pressure pulse, L_p . Cf. table 1 for parameter values.

scaled with the height H(x) of the fibre mat^5 , does increase as result of mat compression, but that this effect is small compared to increased resistance caused by fines particles plugging the pores of the web. This is not accounted for in the present model.

4.3. The velocity boundary layer

Figure 9 contains the velocity profiles $\Delta u_s(y)$ at different positions x/L_p for simulation C. The velocity is scaled with the speed of the fabrics, and the position y with the initial mat thickness $H(x_0)$. The symbols \star indicate the thickness of the mat at the position for which the profile is drawn. It is clear that the velocity boundary layer almost coincides with the fibre mat region. Only a small fraction is found outside of the web. Further, we note that the discontinuity in the velocity gradient mentioned in section 3.5 cannot be observed in the figure. This is a result of the viscosity jump at y = H(x) being small. At the position nearest to the blade (i.e. $x/L_p = 0$), about a quarter of the web next to the wire moves with a velocity close to the speed of the fabrics. This is not as pronounced at the earlier stations. The difference is due to the larger effective viscosity of the mixture in the more compacted mats closer to the blade. As the adopted viscosity function (11) is highly non-linear, the concentration increase has a strong effect on the viscosity.

Let us define $\delta(x)$ to be the distance between the top of the fibre mat, and the position where $\Delta u_s/U < 10^{-5}$, the limit value being chosen arbitrarily. Hence, $\delta(x)$ measures the extent to which the velocity boundary layer protrudes into the region between the two fibre mats. The evolution of $\delta(x)$ during the

 $^{^{5}}$ In their uniaxial filtration experiments, the resistance R/H is dependent on time, rather than the distance x.

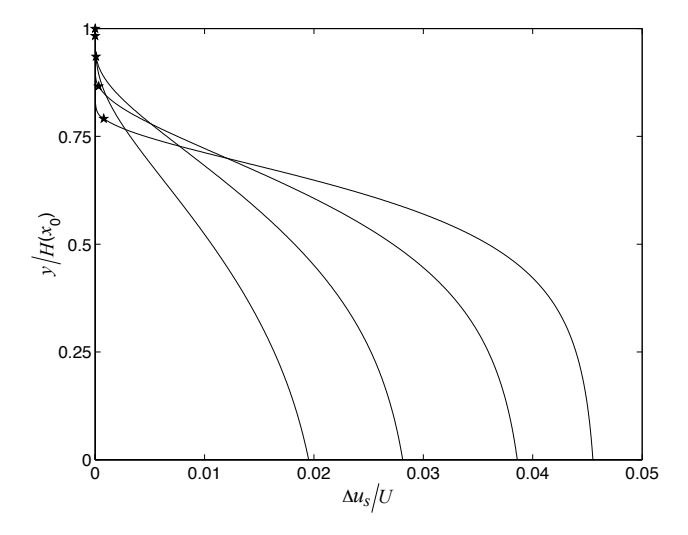


FIGURE 9. The velocity boundary layer at the positions $x/L_p = -1$, -0.75, -0.5, -0.25 and 0, for simulation C. The velocity is scaled with the fabric speed U, and the position y with the initial mat thickness. Note that $u_s = u_{\infty}(x) + \Delta u_s$, where u_s is the suspension velocity relative the fabric, and $u_{\infty}(x)$ is the velocity in the free suspension. Thus $\Delta u_s = 0$ yields $u_s = u_{\infty}(x)$. At y = 0, $\Delta u_s = -u_{\infty}$, yielding $u_s = 0$. Stations closer to the blade correspond to larger velocities at y = 0. Note also that, by assumption $\Delta u_s(y) = 0$ at $x/L_p = -1$. Thus the corresponding profile coincides with the vertical axis. \star indicates the position y = H(x). Cf. table 1 for parameter values.

pressure pulse is presented for simulations A, B and C in figure 10, scaled with the initial mat thickness. During the early stages of the pulse, $\delta(x) = 0$. This is a natural consequence of the simulations, since a certain distance is needed before the velocity boundary layer, that starts from zero thickness, has grown enough to reach detectably outside of the fibre mat (this is further discussed below). The drainage flux towards the wires limits the growth of $\delta(x)$, whose maximum value is in the range 3–5% of the initial mat thickness for the three cases. In simulation E, the velocity layer never extends outside of the mat region. Consequently, the velocity layers do not fill the gap between the fibre mats, which would have prevented the existence of an inviscid region of free suspension surrounded by boundary layers. Since this situation has been assumed, the present analysis would then not have been valid.

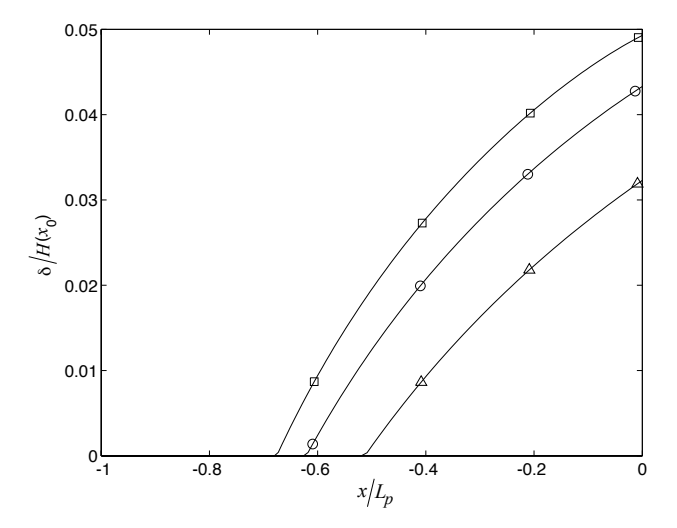


FIGURE 10. The protrusion of the velocity boundary layer into the region between the fibre mats for simulations A (\triangle), B (\circ) and C (\square). δ is the distance between the top of the fibre mat and the point where $\Delta u_s/U < 10^{-5}$. It is scaled with the initial mat thickness. The position x is scaled with the length of the pressure pulse, L_p . Cf. table 1 for parameter values.

From the velocity gradients and the effective viscosity, the Newtonian shear stress component parallel to the fabric, τ_N^{xy} , can be obtained as

$$\tau_N^{xy} = \rho_c \nu(\phi) \frac{\partial u_s}{\partial y} = \rho_c \nu(\phi) \frac{\partial \Delta u_s}{\partial y} \,. \tag{49}$$

By integrating equation (36) in the direction perpendicular to the fabric, from a position y within the velocity boundary layer, to a position far up in the free suspension, we find the following relation for the shear stress at level y,

$$\tau_N^{xy}(y) = \rho_c J(x) \Delta u_s(y) - \rho_c U \int_y^\infty \frac{\partial \Delta u_s}{\partial x} \, \mathrm{d}y, \qquad (50)$$

where, for clarity, only the dependence on the position perpendicular to the fabrics have been written out for $\tau_N^{xy}(x,y)$ and $\Delta u_s(x,y)$. The first term on the right hand side of (50) results from the need to accelerate the free suspension that is convected towards the fabric to the local suspension velocity. The second term represents the shear stress needed to adjust to changes in the machine direction of the relative velocity between the free suspension and the boundary layer mixture, at all levels further away from the fabric. It is recalled that, according to (34), the sum of the liquid and particle pressure is constant throughout the boundary layer, and equal to $p_{\infty}(x)$. Consequently, the gradient $dp_{\infty}(x)/dx$ acts equally on both the free suspension, and the mixture in the boundary layer, and cannot influence the relative velocity Δu_s . This is the

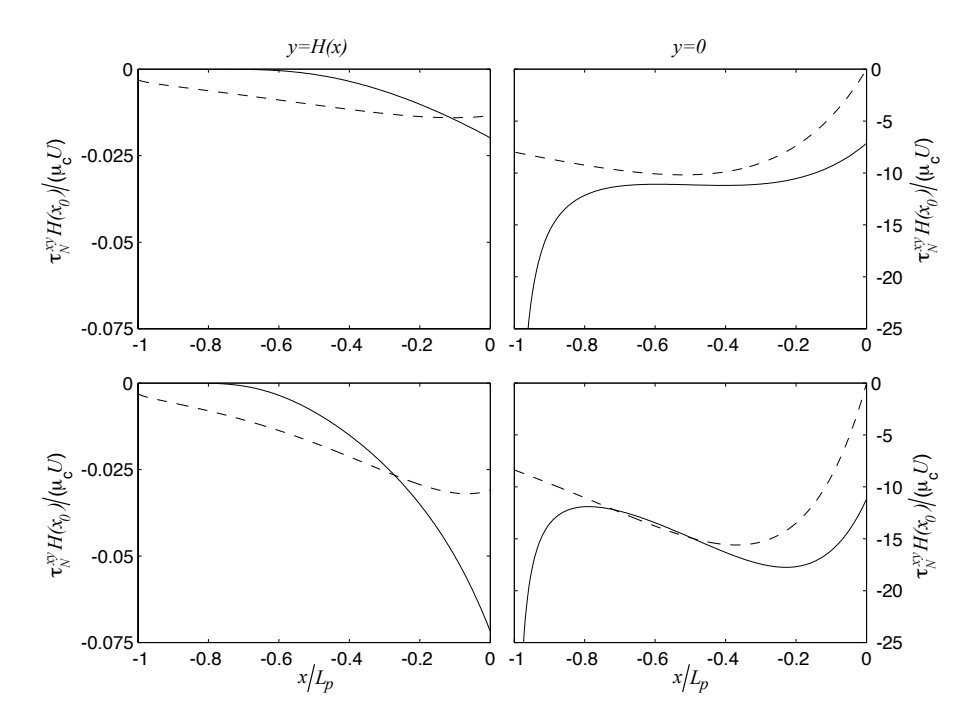


FIGURE 11. The viscous shear stress τ_N^{xy} in the mat at y=0 and y=H(x). Top subfigures: Case A. Bottom subfigures: Case C. The stress is scaled with $\mu_c U/H(x_0)$, and the position x by the length of the pressure pulse, L_p . Solid lines: τ_N^{xy} calculated using (49). Dashed lines: The estimate τ_a obtained by inserting the rectangular profile (51) into (50). Cf. table 1 for parameter values.

reason the free suspension pressure gradient is absent in the balance equation (36). It is the shear stresses that enables the mat to, essentially, retain a velocity close to that of the wire, rather than to be slowed down by the pressure pulse to the same extent as the free suspension. Note that, since J(x) is negative, and $\partial \Delta u_s/\partial x$ is positive, both terms on the right hand side of (50) add to the shear stress. The shear stress distribution during the blade pulse is plotted for the cases A and C in figure 11, for the positions y = 0 and y = H(x).

In a real forming section, the free suspension velocity $u_{\infty}(x)$ decreases gradually as the pressure is built up, and when the position $x=x_0$ is reached (i.e. where the calculations start) there is already a region in the mat where the velocity $\Delta u_s \neq 0$, and the shear stress τ_N^{xy} is finite. Since the velocity profile at the upstream end of the treated domain is not known to us, we have simply assumed the initial condition $\Delta u_s(y) = 0$. Although not correct, the simulations therefore predict vanishingly small shear stresses in the upper regions of the mat during the first part of the pressure pulse, and infinite values

at the wire surface. After some distance, the initial erroneous velocity profile is forgot by the solution. This happens sooner in the regions closer to the fabric, since the boundary velocity is correct. However, it would not be wise to trust the initial predictions of τ_N^{xy} obtained from (49). Instead, an estimate $\tau_a(x,y)$ of the magnitude of the shear stress in the regions far upstream of the blade can be obtained by inserting the approximate velocity profile

$$\Delta u_s(x,y) = \begin{cases} -u_{\infty}(x) & y \le H(x) \\ 0 & y > H(x) \end{cases}$$
 (51)

into equation (50). The estimate is plotted as dashed curves in figure 11.

From figure 11 we conclude that, at the end of the pressure pulse, where it is most likely safe to employ (49), the surface shear stress is -0.59 Pa and -2.2 Pa in simulation A and C, respectively. The shear stresses next to the fabric are of significantly larger magnitude than the surface values. Downstream, of the faulty initial region, these high stresses are a consequence of the integral in (50), which, when y=0, represents the forces needed to achieve an acceleration of the mixture in the entire velocity boundary layer, as observed in the interpretation of the terms in (50). In calculation A, $\tau_N^{xy}(y=0)$ demonstrates a plateau corresponding to -0.34 kPa, before the stress magnitude decreases. On the other hand, calculation C yields a local minimum in the stress magnitude, followed by a maximum corresponding to -0.54 kPa, before the stress level again decreases prior to the peak of the pulse. At the later stages of the blade pulses, when $\tau_N^{xy}(y=0)$ ceases to decrease after the initial large values, the effects of the faulty initial conditions have probably abated, and the observed stress levels can be trusted. The values are impressive, even after noting that they occur in the densest, and consequently also the strongest, part of the mat.

It is evident from the velocity profiles in figure 9 that τ_a is not a very accurate approximation of τ_N^{xy} at the top of the mat, since Δu_s is there significantly smaller than $-u_{\infty}(x)$. At y=0, however, the first term in (50) obtains its correct value when (51) is inserted, and as the shape of the true velocity profiles close to $x/L_p = -1$ probably resemble the one at $x/L_p = 0$ in figure 9, we are entitled to expect better agreement with the actual value. This is supported by the plots in figure 11, where fair agreement is observed between τ_N^{xy} and τ_a for y=0 at the intermediate stages of the pulse. The gradient du_{∞}/dx tends to zero as $x/L_p \to 0$, and $\tau_a(y=0)$ thus approach the value of $\tau_a(y=H(x))$. However, due to the inability (caused by inertia) of the boundary layer mixture to perfectly adapt to the fabric velocity, the integral term in (50) remains of considerable size also as the peak pressure is approached, and the corresponding trend in $\tau_N^{xy}(y=0)$ lag behind. Nevertheless, the results presented in figure 11 highlight the importance to the shear stress of the integral term in (50). Although the region downstream of the peak is not treated in the presented study, it is worth commenting that both experimental and theoretical work (cf. e.g. Zhao & Kerekes 1995; Zahrai et al. 1997) have revealed that the magnitude of the gradient dp_{∞}/dx , and thus du_{∞}/dx , and presumably also $\partial \Delta u_s/\partial x$, are significantly larger in that region than upstream of the pressure maximum.

Hence, it is possible that even higher stresses (though of opposite sign) occur during the part of the pulse not treated here. The decay of $\partial \Delta u_s/\partial x$ towards $x/L_p=0$ also explains why the largest stresses at y=0 occur upstream of the peak of the pressure pulse.

Finally, it should be pointed out that equation (50) would be valid regardless of how we chose to model the strain-rate dependent stress τ_N in (10). Hence, provided the compaction prependicular to the wire is not affected, the magnitude of the stress at the fabric surface is not to a large degree dependent on how we model the displacements in the machine direction, as long as the mat mixture has a fairly strong tendency to follow the wire.

5. Concluding remarks

In the presented work we look at deformations and stresses in a fibre mat, outside of which there is a region of free suspension, when it experiences a blade pulse. A scaling analysis of the governing equations reveals that it is reasonable to consider the region between the forming fabrics as composed of an inviscid core, surrounded by velocity and concentration boundary layers. This situation has in previous studies of forming been assumed a priori (cf. e.g. Zahrai et al. 1997; Martinez 1998).

For the considered sets of parameters and boundary conditions, it is found that the distribution of fibres in the mat does not show a marked tendency to 'clog' the drainage as a result of the pressure pulse. Rather, the concentration exhibits a gradual increase from the gel value at the free suspension side, to a high value corresponding to a network sufficiently strong to carry the drainage load at the fabric surface.

It is observed that the compression of the web, caused by the drainage flow through it, significantly reduces the rate of deposition of fibres at the mat surface. Although the increase of the amount of fibres in the web, as a result of the pulse, is overall rather modest, there is nevertheless a significant change in the resistance to drainage of the free suspension presented by the web. This is a consequence of the reduced permeability in the highly compacted regions of the mat. To the extent that the effects of the dewatering on the resistance is accounted for when modelling the pressure distributions in the forming section, it is commonly assumed proportional to the accumulated amount of expelled liquid⁶ (cf. e.g. Green & Kerekes 1998; Holmqvist 2002). The hypothesis is based on the assumption that the origin of the resistance is the amount of fibres in the mat, and that the rate of change of this quantity in the machine direction is directly proportional to the superficial dewatering velocity, neither of which is thus correct if the mat is not stiff enough to resist compression due to the loads induced by the drainage flow.

In respect to deformations perpendicular to the wires (i.e. compaction), the fibre network is modelled as a plastic-rigid material exhibiting a concentration dependent yield-stress. In order to relate the particle pressure to the

⁶An exception is the study by Zahrai et al. (1998).

concentration, the yield criterion is supposed always fulfilled, which prevents us from relaxing the loads in the fibre network. As a consequence, only the part upstream of the pressure pulse maximum is considered, starting from the value at which the pulse first exceeds the roll pressure used to generate the initial mat. Thus, not to exclude a substantial part of the pulse, the roll pressure is chosen small. When it arrives at the blade, the web is consequently likely to be less dense than it would be in a real paper-machine, where the loads induced by the roll are higher. Further, although perhaps of less importance, the drainage pressure during roll forming is not constant along the machine direction (cf. Holm 2005), a supposition made to obtain the concentration profile of the initial mat. These factors should be kept in mind when considering the presented results.

The drainage flux is seen to limit the protrusion of the velocity boundary layer into the region between the mats. Indeed, the adjustment of the suspension to the velocity difference between the free suspension and the wire occurs almost entirely in the web region. The shear stresses parallel to the fabrics needed to accelerate the drainage flux to the local velocity of the mat mixture is observed to be rather small compared to the shear stresses required to ensure that a large part of the web mixture follows the fabric, instead of takes on the velocity of the free suspension. The total shear stress at the surface of the wire can apparently be of high magnitude. Although not accounted for in the present study, it is likely that the shear loads reduce the bearing capacity of the fibre network, and thus affect the compaction of the web.

In the absence of rate-independent deviatoric stresses, we find that the deformations parallel to the fabric surface are controlled by the rate-dependent (viscous) properties of the fibre mat. Although the presented stress levels at the wires are not greatly influenced by the choice of constitutive model, as long as the suspension mixture has a tendency to follow the fabric in a fairly large part of the mat, the calculated deformations of the web are so. To the papermaker, due to their influence on the characteristics of the final paper sheet, these are among the most important quantities to predict. It would therefore be of significant interest to develop a model that accounts also for the rate-independent deviatoric stresses, that were here neglected at the outset to simplify the treatment.

It is important to realise that many of the results in the current study stand and fall with the hypothesis that it is meaningful to describe the fibre phase as a continuum. The small physical dimension of the fibre mat in the direction perpendicular to the fabric makes this a real issue, indeed. However, due to the relative ease by which continuum mechanical models can be developed, compared to their micro-mechanical counterparts, the concept should be explored also for the fibre sheets in the forming section, provided the inherent limitations are contemplated.

6. Acknowledgements

Financial support was provided by the Swedish Agency for Innovation Systems (VINNOVA) and the industrial partners in the FaxénLaboratory.

References

- Amberg, G., Tönhardt, R. & Winkler, C. 1999 Finite element simulations using symbolic computing. *Math. Comput. Simulation* 49, 257–274.
- Bennington, C. P. J. & Kerekes, R. J. 1996 Power requirements for pulp suspension fluidization. *Tappi Journal* **79** (2), 253–258.
- Buscall, R. & White, L. R. 1987 The consolidation of concentrated suspensions, part 1—the theory of sedimentation. J. Chem. Soc., Faraday Trans. 1 83, 873– 891.
- Dalpke, B., Kerekes, R. J. & Green, S. I. 2004 Modelling jet impingement and the initial drainage zone in roll forming. *Journal of Pulp and Paper Science* **30** (3), 65–70.
- Green, S. & Kerekes, R. 1998 Numerical analysis of pressure pulses induced by blades in gap formers. In *TAPPI Engineering Conference*, pp. 185–192.
- HOLM, R. 2005 Fluid mechanics of fibre suspensions related to papermaking. PhD thesis, Royal Institute of Technology (KTH), Stockholm.
- Holmqvist, C. 2002 Modelling of the pressure distributions in twin-wire blade formers. Licentiate thesis, Royal Institute of Technology (KTH), Stockholm.
- INGMANSON, W. L., ANDREWS, B. D. & JOHNSON, R. C. 1959 Internal pressure distributions in compressible mats under fluid stress. Tappi J. 42 (10), 840–849.
- Kataja, M., Kirmanen, J. & Timonen, J. 1995 Hydrostatic and structural pressure in compressed paper webs and press felts. *Nordic Pulp and Paper Research Journal* **10** (3), 162–166.
- LANDMAN, K. A. & RUSSEL, W. B. 1993 Filtration at large pressures for strongly flocculated suspensions. *Phys. Fluids A* 5 (3), 550–560.
- Landman, K. A., Sirakoff, C. & White, L. R. 1991 Dewatering of flocculated suspensions by pressure filtration. *Phys. Fluids A* **3** (6), 1495–1509.
- Lobosco, V. 2004 On the modelling of mechanical dewatering in papermaking. PhD thesis, Royal Institute of Technology (KTH), Stockholm.
- MARTINEZ, D. M. 1998 Characterizing the dewatering rate in roll gap formers. *Journal of Pulp and Paper Science* **24** (1), 7–13.
- ROSHANZAMIR, A., GREEN, S. & KEREKES, R. 2000 Two-dimensional simulation of suction shoes in gap formers. *Journal of Pulp and Paper Science* **26** (4), 158–162.
- TERZAGHI, K. 1943 Theoretical Soil Mechanics. New York: John Wiley & Sons.
- Ungarish, M. 1993 Hydrodynamics of Suspensions. Springer-Verlag.
- WILDFONG, V. J., GENCO, J. M., SHANDS, J. A. & BOUSFIELD, D. W. 2000 Filtration mechanics of sheet forming. part II: Influence of fine material and compression. *Journal of Pulp and Paper Science* 26 (8), 280–283.
- Zahrai, S. & Bark, F. 1995 On the fluid mechanics of twin wire blade forming in paper machines. *Nordic Pulp and Paper Research Journal* 10 (4), 245–252.

ZAHRAI, S., BARK, F. & NORMAN, B. 1997 An analysis of blade dewatering in a twin-wire paper machine. *Journal of Pulp and Paper Science* 23 (9), 452–459.

Zahrai, S., Martinez, M. D. & Dahlkild, A. A. 1998 Estimating the thickness of the web during twin-wire forming. *Journal of Pulp and Paper Science* **24** (2), 67–72.

ZHAO, R. & KEREKES, R. 1995 Pressure distribution between forming fabrics in blade gap formers: Thin blades. *Journal of Pulp and Paper Science* 21 (3), 97–103.

Appendix A. Simplifications in the free suspension

In the free suspension the momentum equation (10) becomes

$$\rho_c \mathbf{u}_s \cdot \nabla \mathbf{u}_s = -\nabla p_c + \nabla \cdot \boldsymbol{\tau}_N \,. \tag{52}$$

Introduce the following scaled variables,

$$\hat{x} = \frac{x_s}{L}$$
 $\hat{y} = \frac{y}{d_s}$ $\hat{u}_s = \frac{u_s}{u_0}$ $\hat{v}_s = \frac{v_s}{v_0}$ $\hat{p}_c = \frac{p_c}{p_0}$. (53)

Inserting the scaled quantities into the x-component of (52), and using the estimates in section 3.1 to rewrite the constant factors in a more informative form, reveals,

$$\frac{\partial \hat{u}_s}{\partial \hat{x}} + \left(\frac{u_0}{U}\right) \hat{u}_s \frac{\partial \hat{u}_s}{\partial \hat{x}} + \left(\frac{u_0}{U}\right) \hat{v}_s \frac{\partial \hat{u}_s}{\partial \hat{y}} = -\frac{\partial \hat{p}_c}{\partial \hat{x}} + \frac{1}{Re} \frac{\partial^2 \hat{u}_s}{\partial \hat{x}^2} + \frac{1}{Re} \left(\frac{L}{d_s}\right)^2 \frac{\partial^2 \hat{u}_s}{\partial \hat{y}^2} , \quad (54)$$

where rate-dependent stresses are of Newtonian type, the kinematic viscosity being $\nu_0 = \nu_s(\phi_0)$. The Reynolds number Re is defined as LU/ν_0 . As in the free suspension the concentration ϕ_0 is low, it is clear that the viscosity will not differ several orders of magnitude from that of the suspending fluid, which is also confirmed by (11). The typical parameter values in tables 1 and 2 reveal that $Re \gg 1$, and consequently the viscous terms can be dropped. Further, (18) reveals that u_0/U is of size 10^{-2} . Hence the relevant balance in equation (54) is found to be

$$\frac{\mathrm{d}\hat{u}_s}{\mathrm{d}\hat{x}} = -\frac{\mathrm{d}\hat{p}_c}{\mathrm{d}\hat{x}}\,,\tag{55}$$

by which (21) follows. As the order of the original equation is reduced, there must be a boundary layer in the free suspension next to the fibre mat, in which the last term on the left hand side of (54), and the last of the viscous terms, also need to be included in the balance.

Appendix B. Simplifications in the boundary layers

As a measure of the dimensions of the boundary layers perpendicular to the wires, we use the characteristic fibre mat thickness d_m . The velocity and concentration boundary layers are hence assumed to be of comparable size, which is confirmed by our study. However, this is not crucial to the validity of the simplifications undertaken in this section.

Since the constant factors appearing in front of each term in the scaled equations in this appendix have been rewritten in informative forms, using the estimates derived in section 3.1, they will sometimes contain quantities which are neither found in the definitions of the scaled variables, nor in the original dimensional equation.

B.1. The conservation of suspension mixture

First consider the mixture conservation equation (8). For that purpose we introduce the flux density components j^x and j^y relative the fabric according to

$$\mathbf{j} = (U + j^x)\mathbf{e}_x + j^y\mathbf{e}_y, \tag{56}$$

and also the scaled quantities

$$\tilde{x} = \frac{x}{L}$$
 , $\tilde{y} = \frac{y}{d_m}$, $\tilde{j}^x = \frac{j^x}{u_0}$ $\tilde{j}^y = \frac{j^y}{w_0}$. (57)

They should all be of order one. By inserting these into (8) we find,

$$\left(\Lambda \frac{d_m}{d_s}\right) \frac{\partial \tilde{j}^x}{\partial \tilde{x}} + \frac{\partial \tilde{j}^y}{\partial \tilde{y}} = 0.$$
 (58)

Using the parameter values in table 1, only for case E is $\Lambda d_m/d_s$ sufficiently small for the first term on the left hand side of (58) to be safely neglected (the low dewatering resistance makes Λ small). Nevertheless, due to the significant simplification it entails, we shall suppose the boundary layers to be thin in comparison to the free suspension region, thus obtaining equation (23). It should be pointed out that the validity of the solution for $p_{\infty}(x)$ by Zhao & Kerekes (1995), also depends on the requirement that $\Lambda d_m/d_s$ is small. If this is not the case, the inviscid momentum balance employed by them in the direction parallel to the fabrics is not appropriate.

B.2. The concentration boundary layer

From the equations (2)–(5) follows that $\mathbf{j}_d = \phi \mathbf{j} + \phi (1 - \phi) \mathbf{u}_r$. Inserting this into (9), and using the relations (8) and (12), we find an equation for the concentration,

$$\mathbf{j} \cdot \nabla \phi = \nabla \cdot \left(\phi (1 - \phi) \frac{k(\phi)}{\mu_c} \nabla p_d \right). \tag{59}$$

In addition to the variables already defined in (57), introduce the following quantities,

$$\tilde{p}_d = \frac{p_d}{p_0} \quad , \quad K(\phi) = \frac{k(\phi)}{l^2} \,, \tag{60}$$

where l is the length scale of the pores in the network. When (57) and (60) are inserted into equation (59), the result is

$$\left(\frac{d_m}{\Delta h}\right) \frac{\partial \phi}{\partial \tilde{x}} + \left(\frac{u_0}{U} \frac{d_m}{\Delta h}\right) \frac{\partial \phi}{\partial \tilde{x}} + \tilde{j}^y \frac{\partial \phi}{\partial \tilde{y}} = \frac{1}{Pe} \left(\frac{d_m}{L}\right)^2 \frac{\partial}{\partial \tilde{x}} \left(\phi(1-\phi)K(\phi)\frac{\partial \tilde{p}_d}{\partial \tilde{x}}\right) + \frac{1}{Pe} \frac{\partial}{\partial \tilde{y}} \left(\phi(1-\phi)K(\phi)\frac{\partial \tilde{p}_d}{\partial \tilde{y}}\right). \tag{61}$$

Above, a Péclet number has been introduced,

$$Pe = \frac{\mu_c w_0 d_m}{l^2 p_0} \,. \tag{62}$$

As defined in (62), it expresses the ratio between convection of fibres towards the fabrics due to entrainment, and transport away from the wires due to gradients in the inter-particle pressure. Since the fibres are retained, Pe should be of order unity, at least close to the fabric. Therefore we must have

$$w_0 \sim \frac{l^2 p_0}{\mu_c d_m}$$
 (63)

Consistency then requires that the drainage resistance R introduced in section 3.1 is of magnitude $\mu_c d_m/l^2$. The ratio u_0/U has already been found to be of size 10^{-2} . According to the estimates (16) and (17), d_m/L and $d_m/\Delta h$ are of sizes 10^{-2} and 1, respectively. Equation (61) therefore reduces to,

$$\left(\frac{d_m}{\Delta h}\right) \frac{\partial \phi}{\partial \tilde{x}} + \tilde{j}^y \frac{\partial \phi}{\partial \tilde{y}} = \frac{1}{Pe} \frac{\partial}{\partial \tilde{y}} \left(\phi(1-\phi)K(\phi) \frac{\partial \tilde{p}_d}{\partial \tilde{y}}\right), \tag{64}$$

which in dimensional form turns into equation (24).

B.3. The velocity boundary layer

Denote the x- and y-components of the relative velocity by u_r and v_r , respectively. Define the variables

$$\tilde{u}_s = \frac{u_s}{u_0} \quad , \quad \tilde{v}_s = \frac{v_s}{w_0} \quad , \quad \tilde{u}_r = \frac{u_r}{u_0} \quad , \quad \tilde{v}_r = \frac{v_r}{w_0} \, ,$$
 (65)

$$\tilde{p}_c = \frac{p_c}{p_0} \quad , \quad \tilde{\tau}_N^{ij} = \frac{\tau_N^{ij}}{\tau_0^{ij}}, \tag{66}$$

where the τ_0^{ij} are measures of the different deformation-rate dependent stresses. We also note that the scale u_0 is most likely much too large for u_r . Inserting (65), (66) and the applicable quantities in (57) and (60), into the component perpendicular to the wires of equation (10) yields

$$\left(\frac{\rho_c U^2}{T/d_m}\right) \frac{\partial \tilde{v}_s}{\partial \tilde{x}} + \left(\frac{u_0}{U} \frac{\rho_c U^2}{T/d_m}\right) \frac{\partial \tilde{v}_s}{\partial \tilde{x}} + \left(\frac{d_s}{L} \frac{\theta}{\Lambda}\right) \tilde{v}_s \frac{\partial \tilde{v}_s}{\partial \tilde{y}} =
-\frac{\partial \tilde{p}_c}{\partial \tilde{y}} - \frac{\partial \tilde{p}_d}{\partial \tilde{y}} + \left(\frac{\tau_0^{yy}}{p_0}\right) \frac{\partial \tilde{\tau}_N^{yy}}{\partial \tilde{y}} + \left(\frac{d_m}{L} \frac{\tau_0^{xy}}{p_0}\right) \frac{\partial \tilde{\tau}_N^{xy}}{\partial \tilde{x}}
-\left(\theta \frac{d_m}{L}\right) \frac{\partial}{\partial \tilde{x}} \left(\phi (1 - \phi) \frac{\rho_d}{\rho_c} \tilde{u}_r \tilde{v}_r\right) - \left(\frac{d_m d_s}{L^2} \frac{\theta}{\Lambda}\right) \frac{\partial}{\partial \tilde{y}} \left(\phi (1 - \phi) \frac{\rho_d}{\rho_c} \tilde{v}_r \tilde{v}_r\right).$$
(67)

From section 3.1 we know that the curvature of the fabrics during the pressure pulse is of magnitude $\Delta h/L^2$. Thus T/d_m represents a pressure that is a factor $L^2/(d_m\Delta h)\sim 10^4$ larger than the pulse pressure, making the first term on the left hand side of (67) of size 10^{-2} , and consequently negligible. Further, $\Lambda\sim 1$, and the remaining acceleration terms on the left hand side of (67) can thus also be omitted. Considering that d_m/L is of magnitude 10^{-2} , in order for

the viscous shear stress term in (67) to be significant, τ_0^{xy} has to be 100 times larger than p_0 . This is not reasonable, and the term can be neglected. The viscous normal stress is important to the balance of the equation if τ_0^{yy} is of comparable size to p_0 . Since the strain-rate dependent stresses are supposed to exhibit a Newtonian behaviour, τ_0^{yy} can be approximated by $\mu_e w_0/d_m$, where μ_e is a measure of the effective dynamic viscosity of the boundary layer mixture. Thus, $\tau_0^{yy} \sim p_0$ would require that μ_e/μ_c is of the order $Rd_m/\mu_c \sim 10^4$. In regions where the fibre mat is highly compacted, such as close to the fabric, the effective viscosity might indeed become large. Using (11) and the parameter values in table 2, we find that $\phi = 0.2$ yields $\mu_e/\mu_c \sim 10^3$. We shall nevertheless judge the viscous normal stress insignificant. Removing negligible terms, (67) turns into

$$0 = -\frac{\partial \tilde{p}_c}{\partial \tilde{y}} - \frac{\partial \tilde{p}_d}{\partial \tilde{y}}, \tag{68}$$

which is equivalent to equation (34).

We now turn to the momentum balance parallel to the wires. When the scaled quantities from (57), (60), (65) and (66) are inserted into the corresponding component of equation (10), one finds

$$\frac{\partial \tilde{u}_s}{\partial \tilde{x}} + \left(\frac{u_0}{U}\right) \frac{\partial \tilde{u}_s}{\partial \tilde{x}} + \left(\frac{\Delta h}{d_m}\right) \tilde{v}_s \frac{\partial \tilde{u}_s}{\partial \tilde{y}} =
- \frac{\partial \tilde{p}_c}{\partial \tilde{x}} - \frac{\partial \tilde{p}_d}{\partial \tilde{x}} + \left(\frac{\tau_0^{xx}}{p_0}\right) \frac{\partial \tilde{\tau}_N^{xx}}{\partial \tilde{x}} + \left(\frac{L}{d_m} \frac{\tau_0^{xy}}{p_0}\right) \frac{\partial \tilde{\tau}_N^{xy}}{\partial \tilde{y}} - \left(\Lambda \theta \frac{L}{d_s}\right) \frac{\partial}{\partial \tilde{x}} \left(\phi (1 - \phi) \frac{\rho_d}{\rho_c} \tilde{u}_r \tilde{u}_r\right) - \left(\frac{\Delta h}{d_m}\right) \frac{\partial}{\partial \tilde{y}} \left(\phi (1 - \phi) \frac{\rho_d}{\rho_c} \tilde{u}_r \tilde{v}_r\right).$$
(69)

 L/d_s is large, but θ is of such a size that the factor in front of the first term on the last row of (69) is fairly small. As seen in section B.2, $\Delta h/d_m$ is of magnitude 1. Nevertheless, on the basis that the true scale of u_r is probably much smaller than the one introduced in (65), the terms involving the relative velocity will be assumed not to have any influence on the balance. By making the approximation $\tau_0^{xx} \sim \mu_e u_0/L$, we find that the ratio τ_0^{xx}/τ_0^{yy} is of size $(d_m/\Delta h)(u_0/U) \sim 10^{-2}$. Thus, as the viscous normal stress term was removed from (67), consistency requires that the normal stress in (69) is considered insignificant as well. This is reasonable, as it is not likely that $\tau_0^{xx} \sim p_0$. After omitting negligible terms in (69), and reorganising/rewriting the factors, the equation becomes

$$\left(\frac{d_m}{\Delta h}\right) \frac{\partial \tilde{u}_s}{\partial \tilde{x}} + \tilde{v}_s \frac{\partial \tilde{u}_s}{\partial \tilde{y}} = -\left(\frac{d_m}{\Delta h}\right) \frac{\partial \tilde{p}_c}{\partial \tilde{x}} - \left(\frac{d_m}{\Delta h}\right) \frac{\partial \tilde{p}_d}{\partial \tilde{x}} + \left(\frac{\nu_e/w_0}{d_m}\right) \frac{\partial \tilde{\tau}_N^{xy}}{\partial \tilde{y}}, (70)$$

where τ_0^{xy} has been approximated by $\mu_e u_0/d_m$, and an effective kinematic viscosity has been defined for the boundary layer mixture as $\nu_e = \mu_e/\rho_c$. Consider now the viscous shear stress (last) term in (70). The ratio $(\nu_e/w_0)/d_m$ expresses the relative strength of the drainage (cf. the theory of asymptotic suction boundary layers). If the drainage is strong/weak, the viscous stress will be important in a region outside of the fabrics much smaller/larger than

 d_m . As the concentration in the web varies between ϕ_g and ϕ_w , the viscosity ratio $\nu_s(\phi)/\nu_c$ will in the mat take on values ranging from roughly 1 at the top of the web, to perhaps 10^3 close to the fabric, based on (11). Using (11), the relations in section 3.1, and the values in tables 1 and 2, to estimate the size of the viscous shear stress term, it is found that it ranges from between 10^{-2} at the top of the mat, to 10 at the fabric (based on the assumption $\phi_w = 0.2$). We shall include the viscous term in the balance of (70), and let the simulations reveal its importance in different regions. In dimensional form, (70) becomes (32).

Appendix C. Solution method

Consider equation (28). As before, d_m denotes the length scale perpendicular to the fabrics in the concentration boundary layer. Let D_0 be a a representative value of $D(\phi)$. In order for there to be a balance between convection of mixture towards the fabrics, and relative transport of fibres in the opposite direction, we must have $J \sim w_0 \sim D_0/d_m$. A suitable choice for D_0 can thus be obtained from (63) as $D_0 \sim w_0 d_m \sim l^2 p_0/\mu_c$. The parameter values in tables 1 and 2 provide the estimate $D_0 \sim 10^{-5}$ m²/s, i.e. the diffusivity is about $10\nu_c$. However, note that relation (63), and consequently the approximation of D_0 , is not necessarily very accurate far up into the fibre mat. The scaled quantities

$$\bar{y} = \frac{y}{d_m}$$
 , $\bar{J} = \frac{J}{D_0/d_m}$, $\bar{D} = \frac{D}{D_0}$, $\bar{x} = \frac{x}{Ud_m^2/D_0}$ (71)

turn (28) into

$$\frac{\partial \phi}{\partial \bar{x}} + \bar{J}(\bar{x}) \frac{\partial \phi}{\partial \bar{y}} = \frac{\partial}{\partial \bar{y}} \left(\bar{D} \frac{\partial \phi}{\partial \bar{y}} \right) , \qquad (72)$$

where all terms are equally important to the balance of the equation. If the same scaling is employed for the velocity deficit equation (36), the result is

$$\frac{\partial \Delta u_s}{\partial \bar{x}} + \bar{J}(\bar{x}) \frac{\partial \Delta u_s}{\partial \bar{y}} = \frac{\partial}{\partial \bar{y}} \left(\bar{\nu}_s \frac{\partial \Delta u_s}{\partial \bar{y}} \right) , \tag{73}$$

where the scaled viscosity is

$$\bar{\nu}_s(\phi) = \frac{\nu_s(\phi)}{D_0} \,. \tag{74}$$

If $\nu_s(\phi)$ is not typically of magnitude D_0 , the scaling (71) is not physically correct for the velocity equation, and if so is revealed by the thickness of the velocity boundary layer not being of the same size as the concentration boundary layer. If the true magnitude of $\nu_s(\phi)$ is ν_e , the ratio ν_e/D_0 expresses the relative thickness of the velocity and concentration boundary layers. If ν_e/D_0 is small, the drainage effects are dominating, and the suspension velocity parallel to the fabrics, in the fibre mat, essentially equals the velocity in the free suspension. In the opposite situation, convection along the fabrics is dominating over the drainage flux, and the fibre mat will be thin in comparison to the region affected by the velocity difference between the wires and the free

suspension. The actual situation is complicated, as $\nu_s(\phi)$ varies considerably across the thickness of the mat (see B.3).

We now specify that $d_m = H(x_0)$, and define $\bar{H} = H(x)/H(x_0)$. The governing equations (72) and (73) are solved simultaneously, by marching downstream from $\bar{x} = \bar{x}_0$. The consolidation equation should be solved in the region $\bar{y} \in [0, \bar{H}(\bar{x})]$, which is not constant in the marching direction. Equation (73) is solved on the domain $\bar{y} \in [0, \bar{y}_{\infty}]$, \bar{y}_{∞} being a large value representing a position far up in the inviscid free suspension region, where it is assumed that $\bar{y}_{\infty} > \bar{H}(\bar{x})$. The viscosity $\bar{\nu}_s(\phi)$ is discontinuous in this latter domain due to the concentration leap across $\bar{y} = \bar{H}(\bar{x})$. Therefore, the solution domain is split into two parts, $[0, \bar{H}(\bar{x})]$ and $[\bar{H}(\bar{x}), \bar{y}_{\infty}]$, and equation (73) is solved in each part separately, using the conditions of continuous velocity and shear stress at $\bar{y} = \bar{H}(\bar{x})$ to match the solutions. If we introduce a co-ordinate $\Delta \bar{y}$ such that $\bar{y} = \bar{H}(\bar{x}) + \Delta \bar{y}$, the domain above the fibre mat corresponds to $\Delta \bar{y} \in [0, \Delta \bar{y}_{\infty}]$. It is convenient to let \bar{y}_{∞} be a function of \bar{x} , so that $\Delta \bar{y}_{\infty}$ is constant. Now perform the following co-ordinate transformations,

$$\bar{Y} = \frac{\bar{y}}{\bar{H}(\bar{x})},\tag{75}$$

$$\Delta \bar{Y} = \frac{\Delta \bar{y}}{\Delta \bar{y}_{\infty}} \,. \tag{76}$$

The mat region is then $\bar{Y} \in [0, 1]$, and the region above the mat is $\Delta \bar{Y} \in [0, 1]$. The transformation (75) turns the consolidation equation (72) into

$$\frac{\partial \phi}{\partial \bar{x}} + \frac{1}{\bar{H}(\bar{x})} \left(\bar{J}(\bar{x}) - \bar{Y} \frac{\mathrm{d}\bar{H}}{\mathrm{d}\bar{x}} \right) \frac{\partial \phi}{\partial \bar{Y}} = \frac{1}{\bar{H}(\bar{x})^2} \frac{\partial}{\partial \bar{Y}} \left(\bar{D} \frac{\partial \phi}{\partial \bar{Y}} \right). \tag{77}$$

An equation of analogous appearance for Δu_s in the mat is obtained when the same transformation is applied to (73). On the other hand, in the domain above the mat (76) is applied to the velocity equation, yielding

$$\frac{\partial \Delta u_s}{\partial \bar{x}} + \frac{1}{\Delta \bar{y}_{\infty}} \left(\bar{J}(\bar{x}) - \frac{\mathrm{d}\bar{H}}{\mathrm{d}\bar{x}} \right) \frac{\partial \Delta u_s}{\partial \Delta \bar{Y}} = \frac{\bar{\nu}_s(\phi_0)}{\bar{H}(\bar{x})^2} \frac{\partial^2 \Delta u_s}{\partial \Delta \bar{Y}^2} \,. \tag{78}$$

These equations were solved together with transformed versions of the relations (38) and (41), for $\bar{J}(\bar{x})$ and $\bar{H}(\bar{x})$, and the transformed boundary conditions. Note that the rate of displacement of the top of the fibre mat appears explicitly in the transformed equations. The discretisation in the \bar{y} -direction was performed using the Galerkin formulation of the finite element method with linear interpolation functions, whereas the \bar{x} -derivatives were discretised with the implicit-Euler method. The resulting discretisation is hence of second order accuracy in the \bar{y} direction and first order accuracy in the marching direction. Across the thickness of the boundary layers, 500 elements of uniform size were employed, and the step size was typically $\Delta \bar{x} = 10^{-3}$. The value 0.3 was chosen for $\Delta \bar{y}_{\infty}$.

The implementation of the outlined algorithm was carried out by formulating the problem in variational form, and then using the package 'femLego' for automated code generation (see Amberg et al. 1999).

Paper 4

4

Consolidation of sheared, strongly flocculated suspensions

By Claes Holmqvist and Anders Dahlkild

Department of Mechanics, KTH, SE-100 44 Stockholm, Sweden

To be submitted

The concept of a particle concentration dependent yield stress, previously employed in studies of uniaxial consolidation of a flocculated solid phase dispersed in a liquid, is extended to comprise flocculated phase shear strength. The inter-particle stresses are modelled by assuming that the stress state is always located on a yield-surface in stress-space, whose form is adopted from the Camclay plasticity theory for the quasi-static consolidation of soil. The theory is applied to the problem of combined compression and shearing of a strongly flocculated suspension contained between two plates, one being fixed and acting as a perfectly permeable filter, the other movable and acting as a piston by which the load is applied. Qualitatively, the evolution of the volume fraction of solids exhibits the same behaviour as during uniaxial consolidation without shear. Applying shear is however predicted to increase the rate of the drainage process, due to a reduced load bearing capacity of the flocculated phase, and the correspondingly higher pore pressures. A consideration of the large time asymptotic behaviour of the system when a constant compressive load is combined with a constant shearing velocity of the piston, reveals that even a small shearing velocity will increase the total drainage of the consolidation process.

1. Introduction

The separation of the liquid and solids contents of a suspension has widespread practical importance, and the task can be undertaken by e.g. subjecting the suspension to a gravity field (sedimentation) or by pressure filtration. In many situations, not only the rate of the the process is important, but also the morphology of the separated particle phase. Among the many examples of application areas, one finds fields as diverse as ceramics production, mineral processing, sludge treatment and paper manufacturing.

Historically, gravitational thickening has received more attention than pressure filtration. Kynch (1952) presents a kinematic theory of batch sedimentation based on the continuity equation of the solid phase. His main assumption is that the local flux of particles is a function of the local volume concentration of solids ϕ only. Long-range hydrodynamic forces are hence not accounted for

by the Kynch theory, and neither is the possibility that stresses are transmitted through the particle phase. The latter interactions have traditionally been accounted for by introducing a 'particle pressure', dependent upon ϕ , in the mathematical description of the separation process. In this way, a dependence of the flux on the gradient of ϕ is obtained. In a flocculated suspension, which is the kind that is of primary concern to this study, the origin of the particle pressure is the mechanical contact between the particles. Other possibilities exist, however. As an example, in the case of a stable colloidal suspension the particle pressure corresponds to the osmotic pressure. The first study of settling of a flocculated suspension incorporating particle stresses seems to have been the one by Michaels & Bolger (1962). The authors performed an analysis in which a constant uniaxial yield stress was employed. Early works that include concentration dependent particle stresses are the ones by Shirato et al. (1970) and Adorján (1975).

The Kynch analysis predicts the formation of discontinuities in ϕ during the settling process. According to Auzerais et al. (1988), the nature of these discontinuities have been much debated. By retaining both inertial effects and inter-particle stresses in the momentum balance of the batch settling problem, in addition to viscous drag and gravity, they are able to show by scaling arguments when approximate discontinuities in ϕ can be expected. In the case these are caused by stresses transmitted by the particles, the controlling parameter is a Péclet number, Pe, expressing the magnitude of gravity to inter-particle forces. Sharp gradients, separating regions where Kynch's theory is valid, only occur for large Pe. The analysis by Auzerais et al. also resolves the ambiguities previously involved in finding solutions by Kynch's method. Employing the technique of matched asymptotic expansions to the transient settling of a colloidal suspension, Davis & Russel (1988) obtain a solution valid in all regions of the suspension for large values of the relevant Pe.

In their studies of sedimentation of flocculated suspensions, Buscall & White (1987), Landman et al. (1988) and Howells et al. (1990) argue that for sufficiently high solids concentrations, the flocs form an interconnected network that can withstand external forces. To describe this they introduce a concentration dependent yield stress, which is defined as the value of the network stress above which the load cannot be balanced by elastic stresses in the solid phase. The network will then consolidate irreversibly. Unlike e.g. Adorján, they do not assume a priori that the particle pressure equals the yield stress. However, it is found that if the rate of consolidation of the solid phase is limited by the drainage of fluid between the particles, rather than the breaking and reformation of particle-particle bonds, this is likely to be a very good approximation. The same concept is used by Landman et al. (1991), Landman & Russel (1993) and Landman et al. (1995) to model particle stresses during pressure filtration. Buscall et al. (1986), Buscall et al. (1987) and Channell & Zukoski (1997) present experimental observations of yield-stress and elastic

properties of some strongly flocculated colloidal suspensions. Notably, the suspensions are observed to possess finite yield-limits in both shear and uniaxial compression.

All the hitherto cited theoretical studies of pressure filtration deal with uniaxial filtration, in which only normal loads are applied to the network of flocculated particles. However, in certain applications, the network is subjected also to shear loads. It is a reasonable assumption that these additional load components influence the ability of the solid structure to resist the normal load, since they increase the strain on the inter-particle bonds. Practical experience confirms that combining normal and shear loads does indeed have a favourable effect on separation rates (cf. e.g. Gustavsson 2003). Further, the displacements of the suspension constituents are not necessarily restricted to a single direction. It is evident that, to cover additional filtration applications, a more general model is needed for the stresses and strain-rates in the flocculated network, than is provided by the above previous works.

Gustavsson (2003) presents a model for consolidation, in which it is assumed that the inter-particle forces manifest themselves as both an isotropic strain-rate independent stress, and deviatoric viscous stresses. The model is used in a two-dimensional context to consider settling by gravity of a suspension contained in a closed vessel, while shear is applied to the sediment on the deposition surface. Deviatoric rate-independent stresses are however not taken into account.

For granular flows, Savage (1983) puts forward the proposition that, in the intermediate regime where both short-time collisions and continuous contacts occur between particles, the total stresses might be represented as the linear sum of a rate-independent frictional part and a viscous part obtained from the theory for the fully dynamic rapid flow regime. More detailed treatments based on this concept are performed by Johnson & Jackson (1987) and Johnson et al. (1990). The models for the frictional stress tensor are taken from the discipline of soil mechanics, where plasticity models have been developed for the yielding of porous media under general load conditions (cf. the standard textbooks, e.g. Wood 1990). Similarly, in the present study we add the divergence of a strain-rate independent stress tensor to the momentum balance of the particle phase in a two-fluid model of the suspension. For these inter-particle stresses, a plastic constitutive theory is adopted from the field of soil mechanics. In this way, it is possible to generalise the yield-stress concept previously employed for uniaxial consolidation, to also include the shear strength of the flocculated particle structure. By applying the model to plane sheared consolidation, its relation to the previously developed models is made apparent.

2. Formulation

Assume that we trap a flocculating suspension between two parallel, rigid, flat plates of infinite extension, lying in a horizontal xz-plane. One of the plates is

impermeable to both phases, whereas the other is impermeable only to the particle phase, and perfectly permeable to the liquid phase. They will be referred to as the 'piston' and the 'filter', respectively. The initial volume fraction of solids, ϕ_0 , is assumed homogeneous and higher than the gel point $\phi = \phi_g$ at which the solid phase first starts to form an interconnected network. Consequently, the entire space between the plates is filled with a flocculated network having an inner strength and capable of bearing certain loads. While the filter is fixed at y = 0, the piston is movable and its position y = H(t) is a function of time. Its movements, which in the present study will be limited to the xy-plane, is either controlled by specifying the vertical (i.e. in the y-direction) and horizontal (in the x-direction) loads by which it is applied to the suspension, $\Sigma_v(t)$ and $\Sigma_h(t)$, respectively, or by specifying its corresponding velocity components $U_v(t)$ and $U_h(t)$, respectively. A combination of the two modes of control can also be envisaged, one could e.g. specify $\Sigma_v(t)$ and $U_h(t)$.

As the resistance to liquid flow through the filter is zero, the liquid pressure p_c must there equal the ambient pressure, which is arbitrarily set to zero,

$$p_c(y=0) = 0. (1)$$

Both components of the particle phase velocity, denoted u_d , is zero at the filter, as is the horizontal component of the liquid phase velocity, u_c ,

$$\mathbf{u}_d\left(y=0\right) = \mathbf{0}\,,\tag{2}$$

$$(\boldsymbol{u}_c \times \boldsymbol{e}_y) (y = 0) = \boldsymbol{0}. \tag{3}$$

We will use the subscripts c and d to distinguish between the liquid (continuous) and particle (dispersed) phase, respectively. Whenever a subscript is needed denoting either phase, α is used. e_x and e_y are unit vectors pointing in the x- and y-directions, respectively. At the other end of the domain, both phases move with the velocity of the piston,

$$\mathbf{u}_d(y = H(t)) = \mathbf{u}_c(y = H(t)) = U_h(t)\mathbf{e}_x + U_v(t)\mathbf{e}_y.$$
(4)

2.1. Balance equations

We assume that the liquid and the solid constituents are incompressible, and that the phases can be regarded as isotropic continua. To describe the system we shall employ the conservation equations, relating volume averaged interstitial quantities, proposed by Anderson & Jackson (1967). Conservation of mass of the two phases is expressed as,

$$\frac{\partial \phi}{\partial t} + \nabla \cdot (\phi \mathbf{u}_d) = 0, \qquad (5)$$

$$\frac{\partial (1-\phi)}{\partial t} + \nabla \cdot ((1-\phi)\boldsymbol{u}_c) = 0.$$
 (6)

The momentum balance for the dispersed phase reads,

$$\rho_d \phi \frac{\mathrm{D} \boldsymbol{u}_d}{\mathrm{D} t} = -\phi \nabla p_c + \phi \nabla \cdot \boldsymbol{\sigma}_{Nc} - \boldsymbol{m} + \nabla \cdot \boldsymbol{\sigma}_{Nd} - \nabla \cdot \boldsymbol{\sigma}_d , \qquad (7)$$

and for the continuous phase,

$$\rho_c(1-\phi)\frac{\mathrm{D}\boldsymbol{u}_c}{\mathrm{D}t} = -(1-\phi)\nabla p_c + (1-\phi)\nabla \cdot \boldsymbol{\sigma}_{Nc} + \boldsymbol{m}.$$
 (8)

Above, the ρ_{α} are the densities of the constituents. The tensors $\sigma_{N\alpha}$ represents strain-rate dependent stresses due to deformation of the phases, m accounts for the exchange of momentum between the phases, and σ_d refers to rate-independent inter-particle stresses in the solid phase. The latter can be split into an isotropic part represented by p_d , which conceptually can be thought of as a 'particle pressure', and a deviatoric remainder τ_d , according to

$$-\boldsymbol{\sigma}_d = -p_d \boldsymbol{I} + \boldsymbol{\tau}_d \,, \tag{9}$$

where I is the identity tensor. Hence, the sign convention is such that compressive particle stresses are positive. It ought to be mentioned that the deviatoric tensor τ_d was not included in the original equations suggested by Anderson & Jackson. The material time derivatives are defined as

$$\frac{\mathbf{D}\boldsymbol{u}_{\alpha}}{\mathbf{D}t} = \frac{\partial\boldsymbol{u}_{\alpha}}{\partial t} + \boldsymbol{u}_{\alpha} \cdot \nabla \boldsymbol{u}_{\alpha}. \tag{10}$$

The drag term m should depend on the relative velocity between the phases, i.e. $u_d - u_c$. We adopt (the purely viscous) Darcy's law,

$$\boldsymbol{m} = \frac{\mu_c \left(1 - \phi\right)}{k(\phi)} \left(\boldsymbol{u}_d - \boldsymbol{u}_c\right). \tag{11}$$

Here, μ_c is the dynamic viscosity of the continuos phase, and $k(\phi)$ is the permeability of the flocculated network. Several models exist for $k(\phi)$. E.g., for the flow through a network of spherical particles with radius a, the Brinkman model (see e.g. Scheidegger 1957, p. 113) states that,

$$k(\phi) = \frac{2a^2}{9\phi} \frac{(2-3\phi)^2}{3\phi + 4 + 3(8\phi - 3\phi^2)^{\frac{1}{2}}}.$$
 (12)

For the purpose of the present study, we use an expression of more simple form introduced by Ingmanson *et al.* (1959),

$$k(\phi) = \frac{1}{3.5S_0^2 \phi^{1.5}} \,. \tag{13}$$

This is an adaptation of the Kozeny-Carman equation suited to low concentration pulp mats, in which S_0 is the specific surface of the particles. The models (12) and (13) can both be written as $k(\phi) = l^2K(\phi)$, where l is the length scale of the pore sizes in the flocculated network, and $K(\phi)$ is a dimensionless function. Notably, in (13) we have $l = 1/S_0$ and $K(\phi) = 1/(3.5\phi^{1.5})$.

Anderson & Jackson (1967) suggest that the the rate dependent tensors $\sigma_{N\alpha}$ are modelled after a Newtonian pattern, using concentration dependent shear and bulk viscosities that account for both true mechanical stresses and Reynolds stresses.

2.2. Rate independent solid stresses

We shall now proceed to develop constitutive relations for the rate independent stresses p_d and τ_d . To do so, we suppose that the dispersed phase behaves like a plastic-rigid material. Subject to sufficiently small loads, the solid phase resists all deformations. When the local stresses are of sufficient magnitude, represented by some limit in stress-space, the particle phase will deform irreversibly. The ensemble of such stress states is defined by the following yield criterion,

$$F\left(\boldsymbol{\sigma}_{d},\phi\right)=0\,,\tag{14}$$

which is the equation of a yield-surface in stress-space. F is referred to as the yield function. The ϕ -dependence in (14) reveals that we assume the resistance to deformation to be dependent on the local fraction of particles. Whenever $F(\sigma_d, \phi) < 0$, the stress-state lies 'inside' the yield-surface, and, given our assumption about rigidity, locally the dispersed phase behaves like a stiff body. In a general situation the stress state in the particle phase would then not be determinate with the present model. One way to address this problem is to prescribe an elastic behaviour before irreversible deformations occur. We shall however simply postulate that, at any instant, the stresses in the solid phase are such that the criterion (14) is fulfilled. As a consequence, the model will not be able to properly describe unloading, in the sense that the stress-state moves to the inside of the yield-surface. Below it will become evident that this limitation is not quite as restrictive as it might first seem.

Here we adopt the yield-surface introduced by Roscoe & Burland (1968), as part of the modified Cam clay theory in the field of soil mechanics. For the present study, we have essentially used a simple version of that model presented by Wood (1990), pp. 112–137. Thus, the yield surface is taken to be

$$F(p_d, q_d, p_0(\phi)) = q_d^2 - M^2 p_d (p_0(\phi) - p_d) = 0,$$
(15)

which corresponds to an ellipse in the stress plane (p_d, q_d) , centred around $(p_d, q_d) = (\frac{1}{2}p_0(\phi), 0)$, with axis lengths $p_0(\phi)$ and $Mp_0(\phi)$ along the abscissa and the ordinate, respectively². In terms of cartesian components, the invariants p_d and q_d of the stress tensor σ_d are given by

$$p_d = \frac{1}{3}\sigma_d^{kk}$$
 and $q_d = \sqrt{\tau_d^{ij}\tau_d^{ij}} = \sqrt{\left(\sigma_d^{ij} - \frac{1}{3}\delta^{ij}\sigma_d^{kk}\right)\left(\sigma_d^{ij} - \frac{1}{3}\delta^{ij}\sigma_d^{kk}\right)}$. (16)

The deviatoric stress measure q_d equals, up to a constant factor, the von Mises effective stress in classical plasticity theory. To appreciate the choice of p_d and q_d as the two important scalar measures of the stress state, one can observe that in a purely elastic deformed material, p_d determines the stored elastic

¹Although it will not be the case in the present study, the yield-surface is not necessarily closed, wherefore the notion of the stress-state being 'inside' the yield surface is perhaps best thought of as a way of saying that $F(\sigma_d, \phi) < 0$.

²In principal stress space $(\sigma_d^1, \sigma_d^2, \sigma_d^3)$, the yield surface is an ellipsoid of length $\sqrt{3}p_0(\phi)$ and thickness $\sqrt{3}Mp_0(\phi)$, with one end at the origin and extending in the direction of isotropic states, $\frac{1}{\sqrt{3}}(1,1,1)$.

energy due to volumetric deformations, whereas q_d determines the elastic energy stemming from (isochoric) shape changes. The function $p_0(\phi)$ denotes the yield-limit when the solid phase is subject to solely isotropic loads p_d . It is here taken to be of a power-law form,

$$p_0(\phi) = \sigma_0 \phi^n, \tag{17}$$

where σ_0 and n are constants. This is in accordance with the work by Buscall et al. (1987), who find that the ϕ -dependence of the yield-limit in uniaxial compression is consistent with power-law behaviour. Implicitly, (17) implies that $\phi_g = 0$. As $p_0(\phi)$ is a monotonically increasing function of ϕ , it accounts for the hardening that occurs when the particle phase is compressed. The shape-factor M is some positive constant, its value depending on the nature of the dispersed phase.

We further adopt an associated flow rule (see e.g. Wood 1990, pp. 103–104). The flow potential then coincides with the yield surface, and when deformations occur, the components of the strain-rate tensor of the dispersed phase, e_d , are obtained as

$$-e_d^{ij} = -\frac{1}{2} \left(\frac{\partial u_d^i}{\partial x^j} + \frac{\partial u_d^j}{\partial x^i} \right) = X \frac{\partial F}{\partial \sigma_d^{ij}}, \quad X \ge 0.$$
 (18)

Equation (18) implies that the deformation-rate vector (in strain-rate space) is pointing in the direction of the outward normal to the yield surface. The negative sign in front of e_d^{ij} ensures that compression corresponds to negative values of $\nabla \cdot \mathbf{u}_d$, and the proportionality factor X sets the magnitudes of the components. If the six independent deformation rates e_d^{ij} are known, the equations (15) and (18) provide us with seven equations for the six independent stresses σ_d^{ij} and X^3 .

Let us introduce the volumetric and deviatoric strain rate invariants of the dispersed phase, corresponding to (16) for the stresses,

$$e_p = e_d^{kk}$$
 and $e_q = \sqrt{\left(e_d^{ij} - \frac{1}{3}\delta^{ij}e_d^{kk}\right)\left(e_d^{ij} - \frac{1}{3}\delta^{ij}e_d^{kk}\right)}$. (19)

Using the definitions (16) and (19) together with the equations (15) and (18), we can derive that

$$e_p = -X \frac{\partial F}{\partial p_d} = -2XM^2 \left(p_d - \frac{p_0(\phi)}{2} \right) , \qquad (20)$$

$$e_q = X \frac{\partial F}{\partial q_d} = 2X q_d. \tag{21}$$

 $^{^{3}}$ Note that we could not have determined the strain-rates from a known stress state, as (15) only relates the (then) known stress components. In traditional plasticity theory, where the stresses are provided by elastic constitutive relations, the proportionality factor X is determined by requiring that the stress state remains on the yield-surface during its evolution due to strain-hardening (the 'consistency condition'). The strain-rates can then be obtained.

Now, (15) and (20)–(21) are three equations to obtain p_d , q_d and X from the deformation rate measures e_p and e_q . Combining the last two expressions yields the following useful relations for X,

$$X = \frac{e_q}{2q_d} = -\frac{e_p}{2M^2 \left(p_d - \frac{p_0(\phi)}{2}\right)} \ge 0.$$
 (22)

As a consequence of the inequality, compression $(e_p < 0)$ takes place for $p_d > \frac{1}{2}p_0(\phi)$, and expansion for $p_d < \frac{1}{2}p_0(\phi)$. Deformation without volume change can occur only if $p_d = \frac{1}{2}p_0(\phi)$, which is referred to as the critical state. Of course, the deviatoric deformation rate is then not determined by (22). From the yield surface (15) and the flow rule (18), it is possible to obtain an arbitrary deformation-rate component as

$$e_d^{ij} = 2X \left(-\frac{1}{3}M^2 \left(p_d - \frac{1}{2}p_0(\phi) \right) \delta^{ij} + \tau_d^{ij} \right).$$
 (23)

2.3. Scaling

In is instructive to scale the equations presented in the previous sections. A suitable macroscopic length scale is the initial distance between the plates, H_0 . Let U_0 be a velocity measure. By scaling the co-ordinate vector \boldsymbol{x} , the velocities \boldsymbol{u}_{α} , and time as

$$\mathbf{x}^* = \frac{\mathbf{x}}{H_0} , t^* = \frac{U_0 t}{H_0} , \mathbf{u}_{\alpha}^* = \frac{\mathbf{u}_{\alpha}}{U_0} ,$$
 (24)

and inserting the new variables into the continuity equations (5) and (6), we see that they retain the same form (except for the superscripts * denoting non-dimensional quantities). In order to scale the momentum equations (7) and (8), we introduce the quantities

$$p_c^* = \frac{l^2 p_c}{\mu_c U_0 H_0} , \quad \sigma_{N\alpha}^* = \frac{H_0 \sigma_{N\alpha}}{\mu_c U_0} , \quad m^* = \frac{l^2 m}{\mu_c U_0} , \quad \sigma_d^* = \frac{\sigma_d}{\sigma_1}.$$
 (25)

Note that this choice of scales reflects that the liquid pressure should be of the order of the interface drag accumulated over a distance H_0 . The deformation-rate dependent stresses are estimated by assuming a Newtonian behaviour, where the liquid phase viscosity has been used as a measure of the effective shear and bulk viscosities of both phases. The solid stresses σ_d are scaled with σ_1 , denoting some suitable measure to be discussed shortly⁴. Insertion into (7) results in

$$Re_{d} \left(\frac{l}{H_{0}}\right)^{2} \phi \frac{D \boldsymbol{u}_{d}}{D t} = -\phi \nabla p_{c} + \left(\frac{l}{H_{0}}\right)^{2} \phi \nabla \cdot \boldsymbol{\sigma}_{N c}$$
$$-\frac{(1-\phi)}{K(\phi)} \left(\boldsymbol{u}_{d} - \boldsymbol{u}_{c}\right) + \left(\frac{l}{H_{0}}\right)^{2} \nabla \cdot \boldsymbol{\sigma}_{N d} - \frac{1}{P e} \nabla \cdot \boldsymbol{\sigma}_{d}, \qquad (26)$$

⁴Note that chosing σ_0 , i.e. the coefficient in the power-law (17), would not be appropriate. It corresponds to the yield-stress at $\phi = 1$, which is far outside the validity range of that relation.

where the superscripts * have been dropped for clarity. We shall continue to do so. In the same way, (8) yields

$$Re_{c} \left(\frac{l}{H_{0}}\right)^{2} (1 - \phi) \frac{\mathrm{D}\boldsymbol{u}_{c}}{\mathrm{D}t} =$$

$$-(1 - \phi)\nabla p_{c} + \left(\frac{l}{H_{0}}\right)^{2} (1 - \phi)\nabla \cdot \boldsymbol{\sigma}_{Nc} + \frac{(1 - \phi)}{K(\phi)} (\boldsymbol{u}_{d} - \boldsymbol{u}_{c}) . \tag{27}$$

The equations (26) and (27) contain the Reynolds numbers

$$Re_{\alpha} = \frac{\rho_{\alpha} U_0 H_0}{\mu_c} \,, \tag{28}$$

and a Péclet number

$$Pe = \frac{\mu_c H_0 U_0}{l^2 \sigma_1} \,, \tag{29}$$

expressing the ratio between convection of the solid phase, and transport due to network stress gradients. The present study deals with strongly flocculated suspensions, and we expect the term containing the rate-independent stresses in (26) to be $\mathcal{O}(1)$. Hence, we set Pe=1. When the piston is controlled by specifying its velocity, we take U_0 as the initial vertical velocity, $U_v(0^+)$, immediately after the consolidation process starts. The definition of Pe then provide the stress measure σ_1 ,

$$\sigma_1 = \frac{\mu_c H_0 U_0}{l^2} \,. \tag{30}$$

On the other hand, if the process is controlled by the applied loads, we let σ_1 be the initial vertical load, i.e. $\Sigma_v(0^+)$. The velocity scale is then

$$U_0 = \frac{l^2 \sigma_1}{\mu_c H_0} \,. \tag{31}$$

Consider now the relations for the rate independent stresses in §2.2. If we write the isotropic yield limit as $p_0(\phi) = \sigma_1 P_0(\phi)$, where $P_0(\phi) = (\sigma_0/\sigma_1)\phi^n$, and introduce the dimensionless quantities

$$e_d^{ij*} = \frac{H_0 e_d^{ij}}{U_0} , \quad X^* = \frac{H_0 \sigma_1 X}{U_0} ,$$
 (32)

the results (14)–(23) retain the same appearances in dimensionless form, except that $p_0(\phi)$ must be replaced by $P_0(\phi)$ at all occurrences.

The piston velocity components $U_h(t)$ and $U_v(t)$ are scaled with U_0 , and the applied loads $\Sigma_h(t)$ and $\Sigma_v(t)$ with σ_1 . The forms of the boundary conditions (1)–(4) do not change from the scaling. From now on, we shall only refer to scaled quantities, unless otherwise explicitly specified.

3. Analysis

It is now time to adapt the equations presented in §2 to the considered filtration problem. Rather than dealing with two separate phases, we prefer to formulate the problem in terms of a mixture (the suspension) and a dispersed phase, moving relative to the mixture. Let us introduce the flux densities $j_d = \phi u_d$ and $j_c = (1 - \phi)u_c$. Summing (5) and (6) yields an equation for the total suspension flux density j,

$$\nabla \cdot \boldsymbol{j} = 0 \quad , \quad \boldsymbol{j} = \boldsymbol{j}_d + \boldsymbol{j}_c \,. \tag{33}$$

We also define a disperse phase flux density relative to the mixture as

$$\mathbf{j}_r = \mathbf{j}_d - \phi \mathbf{j} = \phi \left(1 - \phi \right) \left(\mathbf{u}_d - \mathbf{u}_c \right). \tag{34}$$

By rewriting (5), it is possible to express continuity of the solid phase like

$$\frac{\partial \phi}{\partial t} + \nabla \cdot (\phi \mathbf{j}) + \nabla \cdot \mathbf{j}_r = 0.$$
 (35)

To simplify the treatment, we now assume that $(l/H_0)^2$ and $Re_{\alpha}(l/H_0)^2$ are small, and neglect the terms containing these factors in (26) and (27). It is easy to estimate a posteriori the magnitude of the inertial terms. As for the rate dependent stresses, we do not know their exact form, but shall nevertheless tacitly suppose that the deformation rates are sufficiently small to make them negligible. This is consistent with the hypothesis made by Buscall & White (1987) that the deformation of the solid phase is rate-determined by the resistance to displace the two phases with respect to each other, rather than by the resistance to relative movements between particles. It has since been employed in several studies, see e.g. Howells et al. (1990) and Landman et al. (1991). Summing what remains of (26) and (27), we obtain the momentum balance for the mixture,

$$0 = -\nabla p_c - \nabla p_d + \nabla \cdot \boldsymbol{\tau}_d, \tag{36}$$

where (9) has been used to split the particle stresses into an isotropic and a deviatoric part. Using (36) to eliminate the liquid pressure in (26), the relative flux density can be expressed as⁵

$$\boldsymbol{j}_r = \phi(1 - \phi)K(\phi)\left(-\nabla p_d + \nabla \cdot \boldsymbol{\tau}_d\right). \tag{37}$$

3.1. One-dimensional compression

Assume a situation of plain strain in the xy-plane. Due to the infinite dimensions of the bounding surfaces, we suppose that there are no horizontal gradients. Thus $e_d^{xx} = e_d^{zz} = e_d^{xz} = e_d^{yz} = 0$. It follows from (22) and (23) that

$$\tau_d^{xx} = \tau_d^{zz} = -\frac{1}{2}\tau_d^{yy} = \frac{1}{3}M^2\left(p_d - \frac{1}{2}P_0(\phi)\right) \quad , \quad \tau_d^{xz} = \tau_d^{yz} = 0.$$
 (38)

⁵In equation (37), j_r is explicitly given by σ_d . However, if a bulk viscosity had been retained from σ_{Nd} , a term containing $\nabla \cdot (j_r/\phi)$ would have appeared on the right hand side.

Above, we have made use of the fact that $\tau_d^{kk}=0$. For the non-zero strain rates we obtain

$$e_d^{xy} = 2X\tau_d^{xy}$$
 , $e_d^{yy} = -2XM^2\left(p_d - \frac{1}{2}P_0(\phi)\right)$. (39)

The assumption made in §2.2 that the stress state always fulfils the yield criterion (15) provides us with a relation between $\sigma_d^{yy} = p_d - \tau_d^{yy}$ and τ_d^{xy} . Using the results (38), the yield surface can be written as

$$\frac{\left(\sigma_d^{yy} - \frac{1}{2}P_0(\phi)\right)^2}{\left(\frac{1}{2}P_0(\phi)\sqrt{1 + \frac{2}{3}M^2}\right)^2} + \frac{\tau_d^{xy^2}}{\left(\frac{1}{2}P_0(\phi)\frac{M}{\sqrt{2}}\right)^2} = 1.$$
 (40)

This is an ellipse in the plane $(\sigma_d^{yy}, \tau_d^{xy})$, centred at $(\frac{1}{2}P_0(\phi), 0)$, and with a major and minor axis of length $P_0(\phi)\sqrt{1+\frac{2}{3}M^2}$ and $P_0(\phi)\frac{M}{\sqrt{2}}$, respectively (see figure 1)⁶. The top of the yield-ellipse always remains on the dashed straight line in the figure, when it expands or contracts due to changes in the concentration. As the flow rule (18) tells us that the deformation-rate of the solid phase is perpendicular to the yield-surface, we can also relate the horizontal and vertical directions in figure 1 with compression in the y-direction and shearing in the x-direction, respectively. Consequently, $\sigma_d^{yy} = P_0(\phi)/2$ separates the possible stress states into two halves, such that when σ_d^{yy} is larger (smaller) than $P_0(\phi)/2$, yielding of the particle phase will result in compression (expansion). This particular value of σ_d^{yy} will be denoted $\sigma_c(\phi)$, and the corresponding value of τ_d^{xy} is denoted $\tau_c(\phi)$. At the stress state $(\sigma_d^{yy}, \tau_d^{xy}) = (\sigma_c(\phi), \tau_c(\phi))$, shearing of the solid phase obviously occurs without volumetric deformations, and this hence corresponds to the critical state mentioned in §2.2. The dashed line in figure 1 is accordingly referred to as the 'critical state line'. To determine the shear rate at the critical state would require us to incorporate the neglected rate dependent stresses in the model. As our interest lies in consolidation of the flocculated suspension, we instead suppose that the stress-states at all positions, and at all times, are such that $\sigma_d^{yy} > \sigma_c(\phi)$, i.e. on the right half of the yield-surface in figure 1. The relation (40) can then be rewritten as

$$\sigma_d^{yy} = f(\phi, \tau_d^{xy}), \tag{41}$$

where f is a single-valued function for $|\tau_d^{xy}| < \tau_c(\phi)$. When the stress τ_d^{xy} increases, the particle network is able to resist less vertical stress σ_d^{yy} before yielding. If the network is not subject to any horizontal shear stresses, the yield-limit is given by the intersection of the ellipse and the horizontal axis. Attempts have been made to determine this limit for some suspensions (see e.g. Buscall $et\ al.\ 1987$).

 $^{^6}$ No deformations take place in the principal stress direction z. Thus, due to the associated flow rule, the yield-ellipse (40) is a line on the surface of the yield-ellipsoid in principal stress space, such that the normal to the surface along the line has no component in the z-direction.

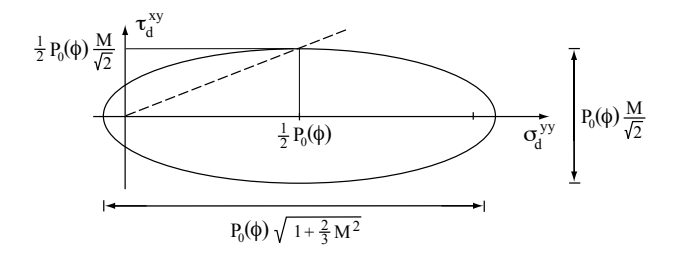


FIGURE 1. The yield-surface in the σ_d^{yy} - τ_d^{xy} -plane. The dashed line indicates the position of the critical stress state at different concentrations.

Eliminating X from the expressions in (39), and introducing σ_d^{yy} , we can relate the deformation rates for a given stress state,

$$e_d^{xy} = -\frac{\left(1 + \frac{2}{3}M^2\right)}{M^2} \frac{\tau_d^{xy}}{\left(\sigma_d^{yy} - \frac{1}{2}P_0(\phi)\right)} e_d^{yy}. \tag{42}$$

The equations (40) and (42) provide the necessary constitutive coupling between stresses and non-zero deformation rates in the flocculated phase.

Now, the vertical flux density of the suspension at the piston must equal $U_v(t)$, which, when used in (33), yields

$$j^y = U_v(t). (43)$$

The total flux density is thus (naturally) a spatial constant. As the horizontal gradients are zero, the x-component of (36) tells us that τ_d^{xy} is constant across the gap between the plates,

$$\tau_d^{xy} = \Sigma_h(t) \,. \tag{44}$$

This is a consequence of there being nothing else than the particle stress to balance the shear stress applied by the piston. In the vertical direction, the situation is different, and equation (36) can be integrated to reveal that

$$p_c + \sigma_d^{yy} = \Sigma_v(t) \,. \tag{45}$$

Equation (37) gives the components of the relative flux density,

$$j_r^x = 0, (46)$$

$$j_r^y = -\phi(1-\phi)K(\phi)\frac{\partial \sigma_d^{yy}}{\partial y}.$$
 (47)

Both phases hence move with the same horizontal velocity. Using the results (41), (43), (44) and (47) in (35), we find an equation for the concentration,

$$\frac{\partial \phi}{\partial t} + U_v(t) \frac{\partial \phi}{\partial y} = \frac{\partial}{\partial y} \left(D(\phi, \Sigma_h(t)) \frac{\partial \phi}{\partial y} \right), \tag{48}$$

where the 'diffusivity function' is

$$D(\phi, \Sigma_h(t)) = \phi(1 - \phi)K(\phi)\frac{\partial f}{\partial \phi}(\phi, \Sigma_h(t)). \tag{49}$$

The advection-diffusion equation (48)⁷ has the same appearance as its counterparts in studies of uniaxial pressure filtration (see e.g. Landman *et al.* 1991). The difference is that generalising the yield-stress concept to include the shear-strength of the flocculated network has introduced an explicit time-dependence in the diffusivity function. As $\Sigma_h(t)$ can be controlled externally, we have some influence over the diffusivity.

The boundary conditions needed to solve (48) are different depending on whether we control the piston by the applied load, or by prescribing its displacement velocity. Assume first the former alternative. The condition (1) and equation (45) then implies that $\sigma_d^{yy}(0,t)$ is known. So is τ_d^{xy} from (44), and thus (41) implicitly provides the volume fraction of particles at the filter. For our particular choice of $P_0(\phi)$ in §2.3, with given vertical and horizontal network loads relation (41) can be inverted, giving

$$\phi(0,t) = f_{\phi}^{-1} \left(\Sigma_{v}(t), \Sigma_{h}(t) \right) , \qquad (50)$$

the subscript ϕ indicating the variable with respect to which the inversion is performed. According to (4), the relative flux is zero at the piston, which through (47) translates into

$$\frac{\partial \sigma_d^{yy}}{\partial y} \left(H(t), t \right) = \frac{\partial \phi}{\partial y} \left(H(t), t \right) = 0. \tag{51}$$

Using the condition (2) and the result (43) in equation (34), we get the vertical relative flux at the filter in terms of $U_v(t)$ and $\phi(0,t)$. The vertical piston velocity is obtained by combining this result with (47),

$$U_{v}(t) = \left[(1 - \phi)K(\phi) \frac{\partial \sigma_{d}^{yy}}{\partial y} \right]_{y=0} = \left[\frac{D(\phi, \Sigma_{h}(t))}{\phi} \frac{\partial \phi}{\partial y} \right]_{y=0}.$$
 (52)

The vertical velocity component is apparently influenced by the applied horizontal shear stress.

To obtain the horizontal velocity of the piston, we first need the deformation rates of the network. Using (41) and (44) to eliminate the network stresses in (42) yields,

$$e_d^{xy} = g\left(\phi, \Sigma_h(t)\right) e_d^{yy}. \tag{53}$$

The deformation rates are related to the flux densities as

$$e_d^{xy} = \frac{1}{2} \frac{\partial j^x}{\partial y} \quad , \quad e_d^{yy} = \frac{\partial}{\partial y} \left(\frac{j_r^y}{\phi} \right) .$$
 (54)

The relative flux density in the relation for e_d^{yy} can be rewritten as an expression containing $D(\phi, \Sigma_h(t))$ and the gradient of ϕ using (41), (47) and (49). Then,

⁷Note that for all $\phi \leq \phi_g$, $\sigma_d^{yy} \equiv 0$, resulting in $D \equiv 0$. (48) is then of hyperbolic type. However, this is of no concern to us, since we have assumed the suspension to be completely flocculated.

insertion of the deformation rates into (53), followed by an integration, yields the horizontal mixture flux density

$$j^{x}(y,t) = 2 \int_{0}^{y} g\left(\phi, \Sigma_{h}(t)\right) \frac{\partial}{\partial y'} \left(\frac{D\left(\phi, \Sigma_{h}(t)\right)}{\phi} \frac{\partial \phi}{\partial y'}\right) dy', \tag{55}$$

where the condition $j^x(0,t) = 0$ has been introduced. As $j_r^x = 0$, it follows that $u_d^x = u_d^y = j^x$, and the desired velocity component is $U_h(t) = j^x(H(t), t)$.

When the piston velocity is set, (51) is still used as a boundary condition. By reshaping (52), a condition for the concentration gradient at y = 0 is obtained, that replaces (50). The shear stress appearing in the equations is obtained by solving (55), evaluated at y = H(t), for $\Sigma_h(t)$ as a function of $U_h(t)$.

Finally, if we decide to specify $\Sigma_v(t)$ and $U_h(t)$, we use equations (50)–(52), but determine $\Sigma_h(t)$ from $U_h(t)$ in the manner just described.

3.2. Solution method

The equations (48)–(55) have been solved numerically. To facilitate the numerical treatment, a change of co-ordinates, $y = H(t)\tilde{y}$, was undertaken in order to have a domain with fixed boundaries, $\tilde{y} \in [0,1]$. The spatial discretisation was then performed using the Galerkin formulation of the finite element method with linear interpolation functions. For the time-derivative, the implicit Crank-Nicolson formulation was employed. The complete discretisation is thus of second order accuracy in both space and time. The implementation of the algorithm was carried out by formulating the problem in variational form, and then using the package femLego for automated code generation (see Amberg et al. 1999).

A shooting method based on (55) was used to obtain $\Sigma_h(t)$ when $U_h(t)$ was specified. At each time-step, the equations (48)–(52) were solved using a guessed value for $\Sigma_h(t)$, which was updated till the correct value of $U_h(t)$ was found.

To produce the presented computational results, the domain $\tilde{y} \in [0, 1]$ was resolved with 400 elements of uniform size. The non-dimensional time step dt was $3.1 \cdot 10^{-7}$.

4. Results

The initial concentration and distance between the plates were set to $\phi_0 = 0.05$ and $H_0 = 0.01$ m. For the parameters in (17) determining the isotropic yield limit, and the specific surface, we chose the values used by Zahrai *et al.* (1998), i.e. $\sigma_0 = 500$ kPa, n = 2.5 and $S_0 = l^{-1} = 18 \cdot 10^5$ m⁻¹, respectively. Buscall *et al.* (1986) conclude that the yield stress in shear for a strongly flocculated polystyrene latex suspension appears to be one to two orders of magnitude smaller than the corresponding uniaxial limit, and Buscall & White (1987) argue that this is reasonable, since in shear a substantially larger fraction of the network bonds are in a state of tension. Consequently, M was set to the

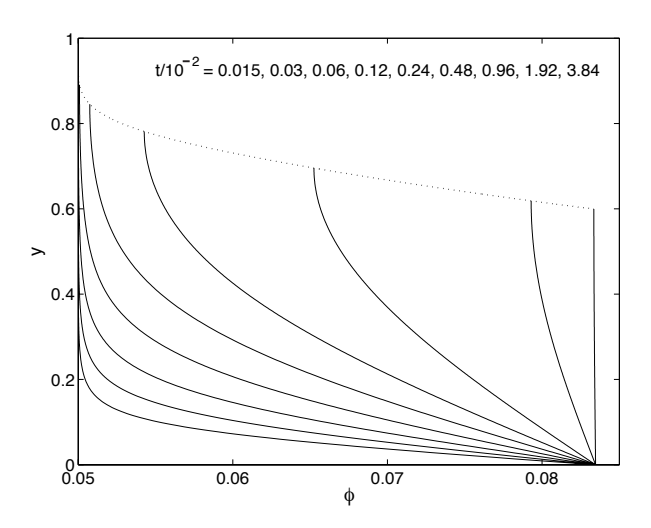


FIGURE 2. Evolution of the volume fraction of solids following an impulsively applied load at t=0 of $\Sigma_v=1$ and $\Sigma_h=0.028$. The profiles correspond to the solution times given in the figure, time increasing from left to right. The dotted line gives the concentration at the position of the piston. Note that the time between two plots doubles with each new profile. $\sigma_0/\sigma_1=500$.

value 0.287, giving a critical shear stress $\tau_c(\phi)$ that is a fraction 0.1 of the yield limit in uniaxial compression. The viscosity of the continuous phase was $\mu_c = 10^{-3}$ Pas.

4.1. Comparison with uniaxial compression

Figure 2 contains volume fraction profiles from a simulation where the loads $\Sigma_v(t)$ and $\Sigma_h(t)$ were abruptly increased at t=0 to 1 and 0.028, respectively, and then held constant. The ratio σ_0/σ_1 in the scaled isotropic yield function $P_0(\phi)$ was 500. At the initial concentration, the flocculated network is weak. Since at all times we must have $\Sigma_h(t) < \tau_c(\phi)$ (cf. §3.1), the value for Σ_h had to be chosen small. Qualitatively the evolution of ϕ in figure 2 shows the same behaviour as is reported in the literature on uniaxial compression (see e.g. Landman et al. 1991). At the filter, the network must balance the load applied by the piston, and ϕ thus immediately reaches its final value. In the rest of the domain, the liquid pressure supports part of the applied load. However, progressively the load is shifted from the liquid to the network, which is then compressed. As can be seen, at the onset the compression rate is very high.

There are, however, differences with respect to the uniaxial case. We note that initially the concentration close to the piston remains at approximately $\phi_0 = 0.05$. This would be the case regardless of whether a horizontal load is

applied or not. Hence, in that region the yield-surface is of its original size for some time after t=0. If $\Sigma_h(t)=0$, the stress state will lie on the abscissa in figure 1. Specifically, σ_d^{yy} is given by the intersection with the ellipse. If $\Sigma_v(t)$ is larger than that value, the remainder of the load is, according to (45), supported by the liquid pressure. In a situation with the same $\Sigma_v(t)$, but a non-zero $\Sigma_h(t)$, the network must also completely balance the latter load. As the stress state remains on the same yield-surface as when no horizontal load is used, figure 1 tells us that the stress σ_d^{yy} is then smaller, and a larger fraction of the vertical load is supported by the liquid. In other words, $\Sigma_h(t) > 0$ yields higher pore pressures, and, as we shall see shortly, faster drainage. When $\Sigma_v(t)$ and $\Sigma_h(t)$ are held constant, the drainage will eventually stop when the stresses in the network equal the piston load. The particle concentration is then homogeneous, and can be deduced by determining how large the yield-surface has to be in order for the stress state to lie upon it. It follows that, for a given stress σ_d^{yy} , a larger τ_d^{xy} necessitates a yield-surface corresponding to a higher concentration. The final degree of consolidation thus increases with the applied shear load.

Figure 3 contains a comparison between uniaxial and sheared filtration, where $\Sigma_v(t)$ and the horizontal piston velocity $U_h(t)$ were impulsively increased at t=0 and then held constant. The ratio σ_0/σ_1 was again 500. The applied shear stresses necessary to achieve the chosen values of U_h are plotted in figure 4. Also in the figures 3 and 4, the initial rate of change is very high.

It is here appropriate to make a short comment on the scaling. From the work on uniaxial pressure filtration by Landman et al. (1991) we know that some of the scales introduced in §2.3 are only relevant after sufficiently long times. Landman et al. find that, when no shearing is done and at small times, the true length and velocity scales of the problem are a fraction \sqrt{t} and $1/\sqrt{t}$, respectively, of those presently used. The result should carry over to sheared consolidation, provided the employed loads $\Sigma_h(t)$, and consequently τ_d^{xy} , are small in comparison with the vertical stresses σ_d^{yy} . As this is the case at the initial stages of the process⁸, it immediately explains the initial high rates in figures 2 and 3. Consider now a situation where the horizontal piston velocity is set to a constant value U_h . The integral in equation (55) evaluated at the piston is then constant. The diffusivity, defined by (49), is not affected by the differing initial scales, and we therefore conclude, based on our knowledge of the behaviour of the length scale, that the function $g(\phi, \Sigma_h(t))$ should scale with \sqrt{t} at small times. From (42) and (53), it follows that τ_d^{xy} , and consequently $\Sigma_h(t)$, must do so as well, which explains the rapid increase of the loads in figure 4. This is confirmed by the logarithmic plots of the small time behaviour of $\Sigma_h(t)$ in figure 5.

⁸Note that the assumption of the stress state always being located on the yield surface, and of $\Sigma_h(0) = 0$, implicitly means that, before the consolidation starts, a vertical load is already applied to the piston that is balanced by a finite vertical stress in the network, its magnitude equal to the uniaxial yield limit when $\phi = \phi_0$.

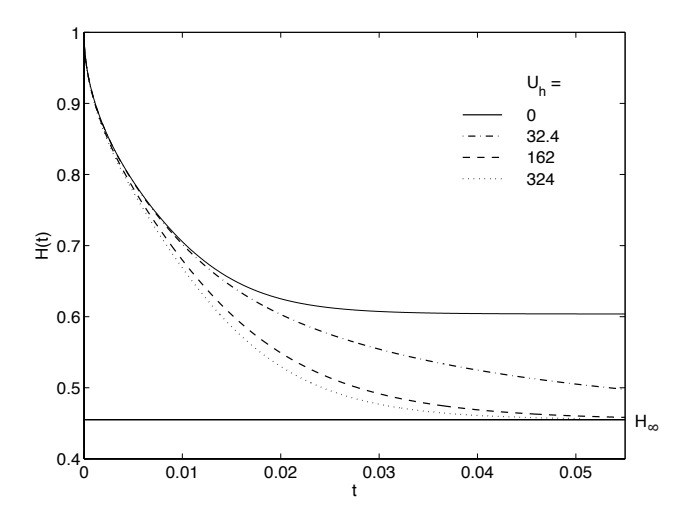


FIGURE 3. The distance between the plates when Σ_v and U_h are impulsively increased at t=0 and then kept at constant values. $\Sigma_v=1$. The horizontal velocities corresponding to the curves are stated in the figure. The solid horizontal line indicates the asymptotic distance $H_{\infty}=0.455$. The asymptotic limit for the non-sheared compression is 0.604. The corresponding asymptotic concentrations are $\phi_{\infty}=0.11$ and $\phi=0.083$, respectively. $\sigma_0/\sigma_1=500$.

We note that, combining a constant vertical load with a constant horizontal piston velocity will eventually result in a situation of pure shear deformation when the compression of the network stops and Σ_v is balanced by the particle stresses. It is a consequence of the associated flow rule that the critical state $(\sigma_c(\phi), \tau_c(\phi))$ has then been reached at all points between the plates. When the compression ceases, the liquid pressure is identically zero, and we have from (45) that $\lim_{t\to\infty} \sigma_d^{yy} = \sigma_c(\phi_\infty) = \Sigma_v$. It follows that the asymptotic limit concentration, denoted ϕ_∞ , can be determined, and that it is necessarily homogeneous. Knowing this, we conclude that the network shear stress τ_d^{xy} , and from (44) the applied load $\Sigma_h(t)$, will asymptotically approach the value $\Sigma_{h\infty} = \tau_c(\phi_\infty)$, regardless of the specified velocity U_h . Conservation of mass also yields the limit distance between the plates, H_∞ . From figure 3 it is clear that the applied shear loads increased the dewatering rates. Such an effect could in a real suspension be attributed to restructuring of the network, and increased loading of the inter-particle bonds.

4.2. The flow field

In figure 6 and 7, the horizontal velocity component, and the non-zero deformation rates e_d^{yy} and e_d^{xy} , are presented for the simulation corresponding to the

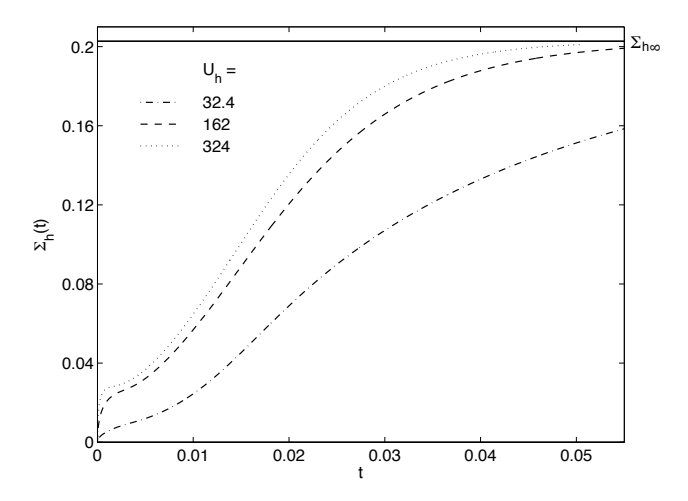


FIGURE 4. The applied horizontal piston load when Σ_v and U_h are impulsively increased at t=0 and then kept at constant values. The same values for Σ_v and U_h were used as in figure 3, and curves of the same line type in the two figures correspond to each other. The solid horizontal line indicates the asymptotic load $\Sigma_{h\infty} = 0.203$. $\sigma_0/\sigma_1 = 500$.

dotted curves in figures 3 and 4, i.e. the vertical load and the horizontal piston velocity were instantaneously increased and then held constant. $U_h = 324$ and $\sigma_0/\sigma_1 = 500$. In the studied situation of one-dimensional compression, we have that $-\phi e_d^{yy} = \mathrm{D}\phi/\mathrm{D}t$. The profiles in the left part of figure 7 hence provide the relative compression rate of the network when following a material point.

Initially, there are no velocity gradients in the region next to the piston. The upper part of the network thus translates like a stiff cake. Close to the filter, the shear-rate and the volumetric deformation-rate attain large values. As time proceeds, an increasing part of the network between the plates become subject to deformations. Since the volume fraction of solids increases close to the filter, the network grows stronger in that region, and the positions of the largest deformation rate magnitudes move towards the piston. Eventually, the critical state will be reached at all points (see §4.1). The volumetric deformation-rate is then zero, and both phases undergo pure shear deformation. Note that the dashed velocity profile corresponding to t=0.05 in figure 6 is not linear, although it represents a time when the system is close to the asymptotic critical state, as can be seen in figures 3 and 4. This can also be concluded from the corresponding non-constant shear-rate profile in figure 7, and is a deficiency in the model originating from our neglect of deformationrate dependent stresses. Suppose for a moment that they had been included. The horizontal load $\Sigma_h(t)$ would then be balanced by the sum of τ_d^{xy} and a shear-rate dependent stress. At the critical state, $\tau_d^{xy} = \tau_c(\phi_\infty)$ which is still a

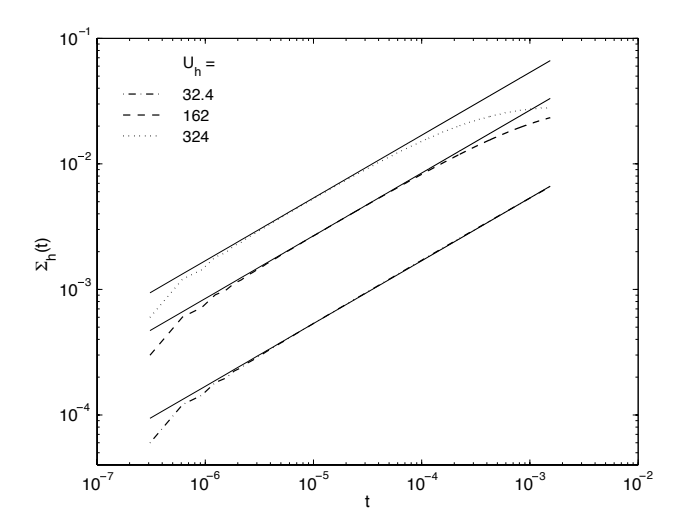


FIGURE 5. The small time behaviour of the horizontal piston load $\Sigma_h(t)$ in the simulations presented in figure 4, where Σ_v and U_h were impulsively increased at t=0 and then kept at constant values. The corresponding solid lines are plots of $\Sigma_h(t) = 5.22 U_h \sqrt{t}$. Values for U_h are stated in the figure. $\sigma_0/\sigma_1 = 500$. Note that $dt = 3.1 \cdot 10^{-7}$, and that the smallest time scales can never be resolved.

constant throughout the network since the concentration at the critical state, ϕ_{∞} , is homogeneous and determined from the applied vertical load (as described in §4.1). The conclusion must be that since the limit value of the total horizontal stress, $\Sigma_{h\infty}$, is a constant, the added shear-rate dependent stress is also asymptotically constant. Thus, the limit velocity profile must be linear, i.e. with a constant shear rate. However, with the present model, there is no reason to expect the system to approach that state. It is clear from figure 4 that the same shear load $\Sigma_{h\infty}$ can yield different velocities U_h , and hence different velocity profiles $\lim_{t\to\infty} u_d^x(y,t)$. The limit profile is determined by the history of the process.

With our without the deformation-rate dependent stresses, the limit concentration ϕ_{∞} will be the same if Σ_v is the same, and thus also the asymptotic stress $\lim_{t\to\infty} \tau_d^{xy}$ (cf. the argument in §4.1). However, the limit value for $\Sigma_h(t)$ will be higher, the difference being constituted by the rate dependent stresses. If these are retained in the mixture equation (36), and are assumed of Newtonian character, the x-component of that relation will yield

$$\left(\frac{l}{H_0}\right)^2 \frac{\bar{\mu}}{\mu_c} \frac{\partial j^x}{\partial y} + \tau_d^{xy} = \Sigma_h(t),$$
(56)

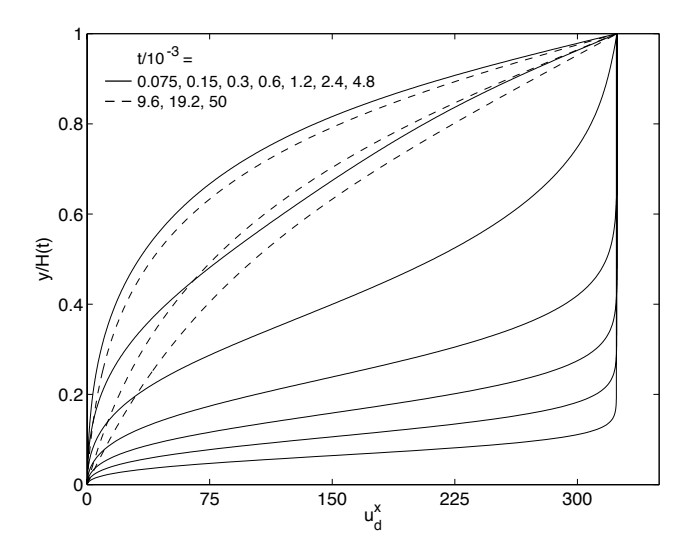


FIGURE 6. The horizontal velocity profiles for the solid phase at different instances (stated in the figure) following the instantaneous application of a constant load $\Sigma_v = 1$ and a fix horizontal velocity $U_h = 324$. The profiles correspond to the dotted curves in figures 3 and 4. For the solid curves, time increases with distance from the abscissa, whereas the opposite is true for the dashed curves. $\sigma_0/\sigma_1 = 500$.

where the contributions from the two phases to the rate dependent term have been lumped together, and $\bar{\mu}$ denote an effective mixture viscosity. The horizontal velocity component of both phases are supposed equal to the mixture flux density j^{x9} . Considering the values for l and H_0 used in the present study, and the shear-rates in figure 7, it is clear that the rate dependent stresses are small in comparison with τ_d^{xy} if $\bar{\mu}/\mu_c \ll 10^5$, where 1000 and 0.2 have been used as typical values of the shear-rate and τ_d^{xy} , respectively. Nevertheless, the viscous stresses, albeit small, would have a quite noticeable effect on the asymptotic velocity profile in figure 6, rendering it linear.

The horizontal deformation of the network that occurs during sheared consolidation is of interest to some applications where it is desirable to smear out inhomogeneities in the particle concentration, e.g. paper manufacturing. Figure 8 therefore shows the deformation of an initially straight vertical material line in the flocculated network. At t=0, the vertical load is increased to $\Sigma_v=1$, and the horizontal velocity of the piston is set to $U_h=32.4$, which is the same case as corresponds to the dash-dotted lines in figures 3 and 4. $\sigma_0/\sigma_1=500$. Some particle trajectories are also plotted.

⁹This is only approximately true in the case of a non-zero liquid phase shear viscosity, but the approximation is at least as good as neglecting the rate dependent term in (56)

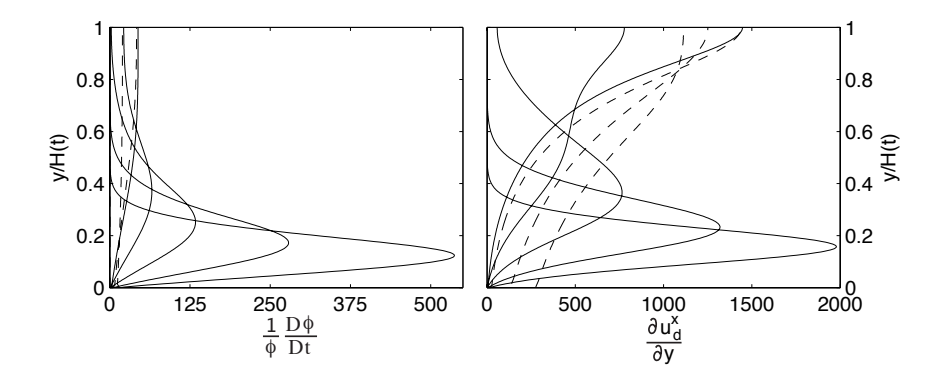


FIGURE 7. The particle phase relative compression-rate (left fig.) and shear-rate (right fig.), following the instantaneous application of a constant load $\Sigma_v = 1$ and a fix horizontal velocity $U_h = 324$, at the instances $t/10^{-3} = 0.3$, 0.6, 1.2, 2.4, 4.8, 9.6, 19.2, 50. The curves correspond to the later time velocity profiles in figure 6. Solid lines: Profiles with the extremum at lower y correspond to earlier times. Dashed lines: Larger maximum values correspond to earlier times. $\sigma_0/\sigma_1 = 500$. At t = 50 the volumetric deformation rate is so small that the profile is not visible.

5. Concluding remarks

Previously, the concept of a particle concentration dependent yield-stress has been used to model uniaxial consolidation of flocculated suspensions (see e.g. Buscall & White 1987, Landman et al. 1991). The present work generalises the yield-stress concept to comprise flocculated phase shear strength. The effects of applying shear during the drainage process are then investigated. It is found that the evolution of the volume fraction of solids quantitatively exhibits the same behaviour as during uniaxial consolidation. Applying a shear load does, however, in the presented model, increase the rate of the dewatering, due to the generation of higher pore pressures. The additional velocity component present during shearing is also interesting to applications, as it provides a way of influencing the morphology of the compressed solid phase, e.g. by smearing out inhomogeneities. When shear-related issues are of interest, the importance of deformation-rate dependent stresses should be considered. It was concluded that even very small rate dependent stresses will have an effect on the long-time asymptotic velocity profile when the piston moves with a constant horizontal velocity, and a constant vertical load is applied.

We have combined a plasticity model for the quasi-static yielding of soil, and incorporated it into a two-phase model for the flocculated suspension. Although here applied to one-dimensional compression, the approach should be possible to extend to more complex situations involving a dispersed solid phase

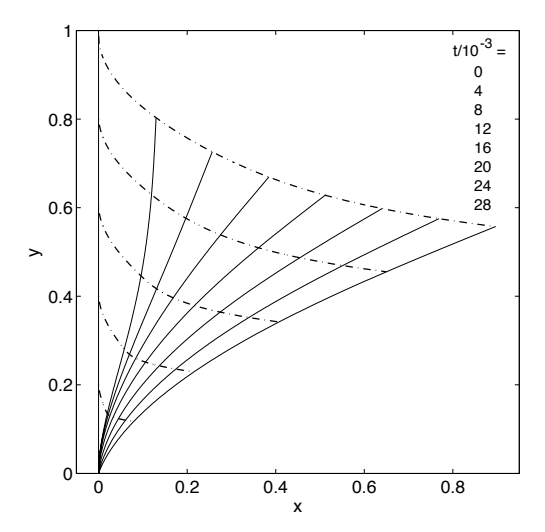


FIGURE 8. The deformation of a material line in the flocculated network. At t=0, the vertical load and the horizontal velocity of the piston are suddenly increased to $\Sigma_v=1$ and $U_h=32.4$, respectively, and then held constant. This figure hence corresponds to the dash-dotted lines in figures 3 and 4. The material line is initially vertical, and is illustrated by the solid curves at the instances stated in the figure. The dash-dotted lines are particle trajectories. $\sigma_0/\sigma_1=500$.

possessing an inner strength. Some complications would appear, however. We have relied heavily upon the assumption that the stress state is always located somewhere on the yield-surface in order to relate stresses and strains. In one-dimensional problems where no relaxation of the applied load occurs, this is not a restriction. However, although possible to make, the assumption that the yield-criterion is always fulfilled would not be adequate in a general situation. If we drop it, in a multi-dimensional problem the stress state would not be determinate with the presented model. A constitutive model is then needed for the flocculated phase behaviour at stress states located inside the yield-surface in stress-space. The natural choice is to prescribe an elastic behaviour in that region.

The modelling choices made, in particular our choice of yield surface and the associated flow rule, were motivated by simplicity. Naturally, they have to be adapted to the suspension under consideration. Unfortunately, we are not aware of any experimental work that provides enough data to trace out the yield surface of a flocculated suspension in e.g. σ_d^{yy} - τ_d^{xy} -space, let alone to determine the flow rule.

It is our hope that it will be possible to continue to draw upon the knowledge and models gathered in the field of solid mechanics to deal with other issues relevant to strongly flocculated suspensions, e.g. the effects of anisotropy.

6. Acknowledgements

Financial support was provided by the Swedish Agency for Innovation Systems (VINNOVA) and the industrial partners in the FaxénLaboratory.

References

- Adorján, L. A. 1975 A theory of sediment compression. In 11th International Mineral Processing Congress, pp. 297–318. Cagliari.
- Amberg, G., Tönhardt, R. & Winkler, C. 1999 Finite element simulations using symbolic computing. *Math. Comput. Simulation* 49, 257–274.
- Anderson, T. B. & Jackson, R. 1967 A fluid mechanical description of fluidized beds. *Ind. Engng Chem. Fundam.* **6** (4), 527–539.
- Auzerais, F. M., Jackson, R. & Russel, W. B. 1988 The resolution of shocks and the effects of compressible sediments in transient settling. *J. Fluid Mech.* **195**, 437–462.
- Buscall, R., McGowan, I. J., Mills, P. D. A., Stewart, R. F., Sutton, D., White, L. R. & Yates, G. E. 1987 The rheology of strongly-flocculated suspensions. J. Non-Newtonian Fluid Mech. 24, 183–203.
- Buscall, R., Mills, P. D. A. & Yates, G. E. 1986 Viscoelastic properties of strongly flocculated polystyrene latex dispersions. *Colloids and Surfaces* 18, 341–358.
- Buscall, R. & White, L. R. 1987 The consolidation of concentrated suspensions, part 1—the theory of sedimentation. *J. Chem. Soc., Faraday Trans.* 1 83, 873–891.
- Channell, G. M. & Zukoski, C. F. 1997 Shear and compressive rheology of aggregated alumina suspensions. *AIChE Journal* **43** (7), 1700–1708.
- DAVIS, K. & RUSSEL, W. B. 1988 An asymptotic description of transient settling and ultrafiltration of colloidal dispersions. *Phys. Fluids A* 1 (1), 82–100.
- GUSTAVSSON, K. 2003 Mathematical and numerical modeling of 1-d and 2-d consolidation. PhD thesis, Royal Institute of Technology (KTH), Stockholm.
- HOWELLS, I., LANDMAN, K. A., PANJKOV, A., SIRAKOFF, C. & WHITE, L. R. 1990 Time-dependent batch settling of flocculated suspensions. Appl. Math. Modelling 14, 77–86.
- INGMANSON, W. L., ANDREWS, B. D. & JOHNSON, R. C. 1959 Internal pressure distributions in compressible mats under fluid stress. Tappi J. 42 (10), 840–849.
- JOHNSON, P. C. & JACKSON, R. 1987 Frictional-collisional constitutive relations for granular materials, with application to plane shearing. J. Fluid Mech. 176, 67–93.
- JOHNSON, P. C., NOTT, P. & JACKSON, R. 1990 Frictional—collisional equations of motion for particulate flows and their application to chutes. J. Fluid Mech. 210, 501–533.

- Kynch, G. 1952 A theory of sedimentation. Trans. Faraday Soc. 48, 166–176.
- LANDMAN, K. A. & RUSSEL, W. B. 1993 Filtration at large pressures for strongly flocculated suspensions. *Phys. Fluids A* 5 (3), 550–560.
- LANDMAN, K. A., SIRAKOFF, C. & WHITE, L. R. 1991 Dewatering of flocculated suspensions by pressure filtration. *Phys. Fluids A* **3** (6), 1495–1509.
- LANDMAN, K. A., WHITE, L. R. & BUSCALL, R. 1988 The continuous-flow gravity thickener: Steady state behaviour. *AIChE J.* **34** (2), 239–252.
- LANDMAN, K. A., WHITE, L. R. & EBERL, M. 1995 Pressure filtration of flocculated suspensions. *AIChE Journal* **41** (7), 1687–1700.
- MICHAELS, A. S. & BOLGER, J. C. 1962 Settling rates and sediment volumes of flocculated kaolin suspensions. *Ind. Engng Chem. Fundam.* 1 (1), 24–33.
- ROSCOE, K. H. & BURLAND, J. B. 1968 On the generalised stress-strain behaviour of 'wet' clay. In *Engineering Plasticity* (ed. J. Heyman & F. A. Leckie), pp. 535–609. Cambridge: Cambridge University Press.
- SAVAGE, S. B. 1983 Granular flows down rough inclines review and extension. In Mechanics of Granular Materials: New Models and Constitutive Relations (ed. J. T. Jenkins & M. Satake), pp. 261–282. Amsterdam: Elsevier.
- Scheideger, A. E. 1957 The Physics of Flow Through Porous Media. University of Toronto Press.
- Shirato, M., Kato, H., Kobayashi, K. & Sakazaki, H. 1970 Analysis of settling of thick slurries due to consolidation. *J. Chem. Engng Japan* 3, 98–104.
- Wood, D. M. 1990 Soil Behaviour and Critical State Soil Mechanics. Cambridge University Press.
- Zahrai, S., Martinez, M. D. & Dahlkild, A. A. 1998 Estimating the thickness of the web during twin-wire forming. *Journal of Pulp and Paper Science* **24** (2), 67–72.

Paper 5

Influence of viscous stresses on the sheared consolidation of flocculated suspensions

By Claes Holmqvist and Anders Dahlkild

Department of Mechanics, KTH, SE-100 44 Stockholm, Sweden

To be submitted

The authors have previously developed a (purely) plastic model for the problem of combined compression and shearing of a flocculated suspension contained between two plates, one being fixed and acting as a perfectly permeable filter, the other movable and acting as a piston by which the load is applied. In the presence of compressive deformations, force balance is achieved by strain hardening of the flocculated network. However, the model experiences failure in situations of isochoric deformations, a deficiency stemming from the lack of a mechanism that can balance the applied external loads, which causes the deformation rates to become indeterminate. We here resolve this deficiency by attributing 'viscous' stresses to the dispersed phase in addition to the plastic stresses. These are modelled after a Newtonian pattern, with a constant effective viscosity. Viscous stresses also eliminates the history dependence of the asymptotic shear rate profile when a constant compressive load is combined with a constant shearing velocity of the piston. The trend of improved drainage rates when higher shear loads are applied by the piston, is observed to persist also when larger loads are employed than could be simulated with the purely plastic model. Finally, the visco-plastic model is employed to obtain an asymptotic solution of the concentration in a mat of flocculated suspension, that is on one side bounded by clear fluid and on the other by a permeable solid surface, subjected to a combined drainage flow and cross flow of clear liquid.

1. Introduction

In a wide range of applications found in e.g. the minerals, chemical, wastewater and paper manufacturing industries, it is necessary to separate flocculated solid material dispersed in a liquid phase. Available techniques include gravity settling, vacuum filtration, centrifugation and pressure filtration. The present study is concerned with the last of these, which can be described as expression of liquid by drained compression. Conceptually, this can be realized in a cylindrical vessel containing the suspension, at one end fitted with a membrane permeable to the liquid phase only, and at the other end equipped with a piston used to force the liquid through the filter. If desired, a shear load can also be applied to the suspension by rotating the piston with respect to the vessel.

In their studies of sedimentation of flocculated suspensions, Buscall & White (1987), Landman et al. (1988) and Howells et al. (1990) argue that for sufficiently high solids concentrations, the flocs form an interconnected network that can withstand external forces. To describe this they introduce a concentration dependent yield stress, which is defined as the value of the network stress above which the load cannot be balanced by elastic stresses in the solid phase. The network will then consolidate irreversibly. Unlike other early works on separation incorporating a yield limit (e.g. Shirato et al. 1970; Adorján 1975), they do not assume a priori that the stresses in the flocculated phase equals the yield value. However, it is found that if the rate of consolidation of the solid phase is limited by the drainage of fluid between the particles, rather than the breaking and reformation of particle-particle bonds, this is likely to be a very good approximation. The same concept is used by Landman et al. (1991), Landman & Russel (1993) and Landman et al. (1995) to model particle stresses during pressure filtration. Buscall et al. (1986), Buscall et al. (1987) and Channell & Zukoski (1997) present experimental observations of yield-stress and elastic properties of some strongly flocculated colloidal suspensions. Notably, the suspensions are observed to possess finite yield-limits in both shear and uniaxial compression.

All the hitherto cited theoretical studies of pressure filtration deal with uniaxial filtration, in which only normal loads are applied to the network of flocculated particles. However, in certain applications, the network is subjected also to shear loads. It is a reasonable assumption that these additional load components influence the ability of the solid structure to resist the normal load, since they increase the strain on the inter-particle bonds. Practical experience confirms that combining normal and shear loads does indeed have a favourable effect on separation rates (cf. e.g. Gustavsson 2003). Further, the displacements of the suspension constituents are not necessarily restricted to a single direction. It is evident that, to cover additional filtration applications, a more general model is needed for the stresses and strain-rates in the flocculated network, than is provided by the above previous works.

For granular flows, Savage (1983) puts forward the proposition that, in the intermediate regime where both short-time collisions and continuous contacts occur between particles, the total stresses might be represented as the linear sum of a rate-independent frictional part and a viscous part obtained from the theory for the fully dynamic rapid flow regime. More detailed treatments based on this concept are performed by Johnson & Jackson (1987) and Johnson et al. (1990). The models for the frictional stress tensor are taken from the discipline of soil mechanics, where plasticity models have been developed for the yielding of porous media under general load conditions (cf. the standard textbooks, e.g. Wood 1990). In a similar fashion, with the ambition to generalise the previously referenced filtration models to comprise flocculated phase shear strength, Holmqvist (2005) (henceforth referred to as H&D) patches the divergence of a rate-independent stress, representing the inter-particle forces,

to the momentum balance of the particle phase in a two-fluid model of the flocculated suspension. The modified Cam-clay constitutive model by Roscoe & Burland (1968) is used to model the particle-stress tensor, and by considering the problem of plane sheared consolidation, the differences with respect to the conventional models are elucidated. Among other things, an increased drainage efficiency is predicted when a shear load is applied during the filtration, as observed in applications.

Soil plasticity theory, combined with elasticity, is also employed by Zhao $et\ al.\ (2003)$ for an analysis of wall effects in a Compression–Permeability Cell¹, and by Owen $et\ al.\ (1998)$ to study the rolling of prepared sugar cane. However, these works do not address the effects of applying shear loads, nor the role played by the deviatoric stresses in the model.

Deformation rate dependent stresses were not included in the momentum balance for the particle phase put forward by H&D. As a result of the choice of constitutive theory, external loads transmitted to the solid phase can only be balanced by strain hardening due to volumetric compression. At certain ('critcal') stress states, resulting in isochoric deformations, this mechanism is not at work and the deformation rates become undefined. This can be avoided by including viscous deviatoric stresses. Gustavsson (2003) presents a viscoplastic model for consolidation in which it is assumed that the inter-particle forces manifest themselves as both an isotropic strain-rate independent stress, and deviatoric viscous stresses. Deviatoric plastic stresses are however not included. In the present study, we shall incorporate the previously neglected viscous stresses into the model by H&D (thus obtaining a description in which viscous and plastic deviatoric stresses co-exist) to prevent model failure at critical stress states. This is of essence, since in a situation of continuous shearing the system will eventually attain such stress states. Further, H&D observes that in certain cases the long time asymptotic strain-rates are dependent on the history of the load process. This artefact is removed when strain-rate dependent deviatoric stresses are accounted for.

2. Formulation

Consider a flocculated suspension trapped between two parallel, rigid, flat plates of infinite extension, lying in a horizontal xz-plane (cf. figure 1). The suspension consists of two incompressible components – a liquid (continuous) phase, and a solid particle (dispersed) phase, the local volume fraction of which is denoted ϕ . Both phases are treated as isotropic continua. One of the plates, located at y=0, is impermeable to the particle phase, but perfectly permeable to the liquid phase. This plate will be referred to as the 'filter', and its position is fix. The other plate, located at y=H(t), is impermeable to both phases, and its position is a function of time. We shall refer to this boundary as the 'piston', and its movements, which we limit to the xy-plane, are either controlled by directly specifying its vertical and horizontal velocity, denoted

¹These devices are used for uniaxial consolidation experiments.

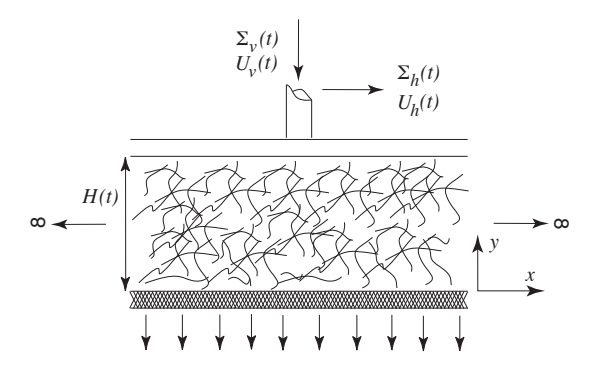


FIGURE 1. Schematic illustration of the considered situation: A flocculated suspension trapped between two parallel flat plates, of infinite extension in the horizontal xz-plane. The upper plate (the piston) is impermeable to both phases. The lower plate (the filter) is impermeable only to the solid phase, and perfectly permeable to the liquid phase. The consolidation process is controlled by specifying either the load $(\Sigma_h(t), \Sigma_v(t))$ by which the piston is applied to the suspension, or its velocity $(U_h(t), U_v(t))$. A combination of the two modes of control is also possible.

 $U_v(t)$ and $U_h(t)$, respectively, or by specifying the vertical and horizontal load components, denoted $\Sigma_v(t)$ and $\Sigma_h(t)$, respectively, by which it is applied to the suspension.

Due to the perfect permeability of the filter, the liquid pressure, p_c , must at the filter surface equal the surrounding atmospheric pressure, which we arbitrarily set to zero, i.e.

$$p_c(y=0) = 0. (1)$$

At the filter, the particle phase is supposed to obey the no slip and no penetration conditions, providing

$$\mathbf{u}_d(y=0) = 0, \tag{2}$$

for the dispersed phase velocity u_d . The subscripts c and d are henceforth used to distinguish between the continuous and the dispersed phase, respectively. Also the liquid velocity component tangential to the plate surface is zero at the filter, and thus

$$(\boldsymbol{u}_c \times \boldsymbol{e}_y)(y=0) = 0, \qquad (3)$$

where e_y , and later e_x , are the unit vectors in the vertical and horizontal directions, respectively. On the piston side, both phases move with the velocity of the plate,

$$\mathbf{u}_d(y = H(t)) = \mathbf{u}_c(y = H(t)) = U_h(t)\mathbf{e}_x + U_v(t)\mathbf{e}_y. \tag{4}$$

Note that u_d and u_c represent the mass averaged interstitial velocities of the phases.

The initial volume fraction of solids, ϕ_0 , is assumed homogeneous and higher than the gel point $\phi = \phi_g$ at which the solid phase first starts to form an interconnected network. Consequently, the entire space between the plates is filled with a flocculated network having an inner strength and capable of bearing certain loads.

The following quantities are also defined,

$$\boldsymbol{j}_d = \phi \boldsymbol{u}_d \,, \tag{5}$$

$$\boldsymbol{j}_c = (1 - \phi) \boldsymbol{u}_c \,, \tag{6}$$

$$\boldsymbol{j} = \boldsymbol{j}_d + \boldsymbol{j}_c \,, \tag{7}$$

$$\mathbf{j}_r = \mathbf{j}_d - \phi \mathbf{j} = \phi (1 - \phi) (\mathbf{u}_d - \mathbf{u}_c), \tag{8}$$

where j_d and j_c are the particle and liquid volume flux densities (i.e. the superficial velocities), j is the mixture (or suspension) volume flux density, and j_r is the disperse phase flux density relative to the mixture.

2.1. Balance equations

The requirement of global volume continuity, and continuity of the dispersed phase, read, respectively,

$$\nabla \cdot \boldsymbol{j} = 0, \tag{9}$$

$$\frac{\partial \phi}{\partial t} + \nabla \cdot \mathbf{j_d} = 0. \tag{10}$$

Neglecting all effects of inertia, the momentum balance for the suspension mixture can be expressed as (see e.g. Ungarish 1993, p. 22),

$$0 = -\nabla p_c + \nabla \cdot \boldsymbol{\tau}_{Nd} - \nabla \cdot \boldsymbol{\sigma}_d. \tag{11}$$

Above, σ_d is the stress tensor originating from deformation-rate independent inter-particle forces, and τ_{Nd} represents rate dependent shear stresses within the particle phase. For simplicity, no such forces have been attributed to the liquid phase. This is justifiable in systems where the viscous liquid stresses are small compared to the components of τ_{Nd} . The stress tensor σ_d can be split into an isotropic 'particle pressure', denoted p_d , and a deviatoric remainder τ_d , according to

$$-\boldsymbol{\sigma}_d = -p_d \boldsymbol{I} + \boldsymbol{\tau}_d \,, \tag{12}$$

where I denotes the identity tensor. Traditionally, τ_d is not included in studies of consolidation. Note that according to (12) compressive stress components are positive. We neglect the possibility of a particle phase bulk viscosity, and assume that the deformation-rate dependent tensor τ_{Nd} is deviatoric and of Newtonian character,

$$\boldsymbol{\tau}_{Nd} = 2\mu_d \left(\boldsymbol{e}_d - \frac{tr\boldsymbol{e}_d}{3} \boldsymbol{I} \right). \tag{13}$$

Here, a constant dispersed phase effective viscosity, μ_d , has been introduced. If desired, it could later be attributed with a concentration dependence. Frequently, power laws are employed for this purpose (see e.g. Bennington & Kerekes 1996). The rate of strain tensor e_d is

$$\boldsymbol{e}_d = \frac{1}{2} \left(\nabla \boldsymbol{u}_d + \nabla \boldsymbol{u}_d^T \right) . \tag{14}$$

To close the system of equations, we adopt the following constitutive relation for the relative flux density,

$$\dot{\boldsymbol{j}}_r = -\phi(1-\phi)\frac{k(\phi)}{\mu_c} \left(\nabla \cdot \boldsymbol{\sigma}_d - \nabla \cdot \boldsymbol{\tau}_{Nd}\right). \tag{15}$$

A similar relation, without the stress tensor τ_{Nd} , has previously been employed by H&D. In (15), μ_c is the dynamic viscosity of the liquid phase, and $k(\phi)$ is the permeability of the particle network, for which we adopt the relation

$$k(\phi) = \frac{1}{3.5S_0^2\phi^{1.5}}. (16)$$

It was suggested by Ingmanson *et al.* (1959) for low concentration pulp mats, and the parameter S_0 is the specific surface of the fibres. The postulate (15) reveals that we suppose the velocity difference between the phases to result from inter-particle forces only.

2.2. Rate independent particle stresses

A model for the rate-independent inter-particle forces is now presented. A somewhat more lengthy treatment is performed by H&D. We assume that in order to deform the solid phase, the following yield criterion must be fulfilled, which stems from the modified Cam-clay theory introduced by Roscoe & Burland (1968) in the field of soil mechanics.

$$F(p_d, q_d, p_0(\phi)) = q_d^2 - M^2 p_d (p_0(\phi) - p_d) = 0,$$
(17)

where q_d is (up to a constant factor) the von Mises effective stress used in classical plasticity theory. It is defined as

$$q_d = \sqrt{\tau_d^{ij} \tau_d^{ij}} = \sqrt{\left(\sigma_d^{ij} - \frac{1}{3}\delta^{ij}\sigma_d^{kk}\right) \left(\sigma_d^{ij} - \frac{1}{3}\delta^{ij}\sigma_d^{kk}\right)}.$$
 (18)

The particle pressure expressed in component form is

$$p_d = \frac{1}{3}\sigma_d^{kk} \,. \tag{19}$$

Equation (17) describes an elliptic 'yield-surface' in p_d - q_d -space, centred around $(p_d, q_d) = (p_0(\phi)/2, 0)$, and with a major and minor axis of length $p_0(\phi)$ and $Mp_0(\phi)$, respectively. At positions where the stress state σ_d is such that the resulting $p_d(\sigma_d)$ and $q_d(\sigma_d)$ lie 'inside' the yield surface (i.e. $F(p_d, q_d) < 0$), it is assumed that the material behaves like a stiff body. In a general situation, the stress state is not determinate in regions where the network is stiff. We shall avoid dealing with the interior of the yield-surface by specifying that criterion (17) is always satisfied. Naturally, this restricts the cases possible to consider,

but it is an adequate assumption for the present study, where we at all times take care not to relax the load experienced by any part of the network. The function $p_0(\phi)$ expresses the yield limit when purely isotropic loads are applied, and we adopt the power law

$$p_0(\phi) = m \left(\phi - \phi_q\right)^n. \tag{20}$$

The dependence of the yield-surface on ϕ , through $p_0(\phi)$, ensures that volumetric compaction of the network induces hardening of the flocculated structure.

Further, we adopt an associated flow rule, according to which the flow potential coincides with the yield surface. The deformations of the solid phase are perpendicular to the flow potential, and hence

$$-e_d^{ij} = -\frac{1}{2} \left(\frac{\partial u_d^i}{\partial x^j} + \frac{\partial u_d^j}{\partial x^i} \right) = X \frac{\partial F}{\partial \sigma_d^{ij}}, \quad X \ge 0.$$
 (21)

The deformation rate e_d^{ij} , viewed as a vector in strain-rate space, is pointing in the direction of the outward normal to the yield-surface, and its magnitude is set by the proportionality factor X. Clearly, compression, i.e. $\nabla \cdot \boldsymbol{u}_d < 0$, causes the yield-surface to expand.

We also define the scalar deformation rate measures,

$$e_p = e_d^{kk}$$
 and $e_q = \sqrt{\left(e_d^{ij} - \frac{1}{3}\delta^{ij}e_d^{kk}\right)\left(e_d^{ij} - \frac{1}{3}\delta^{ij}e_d^{kk}\right)}$. (22)

corresponding to isotropic (volumetric) deformations and deviatoric (shape changing) deformations, respectively. They are related to p_d and q_d as

$$e_p = -X \frac{\partial F}{\partial p_d} = -2XM^2 \left(p_d - \frac{p_0(\phi)}{2} \right) , \qquad (23)$$

$$e_q = X \frac{\partial F}{\partial q_d} = 2X q_d. \tag{24}$$

Combining (23) and (24), we find that

$$X = \frac{e_q}{2q_d} = -\frac{e_p}{2M^2 \left(p_d - \frac{1}{2}p_0(\phi)\right)} \ge 0.$$
 (25)

It is seen that compression $(e_p < 0)$ occur when $p_d > p(\phi)/2$, and expansion $(e_p > 0)$ when $p_d < p(\phi)/2$. Deformations without volume change can only occur at the so called 'critical state', in which $p_d = p_0(\phi)/2$. Note that the deviatoric deformation-rate can then not be determined from (25).

3. Analysis

It is often more instructive to discuss dimensionless quantities, and we shall therefore scale the variables. As a representative length, we chose the initial distance between the filter and the piston, denoted H_0 . We further let U_0 be the velocity scale, and l a typical size of the pores in the particle network. We

shall use $l = 1/S_0$. The magnitude of the rate-independent solid stresses is denoted σ_1 . The following scaled variables are defined,

$$\mathbf{x}^* = \frac{\mathbf{x}}{H_0} , \quad t^* = \frac{U_0 t}{H_0} , \quad \mathbf{u}_{\alpha}^* = \frac{\mathbf{u}_{\alpha}}{U_0} , \quad \mathbf{j}_{\alpha}^* = \frac{\mathbf{j}_{\alpha}}{U_0} , \quad \mathbf{e}_d^* = \frac{H_0 \mathbf{e}_d}{U_0}, \quad (26)$$

$$X^* = \frac{H_0 \sigma_1 X}{U_0} , \quad p_c^* = \frac{l^2 p_c}{\mu_c U_0 H_0} , \quad \boldsymbol{\tau}_{Nd}^* = \frac{H_0 \boldsymbol{\tau}_{Nd}}{\mu_d U_0} , \quad \boldsymbol{\sigma}_{\alpha}^* = \frac{\boldsymbol{\sigma}_{\alpha}}{\sigma_1}, \qquad (27)$$

$$K(\phi) = l^2 k(\phi) , P_0(\phi) = \frac{p_0(\phi)}{\sigma_1},$$
 (28)

where the superscripts * indicate dimensionless quantities. In (26), \boldsymbol{u}_{α} denotes any of the velocities \boldsymbol{u}_d , \boldsymbol{u}_c or $(U_h(t), U_v(t))$. In the same way, \boldsymbol{j}_{α} represents all the flux densities introduced in section 2, and $\boldsymbol{\sigma}_{\alpha}$ is either $\boldsymbol{\sigma}_d$ or $(\Sigma_h(t), \Sigma_v(t))$. Note that the liquid pressure is scaled with an estimate of the inter-phase drag (assumed given by Darcy's law) accumulated over the distance H_0 .

Inserting the scaled variables into (11) and (15), these become, respectively,

$$0 = -\nabla p_c + \Lambda \nabla \cdot \boldsymbol{\tau}_{Nd} - \frac{1}{Pe} \nabla \cdot \boldsymbol{\sigma}_d. \tag{29}$$

$$\boldsymbol{j}_r = -\phi(1-\phi)K(\phi)\left(\frac{1}{Pe}\nabla\cdot\boldsymbol{\sigma}_d - \Lambda\nabla\cdot\boldsymbol{\tau}_{Nd}\right), \qquad (30)$$

where the superscripts * have been dropped for ease of notation. We shall continue to do so. Two dimensionless groups have appeared, a Péclet number

$$Pe = \frac{\mu_c H_0 U_0}{l^2 \sigma_1}$$
, and $\Lambda = \frac{\mu_d}{\mu_c} \left(\frac{l}{H_0}\right)^2$. (31)

Pe expresses the ratio between transport of particles towards the filter by convection, and relative transport away from the filter due to gradients in the inter-particle stresses. Considering that all particles are retained by the filter, these two mechanisms must be equally important in the region next to the filter. We shall therefore set Pe = 1 and use this to determine the unknown scales U_0 and σ_1 . When the vertical piston load is specified, we take as σ_1 some suitable measure of that load, after which (31) provides the estimate

$$U_0 = \frac{l^2 \sigma_1}{\mu_c H_0} \,. \tag{32}$$

Conversely, when the vertical velocity of the piston is given, it will provide U_0 , and

$$\sigma_1 = \frac{\mu_c H_0 U_0}{l^2} \,. \tag{33}$$

The group Λ measures the significance of the viscous stresses. Since l/H_0 is small, these are only important to the momentum balance of the mixture if $\mu_d/\mu_c \gg 1$. As shall become clear below, even small rate-dependent stresses can nevertheless have an influence on the behaviour of the flow field. Further, if there are regions where the solid phase network reaches critical state (cf.

section 3.2), the deformation-rates will be of such magnitude that the viscous stresses are of importance².

The scaled version of (13) is obtained by simply omitting the viscosity from the relation.

Apart from (11), (13) and (15), the relations in section 2 retain their appearances when scaled variables are introduced. The exception is that $p_0(\phi)$ should be replaced by $P_0(\phi)$ at all occurrences in section 2.2. From now on, we shall only refer to scaled quantities, unless otherwise explicitly specified.

3.2. The sheared compression

Assume a situation of plane strain, such that the only non-zero velocity components are those in the xy-plane. Further, as the piston and the filter are of infinite extension, we suppose that there are no gradients in the horizontal direction. Hence, from (9), the mixture flux towards the filter, j^y , is given by the vertical velocity of the piston,

$$j^y = U_v(t). (34)$$

The horizontal and vertical components of the force balance (29) can be integrated to reveal, respectively,

$$\tau_d^{xy} + \Lambda \tau_{Nd}^{xy} = \Sigma_h(t) \,, \tag{35}$$

$$p_c + \sigma_d^{yy} - \Lambda \tau_{Nd}^{yy} = \Sigma_v(t) , \qquad (36)$$

indicating how the applied load is distributed between different types of stresses. From (30), (35) and (36), we obtain the relative flux density components³,

$$j_r^x = 0, (37)$$

$$j_r^y = -\phi(1-\phi)K(\phi)\frac{\partial}{\partial y}\left(\sigma_d^{yy} - \Lambda \tau_{Nd}^{yy}\right). \tag{38}$$

Consequently, both phases have the same velocity in the horizontal direction.

A transport equation for the dispersed phase is obtained by inserting j_d from (8) into (10), and employing the global conservation of volume (9). If (34) is then used in this equation, we find

$$\frac{\partial \phi}{\partial t} + U_v(t) \frac{\partial \phi}{\partial y} + \frac{\partial j_r^y}{\partial y} = 0.$$
 (39)

Under the assumptions made in this paragraph, the yield-surface (17) is in the σ_d^{yy} - τ_d^{xy} -plane, according to the analysis by H&D, given by the relation

$$\frac{\left(\sigma_d^{yy} - \frac{1}{2}P_0(\phi)\right)^2}{\left(\frac{1}{2}P_0(\phi)\sqrt{1 + \frac{2}{3}M^2}\right)^2} + \frac{\tau_d^{xy^2}}{\left(\frac{1}{2}P_0(\phi)\frac{M}{\sqrt{2}}\right)^2} = 1.$$
 (40)

It is illustrated in figure 2. As a result of the associated flow rule, the defor-

 $^{^2}$ More correctly, the solid phase deformation-rates are then determined by the the viscous stresses.

³The flux j_r^x would not have vanished if viscous stresses in the liquid phase were included.

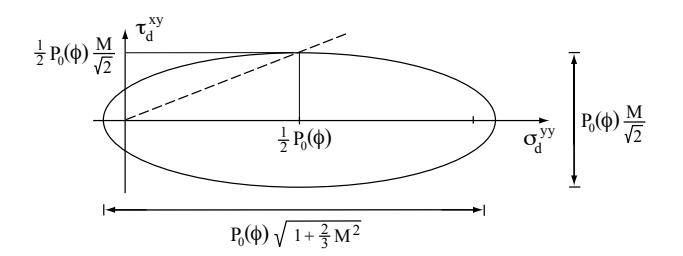


FIGURE 2. The yield-surface in the σ_d^{yy} - τ_d^{xy} -plane. The dashed line indicates the position of the critical stress state at different concentrations.

mation rate vector $(-e_d^{yy}, e_d^{xy})$ is directed along the outward pointing normal to the ellipse in figure 2. Thus, the dashed 'critical state line', whose intersection with the yield-surface is denoted $(\sigma_c(\phi), \tau_c(\phi))$, separates the stress states resulting in volumetric expansion $(\sigma_d^{yy} < \sigma_c)$ from those yielding compression $(\sigma_d^{yy} > \sigma_c)$. When $(\sigma_d^{yy}, \tau_d^{xy}) = (\sigma_c, \tau_c)$, a pure shearing motion takes place. By limiting ourselves to situations in which $\tau_d^{xy} \ge 0$, we can rewrite (40) as a relation for τ_d^{xy} ,

$$\tau_d^{xy} = f(\phi, \sigma_d^{yy}). \tag{41}$$

H&D also shows that the associated flow rule leads to the following coupling between the two non-zero deformation-rates,

$$M^{2}\left(\sigma_{d}^{yy} - \frac{1}{2}P_{0}(\phi)\right)e_{d}^{xy} + \left(1 + \frac{2}{3}M^{2}\right)\tau_{d}^{xy}e_{d}^{yy} = 0.$$
 (42)

It is worth noting that at the critical state, where $\sigma_d^{yy} = \frac{1}{2}P_0(\phi)$, equation (42) turns into $e_d^{yy} = 0$.

From the constitutive relation (13), it is seen that the non-zero viscous stress components are

$$\tau_{Nd}^{xy} = 2e_d^{xy} \,, \tag{43}$$

$$\tau_{Nd}^{yy} = \frac{4}{3}e_d^{yy}. \tag{44}$$

Thus, (43) can be used in (35) in order to determine e_d^{xy} . The normal deformation-rate component is connected to j_r^y through

$$e_d^{yy} = \frac{\partial}{\partial y} \left(\frac{j_r^y}{\phi} \right) \,, \tag{45}$$

which follows from the definitions (5), (8) and (14), together with the result (34).

The equations (35), (38), (39) and (41)–(45) constitute a closed system. However, before an attempt is made to obtain the solution, it is further reduced by first combining (38), (39) and (44), thus obtaining an equation for the concentration,

$$\frac{\partial \phi}{\partial t} + U_v(t) \frac{\partial \phi}{\partial y} - \frac{\partial}{\partial y} \left(\phi(1 - \phi) K(\phi) \frac{\partial}{\partial y} \left(\sigma_d^{yy} - \frac{4\Lambda}{3} e_d^{yy} \right) \right) = 0.$$
 (46)

Again using (38) and (44), this time in (45), yields an equation for the normal deformation-rate,

$$e_d^{yy} + \frac{\partial}{\partial y} \left((1 - \phi) K(\phi) \frac{\partial}{\partial y} \left(\sigma_d^{yy} - \frac{4\Lambda}{3} e_d^{yy} \right) \right) = 0. \tag{47}$$

In addition, the equations (35), (41), (42) and (43) can be used to derive the following algebraic equation, connecting the dependent variables in (46) and (47),

$$M^{2}\left(\sigma_{d}^{yy} - \frac{1}{2}P_{0}(\phi)\right) \frac{\Sigma_{h}(t) - f(\phi, \sigma_{d}^{yy})}{2\Lambda} + \left(1 + \frac{2}{3}M^{2}\right) f(\phi, \sigma_{d}^{yy}) e_{d}^{yy} = 0.$$
 (48)

Using the last equation, we can eliminate e_d^{yy} in (46) and (47). However, by doing this, we restrict our treatment to situations in which $\tau_d^{xy} = f(\phi, \sigma_d^{yy}) = 0$.

The boundary conditions needed to solve (46) and (47) are different depending on whether we control the piston by the applied load, or by prescribing its displacement velocity. Assume first the former alternative. From (1), (36) and (45), we learn that the following condition must be fulfilled at the filter,

$$\left[\sigma_d^{yy} - \frac{4\Lambda}{3}e_d^{yy}\right]_{y=0} = \Sigma_v(t), \qquad (49)$$

into which e_d^{yy} from (48) should be inserted. At the other end of the domain, the vertical velocity of both phases are equal to the velocity of the piston, and thus

$$[j_r^y]_{y=H(t)} = 0. (50)$$

When the piston is load-controlled, its velocity components need to be solved for, notably $U_v(t)$ which appears explicitly in equation (46). Using the condition (2) and the result (34) in equation (8), we get a relation that can be solved for the vertical piston velocity, yielding

$$U_v(t) = -\left[\frac{j_r^y}{\phi}\right]_{y=0} = \left[(1 - \phi)K(\phi)\frac{\partial}{\partial y} \left(\sigma_d^{yy} - \frac{4\Lambda}{3}e_d^{yy}\right) \right]_{y=0}.$$
 (51)

The horizontal component of the solid phase velocity, u_d^x , can be obtained by first calculating the velocity gradient $\partial u_d^x/\partial y$ from (14), (35), (41) and (43), and then integrating in the direction away from the filter, revealing

$$u_d^x(y,t) = \int_0^y \frac{\Sigma_h(t) - f(\phi, \sigma_d^{yy})}{\Lambda} dy', \qquad (52)$$

where the condition $u_d^x(0,t) = 0$ has been used. As $j_r^x = 0$, (52) also provides the horizontal liquid phase velocity, as well as the corresponding mixture flux density component j^x . Further, the piston velocity in the x-direction is $U_h(t) = u_d^x(H(t),t)$.

When the piston velocity is directly controlled, (50) is still used as a boundary condition. However, the relation (51) replaces (49) as the condition applied at the filter. The shear stress appearing in the equations is obtained by solving (52), evaluated at y = H(t), for $\Sigma_h(t)$ as a function of $U_h(t)$. The necessary vertical load $\Sigma_v(t)$ is determined a posteriori from (49).

Frequently, we have also chosen to specify the combination $\Sigma_v(t)$ and $U_h(t)$, in which case (49)–(51) are used as in the load-controlled case, but the necessary shear stress $\Sigma_h(t)$ is determined as in displacement-controlled simulations.

In order to prevent a break-down of the model when some point of the floc-culated phase reaches critical state, it is in our particular plane-strain problem only necessary to include the stress component τ_{Nd}^{xy} . The governing equations for this situation can be obtained from those presented above, by simply inserting $\tau_{Nd}^{yy}=0$. Practically, this amounts to removing the group $4e_d^{yy}/3$ at all occurrences.

3.3. Solution method

The equations (46)–(48) have been solved numerically. To facilitate the numerical treatment, a change of co-ordinates, $y = H(t)\tilde{y}$, was undertaken in order to have a domain with fixed boundaries, $\tilde{y} \in [0,1]$. The spatial discretisation was then performed using the Galerkin formulation of the finite element method with linear interpolation functions. For the time-derivative, the implicit Euler formulation was employed. The complete discretisation is thus of second order accuracy in space, and first order in time. The implementation of the algorithm was carried out by formulating the problem in variational form, and then using the package femLego for automated code generation (see Amberg et al. 1999).

A shooting method based on (52) was used to obtain $\Sigma_h(t)$ when $U_h(t)$ was specified. At each time-step, the equations (46)–(48) were solved using a guessed value for $\Sigma_h(t)$, which was updated using the bisection method till the correct value of $U_h(t)$ was found. However, this was found to be rather time-consuming. The simplified model, in which the only non-zero viscous stress is τ_{Nd}^{xy} , required less computational effort, and it was used instead when the 'mixed' type of piston control was employed.

To produce the presented computational results, the domain $\tilde{y} \in [0, 1]$ was resolved with 400 elements of uniform size. The non-dimensional time step dt was $3.1 \cdot 10^{-7}$.

4. Results

The initial concentration and gap size were set to $\phi_0=0.05$ and $H_0=0.01$ m. Since, by assumption, ϕ_0 exceeds the gel concentration, we simplified the treatment by setting $\phi_g=0$ in equation (20). The parameters σ_0 and n were given the values 500 kPa and 2.5, respectively, and for the specific surface we chose $S_0=1/l=18\cdot 10^5 \ \mathrm{m}^{-1}$. These are the same values as those used by Zahrai et al. (1998). Buscall et al. (1986) conclude that the yield stress in shear for a strongly flocculated polystyrene latex suspension appears to be one to two orders of magnitude smaller than the corresponding uniaxial limit. Thus, by setting M=0.287, we obtain critical shear stresses $\tau_c(\phi)$ that are a fraction 0.1 of the yield limit in uniaxial compression. For the viscosity of the continuous phase, we used $\mu_c=10^{-3}$ Pa s.

At the onset of the consolidation process, the load applied by the piston was in equilibrium with the stresses in the solid phase in such a way that $\Sigma_h(t=0)/\Sigma_v(t=0)=0.01$. A certain initial stress τ_d^{xy} was needed for the algorithm to behave properly, presumably due to the very steep slope of $f(\phi, \sigma_d^{yy})$ (for a given ϕ) when σ_d^{yy} is close to the uniaxial yield limit, and the way in which (48) was used to eliminate e_d^{yy} in section 3.2. In all the presented simulations, the vertical load $\Sigma_v(t)$ was then ramped linearly to its final value $\sigma_1=1$ kPa, and, according to (32), the velocity scale is thus $U_0=3.09\cdot 10^{-5}$ m/s, and the time-scale is $H_0/U_0=324$ s. Also in simulations where U_h was 'given a constant value', there was an initial part during which the horizontal velocity of the piston was increased linearly with time till the final value was reached. The scaled ramp time for both the vertical load and the horizontal velocity was in all cases $3.1\cdot 10^{-4}$.

H&D comments that, according to the work by Landman et al. (1991), the scales employed in this study are only correct after sufficiently long times. It is also worth pointing out that the velocity scale refers to the vertical velocity components, which after a certain time are small. This explains the large values of the horizontal velocity components in the presented results.

Although, according to the scaling analysis in section 3, the solid stresses τ_d^{xy} and σ_d^{yy} are of much larger magnitude than the corresponding viscous components τ_{Nd}^{xy} and τ_{Nd}^{yy} , the latter prevent break-down of the model when $\Sigma_h(t)$ is of such magnitude that parts of the flocculated network reach critical state. Without them, the shear-rate e_d^{xy} would then not be determinate. An example of their effect is given in figure 3, containing results from a computation in which the horizontal component of the piston load at all times is set to a value that exceeds the critical solid stress $\tau_c(\phi_m(t))$ by a constant amount $\Delta \tau = 10^{-3}$, where $\phi_m(t)$ is the lowest concentration of solid phase encountered between the plates. Consequently, $\phi_m(t)$ is the volume fraction at the position where the network is the weakest. The viscosity ratio μ_d/μ_c is here 10^2 , yielding $\Lambda = 5.6 \cdot 10^{-3}$. The left and the right part of figure 3 contains velocity and shear-rate profiles, respectively, at different solution times.

The evolution of the concentration during the same compaction process is provided in figure 4. The progressive increase of the concentration at the filter is an effect of the monotonically increasing shear load $\Sigma_h(t)$ reducing the ability of the network to carry the vertical load. The small time increments between the initial profiles hides this course of events at the onset. Initially, it is only in the region next to the filter that the solid phase network is compressed, and the volume fraction next to the piston remains at the original value. Until the uncompressed upper region has disappeared, $\phi_m(t)$ thus equal ϕ_0 , and the network next to the piston is at critical state. In the upper suspension region, as a result of the balance (35), the viscous stress $\Lambda \tau_{Nd}^{xy}$ then equal the constant $\Delta \tau$, yielding a homogeneous shear rate and a linear velocity profile.

Immediately next to the filter, the network very soon attains a high degree of compaction. It is thus of high strength, and the deformation-rates small.

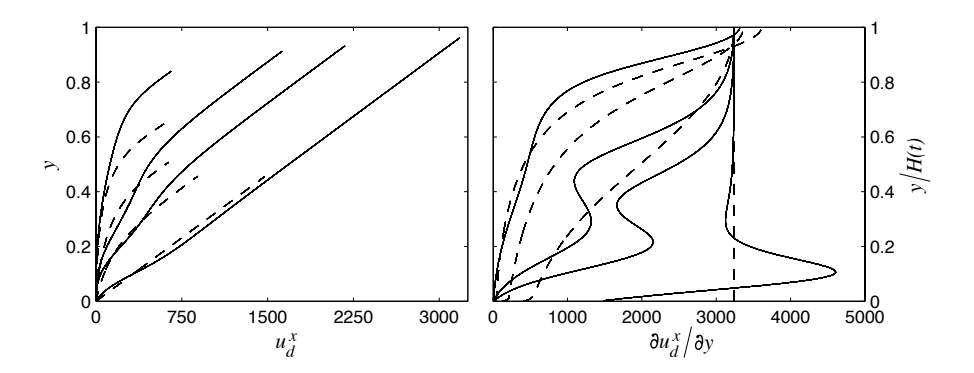


FIGURE 3. Velocity profiles (left subfigure) and shear-rate profiles (right subfigure) when $\Sigma_v = 1$ and $\Sigma_h(t) = \tau_c(\phi_m(t)) + 10^{-3}$, where $\phi_m(t)$ is the volume fraction of solids at the position where the network is weakest. Profiles are plotted for $t/10^{-3} = 0.31, 0.62, 0.93, 2.7, 11, 22, 44, 88$. Time increases from right to left for the solid profiles (earlier times). Then time increases from left to right for the dashed profiles (later times). Both τ_{Nd}^{xy} , $\tau_{Nd}^{yy} \neq 0$. $\Lambda = 5.6 \cdot 10^{-3}$. Note that in the right subfigure, the position y is scaled with H(t), whereas in the left subfigure it is not. Cf. fig. 4 for the corresponding profiles $\phi(y,t)$.

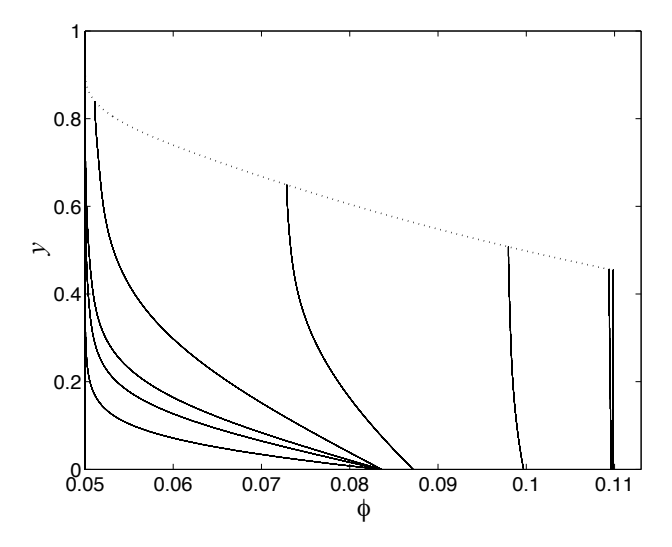


FIGURE 4. Evolution of the volume fraction of solids in the same case, and at the same instances, as in fig. 3. Time increases from the leftmost to rightmost profile. The dotted line gives the concentration at the position of the piston.

Slightly further away from the bottom plate, at the earliest times, the shear-rate (and also the volumetric deformation-rate) is large. The solid stress component τ_d^{xy} is here smaller than $\tau_c(\phi_m(t))$, and the viscous stress $\Lambda \tau_{Nd}^{xy}$ consequently larger than $\Delta \tau$, which explains the peak exhibited by the earliest shear-rate profile in the right part of figure 3.

Eventually, also the network next to the piston must undergo compression. It follows that the particle phase then cannot remain at critical state, since this corresponds to vanishing volumetric deformations. Referring to the yieldsurface in figure 2, the stress state moves along the yield locus in the direction of increasing σ_d^{yy} , resulting in a deformation rate vector $(-e_d^{yy}, e_d^{xy})$ with a finite component e_d^{yy} . Thus, τ_d^{xy} becomes smaller. By consequence, since the weakest part of the flocculated structure is always located next to the piston, $\tau_d^{xy} < \tau_c(\phi_m(t))$. Hence, although we apply a shear load $\Sigma_h(t)$ that is higher than the critical shear stress at the weakest point, there is now no position at which the network is at critical state. The viscous stress $\Lambda \tau_{Nd}^{xy}$ must also exceed $\Delta \tau$ in order for the horizontal balance (35) to be fulfilled next to the piston, and this explains why the shear rates at the upper plate, after a certain time, exceed the asymptotic value in figure 3. Note that the time increment between the different profiles in figure 3 is not uniform, and that this situation actually prevails during almost the entire consolidation process. As $t \to \infty$, the critical state is attained by all parts of the flocculated network, and $\Lambda \tau_{Nd}^{xy}$ is then everywhere equal to $\Delta \tau$, from which the asymptotic shear-rate is easily obtained.

Figure 5 contains a comparison between the horizontal solid phase velocity u_d^x in a visco-plastic simulation, and a purely plastic simulation performed by H&D, when the horizontal velocity of the piston is held at a constant value. The ratio between the viscosities of the two phases is now higher than in the previously discussed simulation, $\mu_d/\mu_c=10^3$, yielding $\Lambda=5.6\cdot 10^{-2}$. For computational efficiency, the stress component τ_{Nd}^{yy} is not included in the visco-plastic calculation. Clearly, there are qualitative differences between the velocity profiles in figures 5 and 3. The initial compression of the flocculated network is also in the cases in figure 5 limited to the region closest to the filter. However, the applied shear load is now such that the critical state is never attained at any position. The flocculated solid phase next to the piston therefore translates like a stiff cake. As the consolidation proceeds, the size of the cake region is progressively reduced till the entire flocculated network contained between the plates undergoes deformations. In the left part of figure 5, it is seen that this happens sooner in the visco-plastic case, than in the purely plastic computation. In both cases, the evolution of the concentration qualitatively follows the pattern in figure 4.

Eventually, the drainage of liquid ceases, the continuous phase pressure vanishes, and σ_d^{yy} is everywhere equal to the piston load $\Sigma_v(t)$, cf. equation

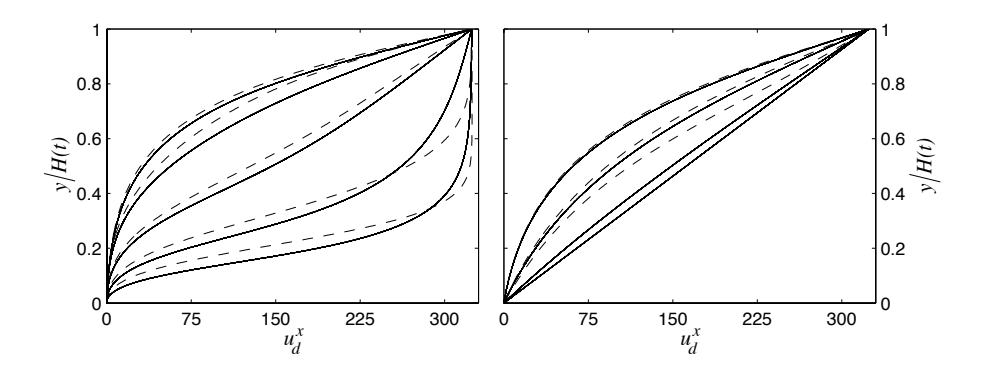


FIGURE 5. Comparison between visco-plastic (solid lines) and purely plastic (dashed lines, from H&D) velocity profiles when Σ_v and U_h are kept at constant values (1 and 324, respectively). Only $\tau_{Nd}^{xy} \neq 0$. Left subfigure: $t/10^{-3} = 0.5$, 0.9, 1.8, 3.5, 7. Time increases with distance from bottom right corner. Right subfigure: $t/10^{-3} = 14$, 57, 100. Time increases with distance from top left corner. Only the visco-plastic profile is plotted for the largest time. $\Lambda = 5.6 \cdot 10^{-2}$.

(36). The concentration in the gap is then homogeneous, $\phi(y,t) = \phi_{\infty}^{-4}$, and further (horizontal) movements must take place without volumetric deformations. Consequently, all parts of the network asymptotically tend to the critical state in the limit $t \to \infty$, and $\Sigma_v(t \to \infty) = \sigma_c(\phi_{\infty})$, a relation which can be used to calculate ϕ_{∞} . In the purely plastic case, from (35) with $\Lambda = 0$, the horizontal load $\Sigma_h(t \to \infty)$ is seen to equal $\tau_d^{xy}(y,t \to \infty) = \tau_c(\phi_{\infty})$, regardless of the value of the specified piston velocity $U_h(t)$. Clearly, the limit velocity profiles $\lim_{t\to\infty} u_d^x(y,t)$ are not uniquely defined by the values of the asymptotic loads. As noted by H&D, it is not even necessary that the purely plastic limit profiles are linear. This remark is supported by the last of the purely plastic profiles in the right part of figure 5. It corresponds to an instant when the concentration and the piston loads are very close to their asymptotic values (cf. fig. 6).

The situation is different in the presence of a non-zero viscous stress τ_{Nd}^{xy} . The solid stress $\tau_d^{xy}(y,t\to\infty)$ still equals $\tau_c(\phi_\infty)$, but, according to (35), the piston load $\Sigma_h(t\to\infty)$ necessary to achieve the specified piston velocity will now depend on the (spatially constant) viscous stress $\Lambda \tau_{Nd}^{xy}$. Asymptotically, a constant dispersed phase effective viscosity will hence yield a spatially constant shear-rate e_d^{xy} , and a linear velocity profile. Note that this would also be the case if the effective viscosity depends on the concentration, since the asymptotic viscosity would then be constant across the gap between the plates, i.e.

⁴An alternative problem formulation, yielding a non-homogeneous asymptotic profile, is discussed in Appendix A.

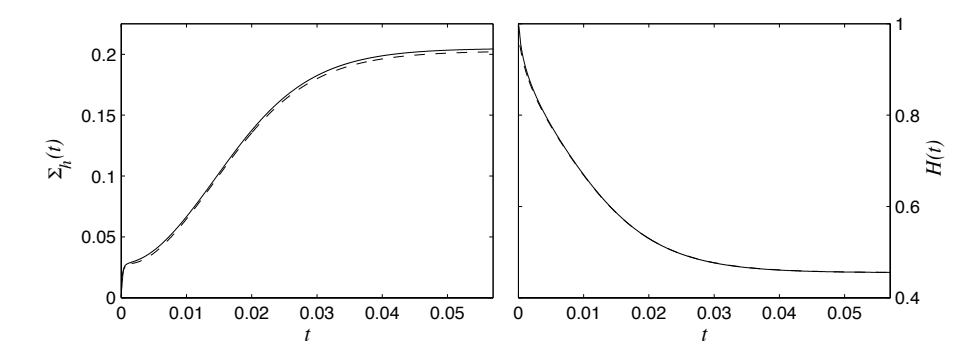


FIGURE 6. The evolution of the applied horizontal stress $\Sigma_h(t)$, and the gap between the plates H(t), when Σ_v and U_h are kept at constant values (1 and 324, respectively). Solid lines: Visco-plastic case (only $\tau_{Nd}^{xy} \neq 0$). Dashed lines: Purely plastic case (from H&D). $\Lambda = 5.6 \cdot 10^{-2}$. Cf. also fig. 5 which contains results from the same computations.

 $\lim_{t\to\infty}\mu_d\bigl(\phi(y,t)\bigr)=\mu_d(\phi_\infty)$. The visco-plastic profile at the largest time in figure 5 is indeed completely linear. It should be kept in mind, however, that the visco-plastic profile corresponding to the last of the purely plastic profiles, is not perfectly linear. Hence, the visco-plastic simulation has at that point not yet reached the asymptotic state. It is likely that the same is true of the purely plastic calculation, for which (due to numerical problems) it was not possible to obtain results at later times than the last profile in figure 5. Therefore, we do not know the shape of $\lim_{t\to\infty}u_d^x(y,t)$ in the purely plastic case. It is however worth observing that the difference between the last purely plastic and the corresponding visco-plastic profiles is significantly larger than at earlier instants in the left subfigure. This could indicate that the purely plastic solution is close to its asymptotic shape, since it evolves at a markedly lower pace than the visco-plastic counterpart.

The evolution of the horizontal piston load $\Sigma_h(t)$ and the gap size H(t) are given in figure 6 for the visco-plastic and purely plastic cases discussed in connection with figure 5. It is seen that although the dispersed phase viscosity is high $(\mu_d/\mu_c = 10^3)$, the viscous stress only slightly affects the load required to maintain the chosen (constant) horizontal velocity. This is in agreement with the predictions made during the scaling analysis in section 3. The evolution of the gap size H(t) in the visco-plastic and the purely plastic cases is practically identical. A larger (albeit still small) difference would have been observed if τ_{Nd}^{yy} had been included in the visco-plastic simulation. From figure 6 we conclude that, at larger times, $\Sigma_h(t)$ and H(t) have almost reached their asymptotic values.

The purely plastic calculations by H&D indicate that applying a shear load to the suspension during the consolidation process yields higher pore pressures

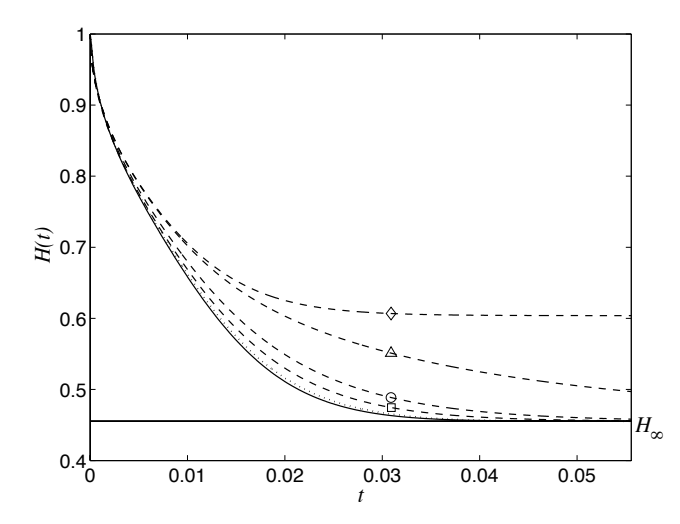


FIGURE 7. A comparison between different cases of the evolution of the gap H(t). In all simulations $\Sigma_v(t)=1$. Dashed lines: Purely plastic calculations by H&D in which U_h is held constant. \diamond : $U_h=0$. \triangle : $U_h=32.4$. \circ : $U_h=162$. \square : $U_h=324$. Solid line: Visco-plastic calculation (only $\tau_{Nd}^{xy}\neq 0$), $U_h=3240$, $\Lambda=5.6\cdot 10^{-3}$. Dotted line: Visco-plastic simulation $(\tau_{Nd}^{xy}, \tau_{Nd}^{yy}\neq 0)$ in which $\Sigma_h(t)=\tau_c(\phi_m(t))+3\cdot 10^{-3}$, $\Lambda=5.6\cdot 10^{-3}$. Cf. fig. 6 for the definition of $\phi_m(t)$. The horizontal line $H=H_\infty$ corresponds to the asymptotic gap size.

and faster drainage, an effect which in a real suspension could be attributed to restructuring of the solid phase network and increased loading of the interparticle bonds. In figure 7, the evolution of the gap size H(t) is presented for a visco-plastic case $(\mu_d/\mu_c=10^2,\tau_{Nd}^{yy}\equiv0)$ in which the horizontal velocity of the piston is held at a high value, $U_h=3240$, as well as for a visco-plastic simulation $(\mu_d/\mu_c=10^2,\tau_{Nd}^{xy},\tau_{Nd}^{yy}\neq0)$ in which the horizontal load $\Sigma_h(t)$ is kept at a value that exceeds $\tau_c(\phi_m(t))$ by an amount $\Delta\tau=3\cdot10^{-3}$ (a case similar to that reported in fig. 3 and 4). For reference, the purely plastic constant horizontal velocity results by H&D are also presented. The corresponding piston shear loads $\Sigma_h(t)$ are given in figure 8.

The maximum plate velocity in the purely plastic calculations is $U_h = 324$. At higher horizontal plate velocities, the solution algorithm used by H&D has been found to run into difficulties before the system reaches the asymptotic state. However, including a viscous shear stress component τ_{Nd}^{xy} permits numerical experiments to be conducted with higher velocities U_h . According to figure 6, the evolution of H(t), as compared to the purely plastic case, is only very slightly influenced by the viscous stress (note that μ_d/μ_c for the viscoplastic case in fig. 6 is a factor 10 larger than for the visco-plastic cases in fig.

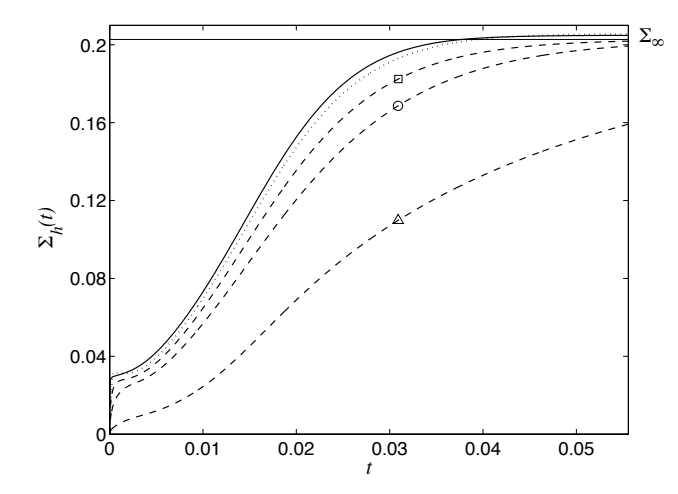


FIGURE 8. A comparison between the same cases as in fig. 7 of the shear load $\Sigma_h(t)$ applied by the piston. Cf. the caption of that figure for an explanation of the different line-types. For the case corresponding to $U_h = 0$, we have $\Sigma_h \equiv 0$. The horizontal line $\Sigma_h = \Sigma_{\infty}$ corresponds to the asymptotic load in the purely plastic simulations.

7 and fig. 8). From the solid line in figure 7 it can be concluded that increasing the piston velocity component $U_h(t)$ beyond the values employed by H&D in his purely plastic calculations increases the compaction rate even further, at the expense of a higher required load $\Sigma_h(t)$.

The plate separation distance H(t) qualitatively exhibits the same behaviour when the horizontal piston load is kept slightly above the critical shear stress at the weakest part of the network, as when U_h is constant. However, in the former case $U_h(t)$ varies between a minimum and a maximum value of about 1160 and 4419, respectively, the latter value being the asymptotic plate velocity. In order to achieve a high drainage, the solid shear stress τ_d^{xy} should be as close to the critical value $\tau_c(\phi)$ as possible, in order to reduce the capacity of the flocculated particle phase to resist the compressive normal stress (cf. the yield-surface in fig. 2). According to the vertical force balance (36), when σ_d^{yy} is reduced (and since the viscous normal stress is relatively small), a larger fraction of the applied load $\Sigma_v(t)$ must then be balanced by the liquid (pore) pressure. Both types of piston control effectively achieves this situation.

In section 2, the inertial terms were neglected in the balance equations. Given the large values of the horizontal velocity components encountered in the results, the question arises whether this is justifiable. In the vertical direction, it is common practice to neglect inertia (see e.g. Landman *et al.* 1995), and an analysis akin to the one we shall perform for the horizontal direction would normally reveal this to be motivated during the predominant part of the

consolidation process of a flocculated suspension. The exception is at the onset of the loading, when a finite force that is suddenly applied to the piston can yield very high drainage velocities if the resistance of the filter is low (indeed, a perfectly permeable filter yields an infinite velocity at $t=0^+$). The scaling analysis by H&D tells us that the inertial terms in the horizontal direction can be estimated by considering the quantity

$$\left(\frac{\rho_d U_0 H_0}{\mu_c}\right) \left(\frac{l}{H_0}\right)^2 \left(\frac{\partial u_d^x}{\partial t} + u_d^y \frac{\partial u_d^x}{\partial y}\right),$$
(53)

where ρ_d is the density of the solid constituent. We here choose to focus on the particle phase, but this is of no importance if the solid and the liquid are of comparable densities and are displaced at similar rates. Inserting the values provided at the beginning of this section, and taking $\rho_d = 10^3$, it is found that the first two factors in (53) are $\mathcal{O}(10^{-1})$ and $\mathcal{O}(10^{-9})$, respectively. We estimate the first term in the third factor using the velocity profiles in figure 3. The velocity change between the first two profiles at some vertical position is typically $\mathcal{O}(10^3)$. As the time interval between the profiles is $\mathcal{O}(10^{-4})$, the term in question is of magnitude $\mathcal{O}(10^7)$. From e.g. the solid curve in figure 7, it is concluded that the average vertical piston velocity between, say, t=0and t = 0.03, is $\mathcal{O}(10)$. This value can be taken as a measure of u_d^y . If the variation in u_d^x across the distance between the plates is $\mathcal{O}(10^3)$, and the distance itself is estimated to $\mathcal{O}(1)$, the second term in the third factor in (53) is $\mathcal{O}(10^4)$. Thus, the acceleration terms are of size $\mathcal{O}(10^{-3})$, and can safely be neglected. However, one should be aware of that the same comment as was made regarding the inertial effects in the vertical direction at the onset of the loading, also applies to the last term in the third factor of (53).

5. Concluding remarks

In the present study, the purely plastic model by H&D for sheared consolidation of a flocculated suspension trapped between two infinite flat plates, is extended to include strain-rate dependent stresses. A set of dimensionless parameters that govern the model can be identified. The relative magnitude of deviatoric to isotropic stresses is measured by the slenderness factor of the yield surface, M. The size of the yield-surface as compared to the applied load is expressed by σ_0/σ_1 , and the strain-hardening is controlled by the exponent in the isotropic yield-limit function, n. The relative size of the viscous stresses to the rateindependent stresses is determined by the group Λ , defined as the product of the ratio between the viscosity of the liquid phase to the effective viscosity of the particle phase, and the ratio between the microscopic length scale of the porous structure to the macroscopic scale of the problem. Further, the initial concentration ϕ_0 and the gel concentration ϕ_q can be considered as independent dimensionless numbers. Although the scaling analysis reveals that the viscous stresses are most likely of comparably small magnitude in many applications, there are nevertheless several reasons to explore their effects.

A characteristic of the inviscid critical state plasticity theory is that, when the solid structure attains critical state, deviatoric deformations occur at an undefined rate. In the original field of application of the theory, soil mechanics, relatively little attention has been paid to the evolution of the system once the critical state is attained, as this usually represent failure of the structure under consideration. As shown by H&D, the Cam-clay critical state theory can be used to generalise the yield-stress concept previously employed to study uniaxial compression (see e.g. Buscall & White 1987, Landman et al. 1991), thus permitting deviatoric rate-independent solid stresses to be accounted for in addition to the isotropic 'particle pressure'. During sheared consolidation, it is however difficult to disregard from the behaviour of the suspension when the particle network reach critical state. By including viscous stresses, in addition to the plastic stresses, the deformation-rates become well-defined also at the critical state. In the present study, viscous stresses of Newtonian character are attributed to the particle phase, and it is seen that this effectively removes the problems experienced by the purely plastic model when some part of the flocculated network attains critical state.

In a more complex situation than the one treated here, the need to prevent a break-down of the model due to the undefined behaviour at critical state is even larger, sincs it is then difficult to conclude *a priori* if the system at some point will reach critical state or not.

An artefact of the purely plastic model by H&D is that, when the piston moves with a constant horizontal velocity under a constant vertical load, the asymptotic value of the horizontal piston load is not dependent on the specified velocity. It leads us to conclude that the asymptotic velocity field is dependent on the load history. By including viscous stresses in the model, this feature is eliminated, which is confirmed by the simulations in section 4.

The observed trend of improved drainage rates when higher shear loads are applied by the piston is observed to persist also for larger loads than those reportedly employed by H&D in the exploration of the purely plastic model.

In Appendix A, the theory developed in this article is employed to derive an asymptotic solution for the concentration in a mat of flocculated suspension, that is on one side bounded by clear fluid and on the other by a permeable solid surface, subjected to a combination of drainage flow and cross flow of pure liquid. This alternative consolidation problem resembles the filtration process in the forming section of a paper-machine, for which H&D presents a model in which the rate-independent deviatoric stresses are neglected. The consolidation process is then essentially uniaxial. An approximate account of the effects of the deviatoric loads on the bearing capacity of the network can in that case be achieved by reducing the uniaxial yield limit of the solid (fibre) phase by some suitable factor, using the results of the present study as guidance. The loads reported by H&D for the paper manufacturing application, indicate that the shear stresses are possibly of quite large magnitude compared to the local values of the critical shear stress. Hence, it is not unreasonable to make the

assumption that the fibre network is everywhere close to being at critical state, suggesting that this factor be set to roughly 0.5.

Finally, the reader's attention is directed to the assumption that the yield criterion is always fulfilled. As long as the load transmitted to the network is not relaxed at any material point, it is valid. In spatially one-dimensional problems, it is fairly straight-forward to ensure that the requirement is fulfilled by choosing appropriate external loads and initial conditions. However, in a general situation, a constitutive description is needed of the behaviour of the suspension at stress states that do not result in yielding of the material.

6. Acknowledgements

Financial support was provided by the Swedish Agency for Innovation Systems (VINNOVA) and the industrial partners in the FaxénLaboratory.

References

- Adorján, L. A. 1975 A theory of sediment compression. In 11th International Mineral Processing Congress, pp. 297–318. Cagliari.
- Amberg, G., Tönhardt, R. & Winkler, C. 1999 Finite element simulations using symbolic computing. *Math. Comput. Simulation* **49**, 257–274.
- Bennington, C. P. J. & Kerekes, R. J. 1996 Power requirements for pulp suspension fluidization. *Tappi Journal* **79** (2), 253–258.
- Buscall, R., McGowan, I. J., Mills, P. D. A., Stewart, R. F., Sutton, D., White, L. R. & Yates, G. E. 1987 The rheology of strongly-flocculated suspensions. *J. Non-Newtonian Fluid Mech.* **24**, 183–203.
- Buscall, R., Mills, P. D. A. & Yates, G. E. 1986 Viscoelastic properties of strongly flocculated polystyrene latex dispersions. *Colloids and Surfaces* 18, 341–358.
- Buscall, R. & White, L. R. 1987 The consolidation of concentrated suspensions, part 1—the theory of sedimentation. *J. Chem. Soc., Faraday Trans.* 1 83, 873–891.
- Channell, G. M. & Zukoski, C. F. 1997 Shear and compressive rheology of aggregated alumina suspensions. *AIChE Journal* **43** (7), 1700–1708.
- Gustavsson, K. 2003 Mathematical and numerical modeling of 1-d and 2-d consolidation. PhD thesis, Royal Institute of Technology (KTH), Stockholm.
- HOLMQVIST, C. 2005 Mechanical modelling of blade forming and drainage of flocculated suspensions. PhD thesis, Royal Institute of Technology (KTH), Stockholm.
- Howells, I., Landman, K. A., Panjkov, A., Sirakoff, C. & White, L. R. 1990 Time-dependent batch settling of flocculated suspensions. *Appl. Math. Modelling* 14, 77–86.
- INGMANSON, W. L., ANDREWS, B. D. & JOHNSON, R. C. 1959 Internal pressure distributions in compressible mats under fluid stress. Tappi J. 42 (10), 840–849.
- Johnson, P. C. & Jackson, R. 1987 Frictional–collisional constitutive relations for granular materials, with application to plane shearing. *J. Fluid Mech.* 176, 67–93.

- JOHNSON, P. C., NOTT, P. & JACKSON, R. 1990 Frictional-collisional equations of motion for particulate flows and their application to chutes. J. Fluid Mech. 210, 501–533.
- Landman, K. A. & Russel, W. B. 1993 Filtration at large pressures for strongly flocculated suspensions. *Phys. Fluids A* 5 (3), 550–560.
- Landman, K. A., Sirakoff, C. & White, L. R. 1991 Dewatering of flocculated suspensions by pressure filtration. *Phys. Fluids A* **3** (6), 1495–1509.
- LANDMAN, K. A., WHITE, L. R. & BUSCALL, R. 1988 The continuous-flow gravity thickener: Steady state behaviour. *AIChE J.* **34** (2), 239–252.
- LANDMAN, K. A., WHITE, L. R. & EBERL, M. 1995 Pressure filtration of flocculated suspensions. AIChE Journal 41 (7), 1687–1700.
- Owen, D. R. J., de Souza Neto, E. A., Zhao, S. Y., Perić, D. & Loughran, J. G. 1998 Finite element simulation of the rolling and extrusion of multi-phase materials, application to the rolling of prepared sugar cane. *Comp. Methods Appl. Mech. Engrg.* **151**, 479–495.
- PARADIS, M. A., GENCO, J. M., BOUSFIELD, D. W., HASSLER, J. C. & WILDFONG, V. 2003 Measurement of drainage under conditions of known shear rate. *Journal* of Pulp and Paper Science 29 (12), 395–400.
- ROSCOE, K. H. & BURLAND, J. B. 1968 On the generalised stress-strain behaviour of 'wet' clay. In *Engineering Plasticity* (ed. J. Heyman & F. A. Leckie), pp. 535–609. Cambridge: Cambridge University Press.
- SAVAGE, S. B. 1983 Granular flows down rough inclines review and extension. In Mechanics of Granular Materials: New Models and Constitutive Relations (ed. J. T. Jenkins & M. Satake), pp. 261–282. Amsterdam: Elsevier.
- Shirato, M., Kato, H., Kobayashi, K. & Sakazaki, H. 1970 Analysis of settling of thick slurries due to consolidation. *J. Chem. Engng Japan* 3, 98–104.
- Ungarish, M. 1993 Hydrodynamics of Suspensions. Springer-Verlag.
- Wood, D. M. 1990 Soil Behaviour and Critical State Soil Mechanics. Cambridge University Press.
- Zahrai, S., Martinez, M. D. & Dahlkild, A. A. 1998 Estimating the thickness of the web during twin-wire forming. *Journal of Pulp and Paper Science* **24** (2), 67–72.
- Zhao, J., Wang, C.-H., Lee, D.-J. & Tien, C. 2003 Plastic deformation in cake consolidation. *Journal of Colloid and Interface Science* **261**, 133–145.

Appendix A. A non-trivial asymptotic concentration profile

When the piston is applied to the suspension with a constant load (Σ_h, Σ_v) , the concentration $\phi(y,t)$ always approach a constant value ϕ_{∞} as $t \to \infty$ (provided, of course, that the piston load everywhere equals or exceeds the yield stresses in the initial flocculated network). The same is true if U_h and Σ_v are maintained at constant values. A non-homogeneous limit concentration is however obtained in an alternative filtration problem of practical interest.

Suppose that we replace the piston in the present study by a an infinite body of liquid, containing a finite amount of particles, so that at the start of our experiment there is a layer of homogeneous suspension above the filter. The (dimensional) thickness of this layer is denoted H_0 , and is employed as the

length scale in the problem. The initial concentration ϕ_0 is assumed lower than the gel value ϕ_g . A constant (dimensional) drainage flow J_m , perpendicular to the filter, is achieved by maintaining a constant pressure p_{∞} in the particle free liquid. We shall here use this pressure as the stress scale, i.e. $\sigma_1 = p_{\infty}$. Also, a (dimensional) flow U_{∞} parallel to the plate (in the x-direction) is generated in the bulk of the clear liquid far above the mat. As before, we assume that the solid phase undergoes plane strains, and that there are no gradients in the horizontal plane. Since the amount of solid phase is limited, all particles will eventually be deposited on the filter. Asymptotically, a situation is reached in which there is a mat of flocculated particles residing on the filter, through which there is a flow of clear liquid. The thickness of the mat⁵ is denoted H.

Like before, the viscous stresses in the liquid are neglected, and hence the relative flux j_r^x vanish in the mat. Now, let U_h be the (dimensional) horizontal velocity component of the two phases at the surface of the flocculated network. The drainage flow induces a shear stress $-\rho_c J_m(U_\infty - U_h)$ on the mat mixture, which when scaled is denoted Σ_h . The parameter ρ_c is the density of the continuous phase. Σ_h is balanced by the particle stresses τ_d^{xy} and τ_{Nd}^{xy} , as expressed by the balance equation (35). In the asymptotic limit, the vertical particle flux vanish, i.e. $j_d^y = 0$, and consequently there is no normal viscous stress τ_{Nd}^{yy} in the flocculated network.

Vertical load is transferred from the liquid to the dispersed phase through inter-phase drag. Consequently, the vertical stress σ_d^{yy} will increase progressively, from $\sigma_d^{yy} = 0$ at y = H, to $\sigma_d^{yy} = 1$ at the filter, where $p_c = 0$. Suppose that the stress state $(1, \Sigma_h)$ is located on the compression side of the critical state line in σ_d^{yy} - τ_d^{xy} -space. It can then be concluded from the yield-surface (see figures 2 and 9) that the upper part of the mat will be in a state of pure shear flow, whereas no deformations will occur in the region closest to the filter. The particle network is hence compacted to such a degree in the region next to the filter that it can support the loads it is subjected to without continuously deforming. The boundary between the two domains is located at $y = y_1$. In the region $y \ge y_1$, all parts of the network are at critical state, and

$$\sigma_d^{yy}(y) = \sigma_c(\phi(y)). \tag{54}$$

On the other hand, if $(1, \Sigma_h)$ is located on the expansion side of the critical state line, the entire mat will be in a state of shear flow, i.e. $y_1 = 0$. We proceed under the assumption that y_1 is finite, knowing that if this is not the case, only minor adjustments of the analysis need to be made, as commented upon below.

Since the network is uncompressed at y=H, the network has zero strength at that position, and

$$\phi(y = H) = \phi_q. \tag{55}$$

⁵It would be more physically relevant to use the asymptotic thickness of the mat as the length scale, but to control this parameter is more difficult than to control H_0 (or, rather, to control the total quantity of particles $\phi_0 H_0$).

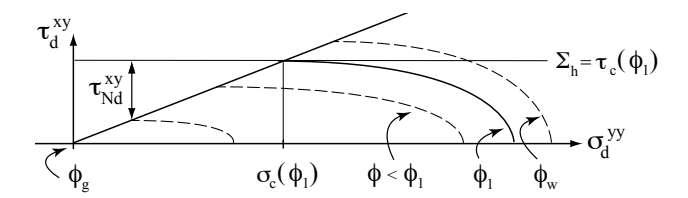


FIGURE 9. Yield surfaces corresponding to different concentrations. The straight line parting from the origin indicates the position of the critical stress states. Cf. Appendix A for the notation.

It follows from equation (35) that the shear load Σ_h must then be completely balanced by the viscous stress τ_{Nd}^{xy} . Further into the mat, the particle network will be increasingly more compressed, and the yield surfaces of finite size. An increasing fraction of Σ_h will therefore be balanced by the solid stress component τ_d^{xy} , and less by the viscous stress τ_{Nd}^{xy} . At $y = y_1$, the system is at critical state, but all load is carried by the rate-independent stress. The concentration at this point is denoted ϕ_1 , and it can be determined from the relation

$$\left[\tau_d^{xy} = \tau_c(\phi_1) = \Sigma_h\right]_{y=y_1}.$$
 (56)

In the region $y < y_1$, the vertical load is of sufficient magnitude for the stress state $(\sigma_d^{yy}, \tau_d^{xy})$ to be located on the compression side of the critical state line in figures 2 and 9, and $\tau_{Nd}^{xy} = 0$ due to the absence of a finite shear-rate. Limiting the treatment to positive values of τ_d^{xy} , the yield surface (40) can be turned into a relation for σ_d^{yy} ,

$$\sigma_d^{yy}(y) = g(\phi(y), \tau_d^{xy}(y)). \tag{57}$$

Equation (57) can, at least when $P_0(\phi)$ is given by (20), be inverted with respect to ϕ . By inserting the normal solid stress at the surface of the filter, as well as $\tau_d^{xy} = \Sigma_h$, the concentration at the filter is found to be

$$\phi(y=0) = \phi_w = g_{\phi}^{-1}(1, \Sigma_h). \tag{58}$$

From (9), the total volume flux perpendicular to the filter is seen to be $j^y = J$. Using (8) and (38), we derive

$$J = (1 - \phi)K(\phi)\frac{\partial \sigma_d^{yy}}{\partial u}.$$
 (59)

The stress σ_d^{yy} is uniquely determined by $\phi(y)$, albeit through different relations in the upper and lower parts of the mat. Consider first the region $0 \le y \le y_1$. Inserting (57) into (59), a separable differential equation is obtained, which when integrated from y = 0 to a position $y \le y_1$ turns into

$$yJ = \int_{\phi_{or}}^{\phi(y)} (1 - \phi') K(\phi') \frac{\mathrm{d}g(\phi'; \Sigma_h)}{\mathrm{d}\phi'} \mathrm{d}\phi' \qquad 0 \le y \le y_1.$$
 (60)

The load Σ_h is regarded as a parameter. Provided J is known, equation (60) permits us to determine $\phi(y)$ at any position in the stagnant part of the mat. Specifically, if (60) is evaluated at $y = y_1$, where $\phi = \phi_1$ is calculated using (56), we obtain an equation for the location of the boundary between the shear-flow and the stagnant domains.

The upper part of the mat is treated in an analogous fashion. The normal solid stress is now given by (54), and we find by integrating the separable differential equation from $y = y_1$ that

$$(y - y_1)J = \int_{\phi_1}^{\phi(y)} (1 - \phi')K(\phi') \frac{\mathrm{d}\sigma_c(\phi')}{\mathrm{d}\phi'} \mathrm{d}\phi' \qquad y_1 \le y \le H. \tag{61}$$

Equation (61) yields the concentration in the shear-flow region, again provided J is known. Evaluating the equation at y = H, where $\phi = \phi_g$, an equation is obtained for the thickness of the mat.

The drainage flux density J is determined from the requirement that the total quantity of solid phase is conserved, i.e.

$$\phi_0 = \int_0^H \phi \, \mathrm{d}y = \int_{\phi_w}^{\phi_g} \phi' \left(\frac{\mathrm{d}\phi'}{\mathrm{d}y}\right)^{-1} \, \mathrm{d}\phi'. \tag{62}$$

The inverse of the concentration gradient can be obtained in the upper and lower part of the mat by inserting, respectively, (54) and (57) into (59). Employing the results in (62), the drainage flux is obtained,

$$J = \frac{1}{\phi_0} \left(\int_{\phi_w}^{\phi_1} \phi'(1 - \phi') K(\phi') \frac{\mathrm{d}g(\phi'; \Sigma_h)}{\mathrm{d}\phi'} \, \mathrm{d}\phi' + \int_{\phi_1}^{\phi_g} \phi'(1 - \phi') K(\phi') \frac{\mathrm{d}\sigma_c(\phi')}{\mathrm{d}\phi'} \, \mathrm{d}\phi' \right). \tag{63}$$

We conclude by considering what changes need to be made to the analysis when $\Sigma_h \geq M/\sqrt{2}$. The shear-flow region then extends over the entire mat, i.e. $y_1 = 0$. In the particular case $\Sigma_h = M/\sqrt{2}$, the loads on the particle network are just of the right strength to bring the stress state $(\sigma_d^{yy}, \tau_d^{xy})$ at the filter surface to the critical state line. Although the flocculated structure is then at critical state at y = 0, the rate-independent network stresses there completely balance the transmitted load, and the viscous stress τ_{Nd}^{xy} is zero. Therefore, equation (58) can still be used to obtain $\phi_w = \phi_1$. At larger values of Σ_h , the concentration $\phi_w = \phi_1$ must instead be obtained from the condition $\sigma_c(\phi_w) = 1$. Apart from this, the analysis proceeds as described above for the shear-flow region.

The solution presented here, for the concentration in a compressible mat with a free surface, subjected to a combined drainage and cross flow, constitutes a generalisation of the asymptotic solution derived by H&D for the corresponding problem in which the deviatoric solid stress tensor τ_d is neglected. In that model, the inter-particle forces are assumed to manifest themselves only as an

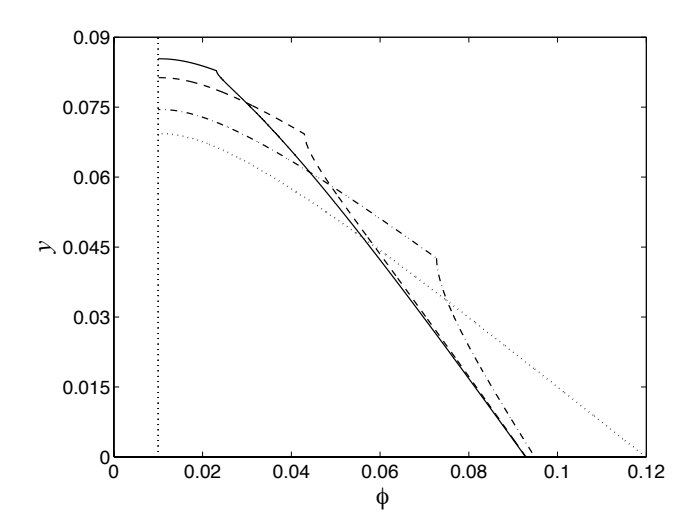


FIGURE 10. Concentration profiles for three different shear loads. Solid line: $\Sigma_h = 10^{-3}$. Dashed line: $\Sigma_h = 10^{-2}$. Dash-dotted line: $\Sigma_h = 5 \cdot 10^{-2}$. Dotted line: $\Sigma_h = M/\sqrt{2}$. The vertical dotted line indicates the gel concentration. The kink on the curves occurs at $y = y_1$. $\sigma_0/\sigma_1 = 500$. n = 2.5, M = 0.287. $\phi_0 = 0.005$. $\phi_q = 0.01$.

isotropic particle pressure, and deviatoric loads must necessarily be balanced by the viscous stresses alone. To illustrate the outlined procedure, concentration profiles corresponding to four different shear loads are plotted in figure 10, including the load $\Sigma_h = M/\sqrt{2}$ at which a stagnant region adjacent to the filter only just fails to appear. The kinks on the curves mark the boundary between the stagnant lower part of the mat, and the shear-flow region on top.

When the concentration profile $\phi(y)$ has been determined, it is straightforward to calculate the viscous stress $\tau_{Nd}^{xy} = \Sigma_h - \tau_c(\phi(y))$ in the region $y_1 \leq y \leq H$. The velocity profile $u_d^x(y)$ is then readily obtained, the result depending on the chosen constitutive model for the rate-dependent stresses. It is worth pointing out that the solution for the concentration is the same for all loads $\Sigma_h \geq M/\sqrt{2}$. The viscous stress τ_{Nd}^{xy} will however change, and, by consequence, the velocity profile. We have in the analysis assumed that Σ_h is given a priori. The (dimensional) horizontal bulk velocity U_∞ required to generate the shear load can be calculated a posteriori once we have $J_m = U_0 J$ and $U_h = U_0 u_d^x(y = H)$.

Paradis et al. (2003) measure the evolution of the drainage resistance of a fibre sheet, as it is formed under constant drainage pressure and a hydrodynamically applied shear load. The drainage resistance coefficient is defined as the drainage pressure divided by the product of the drainage flux and the current mat thickness. In the scaled variables employed in the present study,

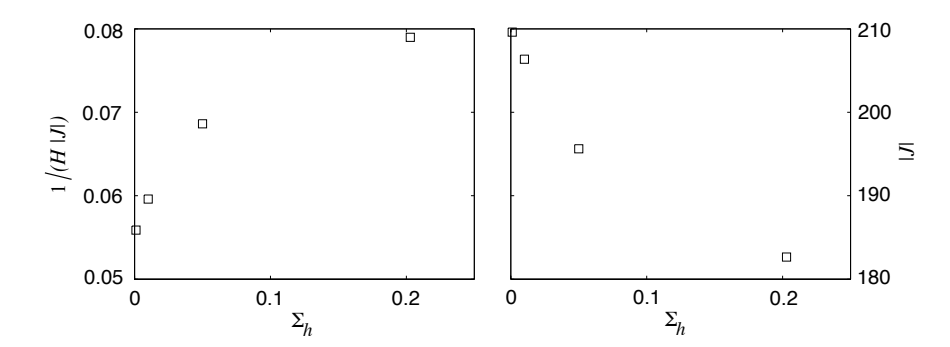


FIGURE 11. Drainage resistance coefficient (left subfigure) and drainage flux (right subfigure) as functions of the shear load for the cases in fig. 10. Cf. the caption of that figure for parameter values.

this corresponds to 1/(H|J|). Paradis *et al.* find that increasing the shear load results in an increased drainage resistance coefficient for a given surface density (i.e. 'basis weight') of the formed sheet. It somewhat dubious to compare the asymptotic analysis in this appendix with measurements during the transient stage of a drainage process, but nevertheless, in figure 11 we have plotted the resistance coefficient as a function of the shear load for the same cases as in figure 10, together with the magnitude of the drainage flux. The same trend regarding the influence of the shear on the resistance coefficient is seen as was observed by Paradis *et al.*.